ENHANCEMENT OF THE ACCURACY OF SINGLE EPOCH POSITIONING FOR LONG BASELINES WITH APPLICATION TO STRUCTURE DEFORMATION MONITORING

ENHANCEMENT OF THE ACCURACY OF SINGLE EPOCH POSITIONING FOR LONG BASELINES WITH APPLICATION TO STRUCTURE DEFORMATION MONITORING

MOHAMMED ASSIADI

School of Civil Engineering and Geosciences,

Newcastle University

Thesis submitted in partial fulfilment

For the degree of Doctor of Philosophy

NOVEMBER 2012

ABSTRACT

Using single-epoch GPS positioning has many advantages, especially when monitoring dynamic targets (e.g. structural movements). In this technique, errors occurring in previous epochs cannot affect the current epoch's accuracy. However, careful processing is required. This research uses the GPS Ambiguity Search Program (GASP) single-epoch software. Resolving the phase ambiguities is essential in this technique. Some statistical ambiguity resolution functions have been introduced to estimate the best values of these ambiguities. The function inputs are the base station position, the approximate roving receiver position, and the shared GPS phase measurements at both receivers.

This work investigates different GPS pseudorange solutions to find the optimal ambiguity function inputs. The noise level in an undifferenced pseudorange coordinate solution is less than in the double-differenced case; thus, using it in the ambiguity function improves the results. Regional correlation between the pseudorange-computed positioning errors exists; therefore, applying a regional filter reduces their effects. Multipath errors approximately repeat themselves every sidereal day in the case of static or quasi-static receivers and applying a sidereal filter mitigates their effects.

The IGS ionospheric model reduces the effect of the ionosphere on the GPS phase measurements. Also, a local code-based ionospheric correction model can be generated. Applying these models improves the quality of the phase measurements, which leads to improvement of the ambiguity function outputs. A Kalman filter applied to the code-based ionospheric model further improves the corrected phase measurements. There is a correlation between the ambiguity function outputs' quality and the phase measurement residuals' σ_0. Applying a σ_0 threshold filter reduces the probability of obtaining inaccurate results.

Data for various baseline lengths, with synthetic displacements added, indicate that the improved GASP results are reliable for monitoring movements exceeding 10 cm for baselines up to 60 km.

It would not have been possible to write this doctoral thesis without the help and support of the kind people around me, to only some of whom it is possible to give particular mention here.

My great appreciation and respect goes to both of my supervisors Dr Stuart Edwards and Professor Peter Clarke for their continuous patience, help and support in the successful completion of this thesis.

I would like to thank Dr Matt King for providing me with the Tidefree software, Iain Woodfine, and Graham Patterson for their technical support.

I would also like to acknowledge the financial support of Aleppo University in Syria particularly in the award of a Postgraduate Research Studentship that provided the necessary financial support for this research.

And finally, my wife for her patience and support.

TABLE OF CONTENTS

LIST OF FIGURES

LIST OF TABLES

LIST OF ABBREVIATIONS

2D	**Two-Dimension**
3D	**Three-Dimension**
AFM	**Ambiguity Function Method**
AFT	**Ambiguity Function Technique**
AFV	**Ambiguity Function Value**
C/A	**Coarse/Acquisition GPS Signal**
Code-DD	**Code Double Differencing**
Code-SPP	**Code Precise Point Positioning**
DD	**Double Differencing**
DOP	**Dilution Of Precision**
DOY	**Day Of Year**
ECEF	**Earth Centered Earth Fixed**
EDM	**Electronic Distance Measurement**
FARA	**Fast Ambiguity Resolution Approach**
FASF	**Fast Ambiguity Search Filter**
F-Test	**Fisher Test**
GASP	**GPS Ambiguity Searching Program**

GF	**Geometry Free**
GLONASS	**GLObal NAvigation Satellite System**
GNSS	**Global Navigation Satellite System**
GPS	**Global Positioning System**
Hz	**Hertz**
IF	**Ionosphere Free**
IGS	**International GNSS Service**
IONEX	**Ionosphere Map Exchange**
IPP	**Ionosphere Pierce Point**
L1	**GPS L-band signal 1 (1575.45 MHz)**
L2	**GPS L-band signal 2 (1226.60 MHz)**
LAMBDA	**Least squares AMBiguity Decorrelation Adjustment**
LSA	**Least Squares Adjustment**
LSAST	**Least Squares Ambiguity Search Technique**
MAD	**Median Absolute Deviation**
MATLAB	**MATrix LABoratory**
MHz	**Mega Hertz**
NASA	**National Aeronautics and Space Administration**
NGS	**National Geodetic Survey**
NOAA	**National Oceanic and Atmospheric Administration**
OS	**Ordnance Survey**

OTF	**On The Fly**
P-code	**Precision Code**
PCV	**Phase Centre Variation**
PDOP	**Position Dilution of Precision**
PPP	**GPS Precise Point Positioning**
PRN	**Pseudo-Random Noise**
RADGPS	**Regional Area Differential GPS**
RINEX	**Receiver Independent Exchange Format Version**
RMS	**Root Mean Square Error**
SA	**Selective Availability**
SD	**Standard Deviation**
SNR	**Signal-to-Noise Ratio**
STD	**Standard Deviations**
SV	**Space Vehicle**
SOPAC	**Scripps Orbit and Permanent Array Centre**
STEC	**Slant Total Electron Content**
TEC	**Total Electron Content**
TECU	**Total Electron Content Unit**
UK	**United Kingdom**
US	**United States**
USA	**United States of America**

UTC	**Coordinated Universal Time**
UV	**Ultraviolet Light**
VCM	**Variance-Covariance Matrix**
WGS84	**World Geodetic System 1984**
ZHD	**Zenith Hydrostatic Delay**
ZWD	**Zenith Wet Delay**
WL	**Wide Lane**

INTRODUCTION

1.1 INTRODUCTION

Monitoring structural stability provides information that can assist in the prediction of hazards which may occur due to movements or structural failure. The advancement of technology over the last few decades has improved the precision of the measurement systems, allowing reliable results for monitoring structural movements to be obtained (Hsieh et al., 2006; Nickitopoulou et al., 2006; Abdel-salam, 2005; Knecht and Manetti, 2001). In addition to geophysical equipment such as strain gauges, tilt meters, extensometers, accelerometers etc., a variety of surveying methods can also be used to gather monitoring/deformation data (e.g. conventional terrestrial surveying methods, Airborne Laser Scanning and aerial/terrestrial photogrammetry, and satellite-based techniques). Conventional terrestrial surveying methods employ levels, theodolites, and total stations. There has been widespread use of these methods in structural integrity monitoring because of their low cost in comparison to some of the other techniques. Satellite-based positioning techniques (Global Navigation Satellite Systems (GNSS)) including; the US Global Positioning System (GPS), the Russian GLObal NAvigation Satellite System (GLONASS); the European Galileo system, and the Chinese Compass system, have many advantages over conventional positioning

methods (Erol, 2010). Such space based technologies offer greater flexibility in the selection of the station location, as visibility between stations is not required. However, sky visibility is necessary, and the locations of GNSS receivers should provide for a sufficient minimum number of shared satellites between stations to allow a differencing solution to be formed. Space based approaches also reduce manpower requirements for conducting deformation surveys, and their measurements can be taken throughout the day and night, and under all weather conditions. They have therefore been considered as an impressive, economic, and efficient technique for any application that requires the determination of positions (Nickitopoulou *et al.*, 2006). Several factors contribute to the design of any engineering monitoring system. For example the nature of the object plays a critical role in deciding the limits of the accuracy, e.g. the required accuracy for monitoring vibrations in structures such as long bridges and tall buildings varies between 10 mm to 200 mm depending on the movement magnitude (Lovse *et al.*, 1995), and more accurate measurements are required for monitoring their deformation (Erol *et al.*, 2004).

GPS provides positions for the monitored object together with corresponding time. The continuous comparison of these positions can be used to create a model of the object's movements. This object could be an engineering structure, a landslide, an Earth tectonic plate or a vehicle. The availability of GPS data allows the monitoring of the movements to be undertaken in real-time or near real-time, which could be a crucial factor in some monitoring tasks (e.g. structural deformation monitoring).

GPS positioning accuracy is affected by errors that affect the observations of the carrier phase and the pseudorange which has a negative aspect on the monitoring procedure. Several techniques have been used to resolve the effects of the GPS errors and noise on monitoring applications. As an example, applying a Kalman filter has been used to reduce the effect of the GPS observation noise on monitoring landslides (Rutledge *et al.*, 2001). Implementing a multi-antenna array system improves the GPS capability in the monitoring of steep wall deformations (Forward *et al.*, 2001). In an area where visibility of satellites is poor (e.g. valleys), pseudolites (ground-based pseudo-satellite transmitters) are used to enhance the satellite geometry constellation. A sub-centimetre accuracy level can be obtained by employing GPS and pseudolites

which can be used to monitor structural (e.g. bridge) movements (Erol *et al.*, 2004). Also, GPS monitoring performance (a centimetre level accuracy) can be improved by using a combination of GPS and triaxial accelerometers (Meng, 2002).

GPS errors can be classified into three main categories according to their source: satellite related, atmosphere related, and receiver/site related errors (Hofmann-Wellenhof *et al.*, 2001). Achieving high GPS positioning accuracies requires great care in dealing with these errors. Applying available correction models reduces the effect of some of these errors as does the use of multiple receivers (relative positioning) at the same time. The accuracy of GPS positioning also depends on the receiver status, i.e. whether it is static or moving. For a static GPS receiver, gathering a large amount of data helps to mitigate error effects, whilst in a moving receiver more sophisticated and complex methods are needed to obtain the highest positioning accuracy.

In addition to the errors that affect the GPS observations, the GPS relative carrier phase measurements are ambiguous by an unknown integer number of cycles, called the GPS carrier-phase ambiguity. Resolving this ambiguity has been considered a great challenge, especially for epoch by epoch GPS applications where the number of observations is limited to the number of observed satellites at each epoch. A variety of ambiguity resolution functions have been introduced. Applying these functions over a long baseline is mainly limited by errors due to the atmospheric effect on the GPS data (Kim and Langley, 2000).

The GPS Ambiguity Search Program (GASP) was developed by the University of Newcastle to deal with the single epoch case using the relative GPS strategy together with dual-frequency receiver data (Ragheb, 2007; Al-Haifi, 1996; Corbett, 1994). It gives the output of the ambiguity resolution for each epoch of processed data separately, which means that errors occurring in previous epochs (e.g. cycle slips) do not affect the current epoch accuracy. Processing data in epoch by epoch software requires a great deal of care due to the limitation of the number of observed satellites at each epoch. On occasion there may not be any redundancy in the number of observation equations in the data processing strategy, and thus the goodness of fit of

the ambiguity resolution cannot be tested perfectly. As a result, strict attention should be paid to the other positioning errors such as receiver dependent biases, satellite dependent biases and signal propagation biases (ionospheric and tropospheric delays). These errors must be eliminated precisely to obtain the highest possible accuracy.

Employing an epoch by epoch technique provides fast data processing which allows structural monitoring to be undertaken quickly (Ince and Sahin, 2000). Using a long baseline allows one GPS reference station to cover a large area of which the monitored objects might span over. This in turn reduces the cost of the monitoring operation. Also, increasing the reference station coverage area is important in cases where the monitored object is expected to move long distances (e.g. vehicle). It is also important to have a distant stable station when the movement is widespread (e.g. tectonic plate motion during earthquakes). Taking advantage of the fast /accurate data processing of the GPS epoch by epoch positioning, a real time monitoring / warning GPS receivers network system has been used to monitor the dam at Metropolitan Water District's Diamond Valley Lake, California, USA (Bock *et al.*, 2001). Single epoch GPS processing has been used to track moving vehicle velocity and positions and to monitor structural deformation (de Jonge *et al.*, 2000). It has also been used to monitor landslide deformation in Jiangxi Province, China (Liu *et al.*, 2005).

The International GNSS Service (IGS) now provides very accurate satellite orbital positions and clock data (Kouba, 2009). The receiver and satellite hardware and clock biases are largely cancelled by applying the double differencing technique. However, there are some correction models which are available for application in order to mitigate the effects of these biases more precisely. Also, the Earth rotation and solid Earth tidal deformation effects can be minimised by applying the double differencing technique. GASP adopts this double differencing technique when dealing with the GPS data. It also employs the Saastamoinen tropospheric model (Saastamoinen, 1972) and Niell Mapping Function (Niell, 1996) to mitigate the effect of the troposphere on the results. As a result, the main error which prevents the extension of the software applications over long baselines is the ionosphere. For GPS positioning software which implements an ambiguity resolution function the baseline length should be less than 10 km to obtain good accuracy (Counselman and Gourevitch, 1981).

1.1 AIMS AND OBJECTIVES

This research will investigate methods of mitigating the ionospheric effect on single epoch ambiguity function resolution. Also, it aims to create the best inputs for the GASP ambiguity function by improving the GPS pseudorange observation solution. The ultimate goal of the research is to demonstrate the accuracy and the reliability of relative single-epoch GPS software over long baseline lengths (up to 200km) and apply it to the monitoring of structural settlement and shaking motions.

The IGS single layer ionospheric model will be applied in order to reduce the effect of the ionosphere. In addition to applying the IGS ionospheric model, the ionosphere will be considered as an unknown parameter in the pseudorange observation equations to absorb the local ionospheric effect that is not described by the IGS model. Also, a pseudorange-based ionospheric model will be created to correct the GASP ambiguity function phase measurement inputs.

To find the best positioning inputs for the ambiguity function, various pseudorange observation solutions will be investigated (e.g. using double differencing and un-differenced techniques, employing a pseudorange geometry free combination, and applying sidereal and regional filters). The positioning results of each solution will be used as positioning inputs to the GASP ambiguity function. Statistical testing will be employed to examine the final solution results and to select the best result. The approved pseudorange solution results will be filtered by applying a Kalman filter to reduce the noise from the pseudorange-based ionospheric model. The Kalman filter parameters will be chosen to give the pseudorange solution clock and positioning results freedom to change from epoch to epoch. The filtered pseudorange solution results will be reused in the ambiguity function to study the effect of filtering them on the final software results. To reduce the probability of obtaining inaccurate positioning results, the final GASP positioning results will be further filtered depending on their σ_0 values to ensure a high percentage of the results are accurate (with 3-D positioning accuracy better than 10 cm) and hence increase solution robustness.

Finally, synthetic RINEX files will be created to simulate real deformation motion. Two types of structural movements will be simulated: settlement and shaking. The modified RINEX files will be used as a moving station to create various baselines. The baseline data will be processed using the modified version of the GASP software. The difference between the GASP results and the modelled height of the station will be analysed in order to study the ability of the GASP software in detecting structural movements.

1.2 THESIS OUTLINE

This study is structured into seven chapters, which are as follows:

Chapter One: Introduction

This chapter presents the research background, aims and objectives, and the thesis outline. It also gives an introduction to this research.

Chapter Two: GPS Overview and Processing Software

In this chapter, the basic concept of GPS positioning is briefly introduced, including the GPS observations, associated errors, and the equations which can be formed by using the GPS observations. The GPS observation differencing techniques used throughout this research, and their linear combinations, are illustrated in detail in this chapter. The various ambiguity function techniques that may be employed are also introduced and detail of the GASP software ambiguity function is provided.

Chapter Three: Ionospheric Effects on GPS Signals and Mitigation Methodologies

The aim of this chapter is to present an introduction to the ionosphere, and its effect on the GPS observations. This chapter also describes some of the available ionospheric correction methodologies (e.g. using differential GPS observations, ionosphere free combination, and global and regional ionospheric models). Each of

these solutions will be checked whether it is suitable to be used in single epoch GPS software or not.

Chapter Four: Using the IGS Products for a Single Epoch GPS Software

The IGS products (precise satellite orbits and ionospheric model) will be used together with various correction models in order to increase the accuracy of the GPS pseudorange observation solutions. A number of differencing techniques will be investigated in these solutions, and sidereal and regional filters will also be applied. The modified solution results will be used as inputs to the GASP software ambiguity function. Data covering several baseline lengths will be used to test the solutions. At the end of this chapter, the best solution result will be used in the software for the following chapters.

Chapter Five: Applying Kalman Filtering to the Ambiguity Function Inputs and σ_0 Filtering to Its Outputs

The computed pseudorange-based ionospheric model developed in chapter 4 is shown to be noisy as it is a result of solving noisy observation equations. However, theory implies that the ionosphere should vary relatively smoothly over time (Enge and Misra, 1999). Therefore a Kalman filter will be applied to the GPS pseudorange observation equations to remove excess noise in the model. Also, a σ_0 filter will be applied to the GASP positioning results to increase their reliability.

Chapter Six: Structural Deformation Settlement and Shaking Synthetic Tests

The Tidefree software will be used to create a receiver motion simulation. Two types of structural movements will be simulated: structural settlement and shaking. The modified RINEX files will be processed using the modified GASP software (Chapter 5) in order to examine its potential applicability for monitoring structural movements.

Chapter Seven: Conclusions and Recommendations

This chapter will present a summary of the results of the work undertaken throughout the research and the conclusions will be extracted from the results. Suggestions and recommendations for future work in the subject area will also be addressed.

GPS OVERVIEW AND PROCESSING SOFTWARE

2.1 INTRODUCTION

The Global Positioning System (GPS) is a satellite-based radio navigation and positioning system made up of a constellation of nominally 24 satellites and several backup satellites placed into their orbits by the USA. GPS satellites transmit coded signals that can be processed to compute position, velocity and time. Each signal is a collection of three components: carrier waves on two frequencies (L1 with an $f_1 = 1575.42$ MHz frequency and L2 with an $f_2 = 1227.60$ MHz frequency), ranging codes and navigation message (Hofmann-Wellenhof *et al.*, 2001). The new generation of the GPS satellites (Block IIF) transmit a new civilian-use GPS signal (L5) with a 1176.45 MHz frequency. The first IIF satellite was launched in May, 2010. This signal is currently not in use as only a few satellites transmit it (two satellites at the time of this thesis submission). The GPS has been built upon the surveying distance – distance intersection problem theory, where knowing distances to reference points leads to the finding of the unknown station location. The GPS satellites have been placed in stable orbits and thus their positions can be computed at

any epoch. These satellites transmit signals at the speed of light allowing the receiver to calculate the ranges between it and them. In addition to the GPS, there are several satellite navigation systems (e.g. the GLObal NAvigation Satellite System (GLONASS), Galileo and Compass). These systems form the Global Navigation Satellite Systems (GNSS) (Groves, 2008).

GPS signals are exposed to many error sources, which affect their positioning accuracy. It is important to understand these errors in order to mitigate and remove their effects (Hofmann-Wellenhof *et al.*, 2001). In the following section, GPS error sources will be expounded and some of their correction methodologies will be illustrated.

2.2 SOURCE OF ERRORS IN GPS OBSERVATIONS

The GPS satellite locations in their orbits are affected by many factors (e.g. solar and lunar gravity, and solar radiation pressure) (Kaplan and Hegarty, 2006). Therefore the US Department of Defense (DoD) has created a control network to monitor and organise the GPS satellites health and motions. This control segment consists of a master control station, monitor stations, and the ground antenna (Kaplan and Hegarty, 2006). The GPS signal's travel time to the receiver is affected by the atmosphere, which makes the satellite-receiver range calculation imperfect. Also the receiver antenna, the Earth different motions, and the receiver's surrounding environment affect the GPS positioning. Figure 2-1 shows the main errors that affect the GPS observations.

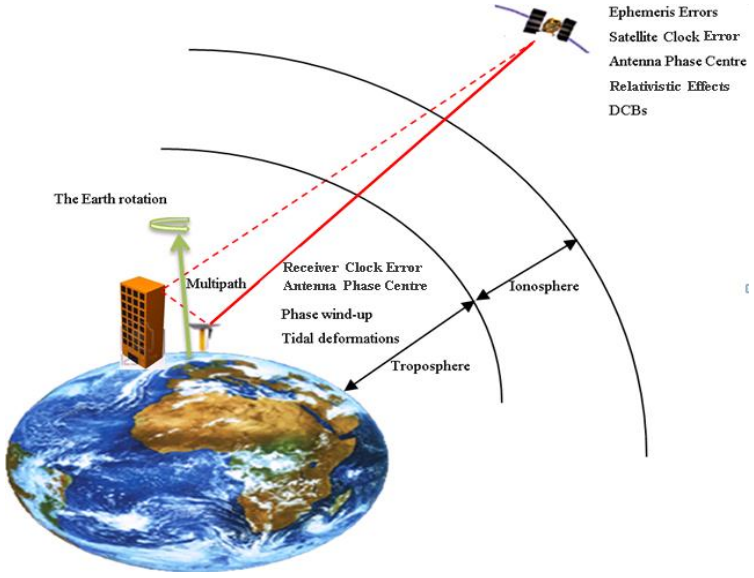

Figure 2-1 Errors on GPS signal

Depending on the source, GPS errors can be classified as satellite, atmospheric and receiver/site related errors.

2.2.1 Satellite Related Errors

The motion of the GPS satellite in its orbit is affected by some forces (e.g. solar radiation pressures and gravity forces). Also, because of the physical body of the satellite, there is a variation between the computed satellite orbit and the signals' original points. According to Kaplan and Hegarty (2006) the GPS satellite errors are ephemeris errors, satellite clock errors, antenna phase centres, relativistic effects, and differential code biases.

2.2.1.1 Ephemeris Errors

Slight shifts of the satellite orbit occur due to many forces affecting the satellite motion such as solar radiation pressure, and gravitation forces etc. For relative positioning, the influence of the orbital errors on the baseline is purely geometrical and can be approximated as (Wells *et al.*, 1986):

$$\frac{db}{b} = \frac{dp}{p} \tag{2.1}$$

Where db is the baseline error, b is the baseline distance, dp is the satellite-receiver distance error, and p is the satellite-receiver distance. This equation indicates that the effect of orbital errors on baselines is limited. The International GNSS Service (IGS) regularly updates the ephemeris computation using tracking data obtained from 438 IGS stations (International GNSS Service, 2012), and makes accurate GPS ephemeris and satellite clock information available over the Internet and in different formats (International GNSS Service, 2012), as shown in the Table 2-1:

GPS Satellites Ephemerides/ Satellite & Station Clocks		Accuracy	Latency	Update	Sample Interval
Broadcast	Orbits	~100 cm	Real time	--	daily
	Sat. clocks	~ 5 ns			
Ultra-Rapid (predicted half)	Orbits	~5 cm	Real time	at 03, 09, 15, 21 UTC	15 min
	Sat. clocks	~ 3 ns			
Ultra-Rapid (observed half)	Orbits	<3 cm	3-9 hours	at 03, 09, 15, 21 UTC	15 min
	Sat. clocks	~150 ps			
Rapid	Orbits	~<2.5 cm	17-41 hours	at 17 UTC daily	15 min
	Sat. & Stn. Clocks	75 ps ns			5 min
Final	Orbits	< 2.5 cm	12-18 days	every Thursday	15 min
	Sat. & Stn. Clocks	<0.75 ps			Sat.: 30s Stn.: 5 min

Table 2-1 The IGS ephemeris products taken from http://igscb.jpl.nasa.gov/components/prods.html

The GPS ephemeris and clocks are given at a nominal epoch, and interpolation is needed to obtain the satellite position and clock correction at the transmission epoch.

2.2.1.2 Satellite Clock Error

GPS satellites use atomic clocks which have stabilities of about 1 part in 10^{13} over a day (Seeber, 2003). If a clock can be predicted to this accuracy, the residual time error is estimated to be about 10 ns Root Mean Squared (RMS) or about 3.5 m.

The IGS SP3 ephemeris files provide satellite clock information given in units of microseconds. The GPS ephemeris and clocks are given at a nominal epoch; therefore an interpolation is needed to obtain the satellite position and clock correction at the transmission epoch. Figure 2-2 shows an example of SP3 ephemeris files.

```
#cP2007  3  7  0  0  0.00000000      96 ORBIT IGS05 HLM  IGS
## 1417 259200.00000000   900.00000000 54166 0.0000000000000
+   31   G01G02G03G04G05G06G07G08G09G10G11G12G13G14G15G16G17
+        G18G19G20G21G22G23G24G25G26G27G28G29G30G31  0  0  0
+          0  0  0  0  0  0  0  0  0  0  0  0  0  0  0  0  0
++         3  3  3  3  3  3  3  2  3  3  3  4  3  3  0  0  0
%c G  cc GPS ccc cccc cccc cccc cccc ccccc ccccc ccccc ccccc
%c cc cc ccc ccc cccc cccc cccc cccc ccccc ccccc ccccc ccccc
%f  1.2500000  1.025000000  0.00000000000  0.000000000000000
%f  0.0000000  0.000000000  0.00000000000  0.000000000000000
%i    0    0    0    0      0      0      0      0         0
/* REFERENCED TO IGS TIME (IGST) AND TO WEIGHTED MEAN POLE:
/* PCV:IGS05_1402 OL/AL:FES2004  NONE     Y  ORB:CMB CLK:CMB
*  2007  3  7  0  0  0.00000000
PG01 -21739.312770 -15008.377953   3264.180677    112.059387 10  9  8 184
PG02  13807.980773  14078.145512 -18146.272717     88.120478 13 11 11 180
PG03 -24488.094208 -10703.130127  -1148.523508     23.925412  9  9 12 174
PG04   6568.277765  24272.878683  -8024.742665      6.883820  7  7  9 154
PG05  22008.533922 -14426.284217   2712.250914     42.296137 11  7  7 176
PG06  12199.032153 -11118.299077 -20627.868893     71.563134 11  9  7 141
PG07   7720.000181 -13616.583412 -21122.651257    393.319918  9 10  8 148
PG08  -1068.724110  26254.820307  -1653.866230    -99.049316  8  8 12 167
PG09  14251.134237  -5435.156877  21139.088619     60.496441  8 10  9 173
PG10  19221.094454   3014.438897 -18334.781840     98.422983 10 10 11 152
```

Figure 2-2 Example of a SP3 file.

The GPS satellite clock correction for each satellite appears in the fifth column in Figure 2-2, as the first column represents the satellite number and the columns from two to four show the satellite location (Spofford and Remondi, 1994). However, one major advantage of single and double differencing is the elimination of the satellite clock error (see section 2.4 for information about the differencing techniques).

2.2.1.3 Satellite Antenna Phase Centre

The IGS satellite orbit model provides the coordinates of the satellite's centre of mass rather than the centre of satellite antenna. The satellite antenna phase centre offset with respect to the centre of the satellite mass is available in a satellite information file (SATELLIT.I05) (Dach *et al.*, 2007). Table 2-2 shows some of the antenna offsets for different GPS satellite blocks as they appeared in the SATELLIT.I05 file.

Satellite Block	ΔX	ΔY	ΔZ
MW TRANSM I	0.210	0.000	1.686
MW TRANSM IIA (1992)	0.279	0.000	2.201
MW TRANSM IIA(1996)	0.279	0.000	2.619
MW TRANSM IIR -B	0.000	0.000	0.614

Table 2-2 The GPS satellite antenna phase centre offsets within the SATELLIT.I05 file (Dach et al., 2007)

ΔX, ΔY and ΔZ in Table 2-2 are given in the satellite fixed body coordinate system, where:

X is along satellite track direction.
Y is toward the negative orbit normal.
Z is toward the geocentre.

Therefore applying the satellite antenna phase centre offset corrections requires knowing the satellite position (given in precise orbit file (SP3)) and the direction of its motion to project the given corrections into the receiver to satellite line-of-sight to correct the GPS observations. The GPS differencing strategies eliminate most of the satellite antenna phase centre offsets' effect on the positions, but they cannot remove their effect 100% as this effect is elevation dependent (Mader, 1999). Therefore applying this correction is very important in order to obtain high precision GPS positioning results, especially for long baseline cases.

2.2.1.4 Relativistic Effects on GPS Satellites Clocks

The GPS satellite clocks are affected by their orbital speed (special relativity). The relativistic effect should be added as a correction to the GPS signal's transmitted time. The GPS satellite clock slows by a factor of (Leick, 2004):

$$\Delta t_R = -\frac{2}{c^2}\sqrt{a\mu}\ esinE = -\frac{2}{c^2}r.v \tag{2.2}$$

Where:

Δt_R is the relativistic clock correction caused by the orbital eccentricity e.

c is the speed of light.

a is the semimajor axis of the orbit.

μ is the gravitational constant.

E is the eccentric anomaly.

r is the position of the satellite at the instant of transmission.

v is the velocity of the satellite at the instant of transmission.

Relativistic corrections depend on the satellite location and speed, so they change over time and vary from satellite to satellite. It could reduce the GPS positioning accuracy by several metres (Witchayangkoon, 2000). Using the double GPS differencing technique reduces the effect of relativity on the GPS positioning results (Zhu and Groten, 1988).

2.2.1.5 Differential Code Biases (DCBs)

Dealing with both GPS frequency observations has to account for inter-frequency hardware biases, usually referred to as Differential Code Biases (DCBs). DCBs are estimated together with the IGS single layer ionospheric model. This estimation can be done by solving the geometry free GPS combination equations (the geometry free combination will be explained in detail in section 2.4.2). For each satellite, the geometry free combination equation is:

$$P_{gf} = P_1 - P_2 = (1 - \gamma)I + HD_{r,gf} - HD_{s,gf} \tag{2.3}$$

Where:

P_1 and P_2 are pseudorange measurements on L1 and L2 frequencies, respectively, in metres.

γ is the first-order scale factor for converting ionospheric delay (I) L1 to L2 frequency $\left({f_1}^2 / {f_2}^2 \right)$, unitless.

In which:

f_1 and f_2 are the two GPS signals' frequencies.

$HD_{r,gf}$ is the receiver differential inter frequency hardware delays (generally called receiver DCB) , in metres.

$HD_{s,gf}$ is the satellite differential inter frequency hardware delays (generally called satellite DCB), in metres.

Considering that $HD_{r,gf}$ is the same for a receiver over all the day, and $HD_{s,gf}$ is fixed for a satellite over 24 hours, solving data equations for a full day over all the stations and satellites by using the Least Squares Method (LSM) or the Kalman filter will determine the satellite and receiver differential code biases in addition to the ionosphere values (Lanyi and Roth, 1988). The IGS provides the satellite DCBs in its ionospheric file header, Figure 2-3.

```
TEC values in 0.1 tec units;  9999, if no value available   COMMENT
DCB values in nanoseconds, reference is Sum_of_SatDCBs = 0  COMMENT
DIFFERENTIAL CODE BIASES                                    START OF AUX DATA
    01    -3.141     0.021                                  PRN / BIAS / RMS
    02     5.693     0.042                                  PRN / BIAS / RMS
    03    -2.735     0.034                                  PRN / BIAS / RMS
    04    -1.548     0.043                                  PRN / BIAS / RMS
    05    -2.886     0.055                                  PRN / BIAS / RMS
    06    -2.432     0.029                                  PRN / BIAS / RMS
    07    -4.260     0.027                                  PRN / BIAS / RMS
    08    -3.160     0.064                                  PRN / BIAS / RMS
    09    -1.937     0.032                                  PRN / BIAS / RMS
    10    -3.922     0.081                                  PRN / BIAS / RMS
    11     2.237     0.041                                  PRN / BIAS / RMS
    12     2.154     0.022                                  PRN / BIAS / RMS
    13     1.810     0.060                                  PRN / BIAS / RMS
    14     0.653     0.016                                  PRN / BIAS / RMS
    15    -3.860     0.021                                  PRN / BIAS / RMS
    16     0.855     0.038                                  PRN / BIAS / RMS
    17     1.311     0.048                                  PRN / BIAS / RMS
    18     1.554     0.063                                  PRN / BIAS / RMS
    19     3.932     0.088                                  PRN / BIAS / RMS
    20    -1.306     0.010                                  PRN / BIAS / RMS
    21     2.243     0.020                                  PRN / BIAS / RMS
    22     6.404     0.103                                  PRN / BIAS / RMS
    23     8.414     0.053                                  PRN / BIAS / RMS
    24    -4.705     0.017                                  PRN / BIAS / RMS
    25    -0.528     0.077                                  PRN / BIAS / RMS
    26    -1.366     0.028                                  PRN / BIAS / RMS
    27    -2.678     0.021                                  PRN / BIAS / RMS
    28     1.283     0.045                                  PRN / BIAS / RMS
    29    -1.027     0.019                                  PRN / BIAS / RMS
    30    -0.239     0.037                                  PRN / BIAS / RMS
    31     3.188     0.103                                  PRN / BIAS / RMS
```

Figure 2-3 Differential P1-P2 code biases for GPS satellites as appear in the IGS ionospheric file header.

These biases are not available in the absolute sense. Therefore it is common to consider the following differential code biases values (Dach *et al.*, 2007):

$$B_{P1-P2} = B_{P1} - B_{P2}$$
$$B_{P1-c1} = B_{P1} - B_{c1} \quad (2.4)$$

Where,

B_{P1}, $B_{P2,}$ and B_{c1} represent the biases on the P1, P2, and C/A code observations respectively.

GPS receivers can be categorised into three main classes depending on their output data (Dach *et al.*, 2007):

1- Receivers provide C1, P1, and P2 code observations (P1/P2).
2- Receivers provide C1 code observation and a particular linear combination of code observables (X2).
3- Receivers provide C1 and P2 code observations (C1/P2).

Table 2-3 shows the differential code bias corrections for the most popular GPS code linear combinations derived from the available code observables:

Linear Combinations LC	P1/P2	C1/X2= C1 + (P2-P1)	C1/P2
f1 frequency observations	$+1.546B_{P1-P2}$	$+1.546B_{P1-P2} + B_{P1-c1}$	$+1.546B_{P1-P2} + B_{P1-c1}$
f2 frequency observations	$+2.546B_{P1-P2}$	$+2.546B_{P1-P2} + B_{P1-c1}$	$+2.546B_{P1-P2}$
ionosphere-free	0	$+B_{P1-c1}$	$+2.546B_{P1-c1}$
geometry-free	$-B_{P1-P2}$	$-B_{P1-P2}$	$-B_{P1-P2} + B_{P1-c1}$
widelane	$-1.984B_{P1-P2}$	$-1.984B_{P1-P2} + B_{P1-c1}$	$-1.984B_{P1-P2} + 4.529B_{P1-c1}$
Melbourne-Wübbena Linear Combination	0	$-B_{P1-c1}$	$-0.562B_{P1-c1}$

Table 2-3 Corrections due to P1-P2 and P1-C1 code for the most important linear combinations (Dach et al., 2007).

Where the numbers in the table represent the following values:

$$\frac{f_2^2}{f_1^2 - f_2^2} = 1.546, \frac{f_1^2}{f_1^2 - f_2^2} = 2.546, \frac{f_1 f_2}{f_1^2 - f_2^2} = 1.984,$$
$$\frac{f_1}{f_1 - f_2} = 4.529, \text{and } \frac{f_1}{f_1 + f_2} = 0.562. \quad (2.5)$$

Where f_1 and f_2 are the two GPS signals' frequencies.

2.2.2 Atmospheric Related Errors

The GPS signals have to go through the atmospheric layers to reach the receiver, Figure 2-4.

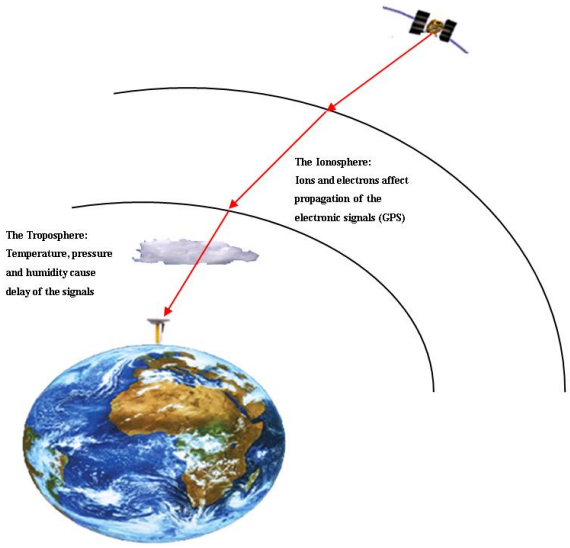

Figure 2-4 Atmospheric errors

The GPS positioning theory assumes that the satellite signals travel at the speed of light and go through a straight line to reach the receiver. This is not true in the GPS signals' case, as the atmospheric layers affect their propagation (Wells, 1974). The atmosphere is divided into two main layers according to their effects on the GPS signals, the ionosphere and the troposphere.

2.2.2.1 Ionospheric Effect

The ionosphere in GPS terms is the upper layer of the atmosphere. This layer contains ions and electrons which are created as a result of a physical reaction between the Sun's ultraviolet light and the atmosphere's atoms. The positive ions and negative electrons in the ionosphere make the electromagnetic waves' (e.g. GPS signals) propagation through it dispersive (Wells, 1974). Therefore it has been considered for a long time as the first protective layer of the earth from outside universal radiation (i.e. Sun's ultraviolet light). Also, during the last century people have used its properties in many beneficial ways (i.e. in communication), but on the other hand it causes a lot of problems for all projects which need signals to travel through this layer. Ionospheric effects are described in detail in Chapter 3.

2.2.2.2 Troposphere Effect

The troposphere is the lowest layer of the Earth's atmosphere (which is the layer in which weather occurs on the Earth). Its thickness varies from around 8 km at the poles to 16 km at the equator. In the troposphere, variations in pressure, temperature, and humidity all contribute to variations in the speed of radio waves. The effect of the troposphere depends on the satellite-receiver geometry, and it ranges between approximately 2.5 m delay in the zenith direction to 28 m when the elevation angle is 5° (Leick, 2004).

The troposphere can be divided into two main components, the hydrostatic (dry) and wet. The hydrostatic component is caused mostly by dry gases and contributes approximately 90% of the total tropospheric refraction, whereas the wet component is a result of water vapour (Leick, 2004). The effect of the troposphere is frequency-independent and cannot be eliminated via dual-frequency observations.

Various tropospheric models have been used e.g. Hopfield (Hopfield, 1963), and Saastamoinen (Saastamoinen, 1972). These models introduced a number of formulas and coefficients in order to find the tropospheric delay. The inputs of these models are the observing point latitude, and height above mean sea level. According to the Saastamoinen model, the zenith hydrostatic delay μ_h and zenith wet delay μ_w in metres at a station with a φ latitude and a H height in metres can be formed as follows (Saastamoinen, 1972):

$$\mu_h = \frac{0.0022768P}{1 - 0.00266\cos(2\varphi) - 0.00028 \times \left({}^{H}/_{1000}\right)} \tag{2.6}$$

$$\mu_w = 0.0122 + 0.00943\delta \tag{2.7}$$

Where P is the atmospheric pressure at the station location. δ is the atmospheric vapour pressure at the station location.

Measuring the atmospheric pressure, temperature, humidity, and vapour pressure at the station requires the presence of some technical tools at the station location (e.g.

hygrometer, barometer and thermometer), which are not available most of the time. Therefore some mathematical formulae have been introduced to model them according to the station location as follows (Niell, 1996; Saastamoinen, 1972):

$$P = P_0(1 - 0.0000226H)^{5.225} \tag{2.8}$$

$$\delta = \frac{h_w}{100}\exp(-37.2465 + 0.213166T - 0.000256908T^2) \tag{2.9}$$

Where P_0 is the standard atmospheric pressure at mean sea level (1013.25 mbar) and H is height above mean sea level. T and h_w are the atmospheric temperature and humidity at the station respectively, and they can be calculated using the following formula:

$$T = T_0 + 0.0065H \tag{2.10}$$

Where T_0 is the standard atmospheric temperature in degrees Kelvin at mean sea level.

$$h_w = h_{w0}\exp(-0.0006396H) \tag{2.11}$$

Where h_{w0} is the standard humidity at mean sea level (50 %).

In addition to the tropospheric models, different mapping functions which form the signal delay as a function of elevation angle are also given (Witchayangkoon, 2000) (e.g. Herring Mapping Function (Bevis *et al.*, 1992), Lanyi Mapping Function (Lanyi, 1984), Davis Mapping Function (Davis *et al.*, 1985), Niell Mapping Function (Niell, 1996) , and Global Mapping Function (Böhm *et al.*, 2006)). As an example, the Niell Mapping Function (NMF) consists of two functions, one is for the hydrostatic tropospheric component m_h and the other is for the wet component m_w. These functions can be formed as follows (Niell, 1996):

$$m_h = \frac{1 + \dfrac{a}{1 + \dfrac{b}{1 + c}}}{\cos(z) + \dfrac{a}{\cos(z) + \dfrac{b}{\cos(z) + c}}} + \frac{H}{1000} \times \left[\frac{1}{\cos(z)} - \frac{1 + \dfrac{a_h}{1 + \dfrac{b_h}{1 + c_h}}}{\cos(z) + \dfrac{a_h}{\cos(z) + \dfrac{b_h}{\cos(z) + c_h}}} \right] \tag{2.12}$$

$$m_w = \frac{1 + \dfrac{a_w}{1 + \dfrac{b_w}{1 + c_w}}}{\cos(z) + \dfrac{a_w}{\cos(z) + \dfrac{b_w}{\cos(z) + c_w}}} \tag{2.13}$$

Where z is the receiver-satellite line zenith angle, H is height above mean sea level and the coefficients a, b and c are constants which depend on the latitude and the processing data day of the year (DOY) calculated as:

$$a = a_{avg} + a_{amp}.cos\left[2\pi \times \frac{DOY - DOY_0}{365.25}\right] \tag{2.14}$$

Where $\mathrm{DOY_0}$ is a constant value that depends on which hemisphere of the Earth the station is on ($\mathrm{DOY_0} = 28$ for the northern hemisphere and $\mathrm{DOY_0} = 211$ for the southern hemisphere), and the average and amplitude values of the coefficients, $\mathrm{a_{avg}}$ and $\mathrm{a_{amp}}$, are given in Table 2-4 (Niell, 1996).

Coefficient (hydro)	Latitude (degree)				
	15	30	45	60	75
	Average				
a_{avg}	1.2769934e-3	1.2683230e-3	1.2465397e-3	1.2196049e-3	1.2045996e-3
b_{avg}	2.9153695e-3	2.9152299e-3	2.9288445e-3	2.9022565e-3	2.9024912e-3
c_{avg}	62.610505e-3	62.83793e-3	63.721774e-3	63.824265e-3	64.258455e-3
	Amplitude				
a_{amp}	0.0	1.2707962e-5	2.6523662e-5	3.4000452e-5	4.1202191e-5
b_{amp}	0.0	2.1414979e-5	3.0160779e-5	7.2562722e-5	11.723375e-5
c_{amp}	0.0	9.0128400e-5	4.3497037e-5	84.795348e-5	170.37206e-5

Table 2-4 Hydrostatic mapping function coefficients

For the a_h, b_h and c_h terms of the dry mapping function, the values are $a_h = 2.53 \times 10^{-5}$, $b_h = 5.49 \times 10^{-3}$ and $c_h = 1.14 \times 10^{-3}$. Whereas, for the a_w, b_w and c_w in the wet mapping function, the values in Table 2-5 have to be interpolated to find them according to the station latitude.

Coefficient (wet)	Latitude (degree)				
	15	30	45	60	75
	Average				
a_{avg}	5.8021897e-4	5.6794847e-4	5.8118019e-4	5.9727542e-4	6.1641693e-4
b_{avg}	1.4275268e-3	1.5138625e-3	1.457252e-3	1.5007428e-3	1.7599082e-3
c_{avg}	4.3472961e-2	4.6729510e-2	4.3908931e-2	4.4526982e-2	5.4736038e-2

Table 2-5 Wet mapping function coefficients

Finally, the total slant tropospheric delay (μ_T) will look like:

$$\mu_T = \mu_h \times m_h + \mu_w \times m_w \tag{2.15}$$

Applying one of these mapping functions on the tropospheric delays obtained by one of the tropospheric models will determine the amount that should be subtracted from the GPS observations.

2.2.3 Receiver and Site Related Errors

The GPS receivers and satellites clocks are not synchronized precisely, which makes measuring the signals' travel time imperfect (Braasch and Van Dierendonck, 1999). The GPS receiver is also affected by the environment around it and the Earth's motions. As a result, the application of receiver and site errors should be taken into account if an accurate GPS positioning is targeted. Some of the GPS receiver and site errors are receiver clock error, receiver antenna phase centre, multipath effects, phase wind up, tidal deformations and Earth rotation.

2.2.3.1 Receiver Clock Error

The internal receiver clock has a large unknown offset with respect to the GPS time, which affects the range computing. Therefore, the receiver clock error appears in the GPS observation equations as an additional unknown parameter (Hofmann-Wellenhof *et al.*, 2001). Receiver clock offset is cancelled when a differencing involving the receiver with more than one satellite is applied.

2.2.3.2 Receiver Antenna Phase Centre

This error occurs because of the non-coincidence of the phase centre and the actual physical antenna centre. The phase centre is defined as being the point where the satellite signal is collected. This point is dependent on the frequency, azimuth, and elevation of the incident signals, so it varies with the changing direction of the incoming satellite signal (Wübbena *et al.*, 1996).

The US National Geodetic Survey (NGS) provides north, east and up Phase Centre Offset (PCO) values in millimetres to be added directly to the receiver north, east and up coordinates. Also it provides Phase Centre Variation (PCV) corrections correlated with the satellite elevation angles, starting from 0 to 90 degrees, with a step of 5 degrees, and for both satellite frequencies (L1 and L2) to be subtracted from the GPS phase observations. Table 2-6 shows an example of the NGS Antenna Calibration file format:

<ant_info.003> <TYP:ABS SRC:igs08_1633.atx,NGS-Database> <NGS-11/05/12=005>

ANTENNA ID + RADOME DESCRIPTION DATA SOURCE (# OF TESTS) YR/MO/DY
|AVE = # in average

[north]	[east]	[up]								| L1 Offset (mm)
[90]	[85]	[80]	[75]	[70]	[65]	[60]	[55]	[50]	[45]	| L1 Phase at
[40]	[35]	[30]	[25]	[20]	[15]	[10]	[5]	[0]		| Elevation (mm)
[north]	[east]	[up]								| L2 Offset (mm)
[90]	[85]	[80]	[75]	[70]	[65]	[60]	[55]	[50]	[45]	| L2 Phase at
[40]	[35]	[30]	[25]	[20]	[15]	[10]	[5]	[0]		| Elevation (mm)

Table 2-6 An example of NGS Antenna Calibration files.

Applying NGS antenna calibration values determines the corrections on distance at different azimuth and elevation angles.

2.2.3.3 Multipath Effects

Due to the signals' reflection off objects, the signal arrives at a receiver via multiple paths. This phenomenon distorts both the carrier and the code of the GPS signal. Solving this problem requires special care in choosing the antenna location together with applying a cut-off angle to accept only certain elevation angle signals (El-Rabbany, 2002). For a fixed GPS station, the multipath effect repeats itself approximately every sidereal day, as the GPS satellites repeat their locations every 23hr 56m 04s. Applying a sidereal filter on a single epoch GPS software positioning over short baseline lengths improves the GPS positioning accuracy (Ragheb *et al.*, 2010).

2.2.3.4 Phase Wind-up

The phase wind-up error is due to the variation in the relative orientation between the satellite antenna and the receiver antenna. The effect of this error is negligible for a double differencing solution for baseline lengths of up to a few hundred kilometres (Kouba and Héroux, 2001). Its effect is quite large for undifferenced GPS point positioning. In this research the double differencing phase measurements solution is applied and the baseline lengths will be less than few hundreds of kilometres. Therefore no phase wind-up correction model will be applied.

2.2.3.5 Tidal Deformations

The Earth is not 100% rigid and it has a certain degree of elasticity, which causes its surface to be affected by solar and lunar gravity fields, oceans and atmospheric tides,

the lithosphere plate movements, and its rotation around itself and the sun (Lambeck, 2005). This deformation is greater near the coasts because of the effect of the sea level oscillations due to the tides. The magnitude of the earth tides may reach up to 60 cm (Guochang, 2003). For GPS solutions which involve two stations the effect of the tides is negligible at the mm level for a baseline length less than 20 km. The maximum value of this deformation effect might reach 1 cm over a 100 km baseline and 5 cm for a 680 km baseline(Biagi *et al.*, 2006).

2.2.3.6 Earth Rotation

The GPS receiver and satellite coordinate reference frame is the Earth-Fixed X, Y, Z (ECEF XYZ) system. The origin of this frame is the centre of the mass of the Earth. The Z-axis is set toward the Earth's North Pole, and the XY plane is set to coincide with the Earth's equatorial plane. The GPS satellite height is about 20200 km above the Earth. With a signal travelling at the speed of light, the signal takes around 0.07 seconds to reach the receiver after being transmitted from the satellite (Guochang, 2003). During this transmission time T_t the Earth rotates around its rotation axis (Z axis). The Earth rotation velocity around the Z axis is $\theta = 0.00007292115147$ radians/second. Thus the satellite coordinates should be corrected for this rotation. The correction is as follows (Kaplan and Hegarty, 2006):

$$\begin{bmatrix} X \\ Y \\ Z \end{bmatrix} = \begin{bmatrix} \cos(\omega) & \sin(\omega) & 0 \\ -\sin(\omega) & \cos(\omega) & 0 \\ 0 & 0 & 1 \end{bmatrix} \begin{bmatrix} x \\ y \\ z \end{bmatrix} \tag{2.16}$$

Where:

x y, and z are the satellite coordinates at the reception time.

X Y, and Z are the satellite coordinates at the transmitted time.

ω is the Earth rotation angle around the Z axis during the GPS signal transmission time:

$$\omega = -\mathrm{T_t}\theta \tag{2.17}$$

However, the transmission time T_t cannot be determined correctly 100% as the receiver coordinates are not known perfectly, so one of the GPS pseudorange observation is used to find it as follows:

$$T_t = \frac{P}{c} \tag{2.18}$$

Where:

P is the pseudorange measurement on L1 or L2 frequencies, in metric units.

c is the speed of light constant, in metres per second.

2.3 GPS OBSERVATION EQUATIONS

GPS satellites transmit two carriers, L1 = 1575.42 MHz (wavelength = 19.0 cm) and L2 = 1227.6 MHz (wavelength = 24.4 cm). The carriers are modulated with a precision (P) code (L1 & L2), and a coarse acquisition code C/A (L1) (Leick, 2004). GPS receivers generate a replica for each of the GPS codes internally, which allows them to measure the signal transmission time. This time is then converted into a range by timing it by the signal speed (the speed of light). The errors on GPS, which were illustrated previously in this chapter, affect this calculation. Therefore the computed range is not genuine and the computed distance is called a pseudorange. Measuring the shift between the received satellite signals and the generated replica in the receiver gives the GPS carrier phase observation. The number of full carrier waves between the satellite and receiver cannot be counted, therefore the measurement is for the phase fraction only, as well as keeping track on the change of the full waves number (Guochang, 2003). The unknown integer number of the phase measurement cycles is called the carrier phase ambiguity. The GPS carrier-phase equations can be formed as follows:

$$\begin{aligned}\Phi_1 &= \mathrm{R} + \mathrm{c}(\mathrm{dT} - \mathrm{dt}) + \mathrm{T} - \mathrm{I} + \lambda_1 \mathrm{N}_1 + \mathrm{hd}_{\mathrm{r},1} - \mathrm{hd}_{\mathrm{s},1} + \mathrm{pb}_{\mathrm{r},1} - \mathrm{pb}_{\mathrm{s},1} + \mathrm{m}_1 + \mathrm{e}_1 \\ \Phi_2 &= \mathrm{R} + \mathrm{c}(\mathrm{dT} - \mathrm{dt}) + \mathrm{T} - \gamma\mathrm{I} + \lambda_2 \mathrm{N}_2 + \mathrm{hd}_{\mathrm{r},2} - \mathrm{hd}_{\mathrm{s},2} + \mathrm{pb}_{\mathrm{r},2} - \mathrm{pb}_{\mathrm{s},2} + \mathrm{m}_2 + \mathrm{e}_2\end{aligned} \tag{2.19}$$

Where:

Φ_1 and Φ_2 are carrier-phase measurements on L1 and L2 frequencies, respectively, in metres.

R	is the geometric distance between satellite and receiver antenna, in metres.
c	is the speed of light constant, in metres per second.
dT and dt	are receiver and satellite clock errors, respectively, in seconds.
T	is the neutral atmosphere delay, in metres.
I	is the L1 frequency ionosphere delay, in metres.
γ	is the first-order scale factor for converting ionospheric delay from L1 to L2 frequency $77^2/60^2$, unitless.
λ_1 and λ_2	are carrier phase wavelengths on L1 and L2 frequencies, respectively, in metres.
N_1 and N_2	are carrier phase integer ambiguities on L1 and L2 frequencies, respectively, in cycles.
$hd_{r,i}$	is receiver carrier phase hardware delays, respectively, in metric units. Where i represents the carrier frequencies (L1 or L2).
$hd_{s,i}$	is satellite carrier phase hardware delays, respectively, in metric units. Where i represents the carrier frequencies (L1 or L2).
$pb_{r,i}$ and $pb_{s,i}$	are receiver and satellite carrier initial phase biases, respectively, in metric units. Where i represents the carrier frequencies (L1 or L2).
m_1 and m_2	are carrier phase multipath on L1 and L2 frequencies, respectively, in metres.
e_1 and e_2	are other un-modelled errors of carrier phase measurements on L1 and L2 frequencies, respectively, in metres.

Similar equations can be formed for the pseudorange observations as follows:

$$\begin{aligned} P_1 &= R + c(dT - dt) + T + I + HD_{r,1} - HD_{s,1} + M_1 + E_1 \\ P_2 &= R + c(dT - dt) + T + \gamma I + HD_{r,2} - HD_{s,2} + M_2 + E_2 \end{aligned} \tag{2.20}$$

Where,

P_1 and P_2	are pseudorange measurements on L1 and L2 frequencies, respectively, in metric units.

$HD_{r,i}$ is receiver pseudorange hardware delays, in metric units. Where i represents the carrier frequencies (L1 or L2).

$HD_{s,i}$ is satellite pseudorange hardware delays, in metric units. Where i represents the carrier frequencies (L1 or L2).

M_1 and M_1 are pseudorange multipath on L1 and L2 frequencies, respectively, in metres.

E_1 and E_2 are other un- modelled errors of pseudorange measurements on L1 and L2 frequencies, respectively, in metres.

Solving single GPS receiver data equations is called single point positioning. As there are too many errors affecting the measurements, a high accuracy positioning is not expected from this solution. Some models and solution techniques have been introduced to deal with the errors affecting this solution (e.g. using the correction models which were discussed previously in this chapter and precise IGS products) to improve this solution positioning accuracy. These new solutions are called GPS Precise Point Positioning (PPP). More details about PPP will be discussed in chapter 4. Many techniques and solutions have also been introduced to reduce the impact of these errors on the results. Examples of these include using differencing techniques, linear combinations of observations, and the use of ambiguity resolution techniques.

2.4 OBSERVABLE DIFFERENCING

The satellite clock offset has approximately the same effect on all the receivers, therefore it is recommended to use a known location receiver (base) data to eliminate the satellite clock offset effect on the rover receiver. Also, using a base receiver reduces the effect of other GPS errors such as orbital errors, ionospheric effects, and tropospheric delays. This reduction depends on the distance between the base and the user receivers, as they are spatially correlated throughout a geographical region.

2.4.1 Single Differencing

Two receivers and one satellite or two satellites and one receiver are deployed in this differencing. The single differencing equations of two receivers A and B and satellite j, Figure 2-5, can be formed as follows:

$$\Delta\Phi^{j}_{1,AB} = \Delta R^{j}_{AB} + c\Delta dT_{AB} + \Delta T^{j}_{AB} - \Delta I^{j}_{AB} + \lambda_1 \Delta N^{j}_{1,AB} + \Delta hd^{j}_{r,1,AB} - \Delta hd^{j}_{s,1,AB} + \Delta pb^{j}_{r,1,AB} - \Delta pb^{j}_{s,1,AB} + \Delta m^{j}_{1,AB} + \Delta e^{j}_{1,AB}$$

$$\Delta\Phi^{j}_{2,AB} = \Delta R^{j}_{AB} + c\Delta dT_{AB} + \Delta T^{j}_{AB} - \gamma\Delta I^{j}_{AB} + \lambda_2 \Delta N^{j}_{,2AB} + \Delta hd^{j}_{r,2,AB} - \Delta hd^{j}_{s,2,AB} + \Delta pb^{j}_{r,2,AB} - \Delta pb^{j}_{s,2,AB} + \Delta m^{j}_{2,AB} + \Delta e^{j}_{2,AB} \quad (2.21)$$

And the pseudorange observations single differenced equations are:

$$\Delta P^{j}_{1,AB} = \Delta R^{j}_{AB} + c\Delta dT_{AB} + \Delta T^{j}_{AB} + \Delta I^{j}_{AB} + \Delta HD^{j}_{r,1,AB} - \Delta HD^{j}_{s,1,AB} + \Delta M^{j}_{1,AB} + \Delta E^{j}_{1,AB}$$

$$\Delta P^{j}_{2,AB} = \Delta R^{j}_{AB} + c\Delta dT_{AB} + \Delta T^{j}_{AB} + \gamma\Delta I^{j}_{AB} + \Delta HD^{j}_{r,2,AB} - \Delta HD^{j}_{s,2,AB} + \Delta M^{j}_{2,AB} + \Delta E^{j}_{2,AB} \quad (2.22)$$

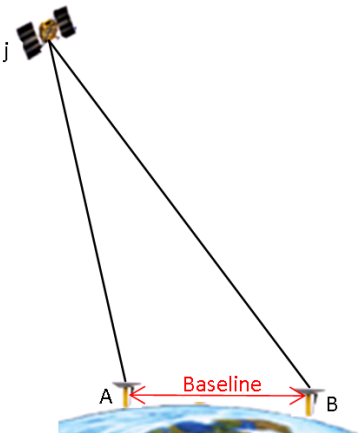

Figure 2-5 GPS single difference; one satellite and two receivers

Applying this differencing cancels the satellite clock error $c$dt, and reduces the effects of the ionosphere, troposphere and satellite hardware biases.

The single differencing phase measurement equations of two satellites j and k and receiver A, Figure 2-6, can be formed as follows:

$$\Delta\Phi^{jk}_{1,A} = \Delta R^{jk}_{A} + cdt^{jk} + \Delta T^{jk}_{A} - \Delta I^{jk}_{A} + \lambda_1 \Delta N^{jk}_{1,A} + \Delta hd^{jk}_{r,1,A} - \Delta hd^{jk}_{s,1,AB} + \Delta pb^{jk}_{r,1,A} - \Delta pb^{jk}_{s,1,A} + \Delta m^{jk}_{1,A} + \Delta e^{jk}_{1,A}$$

$$\Delta\Phi_{2,A}^{jk} = \Delta R_A^{jk} + cdt^{jk} + \Delta T_A^{jk} - \gamma\Delta I_A^{jk} + \lambda_2\Delta N_{2,A}^{jk} + \Delta hd_{r,2,A}^{jk} - \Delta hd_{s,2,A}^{jk} + \Delta pb_{r,2,A}^{jk} - \Delta pb_{s,2,A}^{jk} + \Delta m_{2,A}^{jk} + \Delta e_{2,A}^{jk} \quad (2.23)$$

And the pseudorange observation single differenced equations are:

$$\Delta P_{1,A}^{jk} = \Delta R_A^{jk} + cdt^{jk} + \Delta T_A^{jk} + \Delta I_A^{jk} + \Delta HD_{r,1,A}^{jk} - \Delta HD_{s,1,A}^{jk} + \Delta M_{1,A}^{jk} + \Delta E_{1,A}^{jk}$$
$$\Delta P_{2,A}^{jk} = \Delta R_A^{jk} + cdt^{jk} + \Delta T_A^{jk} + \gamma\Delta I_A^{jk} + \Delta HD_{r,2,A}^{jk} - \Delta HD_{s,2,A}^{jk} + \Delta M_{2,A}^{jk} + \Delta E_{2,A}^{jk} \quad (2.24)$$

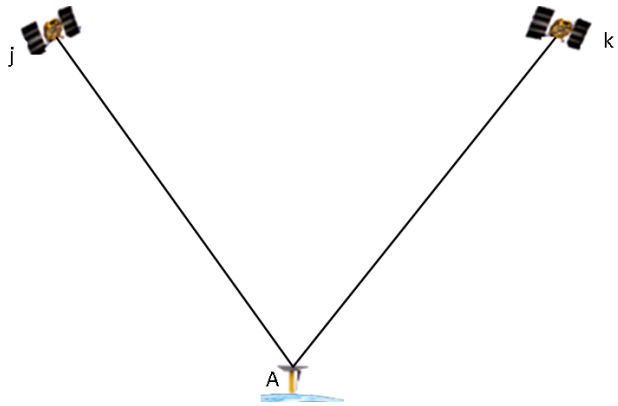

Figure 2-6 GPS single differencing; one receiver and two receivers

Applying this differencing cancels the receiver clock error cdT. On the other hand the effect of the multipath and errors due to receiver noises is amplified.

2.4.2 Double Differencing

It is possible to use two receivers and two satellites to reduce the effect of the GPS observation errors on the positions. The double differencing phase measurement equations of two receivers A and B and two satellites j and k, Figure 2-7, can be formed as follows:

$$\nabla\Delta\Phi_{1,AB}^{jk} = \nabla\Delta R_{AB}^{jk} + \nabla\Delta T_{AB}^{jk} - \nabla\Delta I_{AB}^{jk} + \lambda_1\nabla\Delta N_{1,AB}^{jk} + \nabla\Delta e_{1,AB}^{jk}$$
$$\nabla\Delta\Phi_{2,AB}^{jk} = \nabla\Delta R_{AB}^{jk} + \nabla\Delta T_{AB}^{jk} - \gamma\nabla\Delta I_{AB}^{jk} + \lambda_2\nabla\Delta N_{2,AB}^{jk} + \nabla\Delta e_{2,AB}^{jk} \quad (2.25)$$

And the pseudorange observation double differenced equations are:

$$\nabla\Delta P_{1,AB}^{jk} = \nabla\Delta R_{AB}^{jk} + \nabla\Delta T_{AB}^{jk} + \nabla\Delta I_{AB}^{jk} + \nabla\Delta E_{1,AB}^{jk}$$
$$\nabla\Delta P_{2,AB}^{jk} = \nabla\Delta R_{AB}^{jk} + \nabla\Delta T_{AB}^{jk} + \gamma\nabla\Delta I_{AB}^{jk} + \nabla\Delta E_{1,AB}^{jk} \quad (2.26)$$

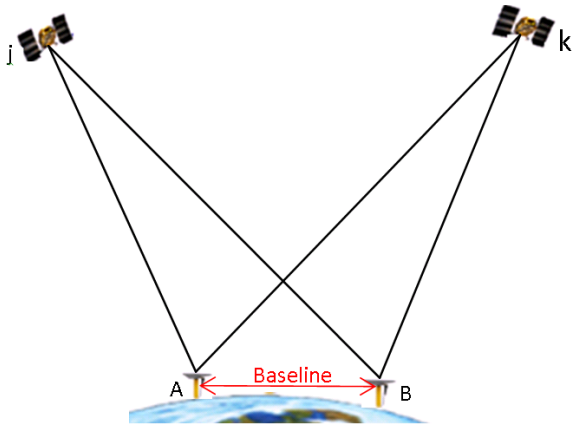

Figure 2-7 GPS double differencing

Applying this differencing removes the receiver and satellite clocks and hardware errors and biases. Also it reduces the effect of the troposphere and ionosphere on the results.

2.5 LINEARLY COMBINED OBSERVATIONS

From dual-frequency observations, various artificial observations can be formed through linear combination (Hofmann-Wellenhof *et al.*, 2001). Each combination is useful in certain applications depending on its wavelength and sensitivity to troposphere and ionosphere delay effects. The three most common are the ionosphere-free observable, the geometry-free observable and the widelane observable (Guochang, 2003).

2.5.1 The Ionosphere-Free Observable

This is useful for eliminating the first-order dispersive ionosphere effect. The carrier Φ_{if} and pseudorange P_{if} ionosphere–free combinations can be formed as follows:

$$\Phi_{if} = \frac{f_1^2}{f_1^2 - f_2^2}\Phi_1 - \frac{f_2^2}{f_1^2 - f_2^2}\Phi_2 \quad (2.27)$$

$$P_{if} = \frac{f_1^2}{f_1^2 - f_2^2} P_1 - \frac{f_2^2}{f_1^2 - f_2^2} P_2 \tag{2.28}$$

From this linear combination, the observation equations can be formed as:

$$\Phi_{if} = R + c(dT - dt) + T + \lambda_{if} N_{if} + hd_{r,if} - hd_{s,if} + pb_{r,if} - pb_{s,if} + m_{if} + e_{if} \tag{2.29}$$

$$P_{if} = R + c(dT - dt) + T + HD_{r,if} - HD_{s,if} + M_{if} + E_{if} \tag{2.30}$$

The use of this linear combination implies that respective wavelengths and ambiguities are also combined resulting in:

$$\lambda_{if} = \frac{f_1^2}{f_1^2 - f_2^2} \lambda_1 - \frac{f_2^2}{f_1^2 - f_2^2} \lambda_2 \tag{2.31}$$

$$N_{if} = \frac{f_1^2}{f_1^2 - f_2^2} N_1 - \frac{f_2^2}{f_1^2 - f_2^2} N_2 \tag{2.32}$$

One of the drawbacks in the ionosphere free combination is the measurement noise, as it is approximately three times higher than for L1 or L2 (Odijk *et al.*, 2002). Moreover, for this research it has a key disadvantage as the initial phase ambiguity results (N_{if}) will not be integer, and there is no way to apply an ionospheric model in the equations.

2.5.2 The Geometry-Free Observable

This is useful for eliminating all the geometrical errors including the troposphere, orbital, and clock offset errors. Its forms can be expressed as follows:

$$\Phi_{gf} = \Phi_1 - \Phi_2 \tag{2.33}$$

$$P_{gf} = P_1 - P_2 \tag{2.34}$$

From this linear combination, the observation equations can be formed as:

$$\Phi_{gf} = -(1-\gamma)I + \lambda_{gf}N_{gf} + hd_{r,gf} - hd_{s,gf} + pb_{r,gf} - pb_{s,gf} + m_{gf} + e_{gf} \tag{2.35}$$

$$P_{gf} = (1-\gamma)I + HD_{r,gf} - HD_{s,gf} + M_{gf} + E_{gf} \tag{2.36}$$

The ionospheric delay on L1 can be estimated by employing this combination. The obtained ionospheric delay values from all satellite observations can then be used to create an ionospheric correction model to correct the code measurements as well as the carrier phase measurements (Teunissen and Kleusberg, 1998).

2.5.3 The Widelane (WL) Observable

This combination is very useful for fixing cycle slips (cycle slips happen when the receiver loses lock on the incoming GPS signal (Xu, 2007) which affects the GPS phase ambiguity resolution, which will be explained in detail later in this chapter), and to resolve ambiguities to their integer values. The carrier and pseudorange of this combination can be formed as follows:

$$\Phi_{wl} = \frac{f_1}{f_1 - f_2}\Phi_1 - \frac{f_2}{f_1 - f_2}\Phi_2 \tag{2.37}$$

$$P_{wl} = \frac{f_1}{f_1 - f_2}P_1 - \frac{f_2}{f_1 - f_2}P_2 \tag{2.38}$$

From this linear combination, the observation equations can be formed as:

$$\Phi_{wl} = R + c(dT - dt) + T + (f_1/f_2)I + \lambda_{wl}N_{wl} + hd_{r,wl} - hd_{s,wl} + pb_{r,wl} - pb_{s,wl} + m_{wl} + e_{wl} \tag{2.39}$$

$$P_{wl} = R + c(dT - dt) + T - (f_1/f_2)I + HD_{r,wl} - HD_{s,wl} + M_{wl} + E_{wl} \tag{2.40}$$

The wide-lane observable wavelength λ_{wl} is about 86.2 cm (Guochang, 2003). Using this combination enhances the ambiguity resolution as its wavelength is about five times larger than the $\phi_1$wavelength. On the other hand, GPS errors and noises effects

are magnified which could cause problems for solutions that look at the size of the phase measurement residuals (our research software case) (Corbett, 1994).

2.6 GPS STATIC AND KINEMATIC

These solutions depend on recording GPS data over a period of time, and solving the collected data equations by using the Least Squares Method (LSM), Kalman filter or any other equations solution. As long as no cycle slips occur, the ambiguity is constant for all epochs of continuous tracking for a satellite-receiver pair. Also, the ionospheric and tropospheric effects will change slightly from epoch to epoch. For a static receiver the receiver position does not change, and the multipath and the phase wind up will be approximately constant over the time. Therefore, collecting the GPS over time provides a redundant number of equations, which makes the solution results more efficient. The solution will be less efficient for the kinematic receiver as the receiver location, multipath and wind up effects change over time, which increases the number of the unknowns in the collected observation equations. To enhance the effectiveness of the kinematic solution, receiver data is collected in static status for a period of time (varies depending on distance from the reference station and local environmental conditions) before allowing the receiver to move to resolve the ambiguity. For more reliability a static status data collection could also be done every time a cycle slip occurs. Applying these solutions has shown a good ability for obtaining a high accuracy positioning by using the GPS data.

Taking advantage of the fact that the integer ambiguity value will not change for continuous satellite tracking; researchers have tried to reduce the number of the unknown parameters in the phase observation equations by resolving the ambiguity separately, and then applying it as a known parameter. Some ambiguity techniques and filters have been introduced for this reason.

2.7 GPS AMBIGUITY RESOLUTION TECHNIQUES

GPS double difference carrier phase observations are corrupted by an unknown integer number of cycles. Determination of the GPS carrier-phase ambiguities has been considered a great challenge, especially for long baselines (Teunissen *et al.*, 1995). Furthermore, the challenge is even greater for epoch by epoch GPS

applications (e.g., monitoring an object's movement) where the ambiguity resolution for each epoch is required separately.

Many filters and techniques have been introduced to resolve the GPS carrier phase ambiguity. These solutions rely on the assumption that all the errors and noise that affect the GPS carrier phase are mitigated, so the double differenced phase measurements equation will look like:

$$\Phi_{AB}^{ij}(t) = \frac{f}{c}\rho_{AB}^{ij}(t) + N_{AB}^{ij} \tag{2.41}$$

Where:

$\Phi_{AB}^{ij}(t)$	is the phase double difference observation (from receivers A&B and satellites i&j).
ρ_{AB}^{ij}	is the double-difference geometrical distance.
N_{AB}^{ij}	is the double-difference initial integer ambiguity.
c	is the speed of light.
f	is the signal frequency.

The first ambiguity resolution function was introduced by Counselman and Gourevitch in 1981 (Counselman and Gourevitch, 1981) and many methods were introduced over the following 20 years (Kim and Langley, 2000). In the following, some of these functions will be explained.

2.7.1 Ambiguity Function Method (AFM) Technique

This function is designed to be used in static, kinematic and single epoch solutions. This technique is derived from complex number considerations to separate between the initial phase ambiguities and the fractional phases. Consequently the AFM uses the trigonometric cosine function to model the fractional part of the carrier frequency (Counselman and Gourevitch, 1981). Equation (2.41) can be reformed as:

$$\Phi_{AB}^{ij}(t) - \frac{f}{c}\rho_{AB}^{ij}(t) = N_{AB}^{ij} \tag{2.42}$$

Applying the cosine function to both sides of the previous equation after converting the cycle units to radians, the following form is obtained:

$$\cos 2\pi(\Phi_{AB}^{ij}(t) - \frac{f}{c}\rho_{AB}^{ij}(t)) = \cos 2\pi N_{AB}^{ij} \tag{2.43}$$

Because N_{AB}^{ij} is an integer number, ($\cos 2\pi N_{AB}^{ij}$) equals one. This leads to the $(\Phi_{AB}^{ij}(t) - \frac{f}{c}\rho_{AB}^{ij}(t))$ value having to be zero.

Depending on the previous illustration, the Ambiguity Function Value (AFV) at a test position (x_i, y_i, z_i) can be represented as follows:

$$AFV(x_i, y_i, z_i) = \frac{1}{ne * nr * nf * ns}\sum_{h=1}^{ne}\sum_{j=1}^{nr}\sum_{l=2}^{ns}\sum_{m=1}^{nf} \cos 2\pi(\nabla\Delta\Phi^{h,j,l,m} - \frac{f}{c}\nabla\Delta\rho^{h,j,l,m}) \tag{2.44}$$

Where ne is the number of epochs (for the single epoch procedure it equals to 1), nr is the number of the reference fixed receivers, nf is the number of observation frequencies (at this time $nf = 2$), ns is the number of observed satellites. The ionospheric effect should be eliminated before using this function as the AFV depends on both GPS frequencies, otherwise the baseline should be limited to a length in which the ionospheric errors can be removed when a differencing solution is applied. Two tests should be done in this ambiguity function method to find the best integer ambiguiy values. The first one is:

$$\cos 2\pi(\nabla\Delta\Phi^{h,j,l,m} - \frac{f}{c}\nabla\Delta\rho^{h,j,l,m}) > minimum\ threshold \tag{2.45}$$

And the second test is:

$$AFV(x_i, y_i, z_i) > minimum\ threshold \tag{2.46}$$

The trial positions are found by adding increments on the receiver initial position. The AFV has been used in this research software, GPS Ambiguity Search Program (GASP), and the implementation of it will be explained in detail later in this chapter.

2.7.2 Least Square Ambiguity Search Technique (LSAST)

This technique is based on the use of observation least squares residuals to measure the disagreement between the phase measurements corresponding to different ambiguity sets being tested. It uses four primary satellites to test the observation residuals and generate potential (trial) positions. Then the remaining satellite's observations residuals are used to determine the correct trial positions and ambiguities. The LSAST formulation is (Hatch, 1990):

$$\sigma_0^2 = \frac{\upsilon^T C_{obs}^{-1} \upsilon}{ns - 4} \tag{2.47}$$

Where σ_0^2 is the estimated variance factor, υ is the residual vector of the phase observations, ns is the number of satellites, and C_{obs}^{-1} is the covariance matrix of the phase observations. To find the correct position/ambiguity set, the χ^2 statistical test (Vanicek and Krakiwsky, 1986) is applied on the ambiguity sets estimated variance factors. The processing time depends on the number of available satellites (Hatch, 1990); the larger their number the less time needed to find the correct position. Also the ionospheric effect should be treated before using the observations in the function.

2.7.3 Least-squares Ambiguity Decorrelation Adjustment (LAMBDA)

The LAMBDA technique provides an integer least squares estimation for the GPS phase observation ambiguity (Teunissen, 1995). Equation (2.41) can be reformulated as follows:

$$y = Aa + Bb \tag{2.48}$$

Where y is the vector of Double Difference (DD) carrier phase residuals, vector a contains the integer vector of DD ambiguities, b is the unknown vector containing the

baseline positioning parameters, A and B are the corresponding design matrices. Applying the least squares method a and b vectors are:

$$\begin{bmatrix}\hat{b}\\ \hat{a}\end{bmatrix} = \begin{bmatrix}B^TB & B^TA\\ A^TB & A^TA\end{bmatrix}^{-1}\begin{bmatrix}B^T\\ A^T\end{bmatrix}y = \begin{bmatrix}Q_{\hat{b}} & Q_{\hat{b}\hat{a}}\\ Q_{\hat{b}\hat{a}} & Q_{\hat{a}}\end{bmatrix}\begin{bmatrix}B^T\\ A^T\end{bmatrix}y \tag{2.49}$$

The solution for this problem will be divided into two steps; the first one is to find the vector $\check{a}$ values taking advantage of the fact that the results should be integers. $\check{a}$ can be found using the formulation:

$$(\hat{a}-a)^T Q_{\hat{a}}^{-1}(\hat{a}-a) = \text{minimum, over integer vectors a.} \tag{2.50}$$

Once $\check{a}$ has been obtained, the positioning parameters, $\check{b}$, can be calculated using the following formulation:

$$\check{b} = \hat{b} - Q_{\hat{b}\hat{a}}Q_{\hat{a}}^{-1}(\hat{a}-\check{a}) \tag{2.51}$$

The LAMBDA function can be applied in the static, kinematic and epoch by epoch GPS double differencing problems.

2.7.4 Fast Ambiguity Resolution Approach (FARA)

This function is built on gathering GPS phase observation data over time and then solving their equations to create ambiguities corresponding to confidence regions of their real estimations (Frei and Beutler, 1990). At the j^{th} epoch the least squares solution will be as follows:

$$\widehat{X_J} = \left[\sum_{k=1}^{j}(A_k^TW_kA_k)\right]^{-1}\sum_{k=1}^{j}(A_k^TW_kb) \tag{2.52}$$

Where $\widehat{X_J}$ is the estimation vector of the unknown double differenced phase measurements (station coordinates and ambiguities), A is the phase observation

equation design matrix, W is the weight matrix, and b is the residual vector (observed minus computed).

The posteriori unit variance $\hat{\sigma}_0^2$ can be computed by using the following formulation:

$$\hat{\sigma}_0^2 = \frac{\hat{V}^T W \hat{V}}{n - m} \tag{2.53}$$

Where $\hat{V}$ is the residuals vector of the phase observations, n is the number of phase observations, and m is the number of unknown parameters.

The confidence region for each ambiguity can be defined by the Student t distribution as:

$$P_i\left\{N_i - t_{\nu,1-\frac{\alpha}{2}}.\sigma_{N_i} < N_i^A < N_i + t_{\nu,1-\frac{\alpha}{2}}.\sigma_{N_i}\right\} = 1 - \alpha \tag{2.54}$$

Where

i denotes the i^{th} ambiguity term

σ_N is the square root of the appropriate element from the adjusted covariance matrix

$t_{\nu,1-\frac{\alpha}{2}}$ is the two tailed Student t distribution with ν degrees of freedom and confidence level $1 - \frac{\alpha}{2}$

All ambiguity sets that pass this probability test will have to pass another test to be acceptable values. The new test is done on the difference of ambiguities as follows:

$$P_i\left\{N_\Delta - t_{\nu,1-\frac{\alpha}{2}}.\sigma_{N_\Delta} < N_\Delta^A < N_\Delta + t_{\nu,1-\frac{\alpha}{2}}.\sigma_{N_\Delta}\right\} = 1 - \alpha \tag{2.55}$$

Where Δ denotes the difference between two ambiguity terms. σ_{N_Δ} for two ambiguity terms N_1 and N_2 is:

$$\sigma_{N_\Delta} = \left\{\sigma_{N_1}^2 - 2\sigma_{N_1}\sigma_{N_2} + \sigma_{N_2}^2\right\}^{1/2} \tag{2.56}$$

All the ambiguities values that pass this test will be used in the least squares solution as known values. This function requires collecting data over various epochs; therefore it is affected by cycle slips.

2.7.5 The Fast Ambiguity Search Filter (FASF)

This filter is based on fixing the ambiguities over time and then using them as known parameters in the GPS phase measurement equations. It uses a Kalman filter, ambiguity search procedure, and an index to check the ambiguity values. In this filter, the ambiguities are searched at every epoch, starting from the first, until they are estimated with a sufficiently high level of confidence. Once the ambiguities are fixed, they will be used as known values in the GPS phase observation equations (Chen, 1993). The following example shows how this filter works:

If there are n ambiguities, they could be arranged in a series as follows $N_1,\ N_2,\ N_3,$ …. $N_{i-2}, N_{i-1}, N_i, N_{i+1}, N_{i+2},$…… N_n. In the search for the N_i integer ambiguity set, $N_1, N_2, N_3,$…. N_{i-2}, N_{i-1} are treated as correct parameters in the adjustment, while $N_{i+1}, N_{i+2},$…… N_n are considered as estimated parameters. The search range for N_i can be expressed:

$$P\left\{\widehat{N}_i\left(\breve{N}_1, \breve{N}_2, \ldots \breve{N}_{i-1}\right) - t_{\nu,1-\frac{\alpha}{2}}.\hat{\sigma}_0.\sqrt{q_{\widehat{N}_i}} < N_i < \widehat{N}_i\left(\breve{N}_1, \breve{N}_2, \ldots \breve{N}_{i-1}\right) + t_{\nu,1-\frac{\alpha}{2}}.\hat{\sigma}_0.\sqrt{q_{\widehat{N}_i}}\right\} = 1-\alpha \tag{2.57}$$

Where:

$\widehat{\mathrm{N}}_{\mathrm{i}}\left(\breve{\mathrm{N}}_1, \breve{\mathrm{N}}_2, \ldots \breve{\mathrm{N}}_{\mathrm{i}-1}\right)$ is the float estimate of $\mathrm{N_i}$, with $\breve{\mathrm{N}}_1, \breve{\mathrm{N}}_2, \ldots \breve{\mathrm{N}}_{\mathrm{i}-1}$ considered as known values, $\mathrm{t}_{\nu,1-\frac{\alpha}{2}}$ is the two tailed Student t distribution with ν degrees of freedom and confidence level $1-\frac{\alpha}{2}$, and $\hat{\sigma}_0.\sqrt{\mathrm{q}_{\widehat{\mathrm{N}}_{\mathrm{i}}}}$ is the standard deviation of $\widehat{\mathrm{N}}_{\mathrm{i}}\left(\breve{\mathrm{N}}_1, \breve{\mathrm{N}}_2, \ldots \breve{\mathrm{N}}_{\mathrm{i}-1}\right)$.

In the case of fixing N_1, the search range is computed without constraining any ambiguities to integers. One of the integers in the search range will be set as the N_1 value if the search range is computed properly, and this value will be used in

searching for N_2.This filter cannot be used for the single epoch GPS problems, as it requires gathering data over the time.

2.8 GPS AMBIGUITY SEARCH PROGRAM (GASP)

A GPS receiver's data is affected by the surrounding environment, therefore obtaining bad data or even losing the data at some epochs is possible. This affects the ambiguity resolution which needs to be solved over a period of time (static and kinematic cases). Solving the large number of equations requires very sophisticated algorithms, which means the solution procedure will run slowly which increases the solution timing. Moreover the ability to resolve integer-cycle phase ambiguities with only a single epoch allows GPS to provide an independent position at each observation epoch. The use of single epoch GPS methodology provides continuous monitoring measurements, which can be used to generate three-dimensional surface profiles. Comparing sequential profiles over time shows the range and geometry of the structural vibrations. This provides a great opportunity to study the responses of the structures towards different kinds of loads (Cheng *et al.,* 2002). However, the success of the technique relies on the consistent and accurate processing of every epoch. For this reason researchers have intended to solve the GPS data epoch by epoch. This research is trying to increase the positioning accuracy of one of the GPS single epoch software, GPS Ambiguity Search Program (GASP).

GASP was introduced by the University of Newcastle in 1991 to deal with the epoch by epoch case using the relative GPS strategy together with dual-frequency receiver data. This software is written in the C programming language. The first person to contribute to this work was S.J. Corbett. (1994). This software has been further developed by Al-Haifi (1996), Gunasingam (2003) and Ragheb (2007). It provides fast data processing which is very useful in real or near real time applications. As GASP is a single epoch software, it eliminates the effect of cycle slips. In addition to the moving station data, at least one fixed station data is required to complete the data running operation in GASP. The fixed station can be a stationary station with a known location or a moving station in which its location is computed by using a code pseudorange solution at each epoch. GASP uses RINEX format receiver data. The required information for running the software (e.g. the names and locations of the

RINEX and SP3 files) is provided in the GASP initial file. However, this information can be supplied by using the keyboard. This software applies a filter to remove bad satellite data and the satellites that are chosen not to be used in the processing in the GASP initial file. If the number of shared satellites between processed stations is not sufficient to process the epoch data (less than four), GASP increases the GPS time by one interval and proceeds to the next epoch. The initial location of the moving receiver (the unknown) is obtained from either the RINEX file header, GASP initial file, or from the previous epoch. The coordinates of satellites are obtained either from broadcast orbits or from a precise orbit file with the application of necessary interpolations. GASP employs the Saastamoinen model with Niell mapping function to remove the tropospheric effects (see section 2.2.2.2 for more details about applying the tropospheric model and the mapping function).

The antenna offset and GPS data are corrected in GASP by applying the receiver antenna phase centre corrections if available. The receiver antenna phase centre variation (PCV) correction values are obtained from the antenna calibration files which are provided by the US National Geodetic Survey (NGS). These values are given in north, east and up format and for both GPS satellite frequencies (L1 and L2) as shown in Table 2-6. The fixed NGS PCV correction values are transferred into their Cartesian coordinates (ΔX, ΔY and ΔZ) by using the following expressions (Hofmann-Wellenhof *et al.*, 2001):

$$\Delta Z = \Delta N \times cos\emptyset + \Delta U \times sin\emptyset \tag{2.58}$$

$$\Delta XY = \Delta U \times cos\emptyset - \Delta N \times sin\emptyset \tag{2.59}$$

$$\Delta Y = \Delta E \times cos\lambda + \Delta XY \times sin\lambda \tag{2.60}$$

$$\Delta X = \Delta XY \times cos\lambda - \Delta E \times sin\lambda \tag{2.61}$$

Where, ΔE, ΔN and ΔU are the phase centre variation Easting, Northing and Up corrections, respectively. $\emptyset$ and λ are the station latitude and longitude, respectively. The ΔX, ΔY and ΔZ are added to the antenna offset directly. The carrier phase

observables are corrected by subtracting the elevation- and azimuth-dependent PCV corrections in the NGS PCV antenna calibration file according to the receiver-satellite line elevation- and azimuth angles.

GASP uses the Ambiguity Function Method (AFM) for resolving the double differenced phase integer ambiguities (see section 2.7.1 for more details about the AFM). The AFM search volume is formed around the receiver initial position. The search size in cycles, β, is provided in the initial file in case the receiver position will be used as it is set in the GASP initial file, but in the case of the computed initial position the search will be calculated using the formal errors of the initial position coordinates as follows (Gunasingam, 2003):

$$\beta = ceil\left(S \times \sqrt{\frac{\sigma_0^2 \times \left(\sigma_x^2 + \sigma_y^2 + \sigma_z^2\right)}{3}} \times \frac{f_1}{c}\right) \tag{2.62}$$

Where, ceil is the function required to round the resultant real number to the nearest higher integer, S is a scale factor (normally S ≈ 1), σ_0 is the unit variance, σ_x, σ_y and σ_z are the a posteriori variances of the initial coordinates; f_1 is the GPS L1 frequency and c is the speed of light. If β exceeds the maximum search size which is provided in the initial file, the maximum search size will be used as the search size. There is also a possibility to get the initial receiver position from the previous epoch results in case of a static receiver and in this case the search size is the computed β. The creation of the search volume in GASP uses four chosen satellites as shown in Figure 2-8, the highest satellite as a reference and the other three satellites which form with the reference satellite the best Positional Dilution of Precision (PDOP) geometry. The volume includes all the possible position choices around the initial position. For each point inside the volume, one L1 cycle is added/ subtracted to one of the three satellites. The point position is then estimated by solving the L1 double differenced phase observation equations. The search volume should be within ± 1.2 m of the correct final position (Corbett, 1994).

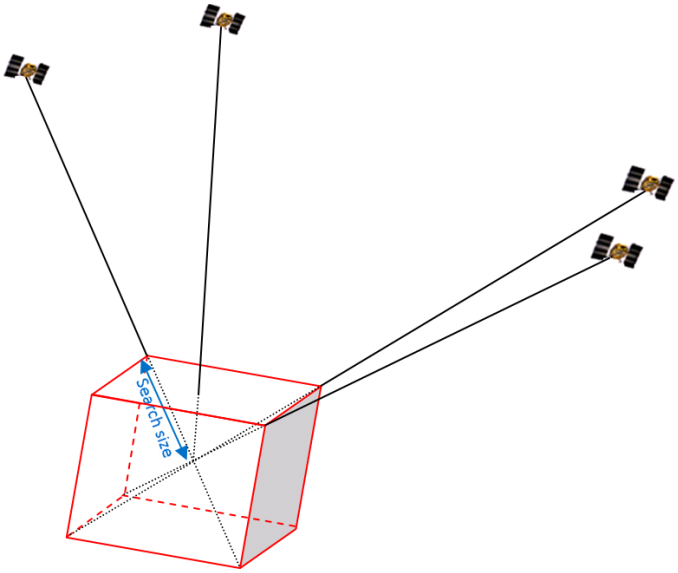

Figure 2-8 GASP search volume

The results of the previous least squares method are used in the AFM. The search for the best receiver location involves L1 and L2 observations of all of the possible double differenced observations for the satellites above the minimum allowed elevation angle. A statistical F-test is performed on all of the successful candidate positions (which have an AFV greater than the ambiguity threshold) to determine the final correct position for each epoch. The tested null hypothesis in this test is:

$$H_0: \hat{\sigma}^2_{0(min)} = \hat{\sigma}^2_{0(i)} \tag{2.63}$$

With the alternative hypothesis:

$$H_A: \hat{\sigma}^2_{0(min)} < \hat{\sigma}^2_{0(i)} \tag{2.64}$$

The double difference carrier phase observations, the satellite coordinates, the fixed receiver coordinates and the successful candidate position are used in the least squares adjustment procedure to calculate the corrections to the candidate position. In this procedure, the L1 and L2 frequencies are used independently. The a posteriori variance factor of each candidate position $\hat{\sigma}^2_0$ can be calculated as follows (Cross, 1994):

$$\hat{\sigma}_0^2 = \frac{V^T W V}{n - m} \tag{2.65}$$

Where,

V is the vector of the residuals on the GPS phase observations.

W is the weight matrix.

n is the number of double difference observation equations in each epoch for L1 and L2 data.

m is the number of unknown parameters. m = 3

In order to test the solution with minimum residuals against other candidate positions, the F test is done as follows (Cross, 1994):

$$F_{\upsilon,\upsilon,1-\alpha} > \frac{\hat{\sigma}_{0(i)}^2}{\hat{\sigma}_{0(min)}^2} \tag{2.66}$$

Where:

$F_{\upsilon,\upsilon,1-\alpha}$ is the critical value from the F probability distribution.

υ is the degree of freedom (υ = n − 3).

α is the level of significance (5% in this case).

In Equation 2.66, if the null hypothesis is rejected, then the candidate position with minimum residuals is the final position (Al-Haifi, 1996). If more than one position passes the F-test, then the position with the smallest $V^T W V$ is set to be the final position.

If all the trial positions fail to pass the AFM test the search size is increased by 1. Adding 1 will continue until one of the trial positions passes the AFM test or the search size reaches the maximum value as set in the GASP initial file. If all of the positions inside the allowable maximum search volume fail in passing the AFM test, the epoch positioning results are considered unreliable.

The unknown receiver coordinates along with their formal errors are written to the output file in different formats (Cartesian, ellipsoidal and topocentric). In addition to

that, the processing information of each epoch data (e.g. the number of common satellites, PDOP value, the number of the successful candidate positions and the processing time) is written to the output file. Figure 2-9 shows a flowchart of GASP software steps and adopted methodology.

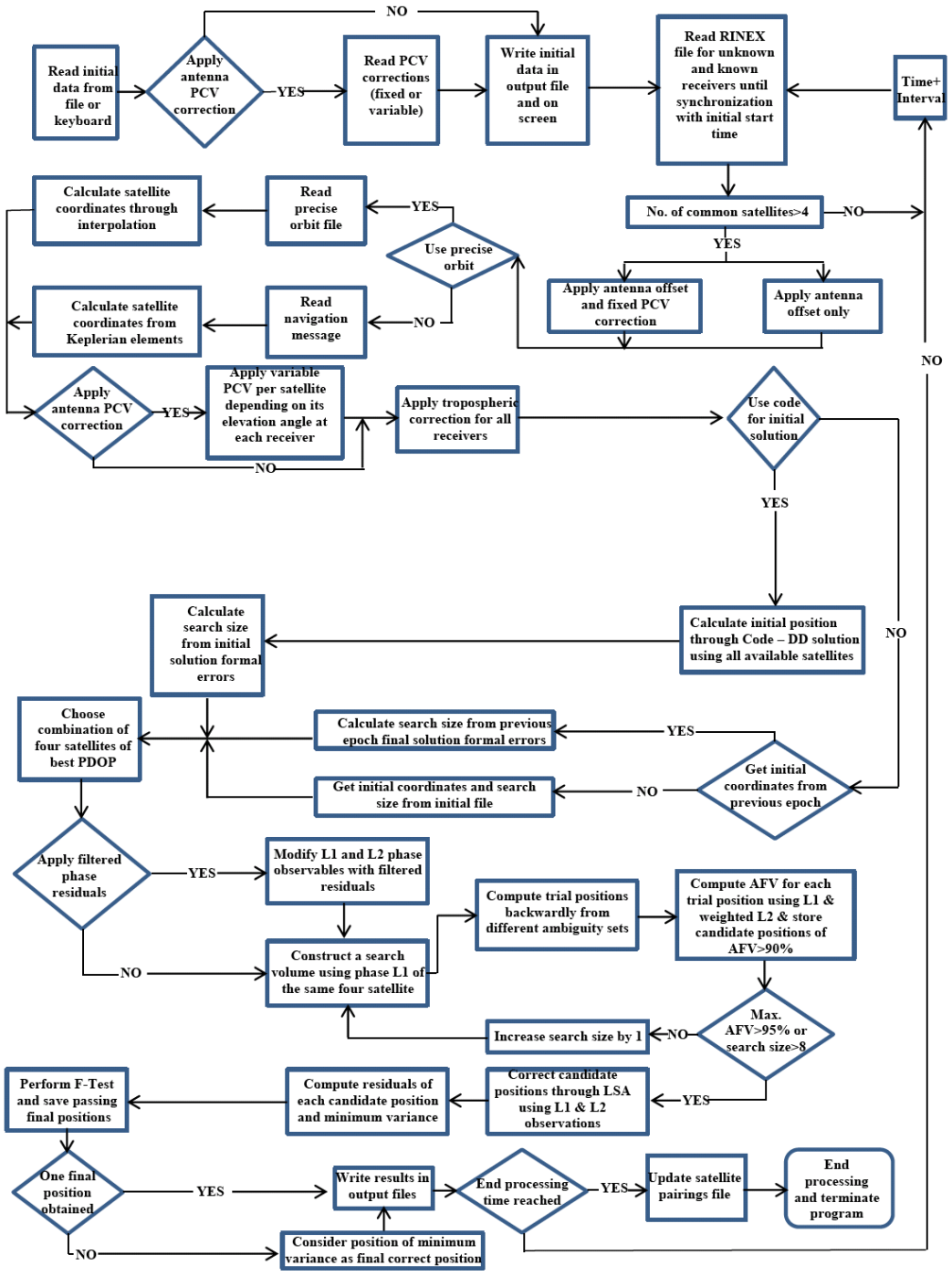

Figure 2-9 GASP software flowchart (Ragheb, 2007)

2.9 SUMMARY

Employing the ambiguity resolution function into single epoch software needs a great deal of care, due to the limitation of the number of observed satellites at each epoch. This means there may not be any redundancy in the number of equations in the data processing, and thus the ambiguity resolution will not be precisely estimated. As a result, more attention should be paid to the other positioning errors such as receiver dependent biases, satellite dependent biases and signal propagation biases (ionosphere delay, troposphere delay) which must be solved precisely to obtain the highest possible accuracy. GASP uses a variety of techniques to remove errors from the measurements. For example, it applies antenna phase centre corrections depending on the antenna model and the elevation angle of the satellites. The tropospheric effect has been treated in GASP by employing the Saastamoinen tropospheric model. Depending on previous studies, GASP shows very high capacities toward solving very short baseline (< 1 km) GPS problems (Al-Haifi, 1996). To increase GASP's ability to get an accurate positioning over longer baselines, the ionospheric effect should be removed. Chapter 3 shows the effect of the ionosphere on the GPS positioning and a review about some of its mitigation solutions.

IONOSPHERIC EFFECTS ON GPS SIGNALS AND MITIGATION METHODOLOGIES

3.1 INTRODUCTION

The transmission of the GPS signal through the ionosphere changes the speed of its propagation, and this causes an error in the measured distance between the receiver and the satellite, which will affect the accuracy of GPS positioning. Some methods have been introduced to reduce the ionospheric effect, e.g. using the relative GPS technique and assuming that the impact of the ionosphere delay can be largely reduced by forming a difference between the measurements made by two receivers. However, this approach is only acceptable for the case of short baselines (less than 10 km to obtain good accuracy (Counselman and Gourevitch, 1981)).

3.2 EFFECT OF THE IONOSPHERE ON THE GPS SIGNALS

A relationship has been observed between the effect of the ionosphere on the propagation of radio waves and the total electron content along the radio wave path (Klobuchar, 1996). The effect of the ionosphere is related to the total amount of electrons along the satellite-receiver line of sight. This amount is called the Total Electron Content (TEC). The unit of TEC is a TECU (TECU = 10^{16} electrons per

square metre). The local electron density is a function of many interrelated variables, including the solar cycle, geomagnetic activity, time of year, time of day, user location and viewing direction (Klobuchar, 1987). Consequently, understanding the variability of TEC is considered a crucial matter to the Global Positioning System (GPS) science. TEC can be computed by integrating the electron density along the signal ray path through the ionosphere as (Hofmann-Wellenhof *et al.*, 2001).

$$\mathrm{TEC} = \int_{s} \mathrm{N}\,\mathrm{dl} \tag{3.1}$$

Where N is the local electron density and the integration is along the signal path s.

When an electromagnetic wave propagates in a free space, its speed is known to be equal to the velocity of light in a vacuum, but when it propagates in the atmosphere, its speed changes due to interaction with particles present in that medium. The amount of refraction is described by a medium specific refractive index. The first-order term of phase refractive index, n_p, and the superimposed code signal group delay refractive index, n_g,were expressed by Hofmann-Wellenhof et al (2001) as:

$$n_p = 1 - \frac{40.28N}{f^2} \tag{3.2}$$

$$n_g = n_p + f\frac{dn_p}{df} = 1 + \frac{40.28N}{f^2} \tag{3.3}$$

Where, N is the electron density, and f is the wave frequency. The signal travel time through the ionospheric medium to a receiver is:

$$dt = \int_{S} \frac{n_{p,g}}{c}\, dS \tag{3.4}$$

Inserting equations 3.2 and 3.3 into equation 3.4 and multiplying by the speed of light, c, yields the following relationships for advanced carrier phase and delayed code measurements:

$$\rho_{phase} = \int_S (1 - \frac{40.28N}{f^2})dS + \delta\rho_{geom} = \rho - \frac{40.28}{f^2}TEC + \delta\rho_{geom} \quad (3.5)$$

Similarly for the code,

$$\rho_{code} = \rho + \frac{40.28}{f^2}\int_S N\,dS + \delta\rho_{geom} = \rho + \frac{40.28}{f^2}TEC + \delta\rho_{geom} \quad (3.6)$$

Where, ρ is the true geometrical distance and $\delta\rho_{geom}$ represents the geometrical errors including the tropospheric, orbital, clock, and multipath effects.

The higher order, second and third, ionospheric effects are small and they are needed only when a millimetre level accuracy is required over long baselines (Petrie et al., 2010; Hoque and Jakowski, 2007). Therefore their effect will be ignored in this research as a few centimetres accuracy level is targeted.

The ionospheric effect is frequency, time and location dependent. Therefore it can be estimated by using the GPS frequency signals. Also, interpolation of the ionospheric values obtained from a regional GPS receiver network can be used to create an ionospheric correction model.

3.3 IONOSPHERIC EFFECT MITIGATION METHODOLOGIES

For a fast relative GPS positioning, resolution of the carrier phase ambiguities to their integer values has been considered the key to achieving the highest precision (mm-cm) positioning. Successful resolution of (double-difference) ambiguities for long baselines is mainly limited by errors due to the ionospheric delay in the GPS-data. Several methods have been introduced to reduce the effect of the ionosphere, and some of these methods use differential GPS observations, the ionosphere free combination, and global and regional ionospheric models.

3.3.1 Using Differential Methods and Linear Combination

The ionospheric delays are correlated in the same region, therefore, applying the double differencing GPS technique minimises the ionospheric effect on GPS positioning. The ionospheric elimination success depends on the baseline length (e.g. the GPS positioning accuracy will be affected by the ionosphere by up to 20 cm for a 25 km baseline, and up to a metre for a 100 km baseline (Grewal *et al.*, 2001)).

Taking advantage of the dispersive property of the ionosphere, the GPS signals operating at two different frequencies can be used to mitigate the effect of the ionosphere on the results by forming an ionosphere free combination. Applying this combination mitigates the ionospheric first order effect, but on the other hand it increases the noise level and removes the integer nature of the phase ambiguity (Xu, 2007).

3.3.2 Using the Klobuchar Model

In this method the ionospheric parameters are broadcast to the GPS users within the navigation message. This requires knowledge of the user's approximate geodetic latitude, longitude, elevation angle and azimuth to each GPS satellite. This model can only correct about 50% of the total ionospheric effects (Klobuchar, 1987), and is only recommended when other models are not available (e.g. using single frequency receiver). This model is not suitable for our study case, so it will not be applied.

3.3.3 Employing an Ionospheric Model (IGS Model)

These models are based on GPS delays measured at ionospheric pierce points as observed from dual-frequency GPS IGS stations. The basic idea of this method is based on the assumption that all electrons in the ionosphere are concentrated in a thin shell about 350km in altitude above the earth's surface (Figure 3-1). Employing an ionospheric model requires knowledge of the user's approximate geodetic latitude, longitude, elevation angle and azimuth to each GPS satellite. Furthermore interpolation is required to find the best value of the ionospheric correction as the ionospheric models provide the correction every two hours.

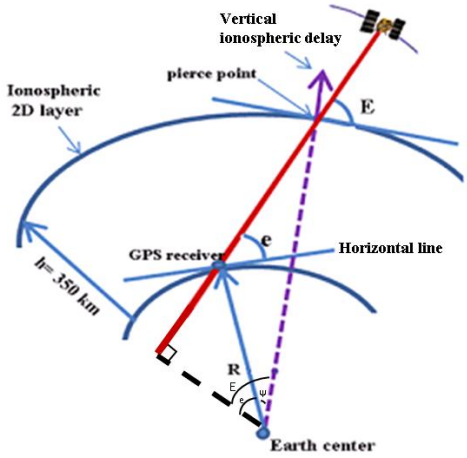

Figure 3-1 Single-layer ionospheric model

The implementation of the single-layer grid model requires computation of the intersection of the line-of-sight between the GPS receiver and the observed satellite on the ionospheric shell as illustrated in Figure 3-1. If the receiver's coordinates (ϕ_r, λ_r) are provided, then the coordinates of the pierce point IPP $(\phi_{IPP}, \lambda_{IPP})$ are derived as follows (Gao *et al.*, 1994):

$$\phi_{IPP} = \phi_r + \Psi \cos A$$
$$\lambda_{IPP} = \lambda_r + \frac{\Psi \sin A}{\cos \phi_{IPP}} \tag{3.7}$$

Where,

A is the azimuth angle of the direction station–satellite:

$$A = \sin^{-1}(\sin(90 - \phi_s) * \sin(\lambda_s - \lambda_r) / \sin(b)) \tag{3.8}$$

Ψ is the offset angle between the IPP and receiver, and it can be calculated as the following:

$$\Psi = E - e \tag{3.9}$$

In which e is the elevation angle at the user receiver:

$$e = \cos^{-1}\left((R_E + H) * \sin(b) / d\right) \tag{3.10}$$

And in which:

E is the elevation angle at IPP:

$$E = \cos^{-1}\left(\left(\frac{R_E}{R_E + H}\right)\cos e\right) \tag{3.11}$$

Where:

H is the altitude of the ionospheric layer (350 km).

R_E is the earth's radius.

d is the distance from the receiver to the satellite:

$$d = \mathrm{sqrt}(R_E * R_E + (R_E + H) * (R_E + H) - 2 * R_E * (R_E + H) * \cos(b)) \tag{3.12}$$

b is the angular distance between the receiver and the satellite:

$$b = \cos^{-1}(\cos(90 - \phi_s) * \cos(90 - \phi_r) + \sin(90 - \phi_s) * \sin(90 - \phi_r) * \cos(\lambda_s - \lambda_r)) \tag{3.13}$$

ϕ_s, λ_s are the satellite's coordinates.

Finally, for an epoch t, two kinds of interpolations can be used to increase the ionospheric estimation accuracy:

I- Temporal interpolation:

The IGS ionospheric model provides a TEC-map for every two hours T_i. Therefore different functions have been used to interpolate the TEC values over time such as (Schaer, 1999):

$$TEC(\phi_{IPP}, \lambda_{IPP}, t) = \frac{T_{i+1} - t}{T_{i+1} - T_i} TEC_i(\phi_{IPP}, \lambda_{IPP}) + \frac{t - T_i}{T_{i+1} - T_i} TEC_{i+1}(\phi_{IPP}, \lambda_{IPP}) \tag{3.14}$$

Where $T_i \leq t \leq T_{i+1}$.

II- Spatial interpolation:

As the IGS ionospheric model is a grid based model, with the dimensions of each grid are $\delta_{lat} = 2.5^{o}, \delta_{lon} = 5^{0}$, an interpolation between the four surrounding vertices of the ionospheric TEC map is needed to be applied. The mathematical formulation for the spatial interpolation of the vertical TEC values looks like:

$$TEC(\phi_{IPP}, \lambda_{IPP}, t) = \sum_{i=1}^{4} W_i(x_{pp}, y_{pp}) TEC(\emptyset_i, \lambda_i, t) \tag{3.15}$$

Where,

$TEC(\phi_{IPP}, \lambda_{IPP}, t)$	is the TEC value for the pierce point to be evaluated.
$W_i(x_{pp}, y_{pp})$	is the inverse distance weighting function.
$TEC(\emptyset_i, \lambda_i, t)$	is the TEC value at the corresponding grid node.
$\emptyset_i, \lambda_i, t$	are the geographic longitude, latitude and the time of the corresponding vertex in the TEC map.

Finally, the IGS ionospheric model provides a vertical ionospheric delay at the pierce point. This value must be multiplied with an ionospheric mapping function $M(e)$ to arrive at the ionospheric correction in the slant direction to the satellite as follows:

$$M(e) = \left\{ 1 - \left[\frac{\cos(e)}{1 + \frac{h}{R_E}} \right]^2 \right\}^{-1/2} \tag{3.16}$$

Where,

e	is the elevation angle at the user receiver.
h	is the altitude of the ionospheric layer (350 km).
R_E	is the Earth's mean radius (6371 km).

The residuals of applying a 2D global ionospheric model are a few TECU at mid latitudes and up to 10 TECU in the equatorial regions (Gao and Liu, 2002). The IGS 2D ionospheric model has been applied and used in Chapter 4.

3.3.4 Modelling Over a Regional Area Differential GPS (RADGPS) Network:

This methodology was developed by the University of Calgary. The main idea is to encapsulate all of the error information from the entire reference receiver network into the measurements of a single reference receiver (Raquet, 1998). This has a great benefit because it makes multi-reference stations available to be used by single reference differential processing techniques. The final equations used to compute the corrections to the carrier-phase observables are as follows (Raquet, 1998):

3.3.4.1 The NetAdjust Method

This methodology was developed by the University of Calgary. The main idea is to encapsulate all of the error information from the entire reference receiver network into the measurements of a single reference receiver (Raquet, 1998). This has a great benefit because it makes using multi-reference station available to be used by single reference differential processing techniques. The final equations used to compute the corrections to the carrier-phase observables are as follows (Raquet, 1998):

$$\widehat{\delta l_r} = C_{\delta l_r,\delta l} B^T (B C_{\delta l} B^T)^{-1} \left(B\overline{\emptyset} - \lambda \Delta \nabla N\right)$$
$$\hat{\delta l} = C_{\delta l} B^T (B C_{\delta l} B^T)^{-1} \left(B\overline{\emptyset} - \lambda \Delta \nabla N\right) \quad (3.17)$$

Where,

δl_r are the corrections to carrier-phase observables collected at the rover receiver, in metres,

δl are the corrections to carrier-phase observables collected at the reference stations, in metres,

$\overline{\emptyset}$ are the measurement-minus-range carrier-phase observables($\overline{\emptyset} = \emptyset - \rho$), in metres assuming that the reference station coordinates are known in order to compute the geometric range ρ,

$\Delta\nabla N$ are the double difference integer ambiguities between the reference stations (assumed to be known),

λ is the carrier-phase wavelength, in metres,

B is the double difference matrix($B = \partial\Delta\nabla\bar{\emptyset}/\partial\bar{\emptyset}$) (made up of the values +1, -1 and 0),

$C_{\delta l}$ is the covariance matrix of the carrier-phase observables collected at the reference stations, and

$C_{\delta l_r,\delta l}$ is the cross-covariance matrix between the carrier-phase observables collected at the rover receiver and at the reference stations.

Using NetAdjust methodology reduces the Root Mean Square (RMS) of the L1 and Widelane (WL) double difference carrier phase residuals by up to 61% (Fortes *et al.*, 2000). More details have been discussed by Raquet (1998).

3.3.4.2 The Ionosphere-Fixed Model

In this method the data from a network of reference stations is used to estimate vertical ionospheric delays. As the coordinates of all network stations are known, the correct integer ambiguities can be estimated easily so that the only parameters that remain unknown are the Double Difference (DD) ionospheric delays. The DD functional model for phase and code observation equations for a single baseline and for a single observation epoch i is (Odijk, 2000):

$$\begin{aligned} \emptyset_1(i) &= A(i)b - \mu_1 I_1(i) + \lambda_1 a_1 \\ \emptyset_2(i) &= A(i)b - \mu_2 I_1(i) + \lambda_2 a_2 \\ p_1(i) &= A(i)b + \mu_1 I_1(i) \\ p_2(i) &= A(i)b + \mu_2 I_1(i) \end{aligned} \tag{3.18}$$

Where:

$\emptyset_1(i)$ and $\emptyset_2(i)$ are the DD phase observables (in units of metres) on L1 and L2,

$p_1(i)$ and $p_2(i)$ are the DD code observables on L1 and L2,

b represents the increments of the components of the baseline vector,

A(i) is the receiver-satellite geometry matrix,

a_1 and a_2 are the unknown integer DD ambiguities,

λ_1 and λ_2 are the known wavelengths,

I_1 (i) is the DD form of the unknown slant ionospheric delays on the L1-frequency and,

$$\mu_j = \frac{\lambda_j^2}{\lambda_1^2} \quad , j = 1,2. \tag{3.19}$$

By rearranging to the previous equations, the DD ionospheric delays for a single epoch and a single-baseline ($\check{I}(i)$) can be formed as:

$$\check{I}(i) = -\frac{1}{\mu_1^2 + \mu_2^2}[\mu_1 \emptyset_1(i)' + \mu_2 \emptyset_2(i)'] + \frac{1}{1 + (\frac{\sigma_p^2}{\sigma_\emptyset^2})} \frac{1}{\mu_1^2 + \mu_2^2}[\mu_1 p_1(i)' + \mu_2 p_2(i)'] \tag{3.20}$$

Where:

$\emptyset_j(i)'$ is the corrected double-difference phase observable:

$$\emptyset_j(i)' = \emptyset_j(i) - \rho(i) + \lambda_j \check{a}_j \qquad with\ j = 1,2.$$

$p_j(i)'$ is the corrected double-difference code observable:

$$p_j(i)' = p_j(i) - \rho(i) \quad \text{with } j = 1,2.$$

ρ is the geometric receiver-satellite range.

$\sigma_\emptyset^2$ is the variance of the phase.

σ_p^2 is the variance of the code.

$\check{a}_j$ is the computed integer DD ambiguity.

And by considering that the precision of the code observations is much less than the phase ($\frac{\sigma_\emptyset^2}{\sigma_p^2} \approx 0$), the previous model can be written:

$$\check{I}(i) \approx -\frac{1}{\mu_1^2 + \mu_2^2}[\mu_1 \emptyset_1(i)' + \mu_2 \emptyset_2(i)'] \tag{3.21}$$

For each individual observation epoch, an interpolation to compute the slant double-difference ionospheric delay $\bar{I}_{1x}^{1s}$ will be carried out for a certain user location x with

respect to a permanent reference station "1" (subscript) and for each satellite (s) with respect to a pivot satellite "1" (superscript) as:

$$\bar{I}_{1x}^{1s} = (c_{x1}^{s}\ c_{x2}^{s} \dots c_{xn}^{s}) \begin{bmatrix} c_{11}^{s} & c_{12}^{s} & \cdots & c_{1n}^{s} \\ c_{21}^{s} & c_{22}^{s} & \cdots & c_{2n}^{s} \\ \vdots & \vdots & \ddots & \vdots \\ c_{n1}^{s} & c_{n2}^{s} & \cdots & c_{nn}^{s} \end{bmatrix}^{-1} \begin{bmatrix} \check{I}_{11}^{1s} = 0 \\ \check{I}_{12}^{1s} \\ \vdots \\ \check{I}_{1n}^{1s} \end{bmatrix} \tag{3.22}$$

Where c_{kl}^{s} is linearly dependent on the distance between the stations, or rather, their ionospheric pierce points:

$$c_{kl}^{s} = l_{max} - l_{kl}^{s} \tag{3.23}$$

In which:

l_{kl}^{s} is the linear distance between the ionospheric points of stations k and l with respect to satellite s. The ionospheric pierce point is the intersection of the receiver-satellite line of sight with a single ionospheric layer (at height about 350 km above the Earth).

l_{max} is an assumed distance which is longer than the largest distance between the ionospheric points of the stations in the network. The larger the distance between the points, the smaller the correlation.

Figure 3-2 shows the interpolation per satellite in the ionospheric layer.

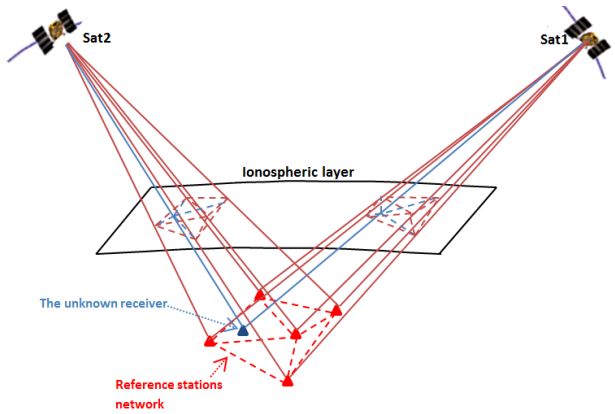

Figure 3-2 The interpolation per satellite in the ionospheric layer (Odijk, 2000)

Once the slant DD ionospheric delay $\bar{I}_{1x}^{1s}$ is known, the double difference equations can be used in an ambiguity resolution function for a long baseline. Using this technique helps to estimate the integer ambiguity value precisely, which leads to a high estimation accuracy in the rover receiver position. More details have been discussed by Odijk et al. (2000).

3.3.4.3 Tomographic Three-Dimensional (3D) Ionospheric Model

According to the electron density property, the ionosphere is spatially divided into different layers, namely, D, E, and F layers. The tomographic model is based on the division of the ionosphere into many small voxels. The electron density is considered consistently distributed in each voxel. The summation of the voxel values along the satellite-receiver ray gives the total electron content (TEC). The voxel-based tomographic model can be described as (Colombo *et al.*, 1999):

$$\lambda_1\Phi_1 - \lambda_2\Phi_2 = \alpha\sum_{i=1}^{I}\sum_{j=1}^{J}\sum_{k=1}^{k}(N_e)_{i,j,k}ds_{i,j,k} + b \tag{3.24}$$

Where:

λ_1 is L1 carrier phase wavelength (m/cycle).

Φ_1 is the carrier phase measurement on L1 frequency.

λ_2 is L2 carrier phase wavelength (m/cycle).

Φ_2 is the carrier phase measurement on L2 frequency.

α is a constant coefficient, $\alpha = 1.05 \times 10^{-17}\mathrm{m}/(\frac{\mathrm{el}}{\mathrm{m}^2})$.

i, j, k are the indices for each voxel corresponding to solar longitude, geodetic latitude and height. Their maximum values are I,J and K, respectively, which determines the number of voxels in the ionosphere.

$(N_e)_{i,j,k}$ is the free electron density for each voxel.

$ds_{i,j,k}$ is the length of the GPS signal ray path crossing each voxel.

b is the alignment term that includes L1 and L2 carrier phase integer ambiguities and inter-frequency biases, which is constant in a given satellite-receiver pair in continuous tracking.

The vertical ionospheric delay value is computed for each of the static network receivers by solving its dual-frequency observation equations. Specific mathematical methods are then applied to create a three dimensional (3D) ionospheric layer over all of the network region (Raymund *et al.*, 1990).

The ionospheric models which are based on a regional network help resolve the GPS phase measurement ambiguities (Colombo et al., 2000; Odijk, 2000; Raquet, 1998). However, this methodology restricts the moving station location to the area which is covered by the network of base stations. In this research only one receiver will be used as a base station and therefore these solutions are not applicable.

3.4 SUMMARY AND CONCLUSION

Precise a priori inputs for the GASP software ambiguity function are required especially over long baselines to obtain precise positioning outputs. Therefore, removing the effect of the ionosphere on the GPS observations is essential. Applying the ionosphere free combination makes the phase ambiguity non-integer. Therefore it cannot be applied in this research because the software ambiguity function is based on the phase ambiguity being integer. Using a regional network-based ionospheric model is not applicable in this research, as only one base station will be used. The GASP software uses the double differencing technique, which reduces the ionospheric effect on GPS positioning. However, the ionospheric mitigation success is baseline length dependent. Therefore other ionospheric mitigation methodologies should be applied with the double differencing technique to obtain precise positioning. The IGS global ionospheric model is available for use online, and applying it reduces the effect of the ionosphere. This model will be applied and investigated in chapter 4. Creating a code-based ionospheric model will also be investigated in the following chapter. Different types of pseudorange observations solutions will be studied to find the best input to the GASP ambiguity function. This solution will include undifferenced solutions in addition to double differencing. Sidereal and regional filters will also be applied to the pseudorange solution results to improve the accuracy of the ambiguity function inputs.

USING THE IGS PRODUCTS FOR A SINGLE EPOCH GPS SOFTWARE

4.1 INTRODUCTION

The GASP software has shown a good ability to give accurate positioning results over short baselines (less than 1 km) (Al-Haifi, 1996), and if the observations are created, transferred and received in uncorrupted condition, accurate positioning can be obtained for baseline lengths of up to 10 km (Corbett and Cross, 1995). GASP results were affected by the Anti-Spoofing (AS) at the time of the Corbett and Cross trial. This effect has been reduced since then by improving the GPS receiver design.. Also, Selective Availability (SA) was on in 1995, which had a bad effect on the GPS positioning accuracy. In 2000 SA was turned off and more accurate GPS observations can now be obtained.

To study GASP software positioning accuracy over medium and long baselines, a set of 10 International GNSS Service (IGS) sites' data has been processed. The baseline length has been varied between 7 - 200 km approximately. The IGS network in California, USA, has been used to create this network of baselines due to the high

density of stations there in comparison to other world regions. Also, the receiver type at all of these stations is ASHTECH, which provides the L1, L2, P1, P2 and C/A observations in the RINEX files. Having all these observations is essential to the undifferenced GPS dual-frequency pseudorange solution which is one of the main innovations in this research. However, the solution can still be done for receivers which provide C/A and P2 only but with less accurate results. Figure 4-1 shows the IGS station network in the Californian region, and the red lines represent the baselines which have had their data processed. The RINEX files are available freely on several internet websites (e.g. ftp://cddis.gsfc.nasa.gov/pub/gps/data/daily).

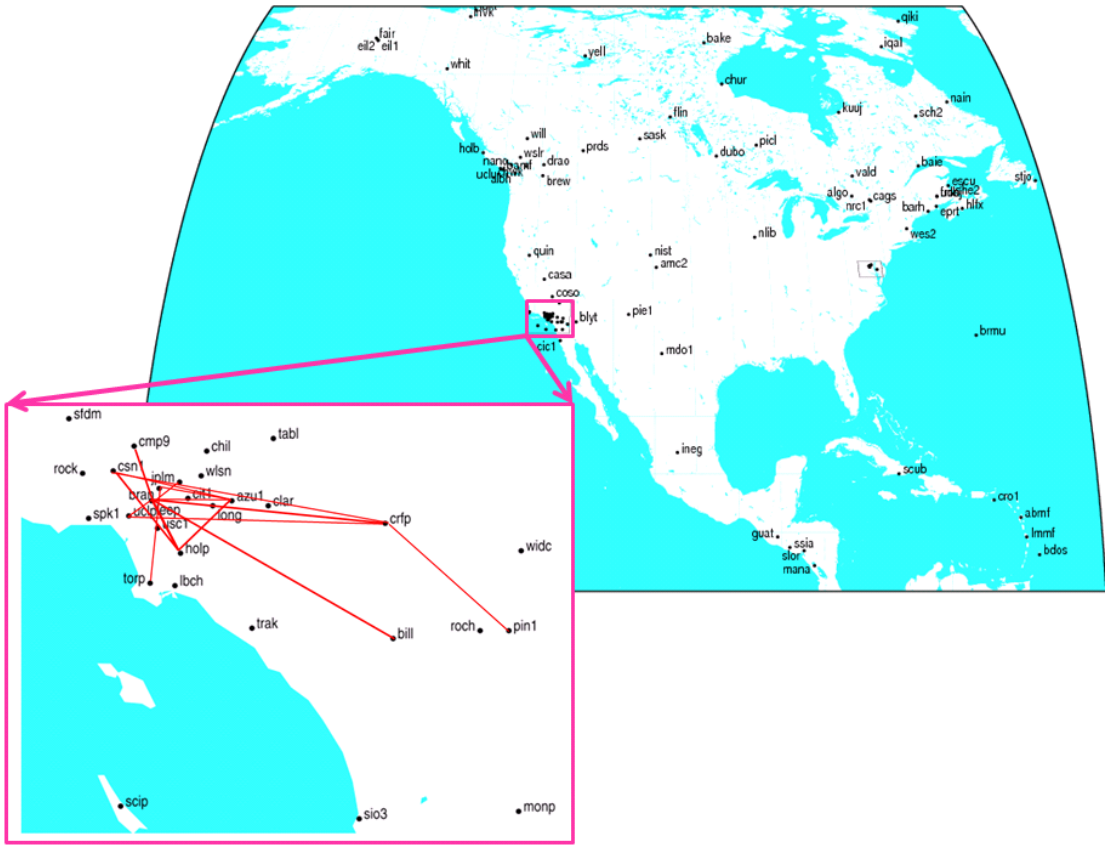

Figure 4-1 The IGS stations which have been used in this study. (http://igscb.jpl.nasa.gov/network/maps/all_socal.html). The red lines show the baselines which have had their data processed see Table 4-1

Table 4-1 shows the processed network stations. The shortest baseline available in this region is 7 km. Data has been processed for different dates and over various periods over different years. However, the results of day 66/2007 will be presented in this study as they are typically representative of the used network stations results (the

results of days 66, 190 and 320 in years 2007, 2009 and 2011 are shown in Appendix A). The downloaded RINEX files contain data for 24 hours. The GASP software interpolates the GPS satellite orbit data over seven orbital intervals (each interval equals 15 minutes), therefore the software has been run for the middle 21 hours of the tested days to avoid the effect of day boundaries. These stations provide epochs with a 30 second interval, therefore the total number of the processed epochs is 2520 epochs.

Base station	Unknown station	Approximate baseline length (km)
BRAN	LEEP	7
UCLP	LEEP	13
UCLP	BRAN	19
LEEP	CSN1	23
HOLP	LEEP	27
AZU1	BRAN	35
AZU1	LEEP	39
BRAN	TROP	44
CSN1	HOLP	50
CSN1	AZU1	60
AZU1	CRFP	75
CRFP	HOLP	99
CRFP	LEEP	113
UCLP	CRFP	123
CSN1	CRFP	133
GOLD	CRFP	155
PIN1	HOLP	160
GOLD	LEEP	198

Table 4-1 The processed baselines

Seven stations from the Figure 4-1 network have been used as moving stations as shown in Table 4-1 to test the applied solutions.

In this chapter, different single epoch pseudorange solutions will be tested to find the best inputs for the GASP ambiguity function, which are the receiver position and the GPS phase observations, equation 2.44. The GASP software ambiguity function positioning inputs have been obtained by solving double differenced or undifferenced pseudorange observation equations. The implementation of the IGS 2D ionospheric model has been investigated in this study, as well as creating an ionospheric model or a model for the residuals of the IGS 2D ionospheric model by solving the GPS pseudorange equations or using the geometry free combination at each epoch to correct the GPS phase measurements. The effect of applying Differential Code Biases (DCBs) values to the solutions has also been investigated. The application of regional and sidereal filters to the GPS pseudorange equation solutions is also tested. As a consequence, ten different combinations of different processing techniques have been used in this research (Table 4-2).

	Solution1	Solution2	Solution3	Solution4	Solution5	Solution6	Solution7	Solution8	Solution9	Solution10
Double differenced XYZ	✓	✓	✓							
Undifferenced pseudorange XYZI				✓	✓	✓	✓	✓	✓	✓
IGS ionospheric model		✓	✓		✓			✓		✓
Geometry free ionosphere			✓							
DCBs		✓	✓		✓	✓		✓		✓
Regional filter							✓	✓	✓	✓
Sidereal filter									✓	✓

Table 4-2 Various inputs and different combinations to create different possible inputs sets to the GASP ambiguity function

The following data have been used in these solutions:

-The receivers' dual frequency pseudorange observations.

-The precise (final) orbit model from the IGS.

-Satellite clock errors (from SP3 file).

-Satellite antenna phase centre offset correction.

-Receiver antenna phase centre offset and variation corrections.

Also the Saastamoinen tropospheric model has been employed to mitigate the effect of the troposphere on the results, and the data has been corrected for relativistic

effects on GPS satellite clocks using equation 2.2. A 15° cut-off angle over the horizon has been applied to minimise multipath effects. The distance between the receiver and each observed satellite has been corrected for the Earth's rotation during signal flight time.

Three main factors have been used to study the effectiveness of each of these processing strategies. The first factor is the effect of each solution on the final GASP software positioning Median Absolute Deviation (MAD). The MAD will show how the results behave around the true position. The second factor is the percentage of the "good" results over the total number of the epochs. A "good" result is defined to be an epoch that gives a 3-D positioning accuracy better than 10 cm. The third factor is the GASP software ambiguity resolution success. A percentage of the epochs which give larger than a threshold Ambiguity Function Value (AFV) will be plotted. Following the studies of Al-Haifi (1996) and Corbett (1994), the threshold value is set to be 0.9. For the position comparison, the true station position coordinates have been used as published on the Scripps Orbit and Permanent Array Center (SOPAC) website. The solutions in Table 4-2 have been tested to decide which of them will give the best positions and corrected phase for the GASP software ambiguity function. However, as there are too many choice and results some of the tested choices results have not been plotted in this chapter (Appendix A contains all ten solution results over the tested days).

4.2 DOUBLE DIFFERENCED SOLUTION

The GASP software has been set to use the Double Differencing Code observations (Code-DD) solution since its design in 1991. The double difference of the moving and fixed receivers' pseudorange observation equations has been solved to find out the moving receiver position for the ambiguity function. This solution involves all the satellites which are observed from the fixed and moved receiver together. The least squares method is used to solve the equations.

The GPS baseline data in Table 4-1 have been processed. Figure 4-2 shows the final GASP software position MAD over different baselines lengths when the Code-DD solution results only are used as the initial inputs into the ambiguity function.

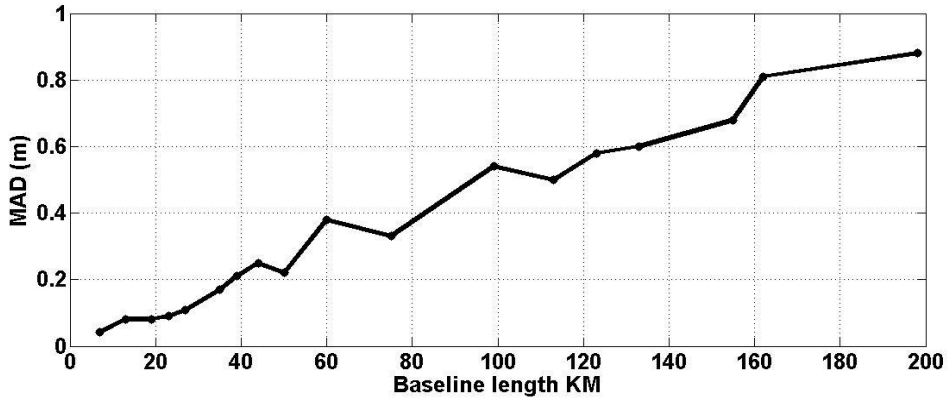

Figure 4-2 Code-DD solution (solution 1), GASP software positioning MAD

Figure 4-3 shows the probability of getting positions within 10 cm around the true position, and Figure 4-4 shows the percentage of epochs which give an Ambiguity Function Value (AFV) larger than 0.9 over different baseline lengths when the Code-DD solution results only are used as the initial inputs into the ambiguity function.

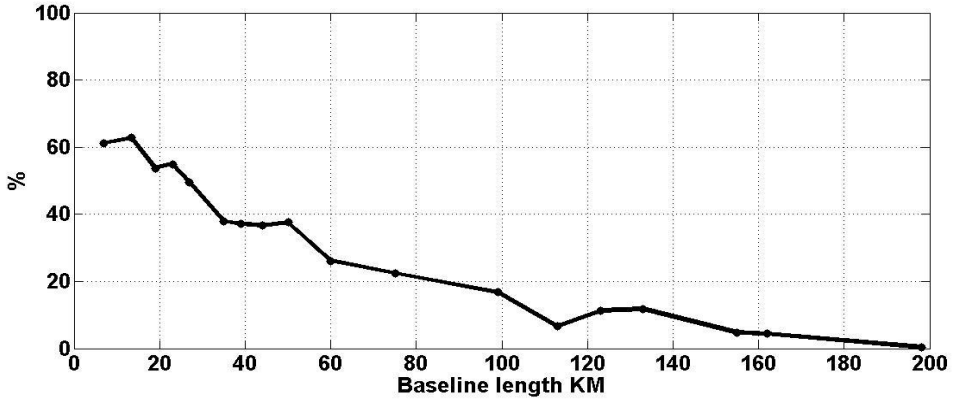

Figure 4-3 Code-DD solution (solution 1), the percentage of the epochs that give better than 10 cm position accuracy

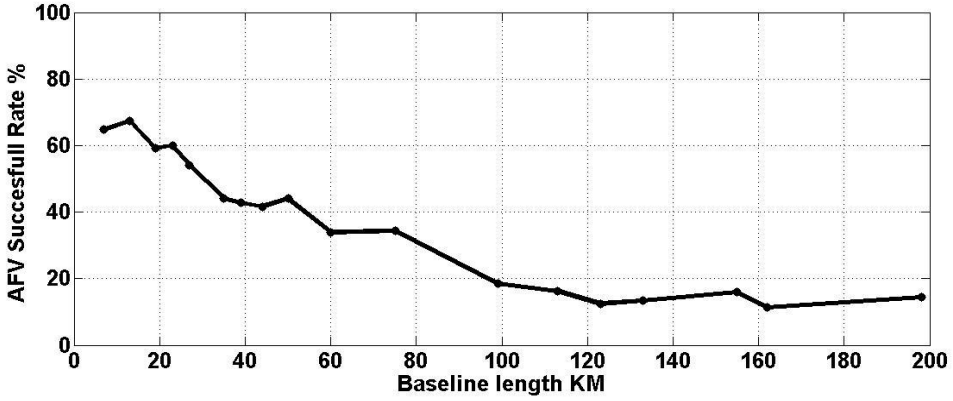

Figure 4-4 Code-DD solution (solution 1), daily AFV successful rates for different baseline lengths

Using a Code-DD solution eliminates the effect of the residuals of the satellites and receiver hardware biases, and the effect of the DCBs. Yet this solution is still affected by the ionosphere.

To deal with the ionospheric problem, a new subroutine has been added to the GASP software to read and employ an IGS 2D ionospheric model (Section 3.3.1 explains the implementation methodology). The subroutine uses temporal and spatial interpolations. The obtained ionospheric values have been converted to ranges, multiplied with an ionospheric mapping function, and used to correct the GPS carrier phase and code measurements. The application of the IGS 2D ionospheric model has been set as an optional choice in the GASP initialisation file.

Figure 4-5, Figure 4-6 and Figure 4-7 show the effect of applying the IGS 2D ionospheric model into the Code-DD solution on the GASP software final results.

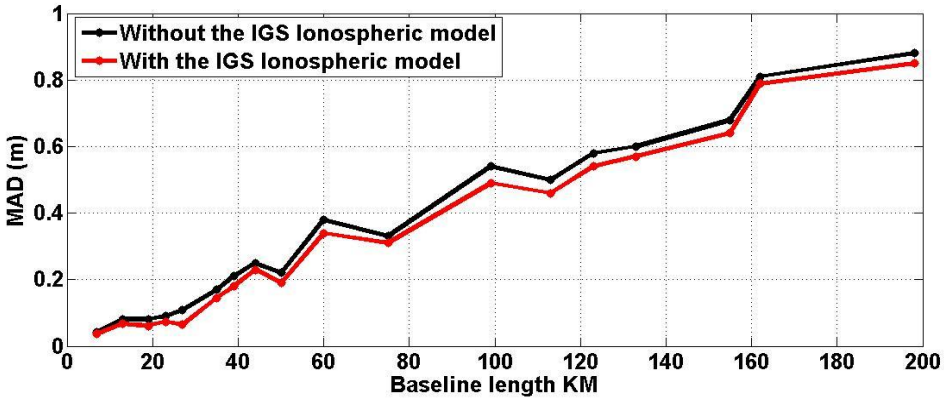

Figure 4-5 Code-DD solution with and without the implementation of the IGS 2D ionospheric model (solutions 1 and 2 respectively), GASP software positioning MAD

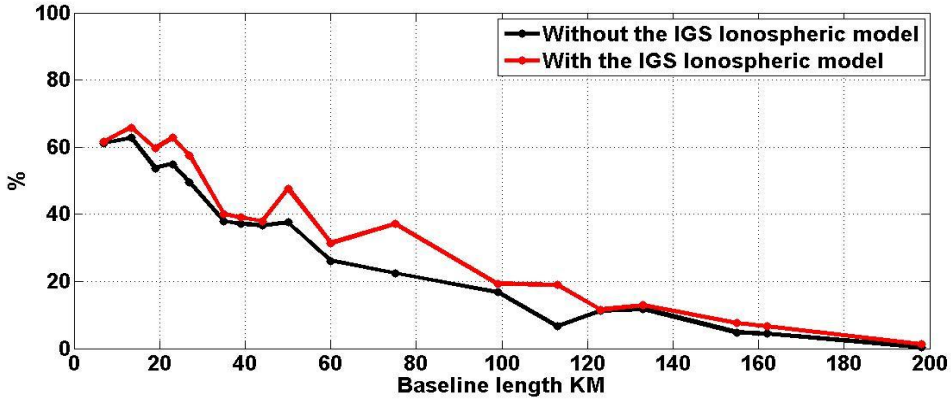

Figure 4-6 Code-DD solution with and without the implementation of the IGS 2D ionospheric model (solutions 1 and 2 respectively), the percentage of the epochs that give better than 10 cm position accuracy

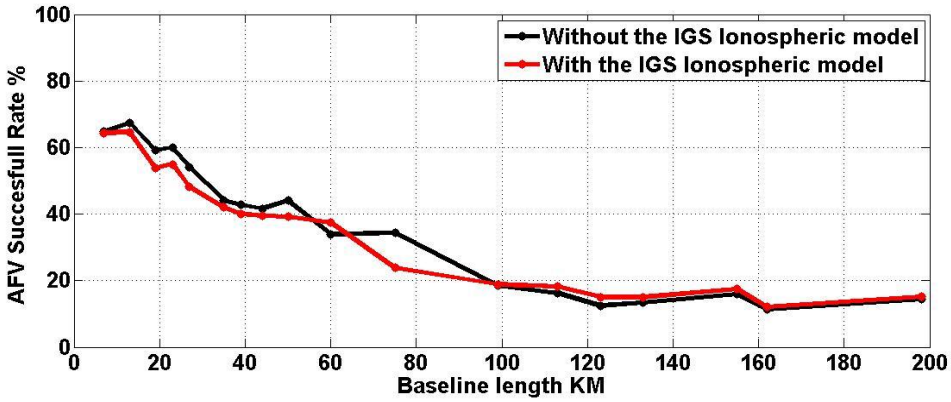

Figure 4-7 Code-DD solution with and without the implementation of the IGS 2D ionospheric model (solutions 1 and 2 respectively), daily AFV successful rates for different baseline lengths

The results shown in Figure 4-5, Figure 4-6 and Figure 4-7 indicate that the IGS model effect is small on the positioning results in the case of the GPS Code-DD solution. This is due to the fact that the spatial resolution of the model is too coarse to affect baselines shorter than several tens of kilometres. Figure 4-8 shows the applied global 2D IGS TEC model every two hours for day 66, 2007.

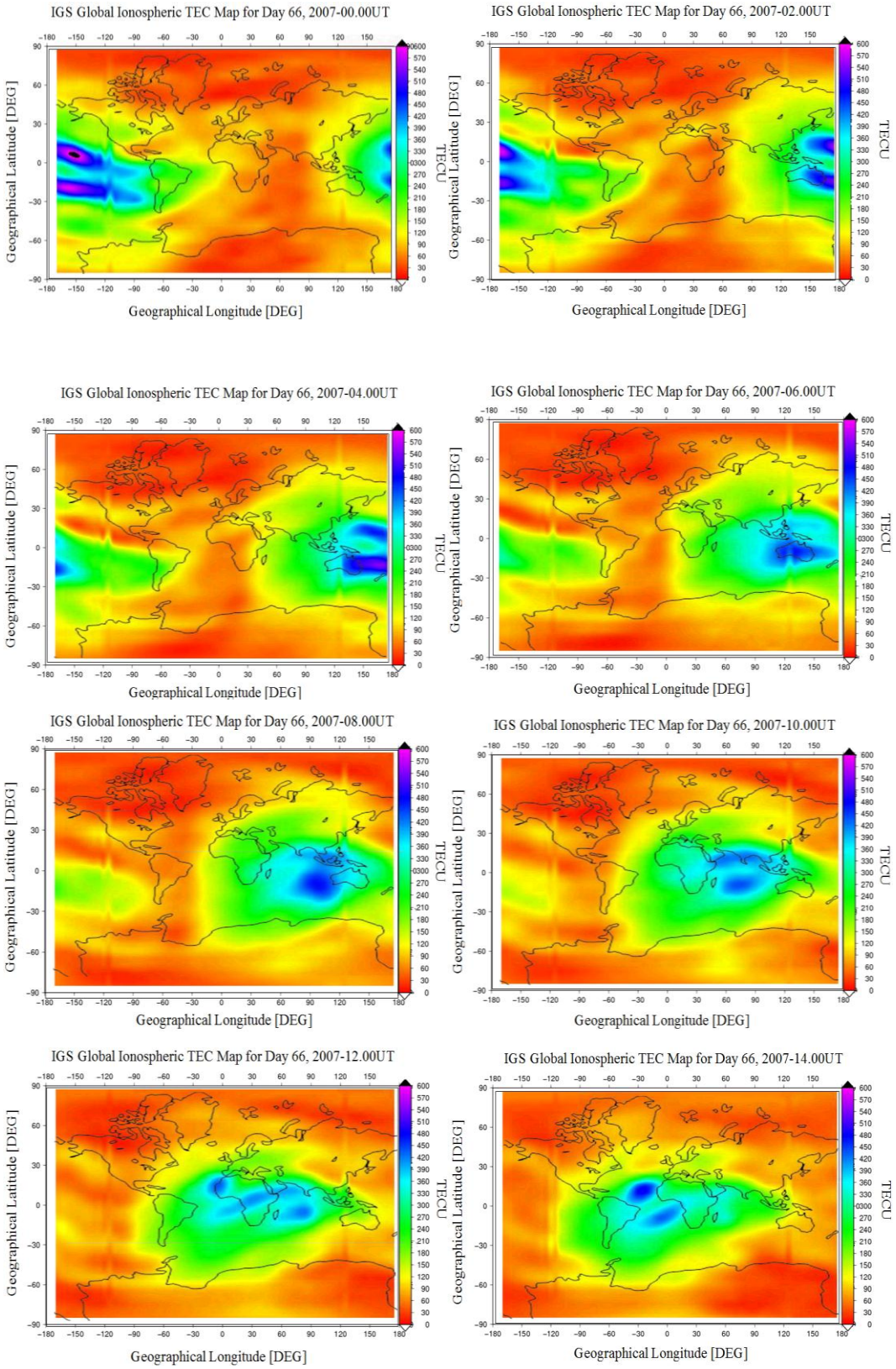
IGS Global Ionospheric TEC Map for Day 66, 2007-00.00UT
IGS Global Ionospheric TEC Map for Day 66, 2007-02.00UT
IGS Global Ionospheric TEC Map for Day 66, 2007-04.00UT
IGS Global Ionospheric TEC Map for Day 66, 2007-06.00UT
IGS Global Ionospheric TEC Map for Day 66, 2007-08.00UT
IGS Global Ionospheric TEC Map for Day 66, 2007-10.00UT
IGS Global Ionospheric TEC Map for Day 66, 2007-12.00UT
IGS Global Ionospheric TEC Map for Day 66, 2007-14.00UT
Geographical Latitude [DEG]
Geographical Longitude [DEG]
TECU

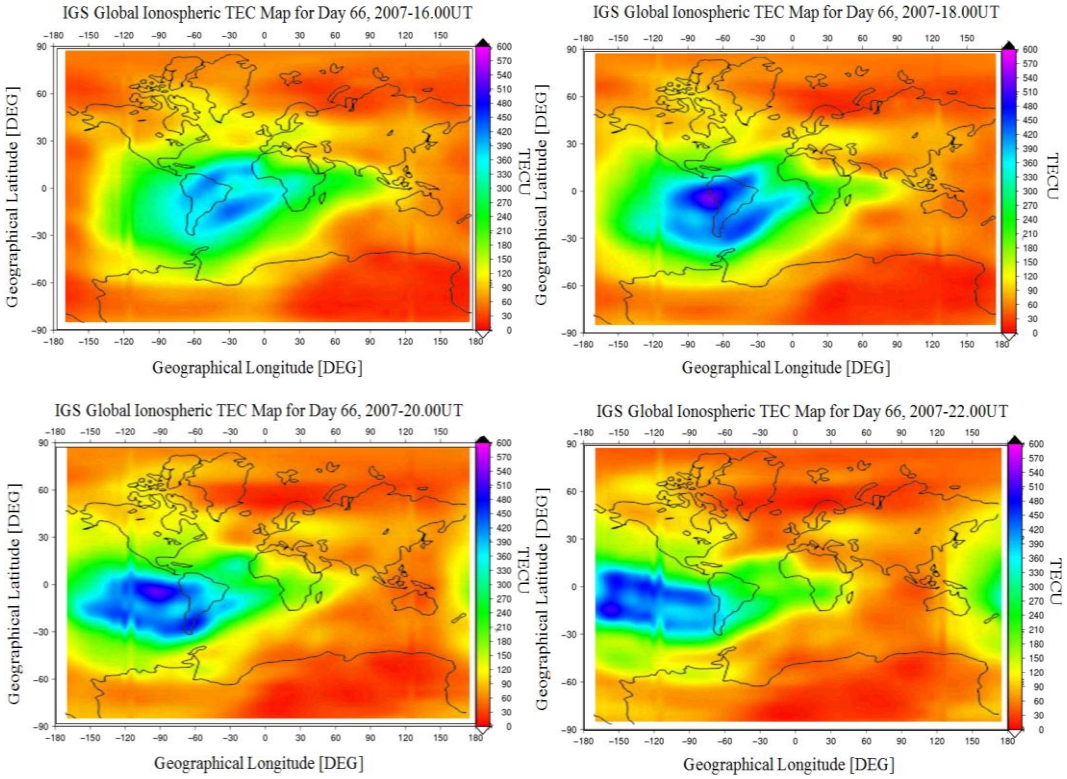

Figure 4-8 Global IGS TEC model for day 66, 2007

The application of the IGS ionospheric model does not remove the effect of the ionosphere on the GPS observations perfectly. The residual of the IGS ionospheric model can be determined by solving the geometry free combination equations of the pseudorange observations (see section 2.5.2) after correcting them by using the model as follows:

$$I_r = \left[(P_2 - P_1).\frac{f_2^2}{f_1^2 - f_2^2} \right] / M(e) \tag{4.1}$$

Where:

I_r is the L1 frequency ionosphere delay at the station zenith point which is caused by the IGS 2D ionospheric model residuals , in metres.

P_1 and P_2 are pseudorange measurements on L1 and L2 frequencies, respectively, in metres.

f_1 and f_2 are the two GPS signal frequencies on L1 and L2.

$M(e)$ is the ionospheric mapping function.

Figure 4-9 shows the 2D IGS ionospheric model residuals at the IGS BRUS station zenith point. The IGS BRUS station has been chosen for this example, because it is one of the used IGS GPS stations in the creation of the IGS global ionospheric model.

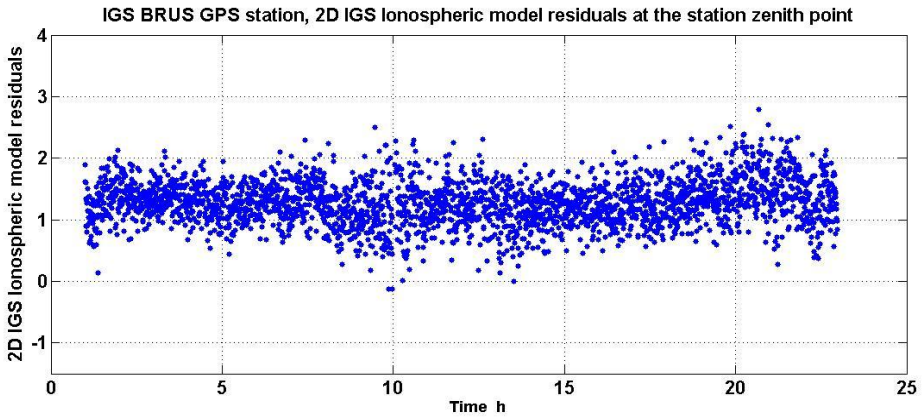

Figure 4-9 The 2D IGS ionospheric model residuals

A main component of the IGS ionospheric model residuals is the inter-frequency bias in the satellite and the receiver, as it affects the measuring of the Total Electron Content (TEC) along the path from the satellite to the receiver (Feltens, 2003). The Ionosphere Map Exchange file (IONEX) provides the inter-frequency biases for the IGS GPS stations whose data is involved in the ionospheric model computation, Figure 4-10.

```
     1.0            IONOSPHERE MAPS     MIX                 IONEX VERSION / TYPE
cmpcmb v1.2         gAGE/UPC            19-mar-07 09:24     PGM / RUN BY / DATE
ionex file containing IGS COMBINED Ionosphere maps          COMMENT
global ionosphere maps for day 066, 2007                    DESCRIPTION
IONEX file containing the COMBINED IGS TEC MAPS and DCBs    DESCRIPTION
      IONEX files of the following IAACs were combined: cod DESCRIPTION
   DIFFERENTIAL CODE BIASES                                    START OF AUX DATA
    01    -3.178     0.024                                    PRN / BIAS / RMS
    02     5.718     0.038                                    PRN / BIAS / RMS
    03    -2.696     0.028                                    PRN / BIAS / RMS

      acu5                    -0.894     0.000               STATION / BIAS / RMS
      brus 13101M004          -4.283     0.033               STATION / BIAS / RMS
```

Figure 4-10 Inter-frequency biases in the IONEX file

Applying this bias correction to the IGS model residuals, Figure 4-11 shows the rest of the noise and un-modelled errors.

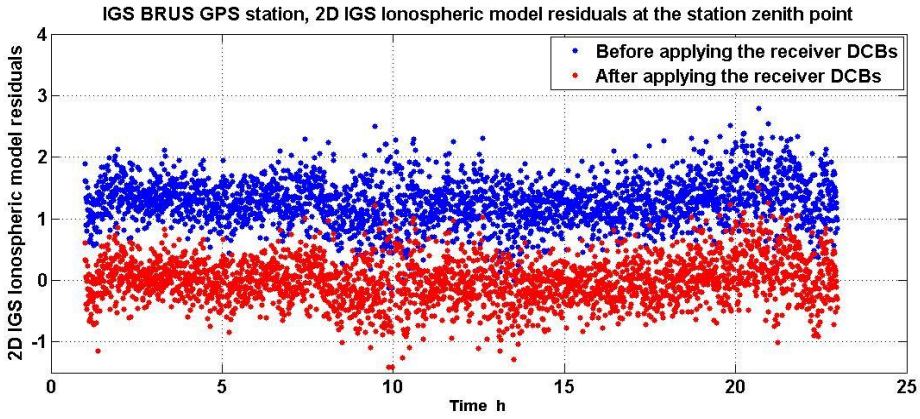

Figure 4-11 The 2D IGS ionospheric model residuals after applying the receiver inter-frequency biases correction

Applying the inter-frequency bias reduces the mean value of the IGS ionospheric model residuals at the station zenith from 1.28 m to - 0.004 m. Considering the Root Mean Square (RMS) of the bias measured at the BRUS station is 0.033 ns as shown in Figure 4-10, the mean value of the remaining bias is less than $3 * \sigma = 0.0297m$. The zenith ionospheric residuals in Figure 4-9 have been used to correct the GPS phase measurements as follows:

$$\Phi_{1c} = \Phi_1 + M(e) I_r f_1 / c$$
$$\Phi_{2c} = \Phi_2 + \gamma\, M(e) I_r f_2 / c \qquad (4.2)$$

Where:

Φ_{1c} and Φ_{2c} are corrected carrier-phase measurements on L1 and L2 frequencies, respectively, in metric units.

Φ_1 and Φ_2 are carrier-phase measurements on L1 and L2 frequencies, respectively, in metric units.

γ is the scale factor for converting from L1 ionosphere delay to L2 frequency $\left(77^2/60^2\right)$, unitless.

c is the speed of light constant, in metres per second.

Figure 4-12, Figure 4-13 and Figure 4-14 show the effect of correcting the phase measurements on the GASP positioning statistical factors.

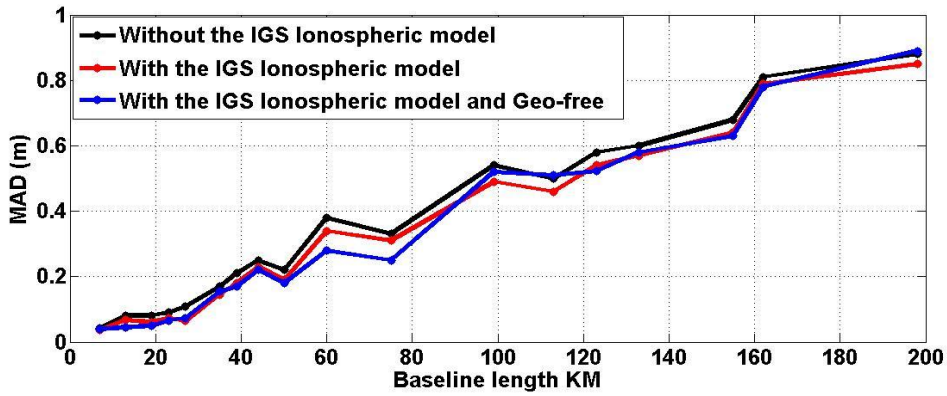

Figure 4-12 Code-DD solutions with and without implementation of the Geo-free results to correct the phase measurements (solutions 1, 2 and 3 respectively), GASP software positioning MAD

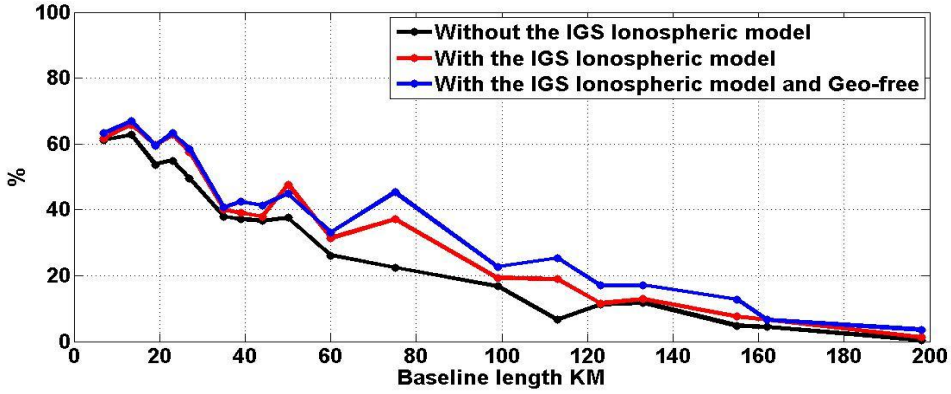

Figure 4-13 Code-DD solutions with and without implementation of the Geo-free results to correct the phase measurements (solutions 1, 2 and 3 respectively), the percentage of the epochs that give better than 10 cm position accuracy

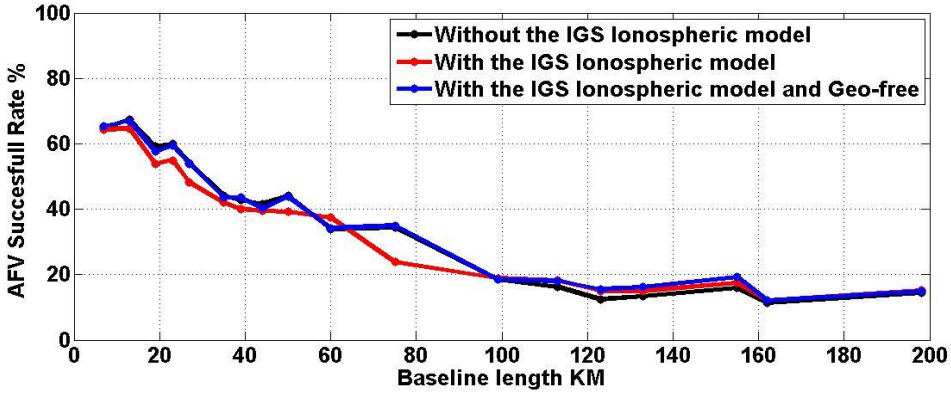

Figure 4-14 Code-DD solutions with and without implementation of the Geo-free results to correct the phase measurements (solutions 1, 2 and 3 respectively), daily AFV successful rates for different baseline lengths

Figure 4-12, Figure 4-13 and Figure 4-14 indicate that using Code-DD with the IGS ionospheric model and the geometry free solution gives the best results over the three tried solutions so far. The average value of the solution 3 results MAD is 9.3% less than that of the solution 1 results, and 1.5% less than that of the solution 2 results. The percentage of getting epochs with better than 10 cm position accuracy by using solution 3 is 23.9% higher than the percentage of using solution 1 and 7.4% higher than using solution 2. The percentage of getting AFV successful value is 1.5 % higher when using solution 3 rather than solution 1, and 6.2% higher in comparison to solution 2. Therefore the geometry free solution will represent the Code-DD solution in the coming comparisons with other solutions.

4.3 UNDIFFERENCED SOLUTION

The International GNSS Service (IGS) now provides very accurate satellite orbital positions and clocks data (Kouba, 2009) . Taking advantage of this availability, the moving receiver dual frequency pseudorange observations will be used to find the initial receiver position and to create an ionospheric model to correct the phase measurements. This solution will be called Code-SPP (solution 5) to verify it from the GPS Precise Point Positioning (PPP) where the code and phase observations are involved in the solution (Zumberge *et al.*, 1997). The applied data and correction models in this chapter (see the introduction of this chapter) reduce the number of unknown parameters in the GPS pseudorange observations (equations 2.20), and so for each satellite the equations can be reformed as follows:

$$\begin{aligned} P_1 &= \rho + c(dT) + M(e)I_r \\ P_2 &= \rho + c(dT) + M(e)\gamma I_r \\ C_1 &= \rho + c(dT) + M(e)I_r \end{aligned} \tag{4.3}$$

Where:

P_1, P_2 and C_1 are GPS pseudorange measurements on L1 and L2 frequencies, respectively, in metres.

ρ is the geometric distance between satellite and receiver antenna, in metres.

dT is the receiver clock error, in seconds.

γ is the first-order scale factor for converting ionospheric delay from L1 to L2 frequency $77^2/60^2$, unitless.

The Least Squares Method has been used to solve this group of equations as follows:

$$x = (A^T W A)^{-1} A^T W b \tag{4.4}$$

Where,

x is the state vector:

$$x = \begin{bmatrix} X \\ Y \\ Z \\ \mathrm{I}_r \\ dT \end{bmatrix}$$

Where:

$X, Y\ and\ Z$ are the geocentric Cartesian station coordinates m.

A is the design matrix:

$$A = \begin{bmatrix} a_{x,1} & a_{y,1} & a_{z,1} & a_{I_r,1} & a_{c,1} \\ a_{x,2} & a_{y,2} & a_{z,2} & a_{I_r,2} & a_{c,2} \\ a_{x,3} & a_{y,3} & a_{z,3} & a_{I_r,3} & a_{c,3} \\ a_{x,4} & a_{y,4} & a_{z,4} & a_{I_r,4} & a_{c,4} \\ a_{x,n} & a_{y,n} & a_{z,n} & a_{I_r,n} & a_{c,n} \end{bmatrix}$$

Where:

$a_{x,i}$, $a_{y,i}$ and $a_{z,i}$ are the Cartesian components of a unit vector pointing from the user's estimated position to the satellite(i).

$a_{I,i} = \frac{1}{M\,(e)}$ for L1 frequency observations.

$a_{I_r,i} = \frac{\gamma}{M\,(e)}$ for L2 frequency observations.

$a_{c,i} = 1$

W is the weight matrix.

$$W = \begin{bmatrix} {}^{1}/_{sin(e_i)^2} & 0 & \dots & 0 \\ 0 & {}^{1}/_{sin(e_i)^2} & & \vdots \\ \vdots & & \ddots & 0 \\ 0 & \dots & 0 & {}^{1}/_{sin(e_i)^2} \end{bmatrix}$$

Where:

e_i is the elevation angle of the satellite i at the user receiver site.

b is the misclosure vector.

Figure 4-15 shows the receiver clock offset, the ionospheric value at the station zenith point and the differences between the computed positions and the true position coordinates for four of the moving stations in Table 4-1.

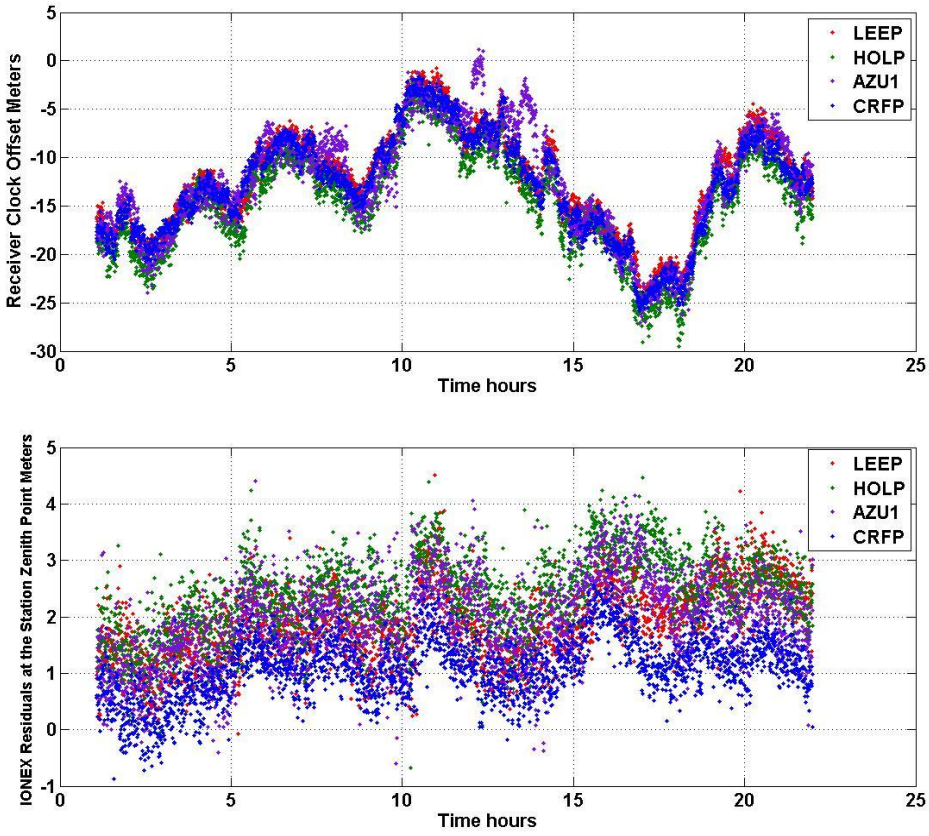

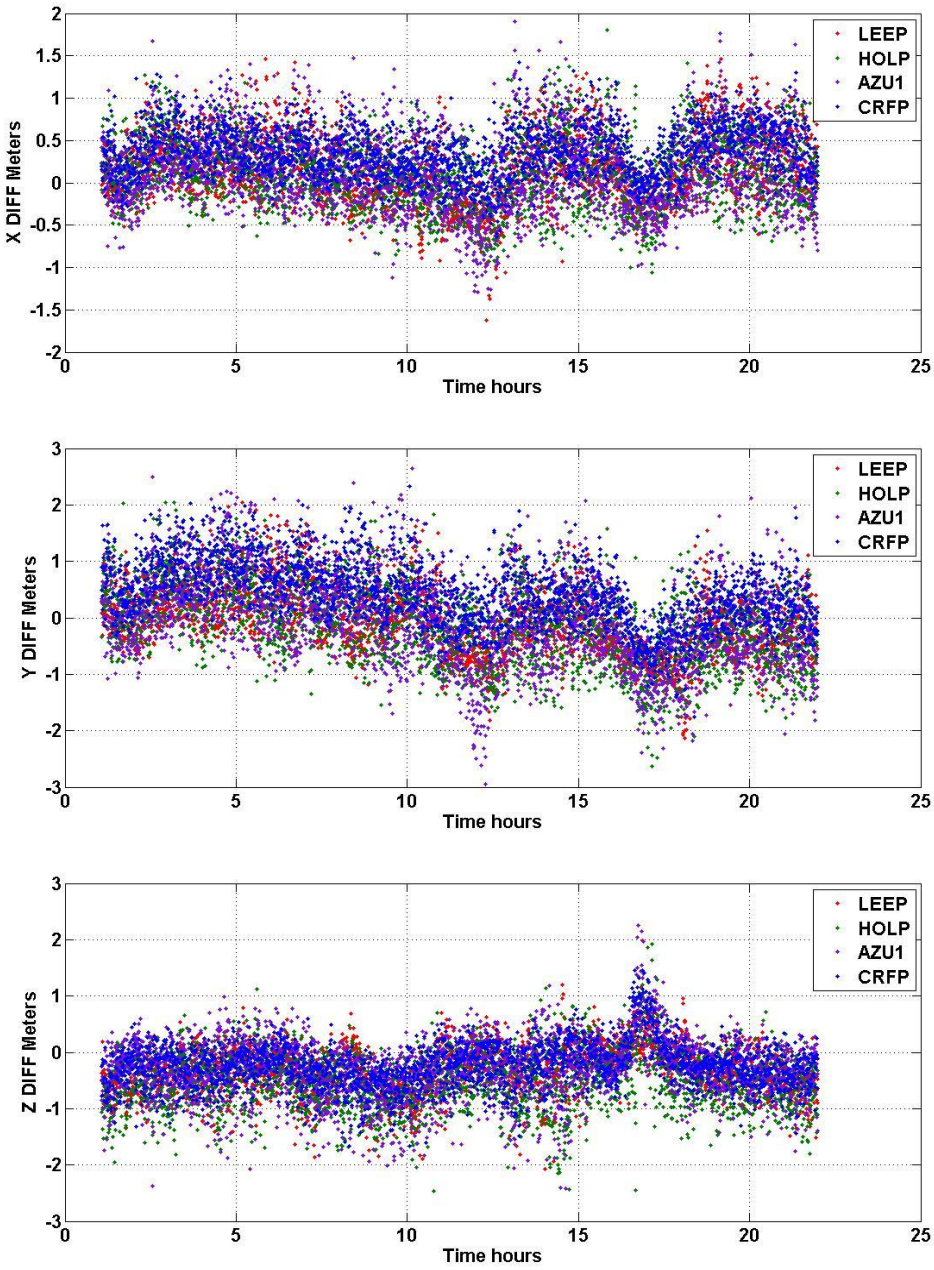

Figure 4-15 Code- SPP solution results

The positioning results in Figure 4-15 have been used as position inputs into the GASP software ambiguity function, while the ionospheric values within have been used to correct the GPS phase measurements. Figure 4-16, Figure 4-17 and Figure 4-18 show comparisons between the GASP ambiguity function results statistical factors in the cases of using the Code-DD and Code-SPP results as initial inputs into the GASP ambiguity function.

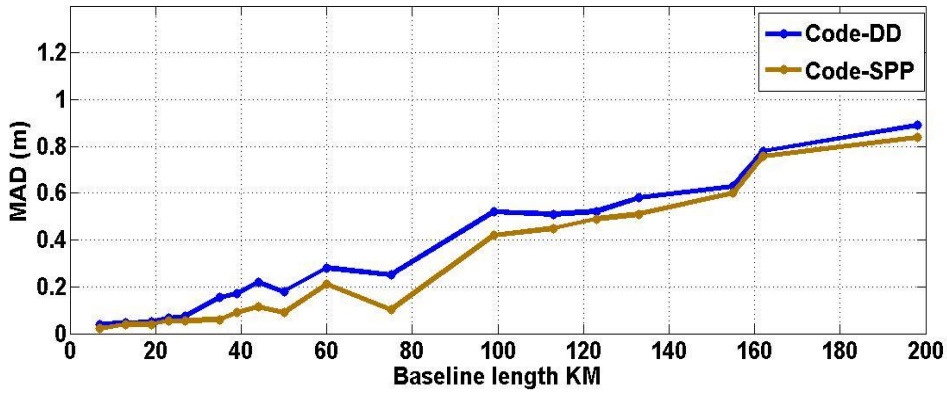

Figure 4-16 Code-SPP and Code-DD solutions with the implementation of the IGS 2D ionospheric model (solutions 5 and 3 respectively), GASP software positioning MAD

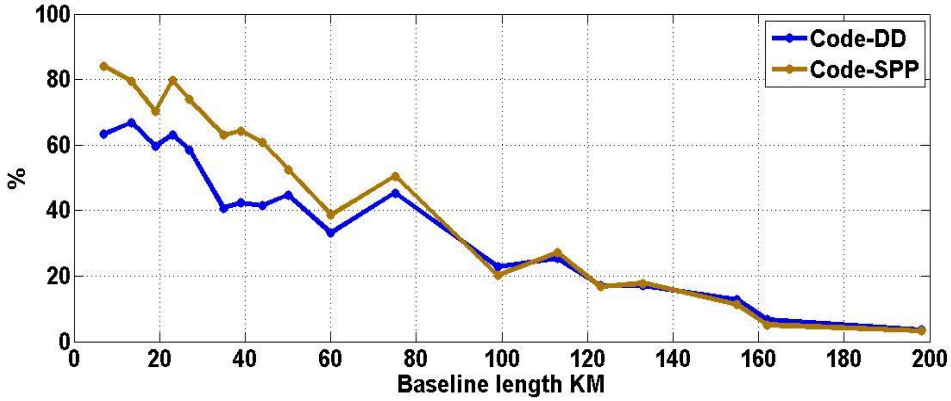

Figure 4-17 Code-SPP and Code-DD solutions with the implementation of the IGS 2D ionospheric model (solutions 5 and 3 respectively), epochs that give better than 10 cm position accuracy

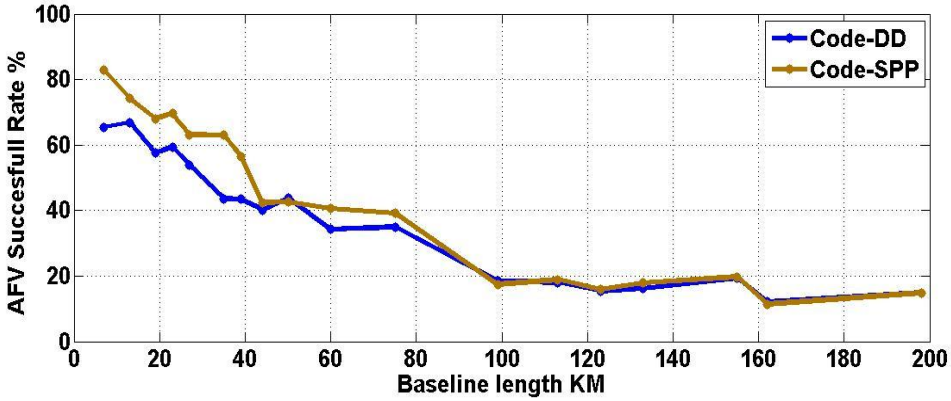

Figure 4-18 Code-SPP and Code-DD solutions with the implementation of the IGS 2D ionospheric model (solutions 5 and 3 respectively), daily AFV successful rates for different baseline lengths

Figure 4-16, Figure 4-17 and Figure 4-18 show that using the Code-SPP results in the GASP ambiguity function gives better positioning results than using the Code-DD solution. This is because the Code-SPP solution results are less noisy than those of the Code-DD. Figure 4-19 shows the standard deviations of the double and zero differencing pseudorange observations solutions positioning results for the IGS LEEP station over different baselines. This is because the multipath effect is larger in the case of Code-DD as two stations are involved. Also, more satellite data are available for use in the Code-SPP solution than in the Code-DD solution, as there is no need to use the shared satellites only between both baseline receivers.

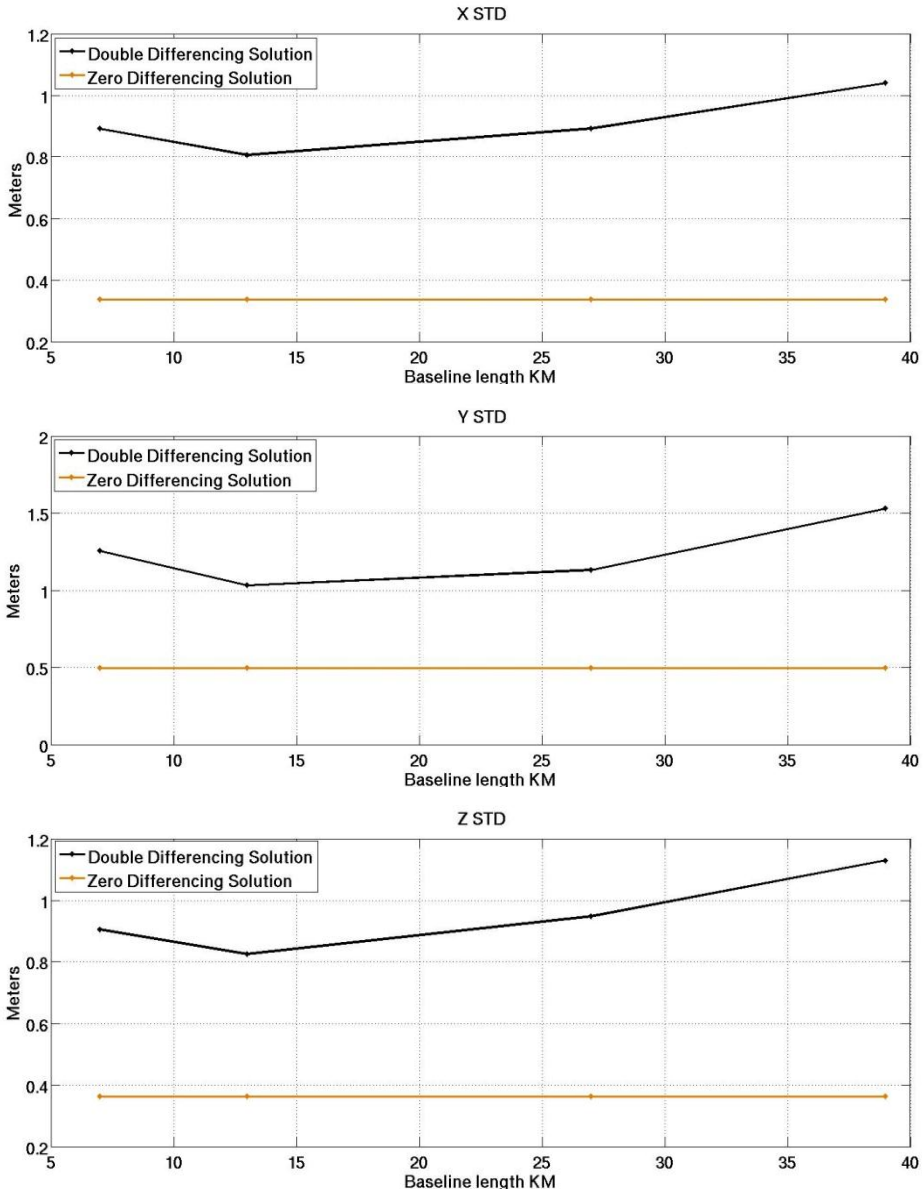

Figure 4-19 IGS LEEP station, Code-SPP and Code-DD solutions X,Y and Z standard deviations

It has been observed in plots (Appendix A) that the IGS ionospheric model has a great effect on the Code-SPP results, as it mitigates the effect of the satellites' DCBs as well as reducing the effect of the ionosphere on the results (solutions 4 and 5). The satellite DCB values are approximately stable over time. Figure 4-20 shows the GPS satellite PRN1 DCBs over the year 2007 as they appear in the IGS 2D ionospheric models headers. The DCBs' range over that year is 0.361 nanoseconds. Therefore the GPS satellites DCBs values can be predicted if the IGS 2D ionospheric model is not available and used in the solutions.

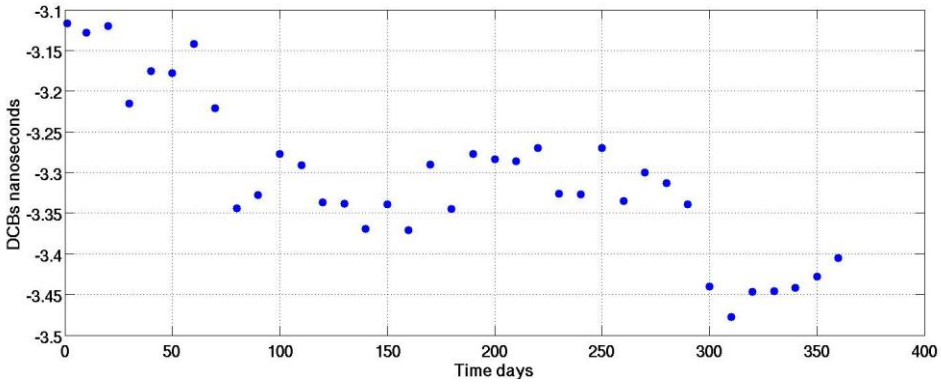

Figure 4-20 The GPS satellite PRN1 DCBs over year 2007

It has been seen in plots (Appendix A) that employing the DCBs alone to the Code-SPP solution gives better results than using the Code-SPP solution without any ionospheric correction (solutions 4 and 6).

The Code-SPP solution improves the quality of the GASP software positioning results, and does not affect the data processing time significantly as it is done by applying a simple least squares method. However, the GASP software positioning results with the implementation of the Code-SPP solution accuracy is still baseline length dependent, which is explained by the fact that the final GASP software positioning step is done by a double differenced combination.

In the next sections, regional and temporal filters will be applied to the Code-SPP results.

4.4 REGIONAL FILTER

Figure 4-15 shows a regional correlation between the results; therefore a regional filter has been applied to this solution to improve the quality of the results (solution 8). The Code-SPP solution has been computed separately for the fixed and moving stations in each baseline. The results of the fixed station have been used to correct the results of the moving station as follows:

$$\begin{aligned} C_m &= C_{m0} - (C_{f0}) \\ I_m &= I_{m0} - (I_{f0}) \\ X_m &= X_{m0} - (X_{f0} - X_{ft}) \\ Y_m &= Y_{m0} - (Y_{f0} - Y_{ft}) \\ Z_m &= Z_{m0} - (Z_{f0} - Z_{ft}) \end{aligned} \tag{4.5}$$

Where:

$I_{m0}, C_{m0}, X_{m0}, Y_{m0} and\ Z_{m0}$	are the moving station single epoch undifferenced pseudorange solution results.
$I_{f0}, C_{f0}, X_{f0}, Y_{f0} and\ Z_{f0}$	are the fixed station single epoch undifferenced pseudorange solution results.
$X_{ft}, Y_{ft} and\ Z_{ft}$	are the true fixed station position coordinates as published on the (SOPAC) website.
I_m	is the difference between the moving receiver zenith ionosphere and the fixed receiver zenith ionosphere.
C_m	is the difference between the moving receiver clock offset and the fixed receiver clock offset.
$X_m, Y_m and\ Z_m$	are the final moving station coordinates according to this solution.

Figure 4-21 shows the receiver clock offset, the ionospheric value at the station zenith point and the differences between the computed positions and the true position coordinates for the 60 km baseline (the 60 km baseline results have been plotted in

this chapter as they are typically representative of the other tried baseline results. All tested baseline results are shown in Appendix B).

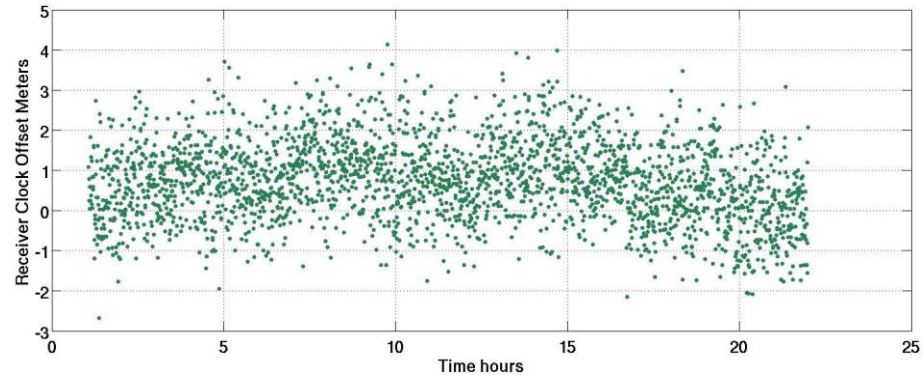

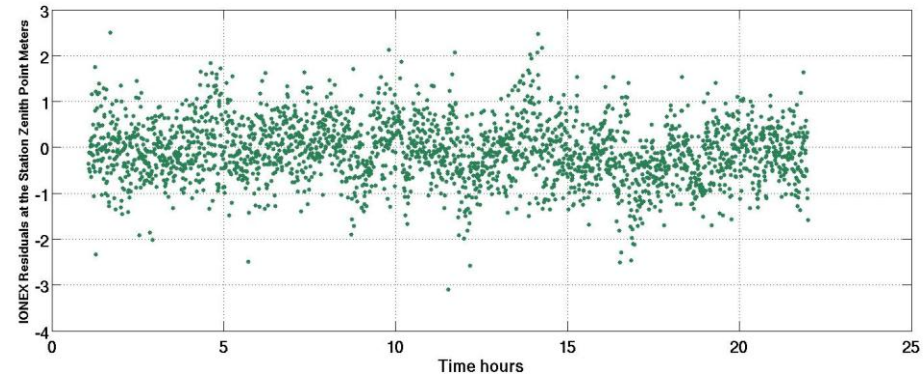

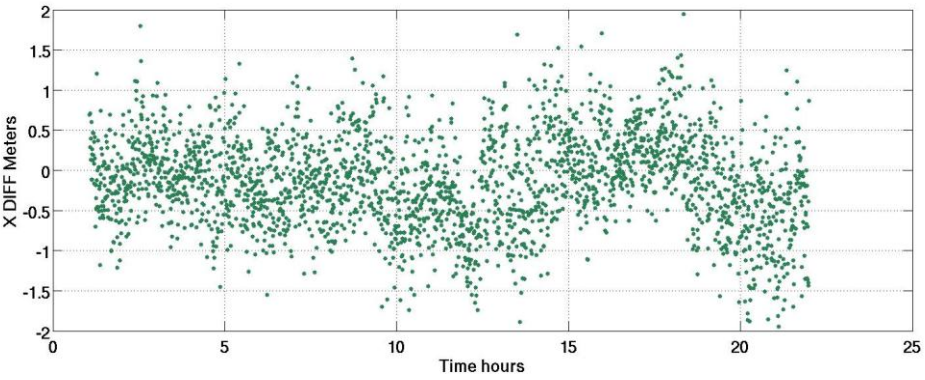

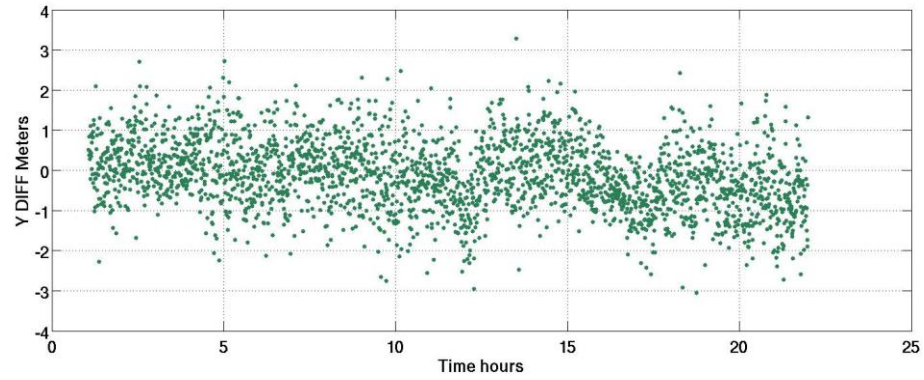

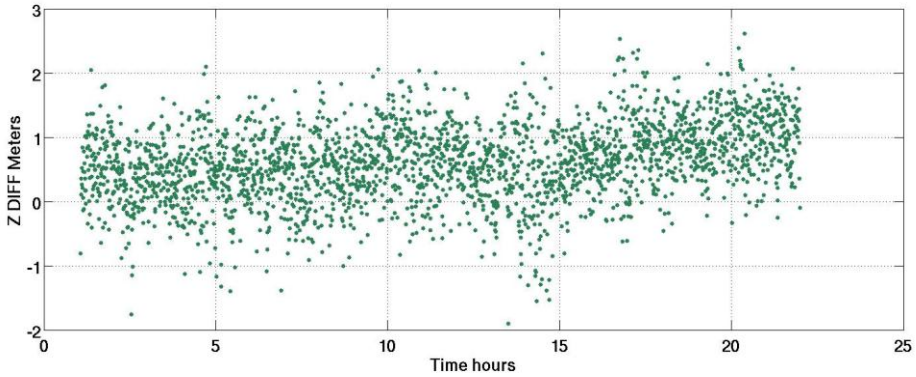

Figure 4-21 Regional filter solution results

The $X_m, Y_m, and\ Z_m$ values have been used as positional inputs into the GASP software ambiguity function, while the phase measurements are corrected for a I_{m0} zenith ionospheric value. Figure 4-22 shows the final GASP software positioning results MAD, the probability of getting positions with accuracy better than 10 cm, and the probability of obtaining epochs with an AFV larger than 0.9 over different baseline lengths when the Code-DD, Code-SPP and regional filter results are used in the GASP ambiguity function.

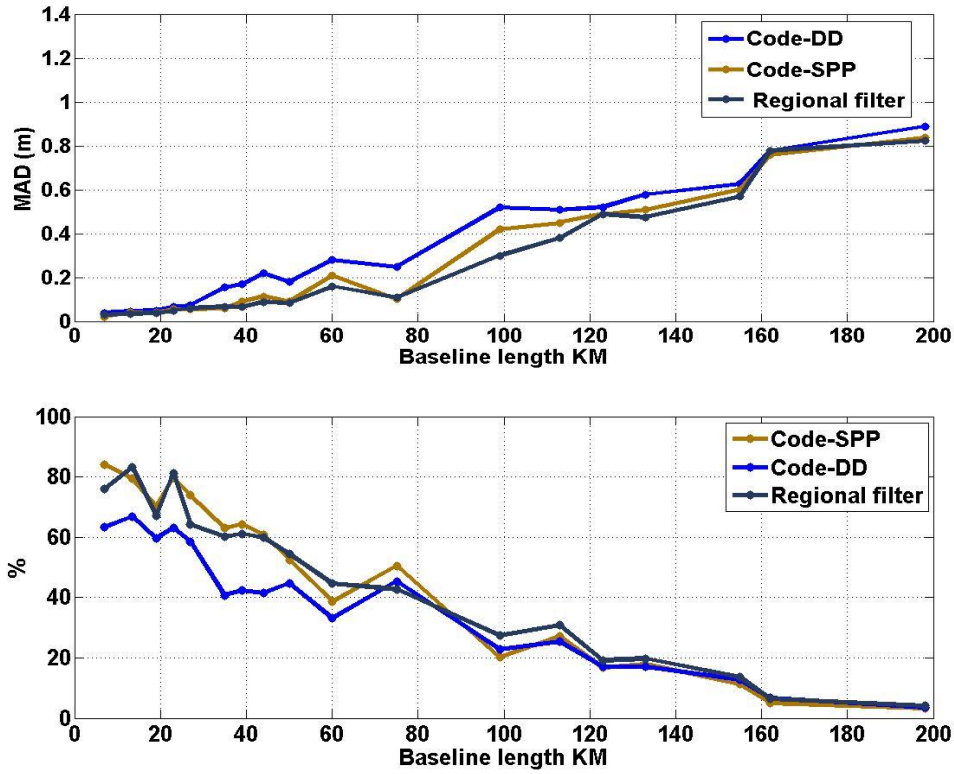

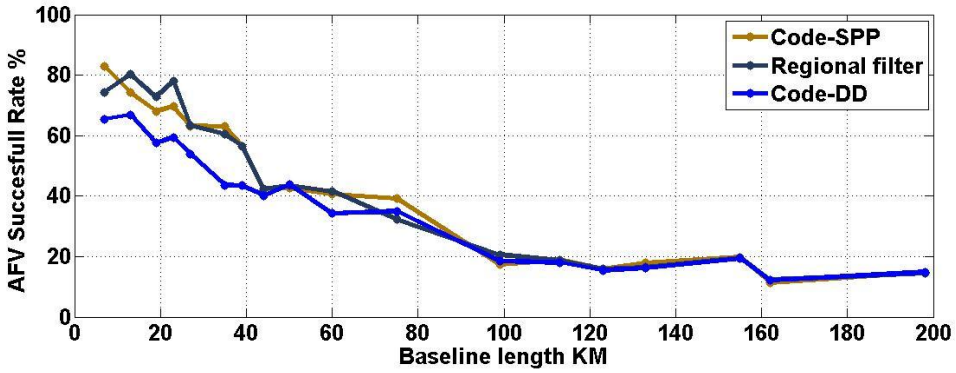

Figure 4-22 Code-DD, Code-SPP and Regional filter results (solutions 3, 5 and 8 respectively) statistical factors

As a result, applying the regional filter has given better positioning accuracy than the Code-DD solution (Figure 4-22). The regional filter solution results are less noisy than the Code-DD results, as it is a combination of two Code-SPP solutions where more satellites are available to be used. Figure 4-23 shows a comparison between both solutions' positioning results and the true station coordinates for a 60 km baseline.

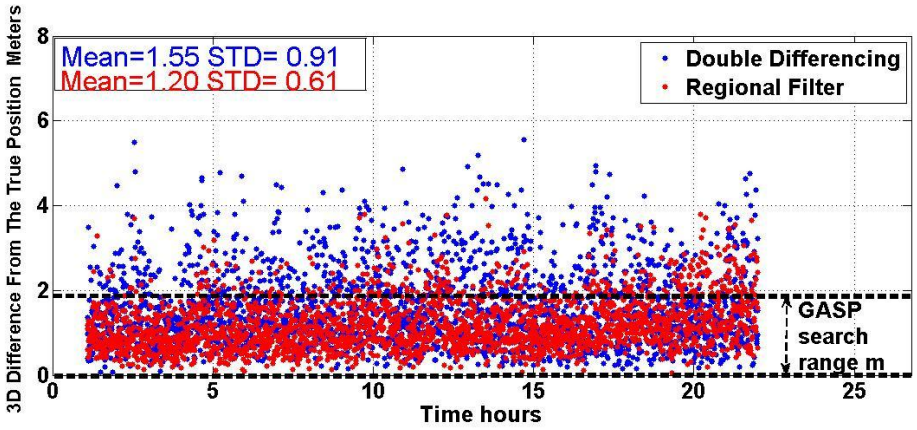

Figure 4-23 60 km baseline (CSN1 – AZU1), Regional filter and Code-DD solutions results

Figure 4-22 shows that there is no big difference in results in the cases of using the Code-SPP or regional filter solutions. The Code-SPP solutions have been done for the 60km baseline moving station (AZU1) and its results against those of the regional filter have been plotted in Figure 4-24.

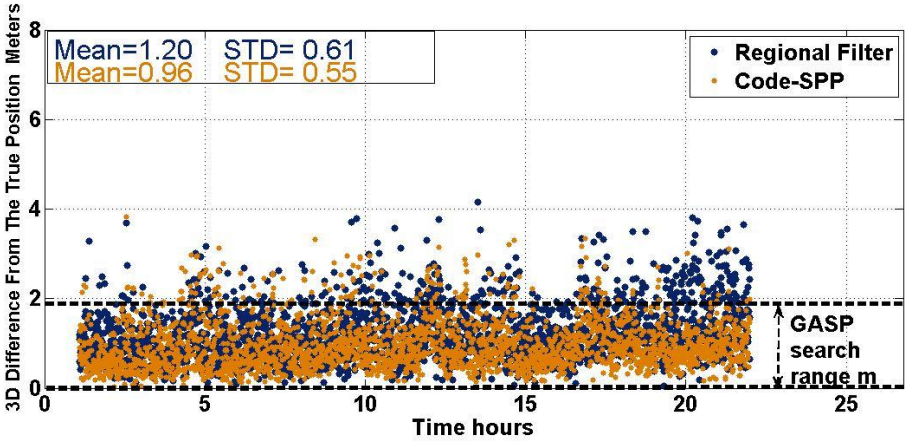

Figure 4-24 AZU1 station Code-SPP and regional (with baselin length equals to 60km) results

The regional filter has a positive effect on the GASP software positioning results, and in the next section a temporal filter will be investigated.

4.5 SIDEREAL FILTER

For the same site, the GPS satellite constellation is set to be approximately the same every sidereal day (23h 56m 4s). However, due to the Earth's shape, the GPS satellite constellation repeats itself in a time slightly less than this period (Choi *et al.,* 2004). The GPS satellite constellation repeating time was computed by Agnew and Larson (2007)and they found that the mean sidereal lag is 86154 seconds (23h 55m 54s) which was also verified by Ragheb et al.(2007) As a result, the GPS pseudorange observations, satellite orbits and hardware errors, the atmospheric effects, and multipath approximately repeat themselves every mean sidereal day (23h 55m 54s) for a stationary receiver. This causes the pseudorange observation solution results to repeat approximately every sidereal day. Figure 4-25 shows the regional filter solution (solution 8) results for the 60 km baseline over two days, 65 and 66/2007.

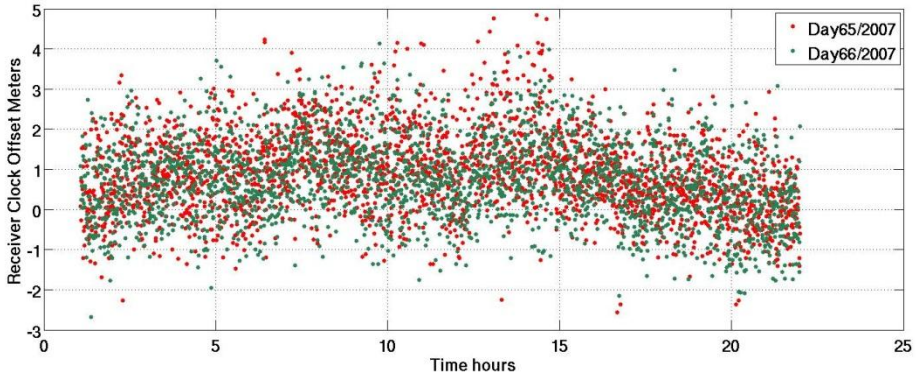
Receiver Clock Offset Meters
Time hours
Day65/2007
Day66/2007

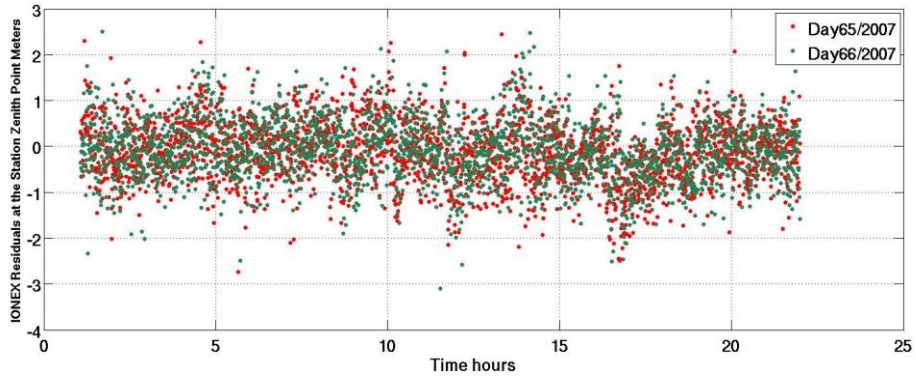
IONEX Residuals at the Station Zenith Point Meters
Time hours
Day65/2007
Day66/2007

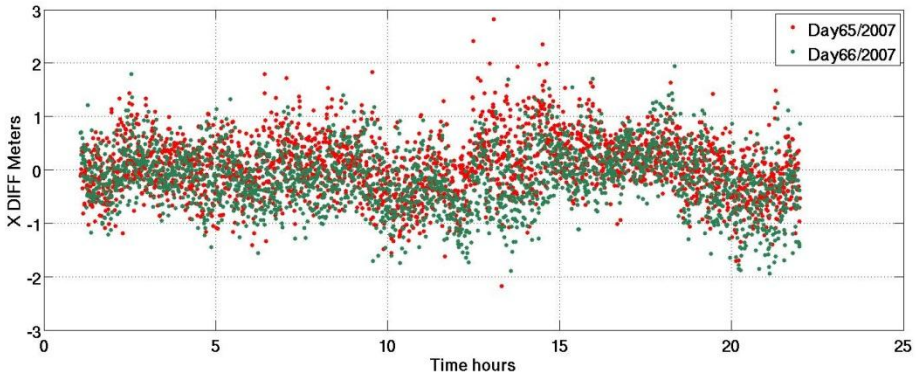
X DIFF Meters
Time hours
Day65/2007
Day66/2007

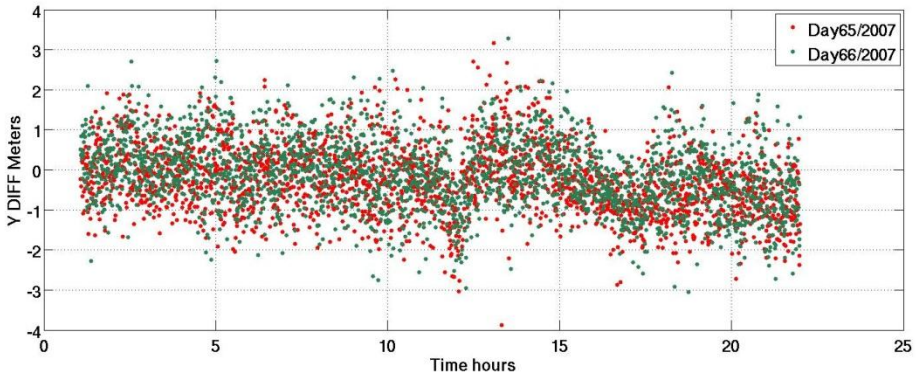
Y DIFF Meters
Time hours
Day65/2007
Day66/2007

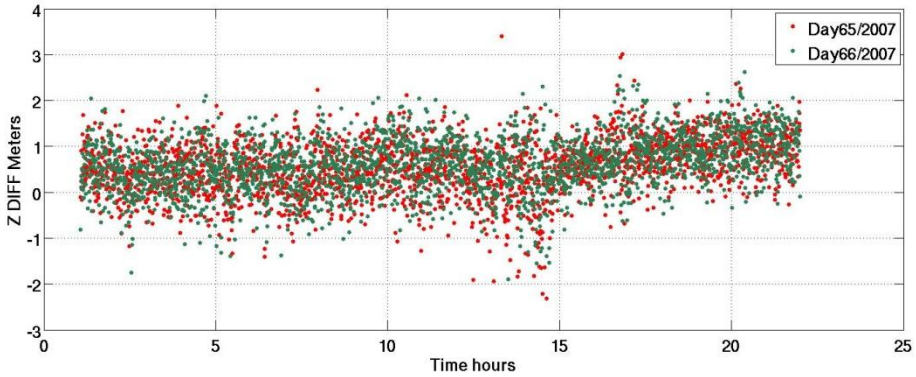

Figure 4-25 60 km regional filter (solution 8) results over two sidereal days

The station Code-SPP solution results have been corrected by using its previous mean sidereal day solution results as follows:

$$
\begin{aligned}
C_m &= C_{m0} - (C_{mp}) \\
I_m &= I_{m0} - (I_{mp}) \\
X_m &= X_{m0} - (X_{mp} - X_{mt}) \\
Y_m &= Y_{m0} - (Y_{mp} - Y_{mt}) \\
Z_m &= Z_{m0} - (Z_{mp} - Z_{mt})
\end{aligned}
\tag{4.6}
$$

Where:

$I_{m0}, C_{m0}, X_{m0}, Y_{m0} and\ Z_{m0}$	are the moving station regional filter solution results .
$I_{mp}, C_{mp}, X_{mp}, Y_{mp} and\ Z_{mp}$	are the moving station previous mean sidereal day regional filter solution results .
$X_{mt}, Y_{mt} and\ Z_{mt}$	are the true moving station position coordinates as published on the (SOPAC) website.
I_m	is the difference between the regional filter zenith ionospheric result at the epoch and at a mean sidereal day time previous to the epoch time.
C_m	is the difference between the regional filter solution receiver clock offset result and the receiver clock offset result at a mean sidereal day time previous to the epoch time.

$X_m, Y_m and\ Z_m$ are the final moving station coordinates according to this solution.

Figure 4-26 shows the 60 km baseline sidereal filter solution (solution 10) results for day 66/2007 after removing the day 65/2007 solution residuals.

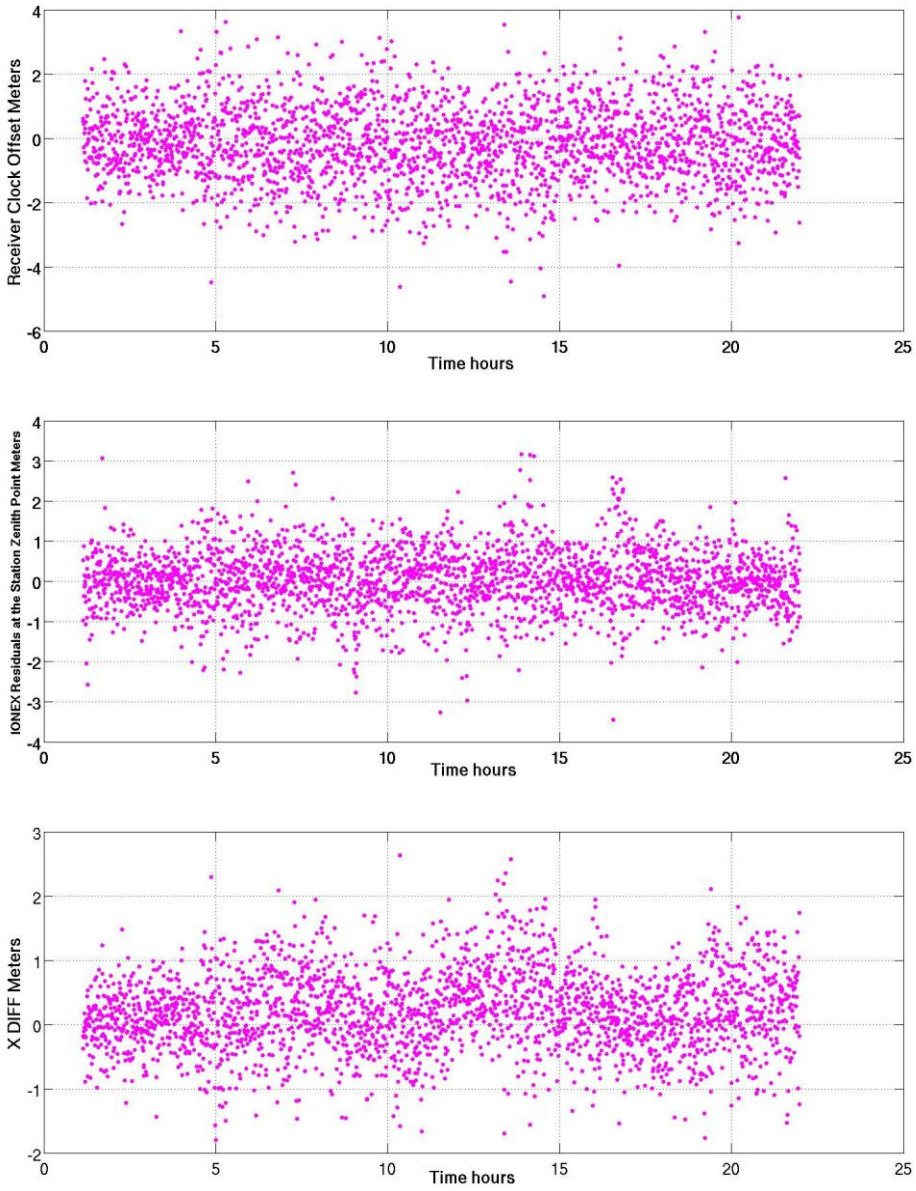

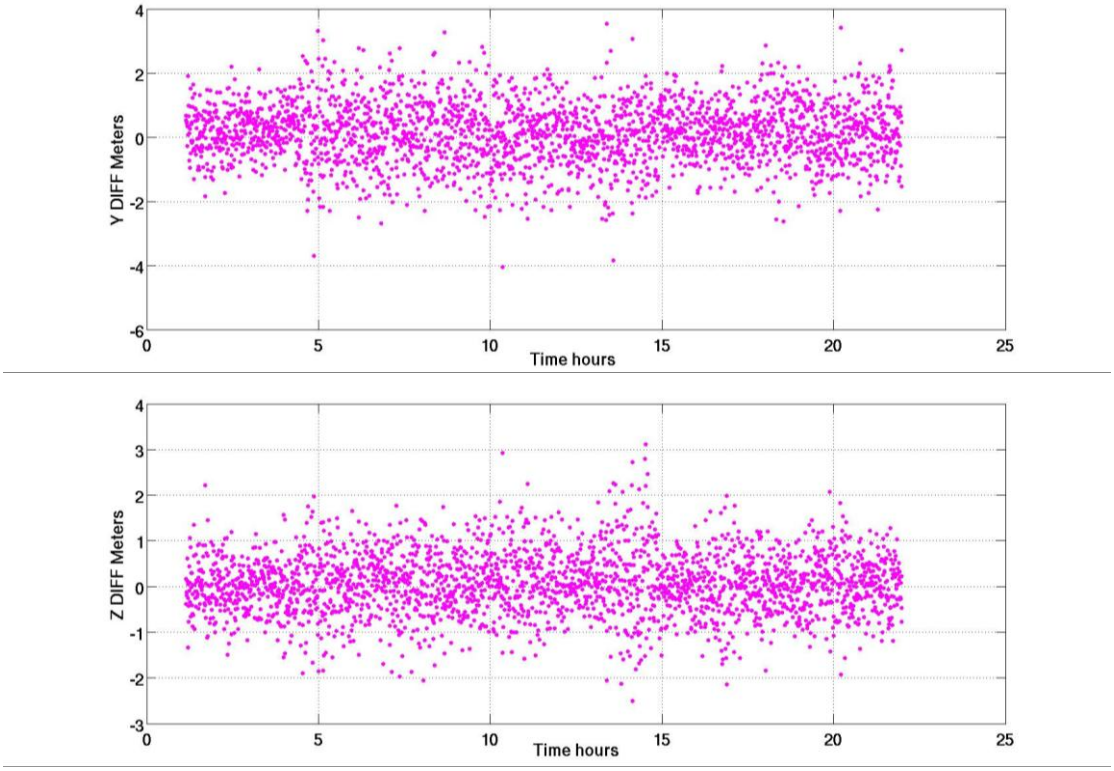

Figure 4-26 60 km baseline, sidereal filtering for a regional filter solution results

The $X_m, Y_m, and\ Z_m$ as positional inputs into the GASP software ambiguity function and the Code-SPP solution ionospheric results for the moving station have been used to correct the GPS phase measurements. Figure 4-27 shows the MAD of the final GASP software position results, Figure 4-28 shows the probability of getting positions within 10 cm radius to the true position and Figure 4-29 shows the percentage of the epochs which give an AFV larger than 0.9 over different baseline lengths when a sidereal filter is applied into the regional filter results.

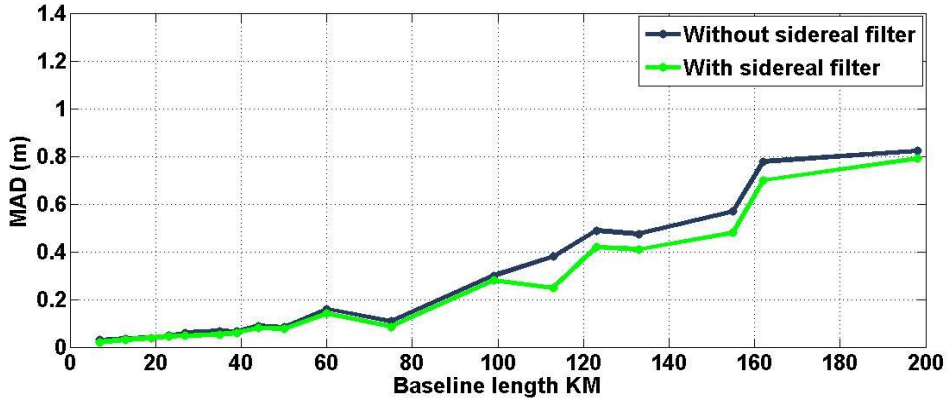

Figure 4-27 Regional filter with and without the implementation of the sidereal filter (solutions 8 and 10 respectively), GASP software final results MAD

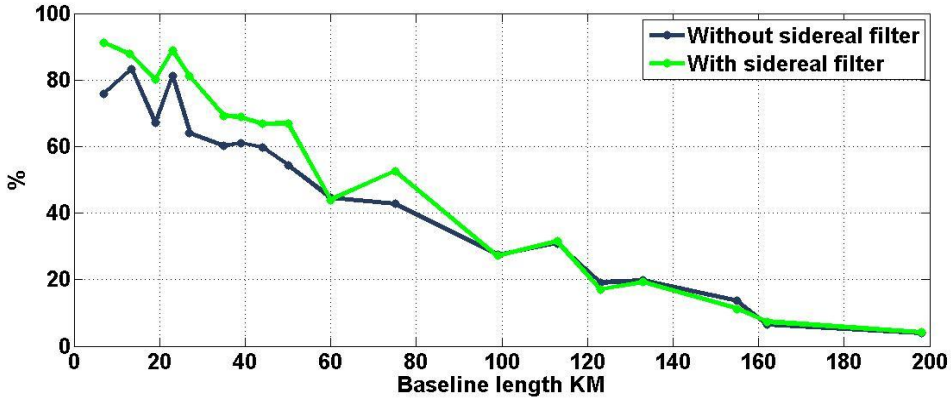

Figure 4-28 Regional filter with and without the implementation of the sidereal filter (solutions 8 and 10 respectively), epochs that give better than 10 cm position accuracy

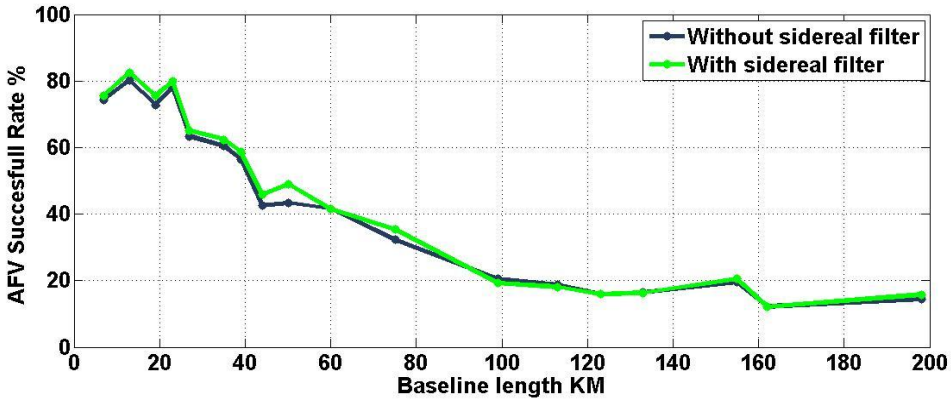

Figure 4-29 Regional filter with and without the implementation of the sidereal filter (solutions 8 and 10 respectively), daily AFV successful rates for different baseline lengths

The sidereal filter has also been applied to the Code-SPP results (Solution 9), and it has been observed in plots (Appendix A) that the GASP software final positioning results of this implementation are better than when using a plain Code-SPP solution (solution 4). Also it has been seen that applying a sidereal filter removes a lot of the ionosphere, as it depends on the time of day (see chapter 3).

4.6 CONCLUSION

The implementation of the IGS 2D ionospheric model has improved the results of all of the applied solutions in this research. Figure 4-30 shows the GASP software final positions MAD, Figure 4-31 shows the probability of getting better than 10 cm

accuracy, and Figure 4-32 shows the probability of getting an AFV larger than 0.9 of the applied four solutions over different baseline lengths for the nine tested days.

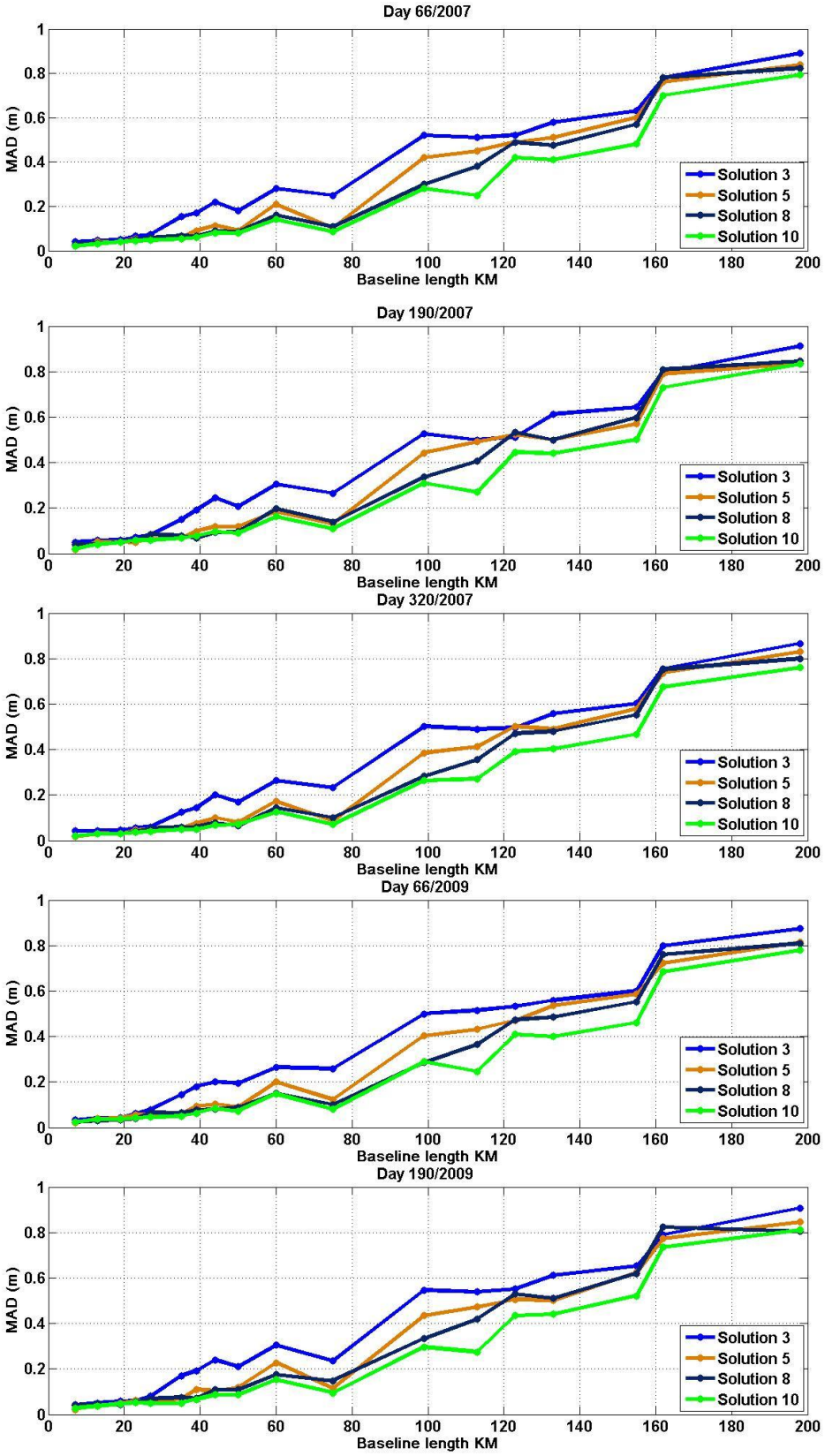

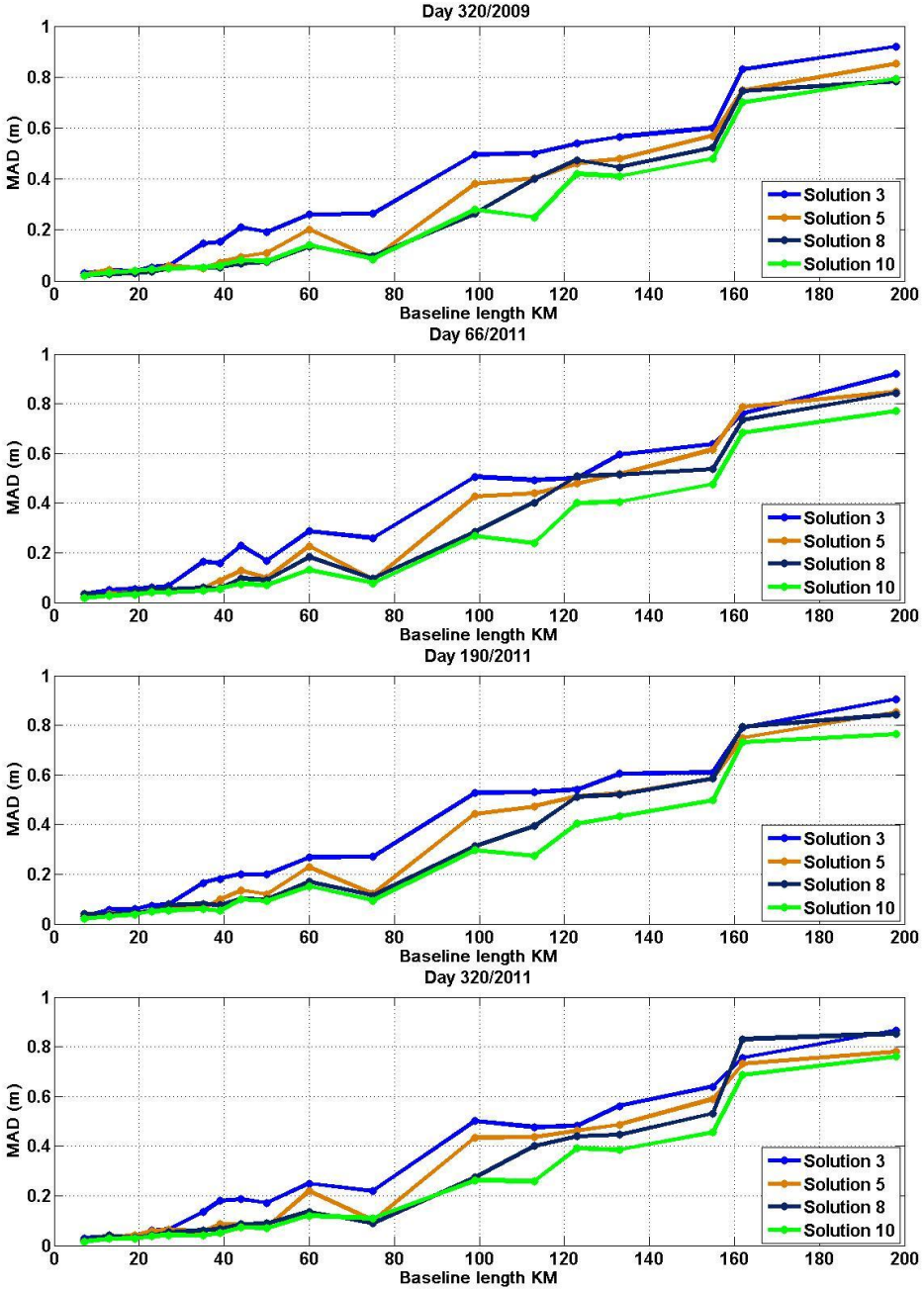

Figure 4-30 The applied four solution, GASP software final positions MAD over the nine tested days

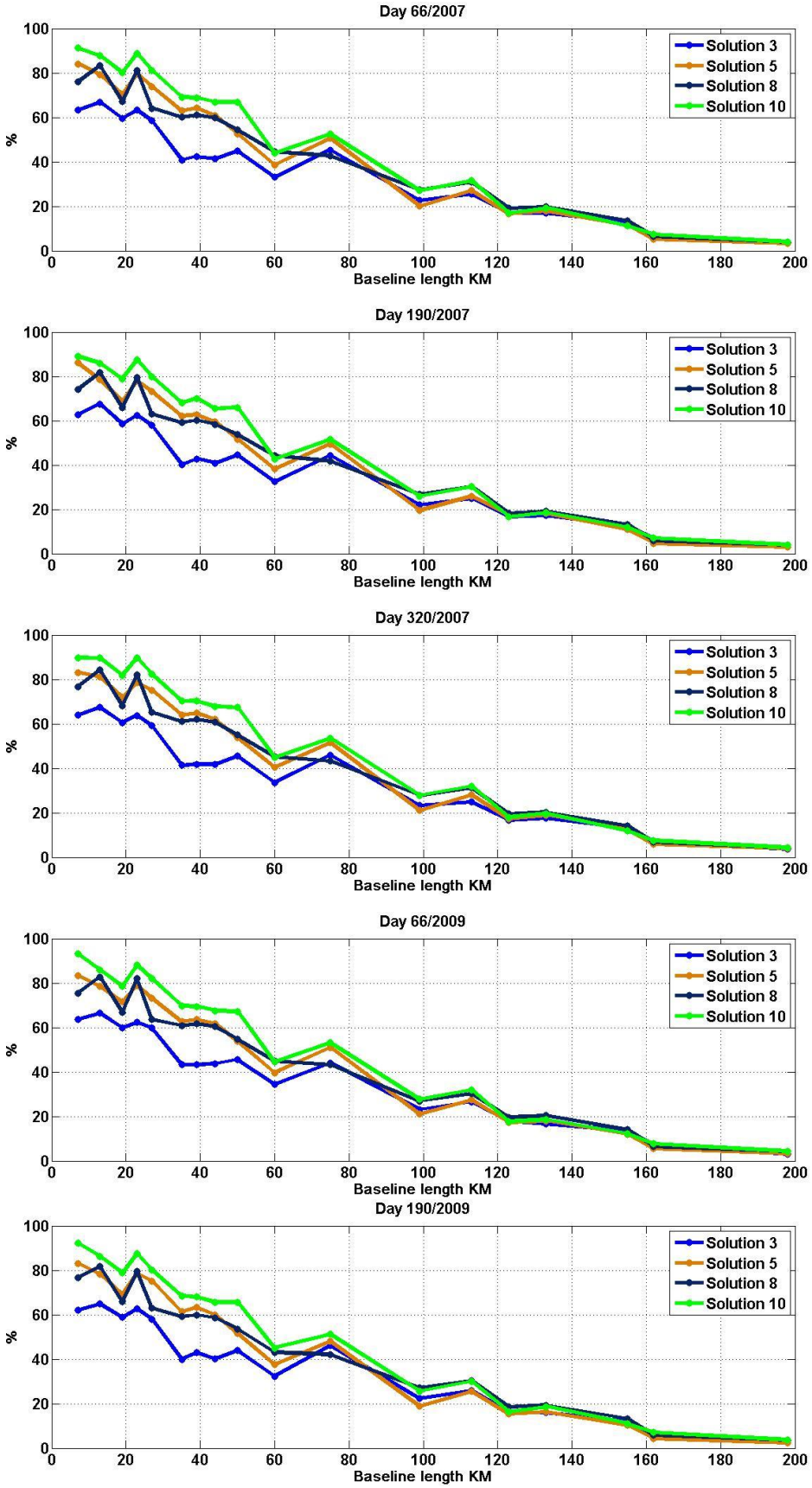
Day 66/2007
Day 190/2007
Day 320/2007
Day 66/2009
Day 190/2009
Solution 3
Solution 5
Solution 8
Solution 10
%
Baseline length KM
0
20
40
60
80
100
120
140
160
180
200

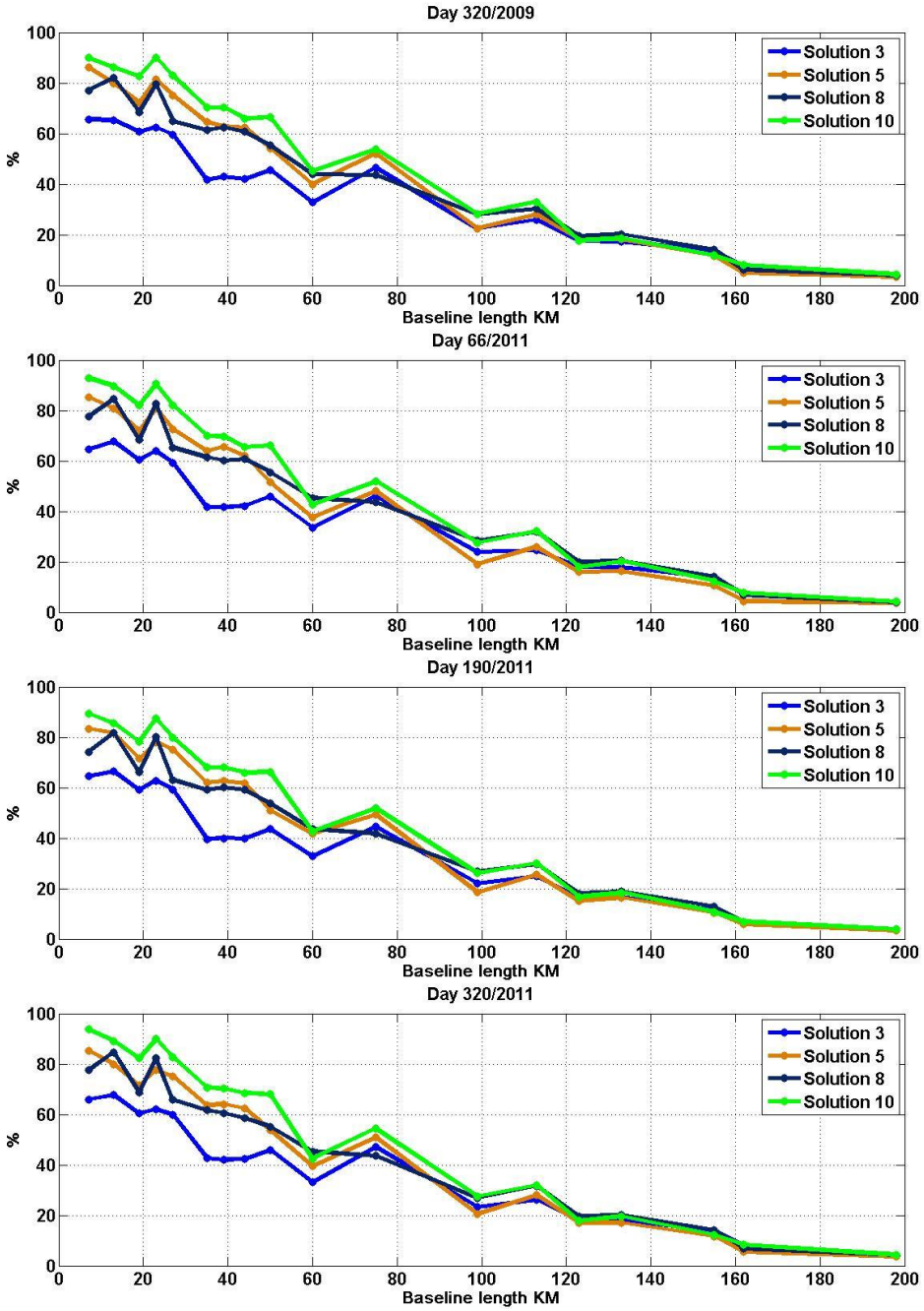

Figure 4-31 The applied four solutions, epochs that give better than 10 cm position accuracy over the nine tested days

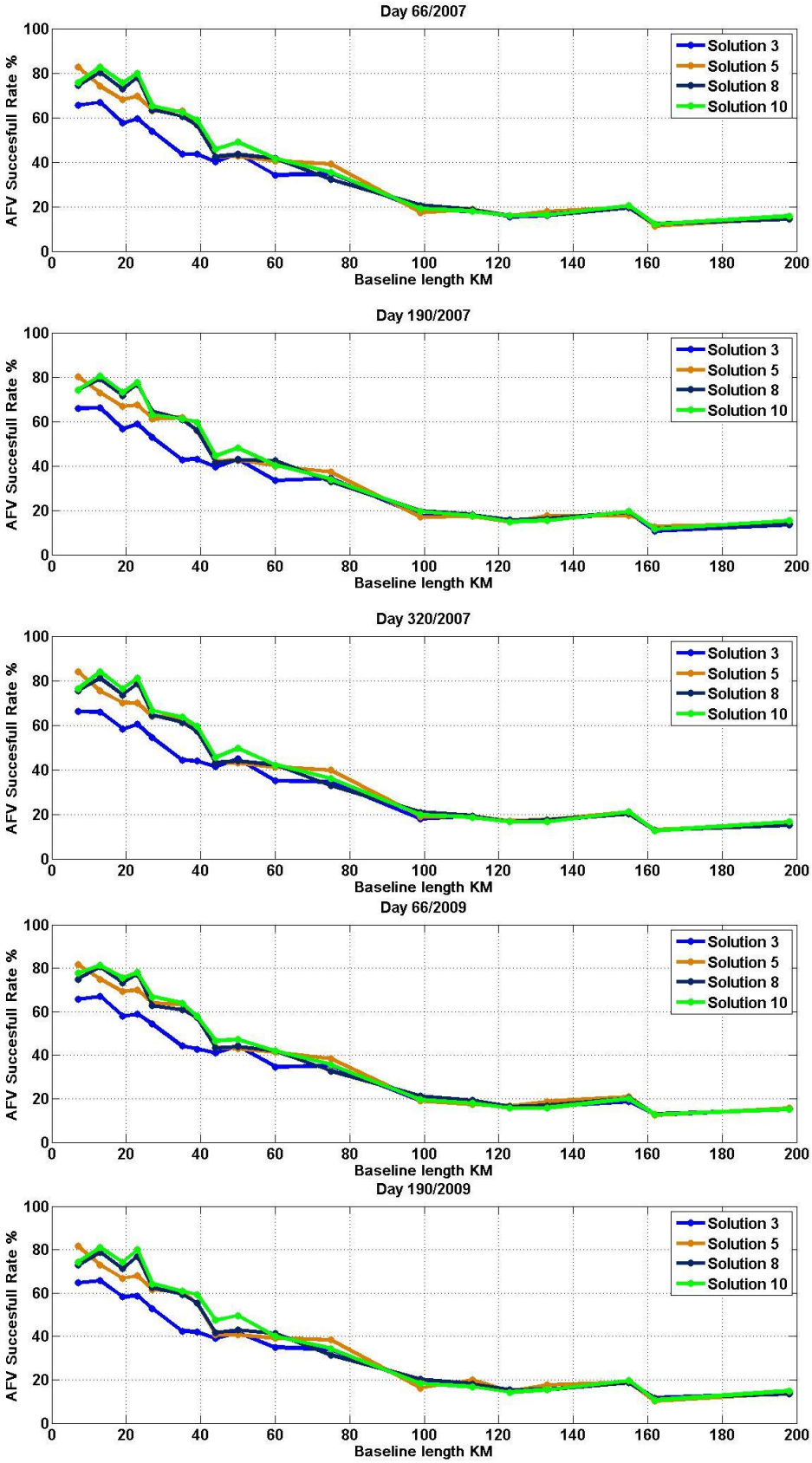
Day 66/2007
Day 190/2007
Day 320/2007
Day 66/2009
Day 190/2009
AFV Succesfull Rate %
Baseline length KM
Solution 3
Solution 5
Solution 8
Solution 10
0
20
40
60
80
100
120
140
160
180
200

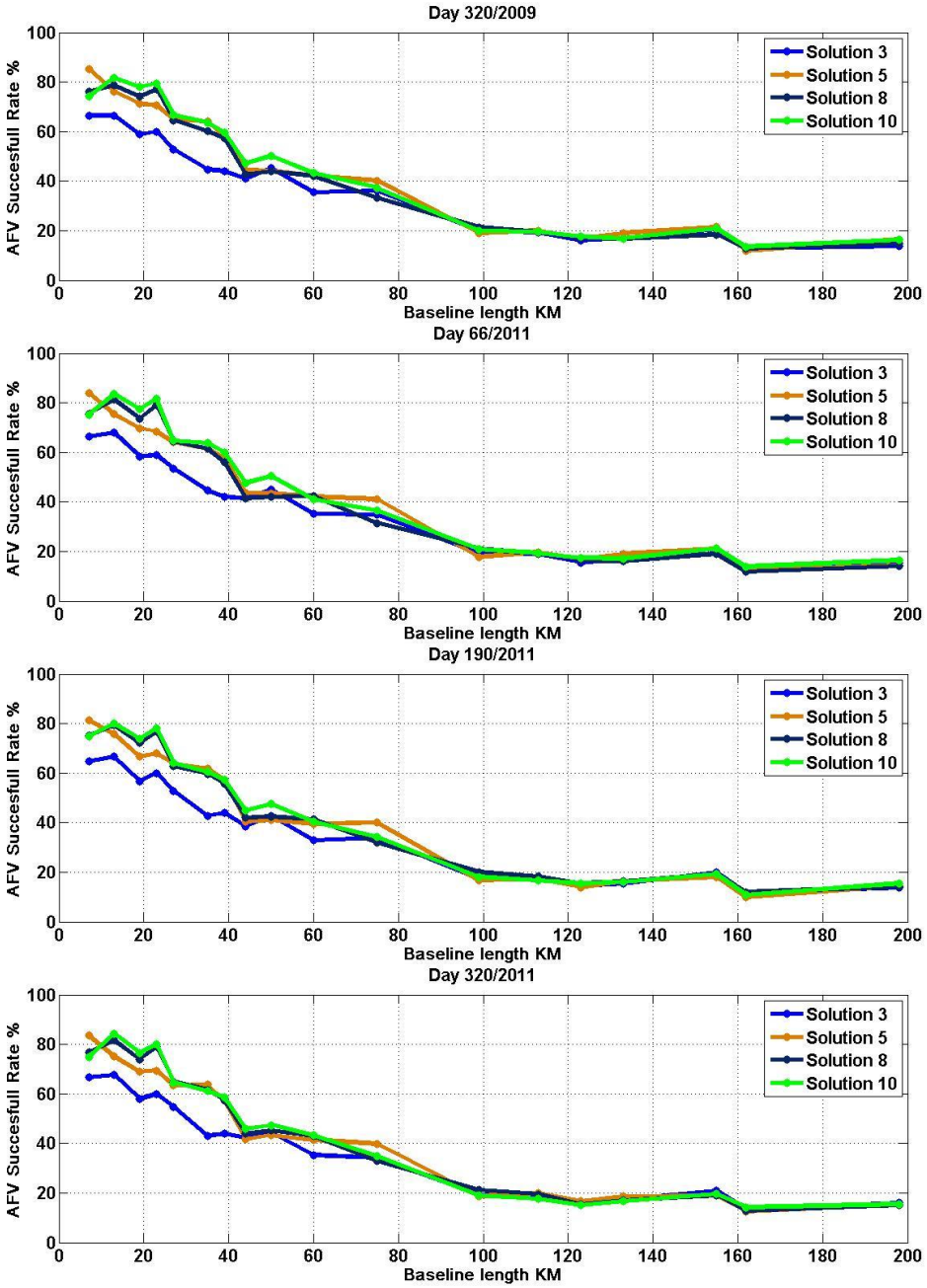

Figure 4-32 The applied four solutions, daily AFV successful rates for different baseline lengths over the nine tested days

Applying the sidereal filter to the regional filter results gives the best single epoch positioning results accuracy as shown in Figure 4-30, Figure 4-31 and Figure 4-32. However, it has a few drawbacks as it is only available in the case of a stationary or near-stationary receiver; where the GPS data and errors effects have daily sidereal patterns. It also requires the availability of the station data for a mean sidereal day before the processing epochs.

Using the regional filter or Code-SPP solution results in the GASP software ambiguity function gives better results than using the Code-DD solution. The final GASP positioning results with a regional filter are approximately the same as those with the Code-SPP solution, but solving the fixed station data in the regional filter, will reduce the speed of the software data processing. Also, the possibility of getting corrupted GPS pseudorange data or losing it is higher in the regional filter than in the Code-SPP. Moreover, Figure 4-24 shows that the results when using one station data in the Code-SPP solution have less noise than using two stations in the regional filter solution. Considering the software data processing speed and the data availability, the Code-SPP together with the implementation of the IGS 2D ionospheric model solution (solution 5) will be used, but after treating its results with the Kalman filter to reduce the noise level of its estimated values. Figure 4-33 shows a flowchart of GASP software with the new adopted steps (in red frames).

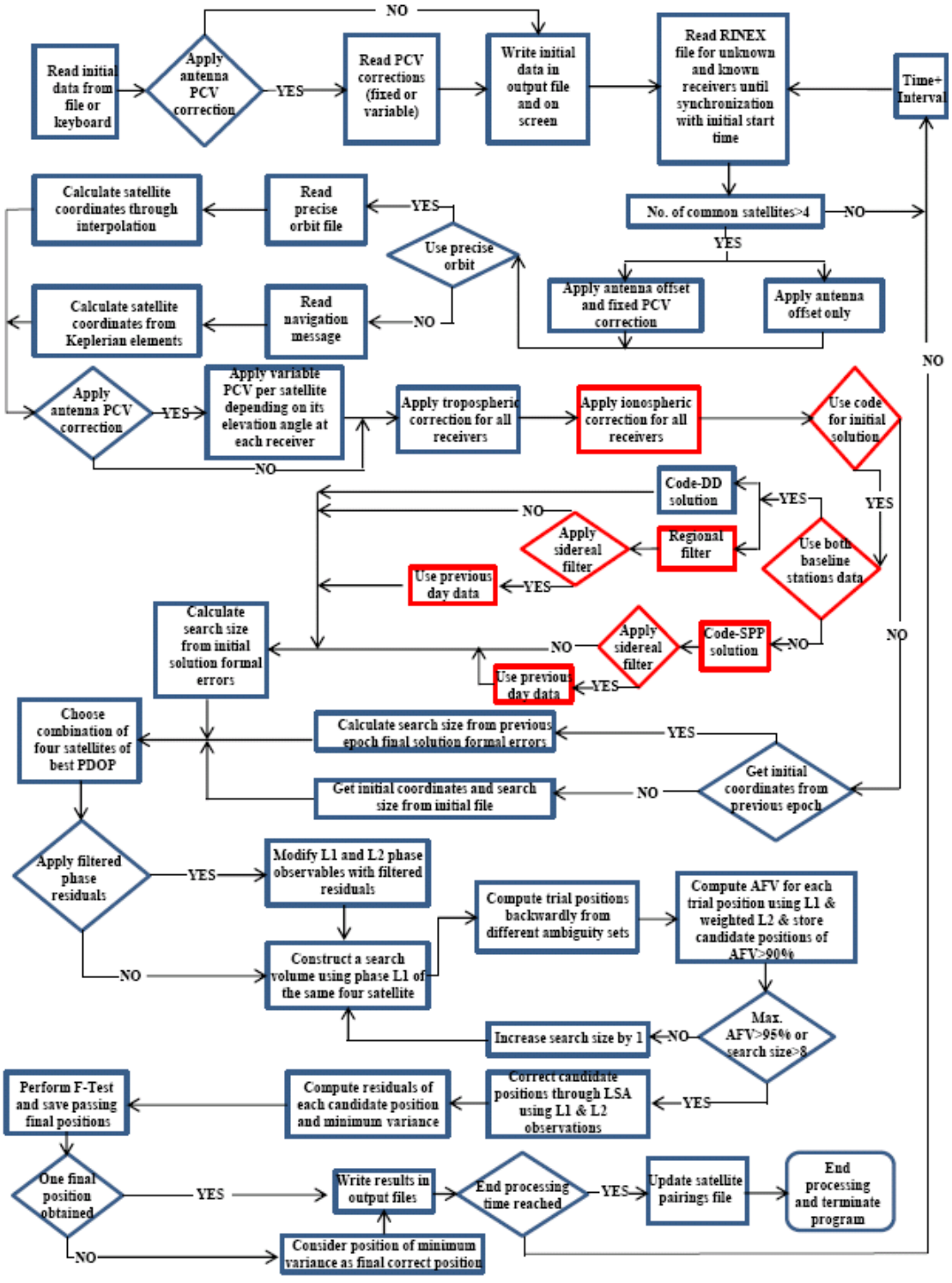

Figure 4-33 GASP software flowchart

APPLYING KALMAN FILTERING TO THE AMBIGUITY FUNCTIONINPUTS AND σ_0 FILTERING TO ITS OUTPUTS

5.1 INTRODUCTION

The GPS code observations are more noisy than the phase observations at each epoch (Tiberius and Kenselaar, 2003), which makes their results less precise than those obtained by the phase observations. In Chapter 4 it was concluded that using the local code-based zenith ionospheric delay model to correct the phase observations improves the precision of the GASP ambiguity function positioning. However, this improvement is affected by the noise on the ionospheric delay model as the latter is one of the results of solving the GPS code observation equations. The ionosphere is not expected to change rapidly from epoch to epoch (Enge and Misra, 1999); therefore it is possible to smooth the code-based ionospheric delay model values by combining the code observation results over time. A good way to combine data over time is to employ a Kalman filter. This filter has been employed to improve the estimation of the code-based zenith ionospheric model, and to improve the smoothing of its values over time. The unknown parameters will be the smoothed receiver

position, receiver clock and code-based zenith ionospheric delay at each epoch, and the observations will be the unsmoothed single-epoch Code-SPP solution results (receiver position, receiver clock, and local zenith ionospheric delay correction).

The Kalman filter is essentially a set of mathematical equations that provides an efficient estimation of a dynamic system state from a series of noisy measurements (Maybeck, 1979; Kalman and Bucy, 1961; Kalman, 1960). It employs a dynamic model to predict the state and an observation model to correct the predicted state. The Kalman filter has found widespread usage in GPS applications, especially as an estimator to the error state vector behaviour over time (e.g. the ionospheric error). Kalman filtering consists of two data-processing stages (Welch and Bishop, 1995) described in the following sections.

5.1.1 Prediction Stage

This stage is responsible for projecting forward (in time) the current state and error covariance estimates to obtain the a priori estimates for the next time state. This stage can be done at the epoch k by applying a dynamic model to the state vector. The dynamic model is usually represented by a transition matrix M_k. This matrix describes how the state vector behaves over time; therefore it is made up of a set of differential equations. In the case of a linear dynamic system with equal time steps (this research study case), the M_k becomes a constant matrix. The dynamic model is used in the Kalman filter to predict the state vector and its covariance matrix as follows:

$$\check{x}_{k+1} = M_k \hat{x}_k \tag{5.1}$$

Where

$\check{x}_{k+1}$ is the predicted state vector at the next epoch.

$\hat{x}_k$ is the updated state vector at the last epoch.

$$C_{\check{x}_{k+1}} = M_k C_{\hat{x}_k} M_k^T + Q_k \tag{5.2}$$

Where

$C_{\check{x}_{k+1}}$ is the predicted covariance matrix at the next epoch.

$C_{\hat{x}_k}$ is the updated covariance matrix at the last epoch.

Q_k is the covariance matrix of the process noise (it will be explained in detail shortly).

5.1.2 Updating Stage

In this stage the Kalman filter attempts to optimise the adjustment for the predicted values. The first matrix in this stage is the gain matrix (G_k). The purpose of the gain matrix is to scale the innovations (the difference between the current measurements and their predicted values). It can be computed at the epoch k as follows:

$$G_k = C_{\check{x}_k} A_k^T \left[A_k C_{\check{x}_k} A_k^T + R_k\right]^{-1} \tag{5.3}$$

Where:

A_k is the design matrix of partial derivatives, which describes the linearised relationship between the measurements and state vector at epoch k.

R_k is the covariance matrix of the measurement noise.

Then the Kalman gain matrix (G_k) is used to update the state of the estimation and the covariance matrix of the state as follows:

$$\begin{aligned} \hat{x}_k &= \check{x}_k + G_k \check{v}_k \\ C_{\hat{x}_k} &= [\, I - G_k A_k] C_{\check{x}_k} \end{aligned} \tag{5.4}$$

Where:

$\check{v}_k$ is the measurement innovation, or the residual.

$$\check{v}_k = [\, z_k - A_k \check{x}_k] \tag{5.5}$$

z_k is the measurement vector at time k.

5.2 KALMAN FILTER PARAMETERS

The following parameters have been used to apply the Kalman filter into the Code-SPP solution results:

5.2.1 The Measurements:

The measurements input to the filter are:

$$z_k = \begin{bmatrix} X \\ Y \\ Z \\ \mathrm{I}_r \\ dT \end{bmatrix}$$

Where X, Y, Z, I_r and dT are the Code-SPP solution results with the implementation of the IGS ionospheric model (see section 4.3).

5.2.2 Kalman Vectors and Matrices

Observation variance-covariance matrix (R_k):

The measurement noise covariance matrix for the Kalman filter is:

$$R_k = VCM = \begin{bmatrix} \sigma_X^2 & \sigma_{XY} & \sigma_{XZ} & \sigma_{XI_r} & \sigma_{XdT} \\ \sigma_{XY} & \sigma_Y^2 & \sigma_{YZ} & \sigma_{YI_r} & \sigma_{YdT} \\ \sigma_{XZ} & \sigma_{YZ} & \sigma_Z^2 & \sigma_{ZI_r} & \sigma_{ZdT} \\ \sigma_{XI_r} & \sigma_{YI_r} & \sigma_{ZI_r} & \sigma_{I_r}^2 & \sigma_{I_r dT} \\ \sigma_{XdT} & \sigma_{YdT} & \sigma_{ZdT} & \sigma_{I_r dT} & \sigma_{dT}^2 \end{bmatrix}$$

Where VCM is the variance-covariance matrix of the Code-SPP results.

Kalman state vector (x):

The state vector of the Kalman filter used in this project is:

$$x_k = \begin{bmatrix} X \\ \mathrm{Y} \\ Z \\ \mathrm{I}_r \\ dT \\ V_x \\ V_y \\ V_z \end{bmatrix}$$

Where:

$X, Y\ and\ Z$ are the station coordinates in metres.

dT is the receiver clock offset in metres.

$\mathrm{I_r}$ is the ionospheric delay at the receiver zenith point (additional to the IGS model delay).

$\mathrm{V_x}, \mathrm{V_y}$ and $\mathrm{V_z}$ are the station velocities in metres/second.

Kalman transition matrix

The transition matrix of the Kalman filter for this linear dynamic case is:

$$M_k = \begin{bmatrix} 1 & 0 & 0 & 0 & 0 & \Delta t & 0 & 0 \\ 0 & 1 & 0 & 0 & 0 & 0 & \Delta t & 0 \\ 0 & 0 & 1 & 0 & 0 & 0 & 0 & \Delta t \\ 0 & 0 & 0 & 1 & 0 & 0 & 0 & 0 \\ 0 & 0 & 0 & 0 & 1 & 0 & 0 & 0 \\ 0 & 0 & 0 & 0 & 0 & 1 & 0 & 0 \\ 0 & 0 & 0 & 0 & 0 & 0 & 1 & 0 \\ 0 & 0 & 0 & 0 & 0 & 0 & 0 & 1 \end{bmatrix}$$

Where Δt is the difference in time between the current and previous epoch.

Design matrix (A):

The Kalman filter design matrix according to the state vector and measurements is:

$$A_k = \begin{bmatrix} 1 & 0 & 0 & 0 & 0 & 0 & 0 & 0 \\ 0 & 1 & 0 & 0 & 0 & 0 & 0 & 0 \\ 0 & 0 & 1 & 0 & 0 & 0 & 0 & 0 \\ 0 & 0 & 0 & 1 & 0 & 0 & 0 & 0 \\ 0 & 0 & 0 & 0 & 1 & 0 & 0 & 0 \end{bmatrix}$$

Covariance matrix of the system noise (Q_k):

The covariance matrix of the system noise (also known as plant noise or process noise) is used in the Kalman filter to account for un-modelled variance of each of the state vector parameters (the station coordinates and their velocities, the ionospheric delay, and the receiver clock offset) (Kaplan and Hegarty, 2006). To determine the most suitable process noise a set of trials was undertaken on the day 66/2007 results. In performing these trials the targeted values gave the clock and position values freedom of change from epoch to epoch, whilst attempting to reduce the noise in the code-based ionospheric delay model. This is because the ionospheric value is relatively stable over time, while for a kinematic receiver the position and the clock could vary from epoch to epoch. However, for civil engineering applications, the receiver acceleration will not be a large value (e.g. the magnitude of the 19th floor dynamic acceleration was about 0.2g during the San Francisco earthquake on 9th of February 1971 (Foutch *et al.*, 1975)). The applied process noise matrix according to the inputs and targeted results looks like:

$$Q_k = \begin{bmatrix} Q_X^2 & 0 & 0 & 0 & 0 & 0 & 0 & 0 \\ 0 & Q_Y^2 & 0 & 0 & 0 & 0 & 0 & 0 \\ 0 & 0 & Q_Z^2 & 0 & 0 & 0 & 0 & 0 \\ 0 & 0 & 0 & Q_{I_r}^2 & 0 & 0 & 0 & 0 \\ 0 & 0 & 0 & 0 & Q_{dT}^2 & 0 & 0 & 0 \\ 0 & 0 & 0 & 0 & 0 & Q_{V_X}^2 & 0 & 0 \\ 0 & 0 & 0 & 0 & 0 & 0 & Q_{V_Y}^2 & 0 \\ 0 & 0 & 0 & 0 & 0 & 0 & 0 & Q_{V_Z}^2 \end{bmatrix}$$

Different process noise matrices have been studied to find out the best process noise values for our case study. Some of the tested matrices are:

	Q_X^2, Q_Y^2 and Q_Z^2 (m^2)	$Q_{I_r}^2$ (m^2)	Q_{dT}^2 (m^2)
Set1	0.01	1	0.1
Set2	0.1	0.1	1
Set3	1	0.01	10
Set4	1	0.001	100

Table 5-1 Tested process noise matrices

For each set, the process noises of the station velocities are set to be equal to the coordinate process noises (but with a m^2/s unit):

$$Q_{V_x} = Q_{V_y} = Q_{V_z} = \ Q_x = Q_Y = Q_z$$

The Kalman filter has been applied for all the studied network stations. The IGS GOLD station results are used to show the effect of the application of the Kalman filter in this thesis, as its results are typically representative of the studied network station results. For each process noise set, the standard deviations of individual 30-minute windows of 30 second processed data for each of the Code-SPP results have been plotted in Figure 5-1. The standard deviations for each 30 minute window of the unfiltered Code-SPP results have been also plotted in Figure 5-1 to make a comparison between the filtered and non filtered results.

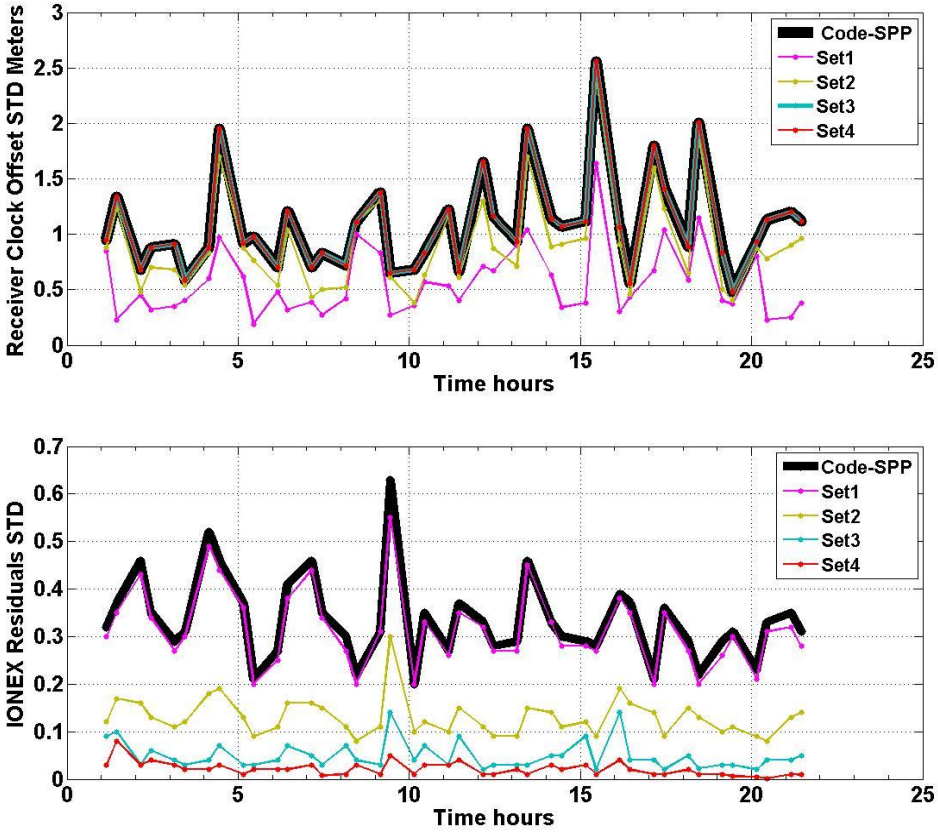

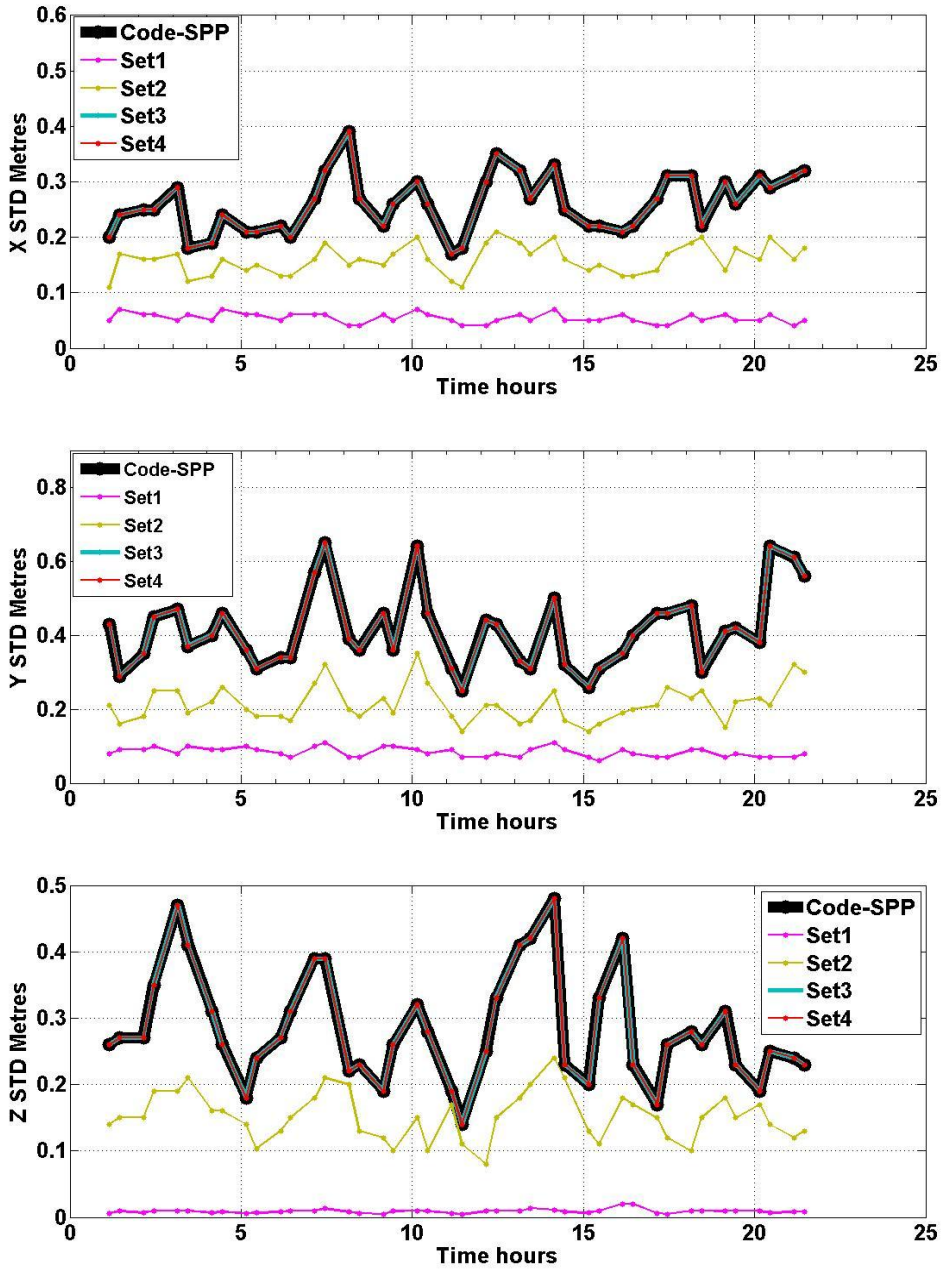

Figure 5-1 IGS GOLD station, Standard deviations for every 30 minutes results of the unfiltered Code-SPP and the Kalman filter with the implementation of different process noise sets

Figure 5-1 shows that sets 1 and 2 of the process noise restrict the receiver position and clock offset, while sets 3 and 4 allow them to change freely. Applying set 1 of the process noise has very little effect on the ionospheric model, and this effect increases when the ionospheric process noise value becomes less in sets 2, 3 and 4. Employing set 4 eliminates most of the noise and the mean value of the standard deviations of the filtered Code-SPP ionospheric results becomes 0.015 m. In turn, this complies with

the fact that the ionosphere changes slowly over time unless unusual phenomena happen to the environment. As a result, the set 4 process noise matrix in Table 5-1 has been approved to be used in filtering the results. Figure 5-2 shows the effect of applying this process noise set into the IGS GOLD station Code-SPP results.

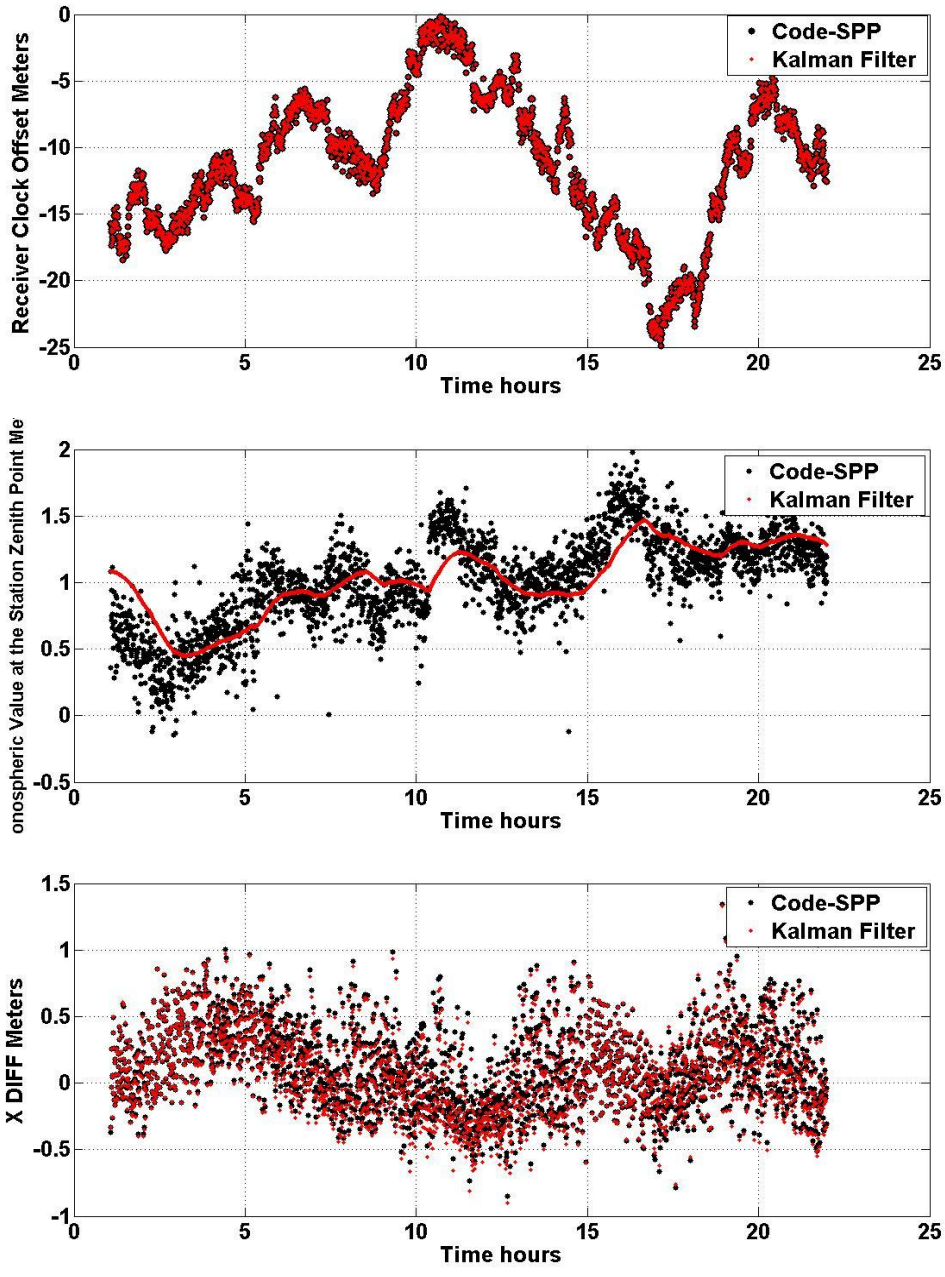

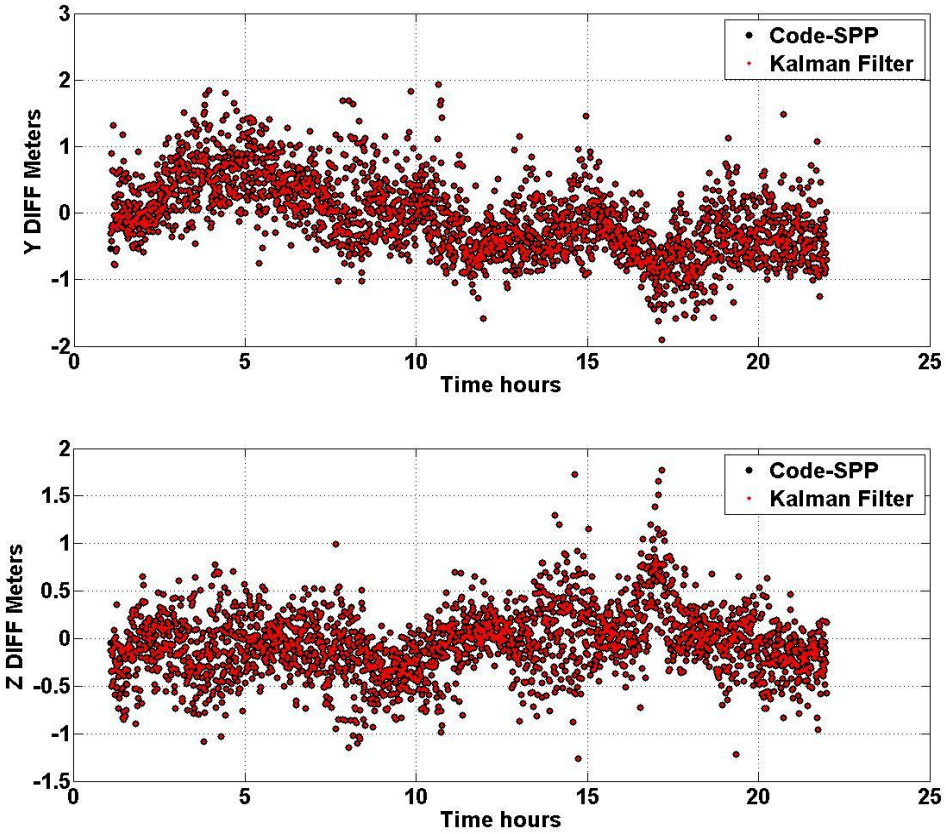

Figure 5-2 IGS GOLD station, Code-SPP solution and Kalman filter (with set4 process noise) results

The Kalman filter will be applied to the Code-SPP results of the moving receivers in Table 4-1 in order to investigate the effect of smoothing the code-based zenith ionospheric model on the final GASP positioning results.

5.3 THE KALMAN FILTER RESULTS

The positioning results of the Kalman filter have been used as the moving receiver initial position coordinates in the GASP software ambiguity function. Its ionospheric values have been used to correct the GPS phase measurements before using them in the ambiguity function. Figure 5-3, Figure 5-4 and Figure 5-5 show the effect of applying the Kalman filter model into the Code-SPP solution on the GASP software final results.

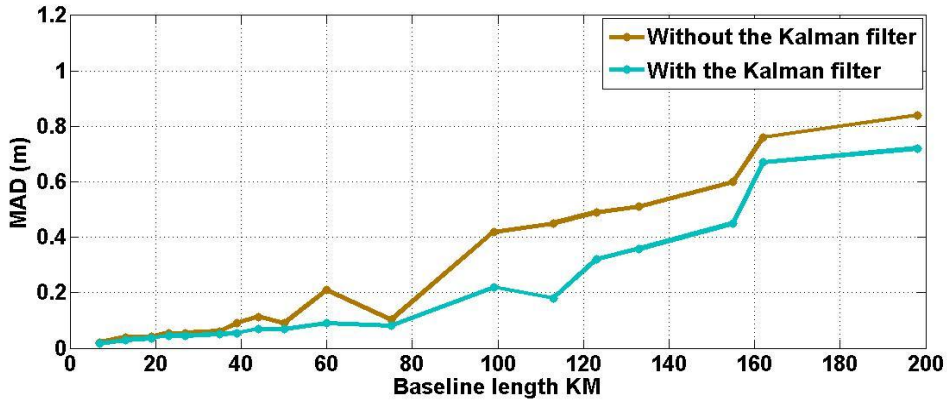

Figure 5-3 GASP software positioning MAD for different baseline lengths when the Code-SPP and Kalman filter results are used as used as moving station positioning inputs and ionospheric correction in the software ambiguity function.

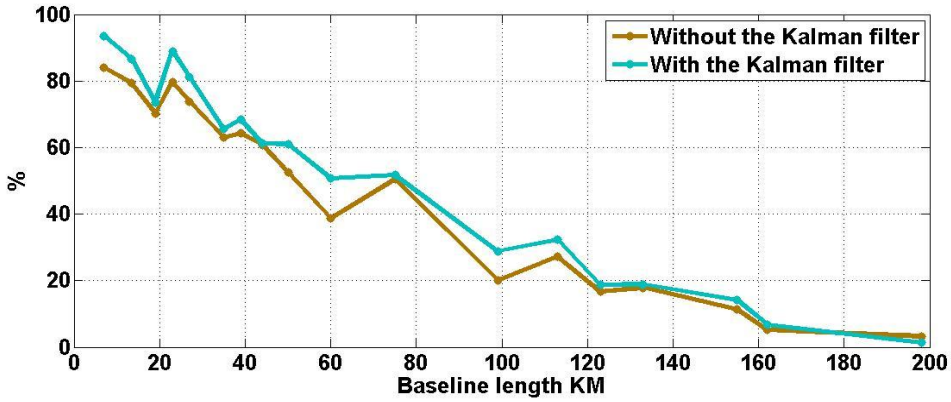

Figure 5-4 Percentage of epochs that give better than 10 cm positioning accuracy for different baseline lengths when the Code-SPP and Kalman filter results are used as the moving station positioning inputs and ionospheric correction in the GASP software ambiguity function.

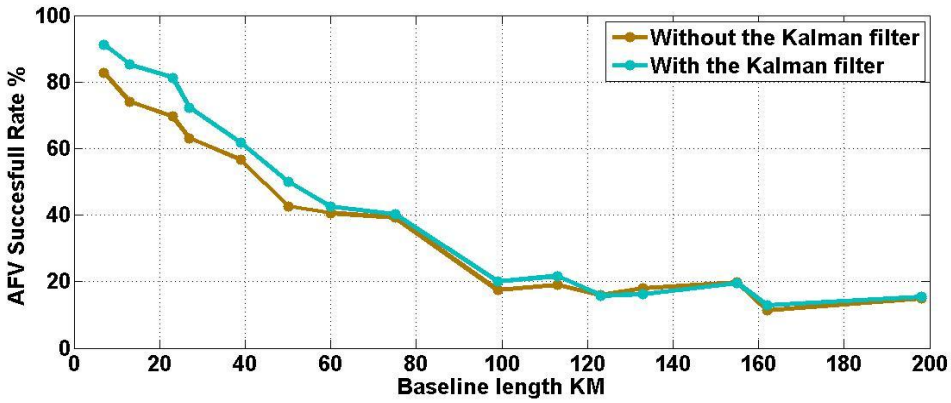

Figure 5-5 Daily AFV success rates for different baseline lengths when the Code-SPP and Kalman filter results are used as the moving station positioning inputs and ionospheric correction in the GASP software ambiguity function.

Figure 5-3, Figure 5-4 and Figure 5-5 show that by applying the Kalman filter the results are improved, and this improvement is baseline length dependent because the longer the baseline, the fewer shared satellites are observed from its stations. Therefore the baseline lengths longer than 100 km have been ignored in the following sections. In the following section a filter will be applied to the results to eliminate a maximal amount of bad results and try to keep a maximal amount of good results.

5.4 FILTERING THE GASP SOFTWARE POSITIONING RESULTS

The GASP software applies the F-test on all of the candidate positions that pass the Ambiguity Function Value (AFV) test (see section 2.7.1 for more details about the AFV test) to obtain the final correct position for each epoch (see section 3.8). Therefore the σ_0 value is considered as a main factor in choosing the final position of the GPS station. This value has been studied to see if it could be used to filter the results and reject some results that have bad accuracy. For each tested baseline, the number of the successful epochs which have less than a specified σ_0 value has been divided by the total number of the baseline successful epochs to create Figure 5-6, and the same has been done for the unsuccessful epochs to create Figure 5-7. The baselines with lengths 7 -99 km in Table 1-1 have been used in this test, and the σ_0 thresholds vary between 0.2 and 14 (the maximum σ_0 value of the tested baseline results is 14). Figure 5-6 and Figure 5-7 show that the proportion of successful epochs tends to increase rapidly at the lower σ_0 values in comparison to the proportion of unsuccessful epochs for each baseline. Therefore a σ_0 threshold can be used to filter out the results to accept only results with high chance of being successful.

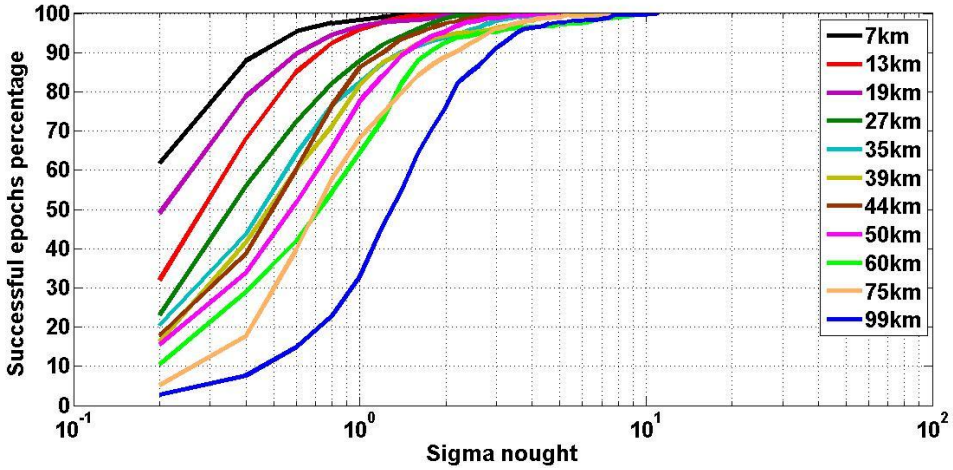

Figure 5-6 The percentage of the succesful epochs (accuracy within 10 cm 3D of the known position, see chapter 4) for which σ_0 is less than or equal to the given value for different baseline lengths

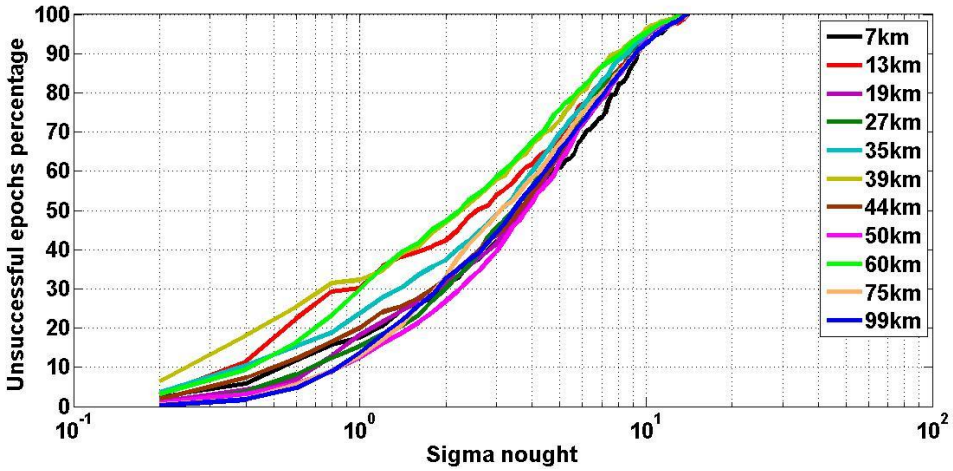

Figure 5-7 The percentage of the unsuccesful epochs (accuracy is not within 10 cm 3D of the known position) for which σ_0 is less than or equal to the given value for different baseline lengths

Figure 5-6 and Figure 5-7 show that the trend of the successful epoch's percentage line is baseline length dependent, therefore the σ_0 threshold should be different for each individual baseline. The relationship between the successful results and σ_0 values has been plotted for each baseline separately in Figure 5-8. Also the σ_0 value that determines 80% of the successful epochs has been plotted to each baseline in the Figure 5-8. (80% has been chosen as the indicative level of performance because using a higher percentage will lead to the rejection of too many epochs).

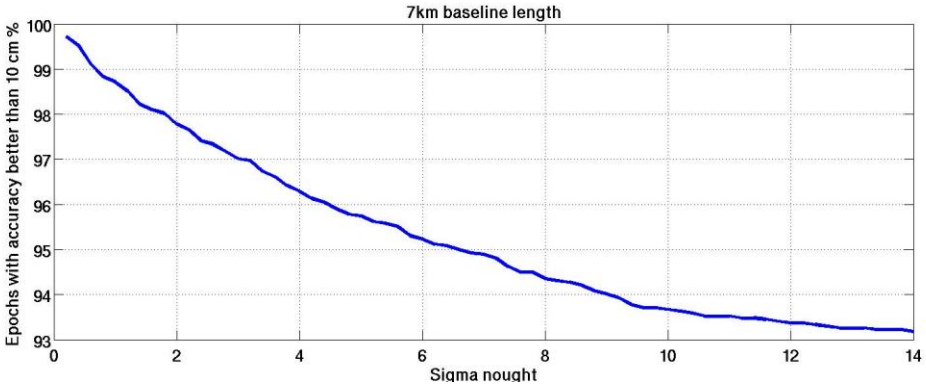
7km baseline length
Epochs with accuracy better than 10 cm %
Sigma nought

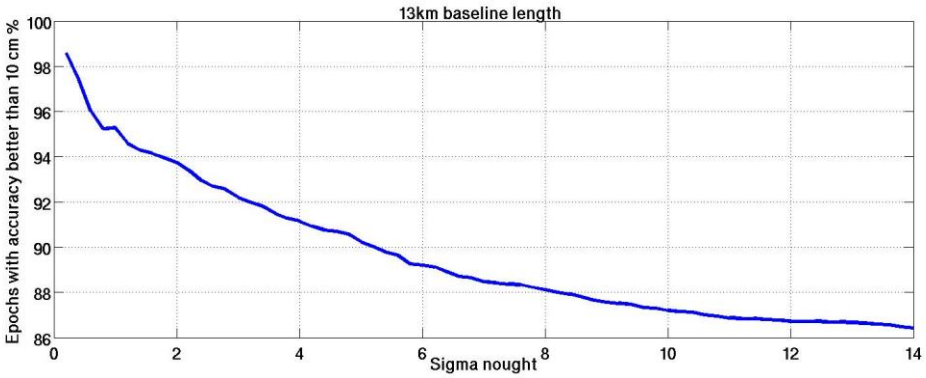
13km baseline length
Epochs with accuracy better than 10 cm %
Sigma nought

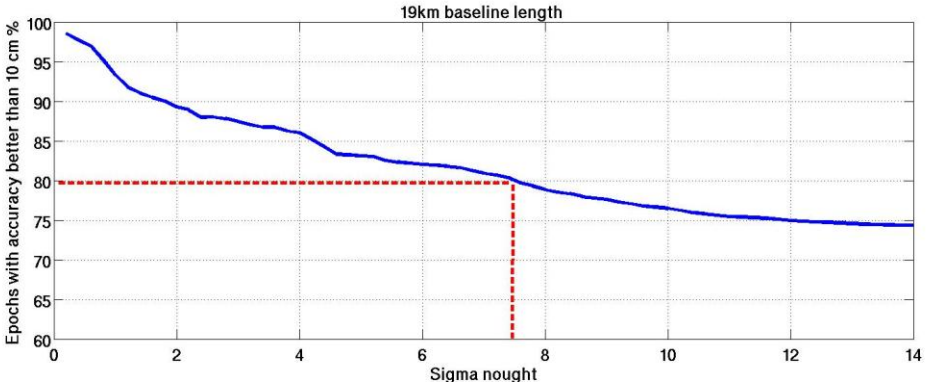
19km baseline length
Epochs with accuracy better than 10 cm %
Sigma nought

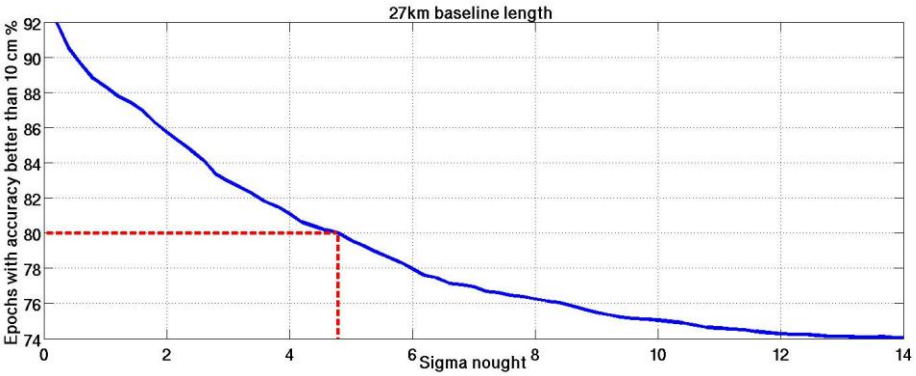
27km baseline length
Epochs with accuracy better than 10 cm %
Sigma nought

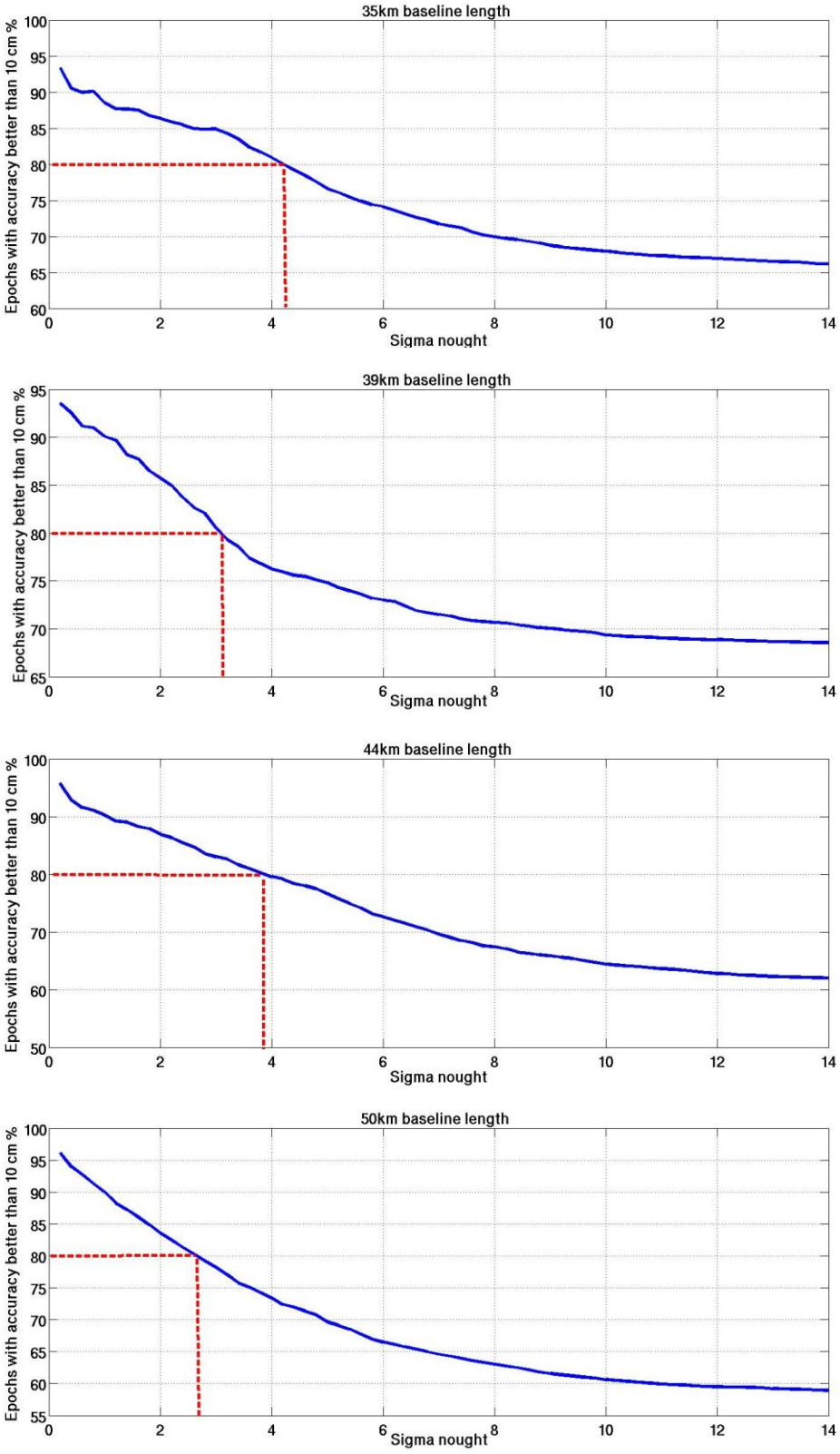
35km baseline length
Epochs with accuracy better than 10 cm %
Sigma nought
39km baseline length
Epochs with accuracy better than 10 cm %
Sigma nought
44km baseline length
Epochs with accuracy better than 10 cm %
Sigma nought
50km baseline length
Epochs with accuracy better than 10 cm %
Sigma nought

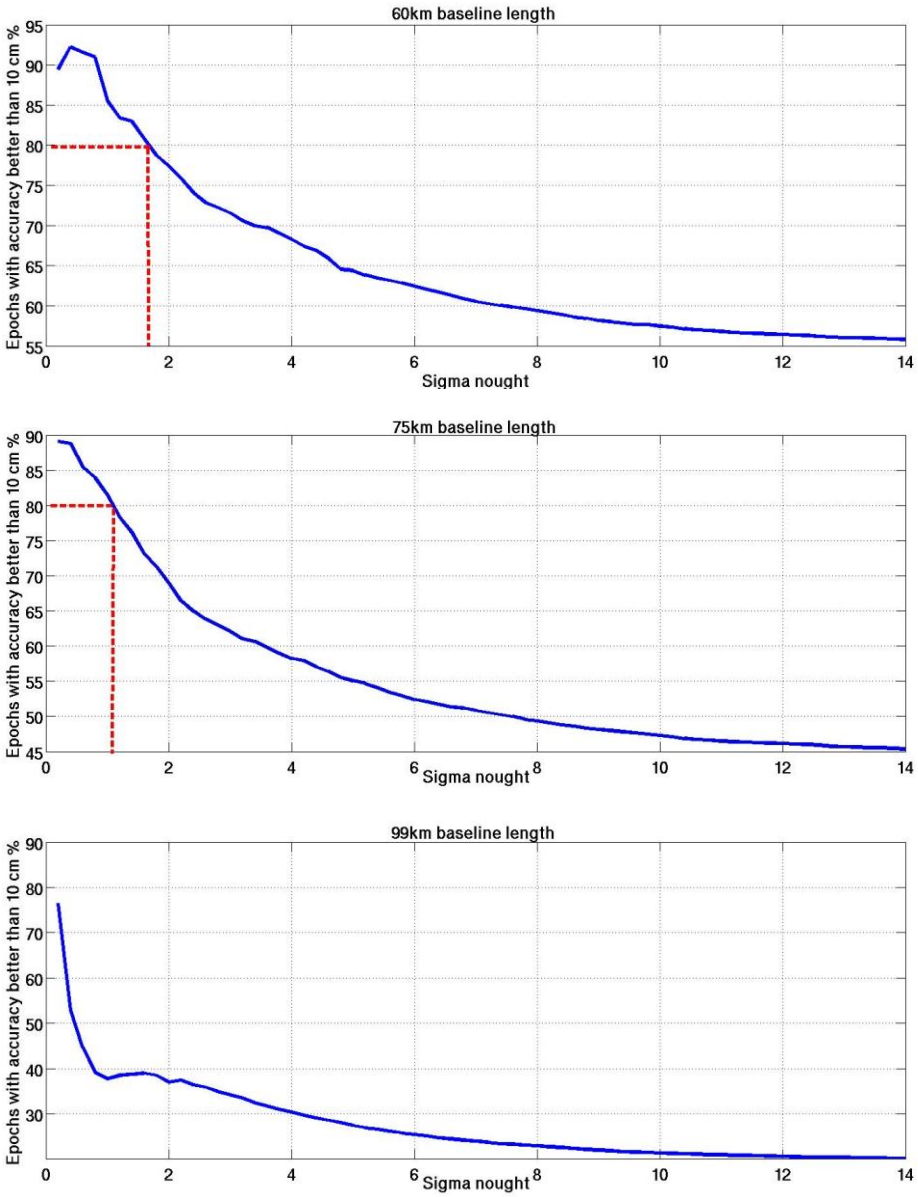

Figure 5-8 The percentage of the succesful epochs for which σ_0 is less than or equal to the given value for each baseline

According to Figure 5-8 a minimum of 80% of the results will pass the 10 cm accuracy test if σ_0 cut-off values in Table 5-2 are applied.

Baseline length	σ_0 threshold
7km	14
13km	14
19km	7.5
27km	4.7
35km	4.3
39km	3.2
44km	3.8
50km	2.7
60km	1.7
75km	1.2
99km	-

Table 5-2 σ_0 threshold values for the tested baselines

Table 5-2 indicates that more than 80% of the successful results for a baseline with less than 13 km length can be achieved at any σ_0 value. It also shows that it is impossible to get 80% of the successful epochs over all of the σ_0 values for the 99 km baseline length. The σ_0 threshold values in Table 5-2 for the baseline lengths 19 – 75 km have been plotted in Figure 5-9. To ensure that at least 80% of the successful results are obtained, a best fitting line equation to the lower bound (envelope) of the σ_0 cut-off values is sought.

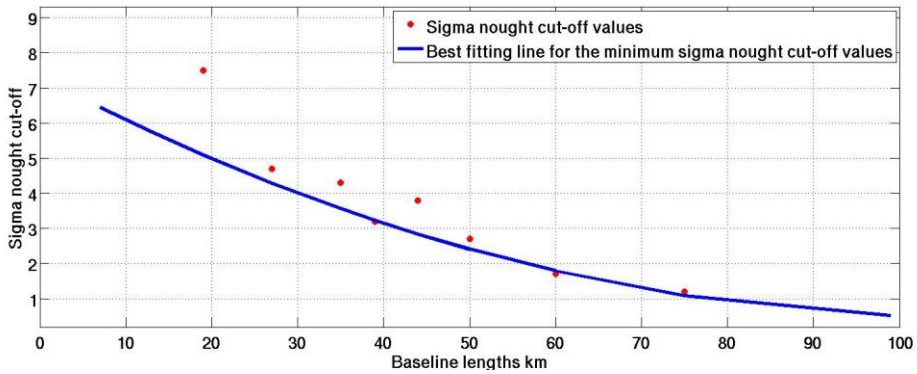

Figure 5-9 σ_0 cut-off values according to the baselines and the best fitting envelope

The equation of the best fit the line for the lower points envelope in Figure 5-9 is:

$$y = 0.0006x^2 - 0.127x + 7.15 \tag{5.6}$$

Where,

x is the baseline length in km.

y is the σ_0 threshold value.

The best fitting line equation has been applied to the tested baselines to find the σ_0 threshold for each one of them. To study the effect of applying this filter, the successful, unsuccessful and all epochs (successful + unsuccessful) percentages according to the σ_0 threshold have been plotted in Figure 5-10.

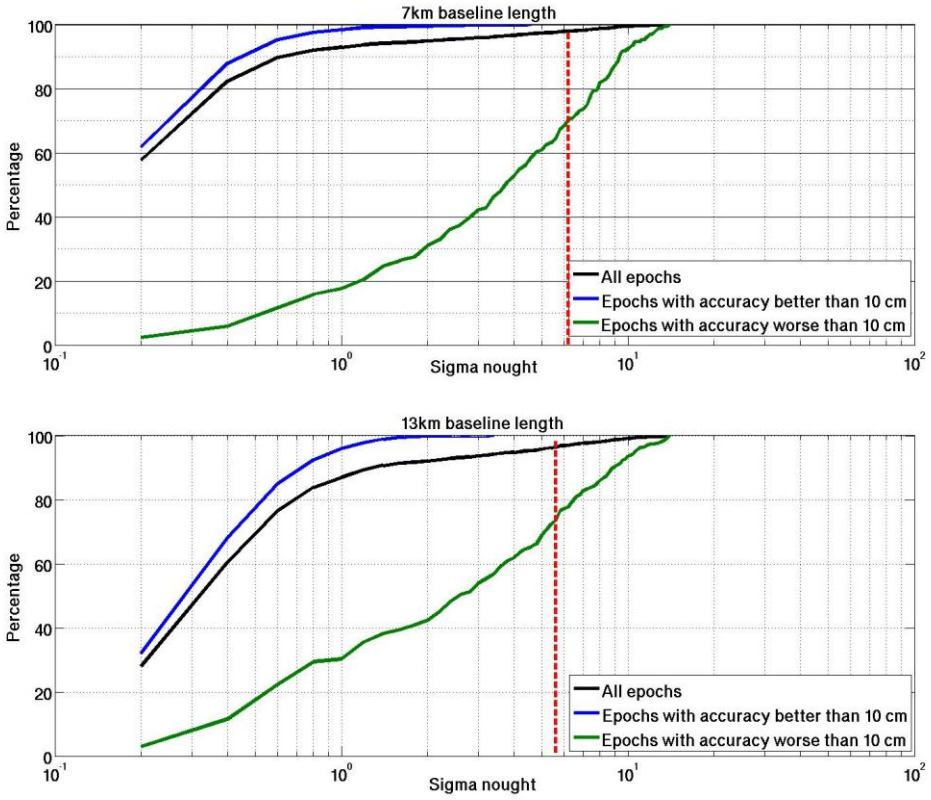

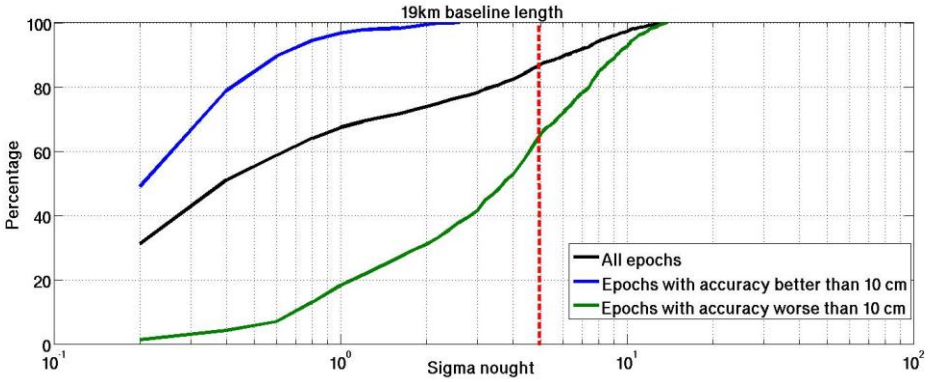
19km baseline length
Percentage
Sigma nought
All epochs
Epochs with accuracy better than 10 cm
Epochs with accuracy worse than 10 cm

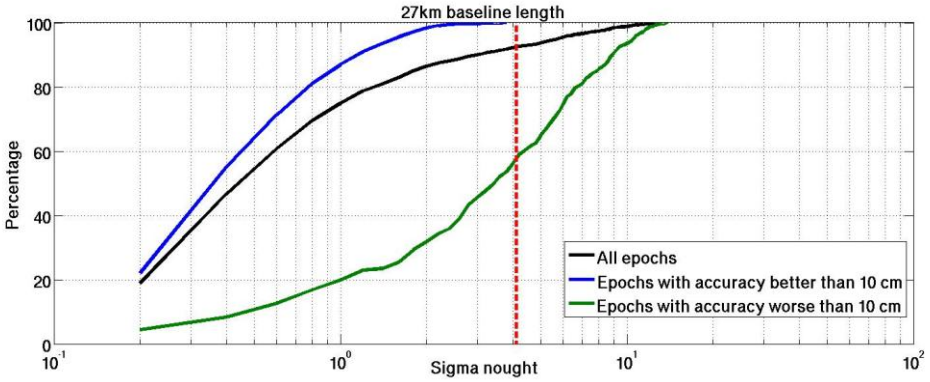
27km baseline length
Percentage
Sigma nought
All epochs
Epochs with accuracy better than 10 cm
Epochs with accuracy worse than 10 cm

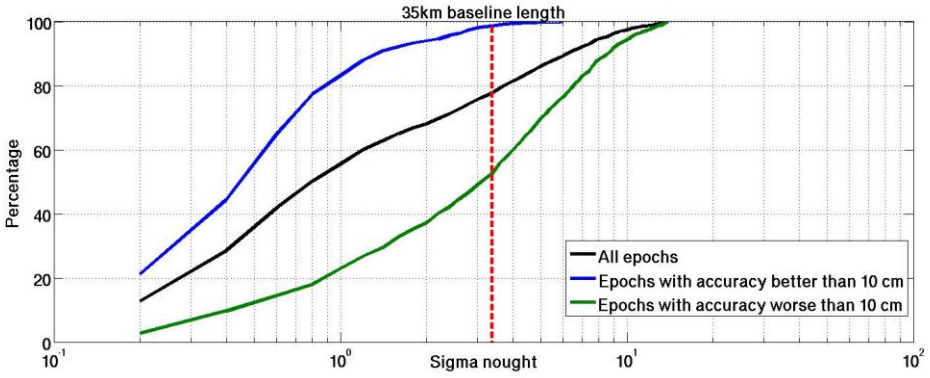
35km baseline length
Percentage
Sigma nought
All epochs
Epochs with accuracy better than 10 cm
Epochs with accuracy worse than 10 cm

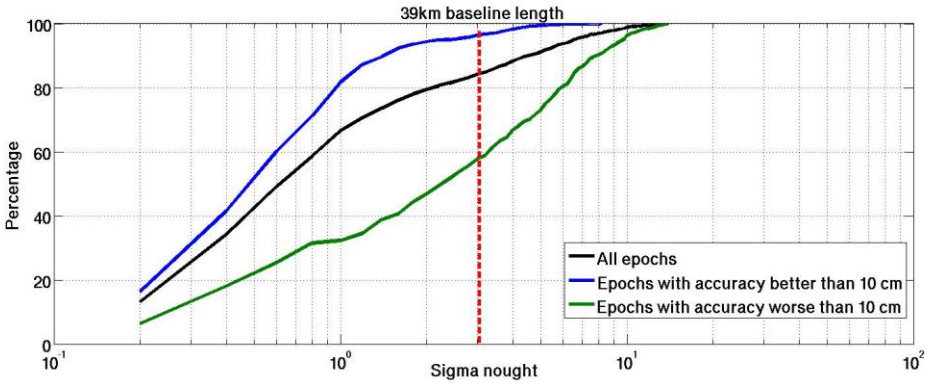
39km baseline length
Percentage
Sigma nought
All epochs
Epochs with accuracy better than 10 cm
Epochs with accuracy worse than 10 cm

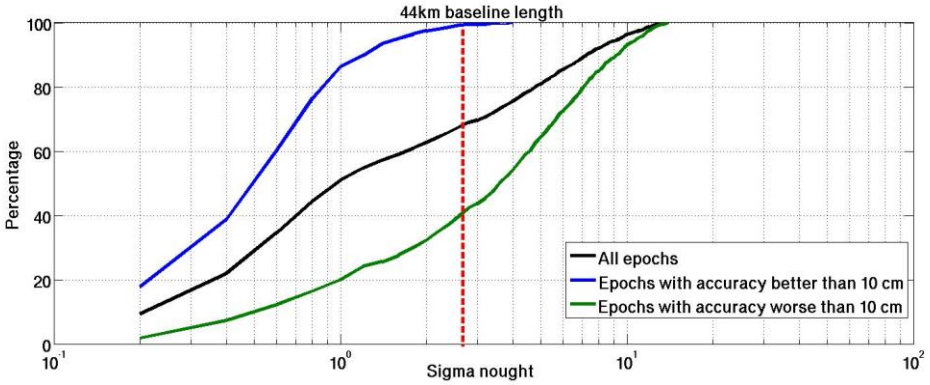
44km baseline length
Percentage
Sigma nought
All epochs
Epochs with accuracy better than 10 cm
Epochs with accuracy worse than 10 cm

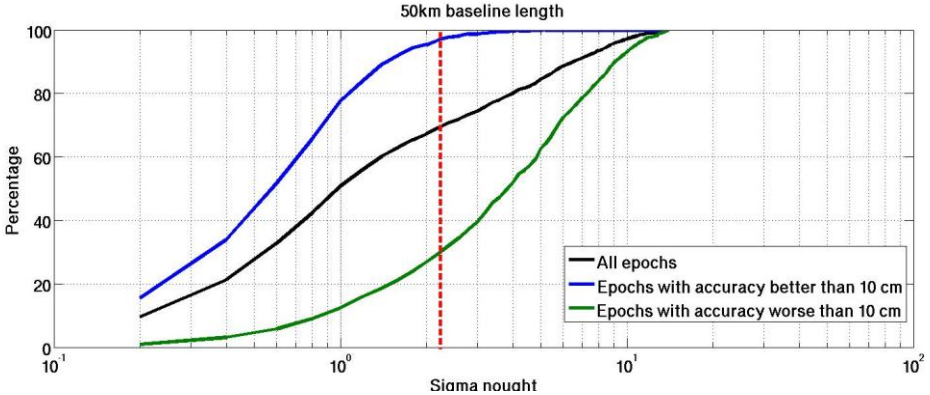
50km baseline length
Percentage
Sigma nought
All epochs
Epochs with accuracy better than 10 cm
Epochs with accuracy worse than 10 cm

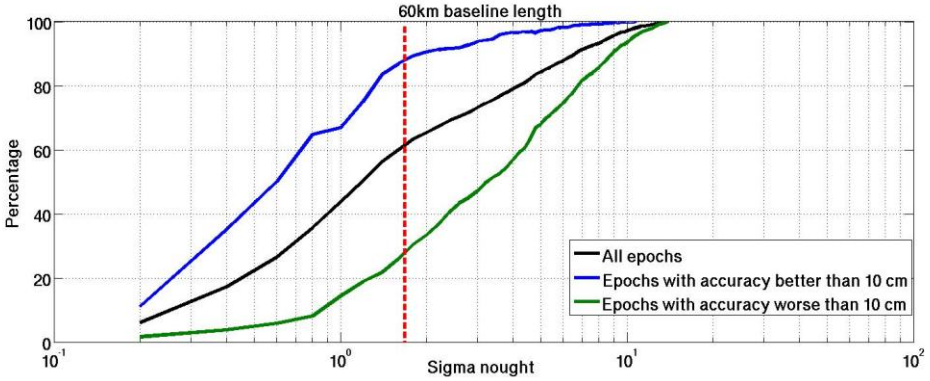
60km baseline length
Percentage
Sigma nought
All epochs
Epochs with accuracy better than 10 cm
Epochs with accuracy worse than 10 cm

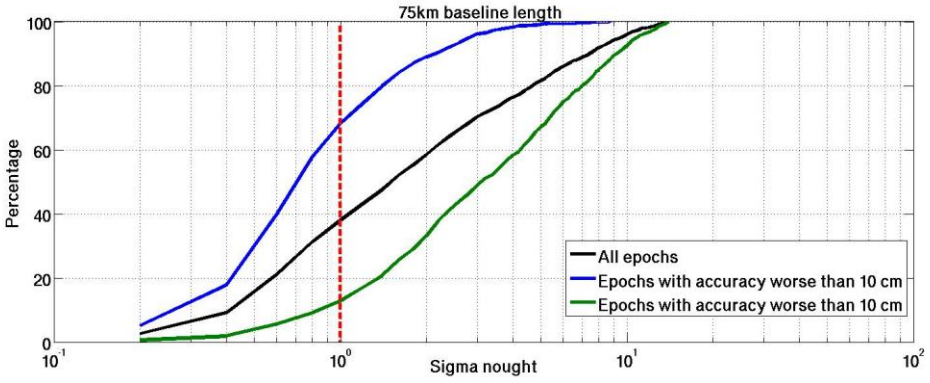
75km baseline length
Percentage
Sigma nought
All epochs
Epochs with accuracy worse than 10 cm
Epochs with accuracy worse than 10 cm

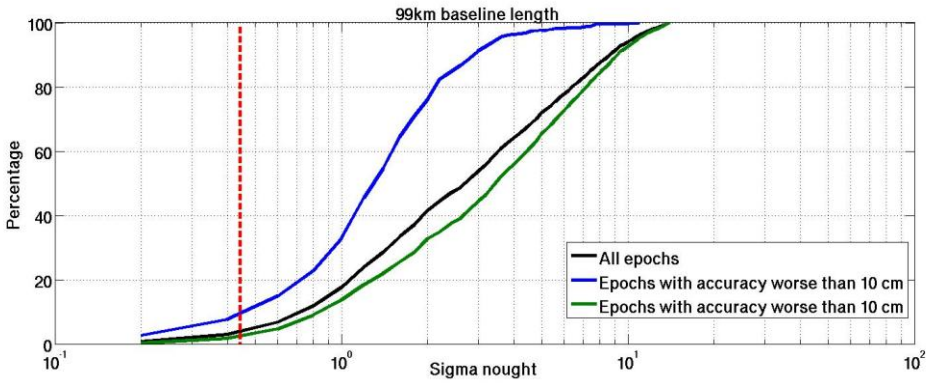

Figure 5-10 The distribution of successful, unsuccessful and all epochs percentages over the σ_0 values for each baseline with σ_0 cut-off values

According to Figure 5-10, applying this filter to the baseline results rejects percentages of epochs as given in Table 5-3:

Baseline length	Rejected epochs		
	of all epochs	of successful epochs	of unsuccessful epochs
7km	2%	0%	30%
13km	3	0	27
19km	14	0	36
27km	8	0	43
35km	23	2	48
39km	16	3	43
44km	32	1	59
50km	31	3	70
60km	39	12	72
75km	63	33	87
99km	96	90	97

Table 5-3 Rejected epoch percentages due to apply the σ_0 cut-off filter

Table 5-3 shows that applying the σ_0 threshold filter on a baseline up to 30 km will keep all the successful epochs, while at least 27% of the unsuccessful epochs are rejected (it should be noted that the actual number of unsuccessful epochs is low for

these baseline lengths). For a 35 – 50 km baseline, a maximum percentage of 3% of the successful epochs are rejected when this filter is applied, and around half of the unsuccessful epochs will be removed. When applying this filter on the results of baselines longer than 60 km, a high percentage of the unsuccessful epochs are removed. However it leaves gaps in the results as it rejects as much as 39% of the whole epochs. Figure 5-11 shows the GASP software final coordinates results with and without applying σ_0 threshold filter values on the tested baselines results.

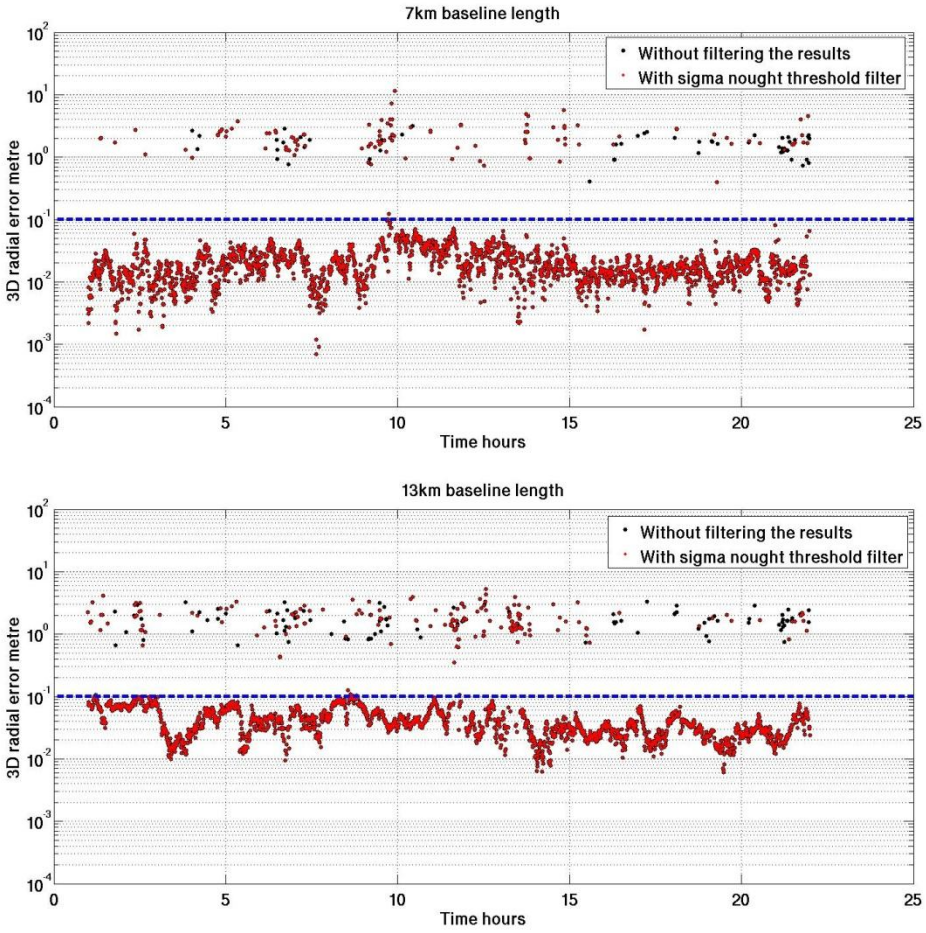

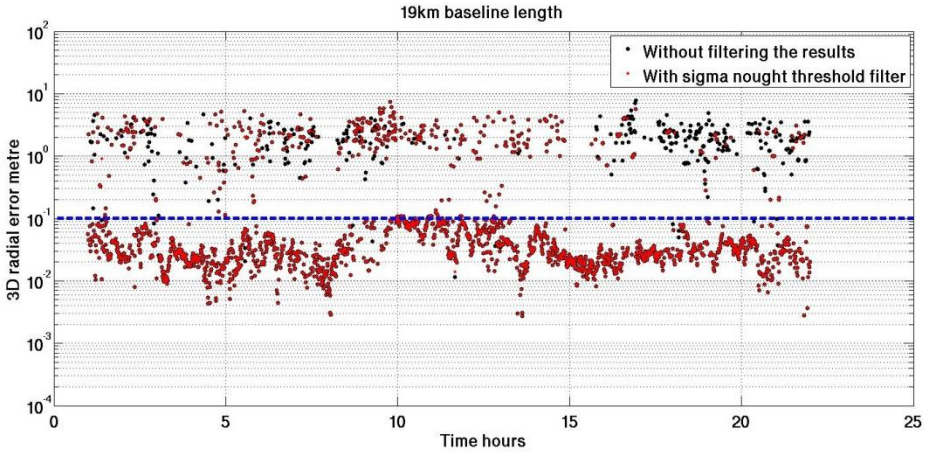
19km baseline length
Without filtering the results
With sigma nought threshold filter
3D radial error metre
Time hours

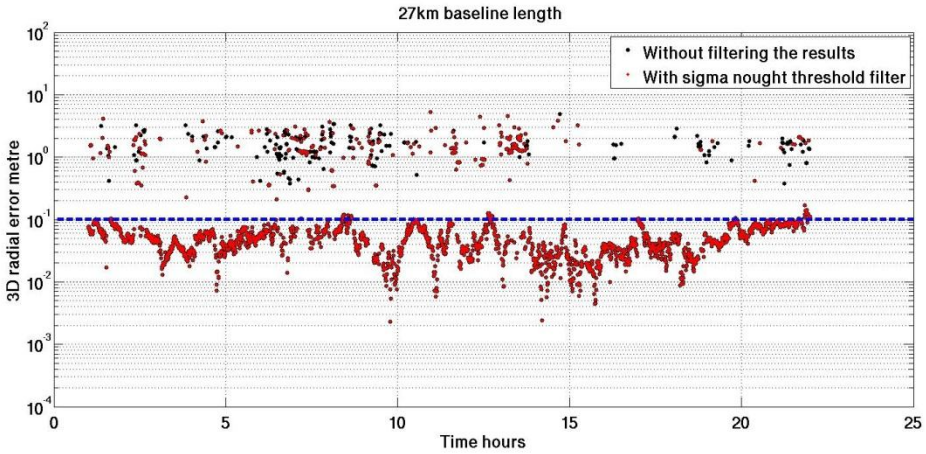
27km baseline length
Without filtering the results
With sigma nought threshold filter
3D radial error metre
Time hours

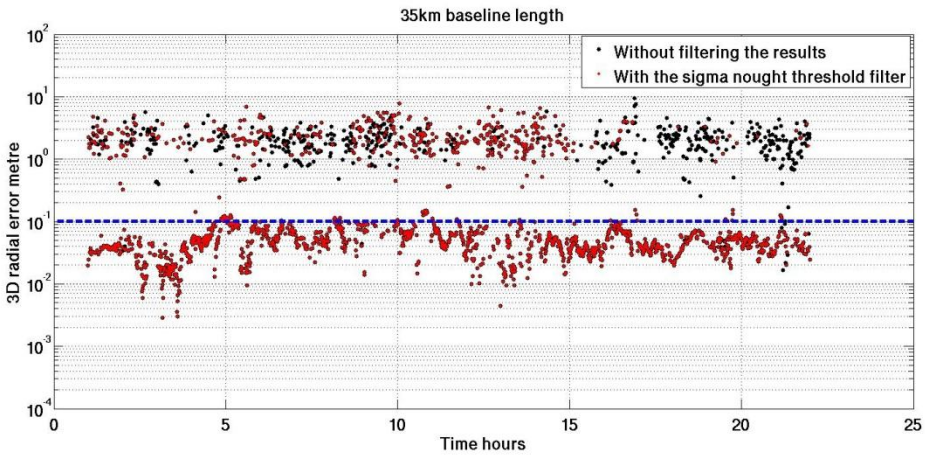
35km baseline length
Without filtering the results
With the sigma nought threshold filter
3D radial error metre
Time hours

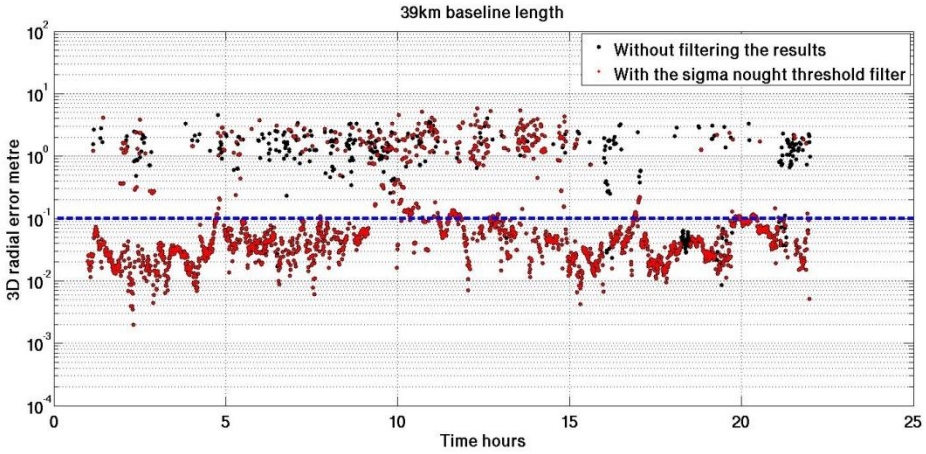
39km baseline length
Without filtering the results
With the sigma nought threshold filter
3D radial error metre
Time hours

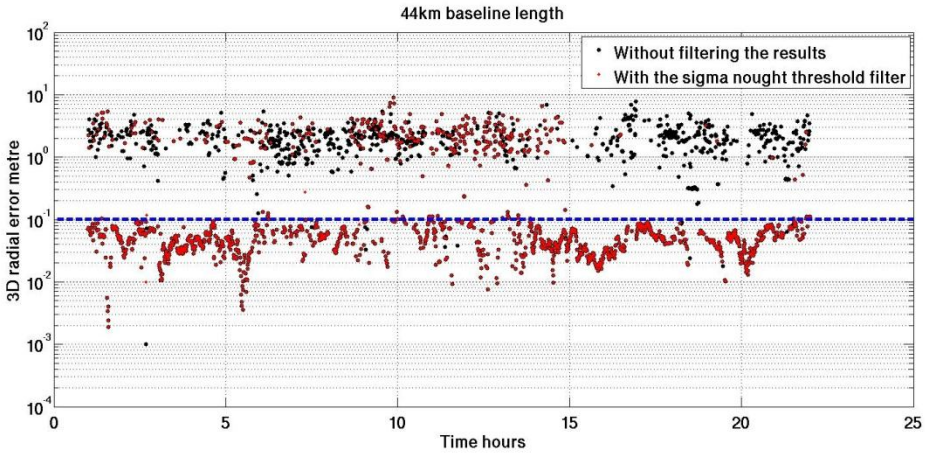
44km baseline length
Without filtering the results
With the sigma nought threshold filter
3D radial error metre
Time hours

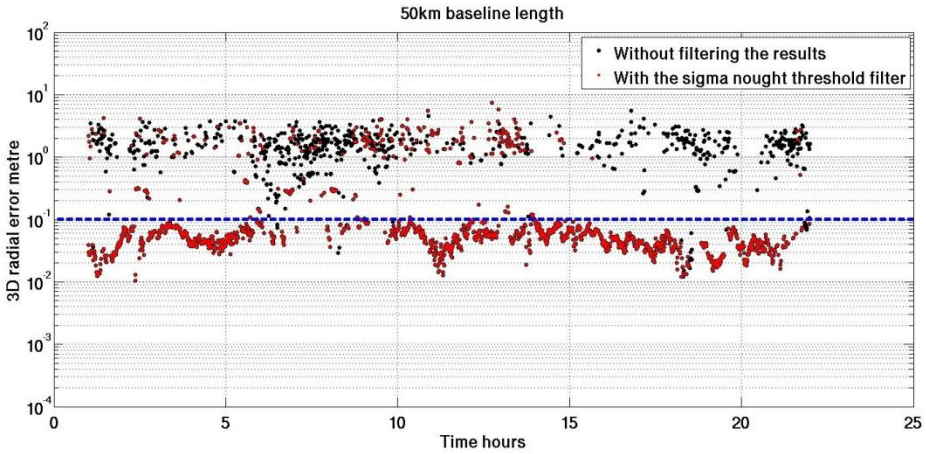
50km baseline length
Without filtering the results
With the sigma nought threshold filter
3D radial error metre
Time hours

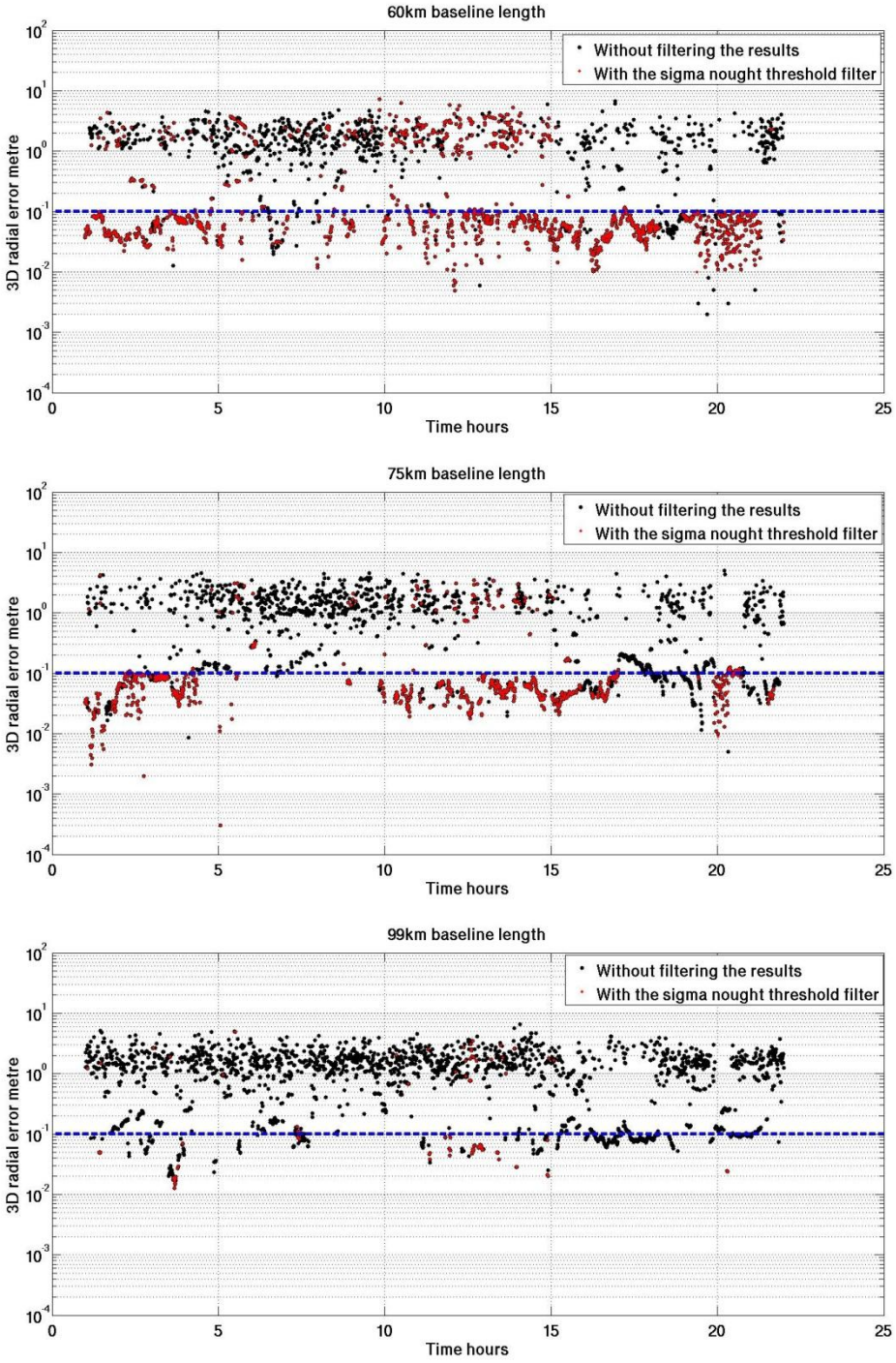

Figure 5-11 The 3D radial error (log scale) of the final GASP positioning results with and without applying a σ_0 threshold filter. The blue dash line represents the positioning accuracy threshold (10 cm radius to the true position)

Applying the σ_0 threshold helps to filter the results and improve the reliability of the obtained results. On the other hand, it has a negative aspect as it rejects some of the positioning outputs, which affects the frequency of the results, particularly for long

baselines. However, if less accurate results are targeted then the σ_0 threshold will be larger for each baseline and therefore the amount of rejected data will be less. This rejection of data may be accepted depending on the density of the epochs over time and how frequent the required results are for the studied case.

To check the effects of the applied improvements on the GASP software results, the positioning results Median Absolute Deviation (MAD), the daily Ambiguity Function Value (AFV) success rate (the AFV value is successful when its value is larger then 0.9), and the probability of getting positions within 10 cm radius to the true position for the original and final versions of GASP have been plotted in Figure 5-12, Figure 5-13 and Figure 5-14 respectively.

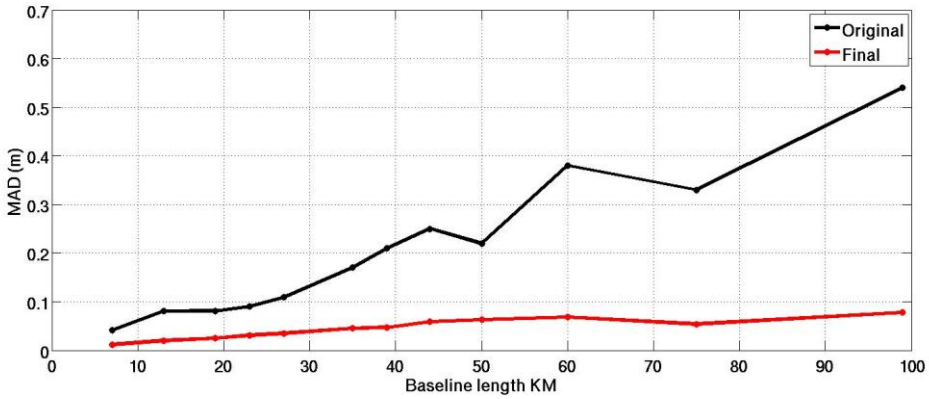

Figure 5-12 The positioning results MAD for the original and final versions of the GASP software for different baseline lengths

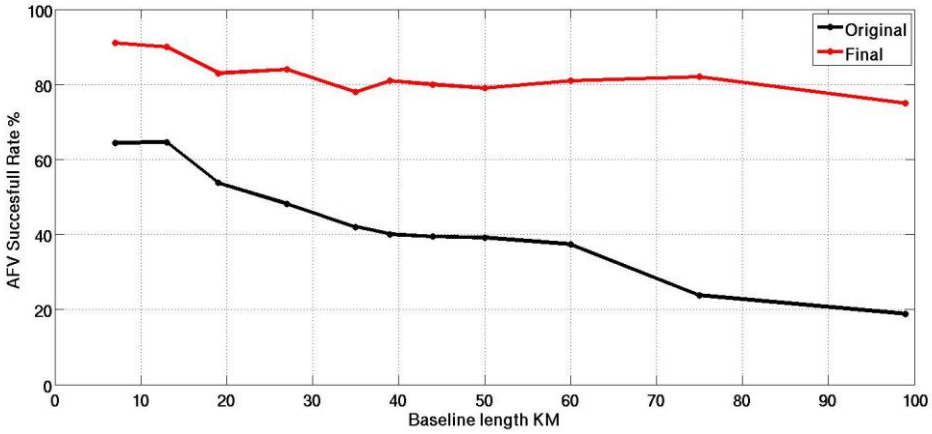

Figure 5-13 Daily AFV success rates of the original and final GASP versions for different baseline lengths

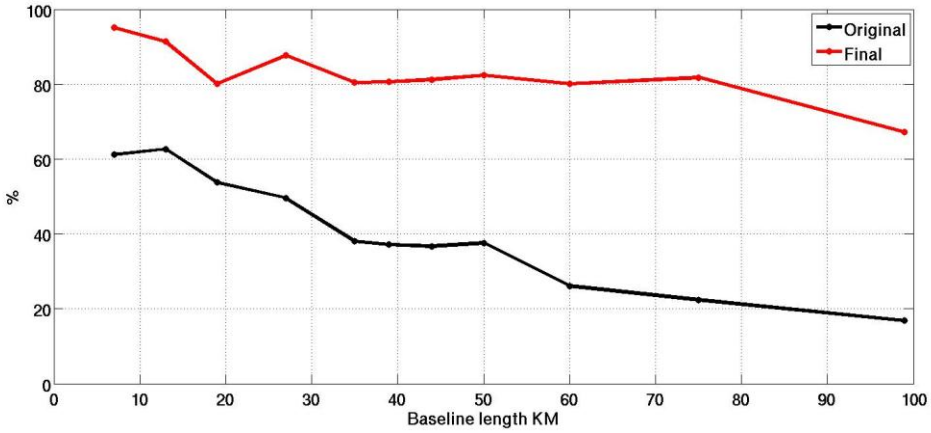

Figure 5-14 The percentages of the original and final GASP versions results which have better than 10 cm positioning accuracy for different baseline lengths

Figure 5-12, Figure 5-13 and Figure 5-14 show the applied improvements make the GASP positioning more accurate and reduce the noise level of the results.

In the following chapter the GASP positioning results' accuracy will be checked to see whether its' results accuracy and density are sufficient for monitoring structural movements. This task needs a high data frequency; therefore the baselines with a rejected data percentage over 40% will be ignored (baselines with a length longer than 60 km). Figure 5-15 shows a flowchart of GASP software with applied filters (in green frames).

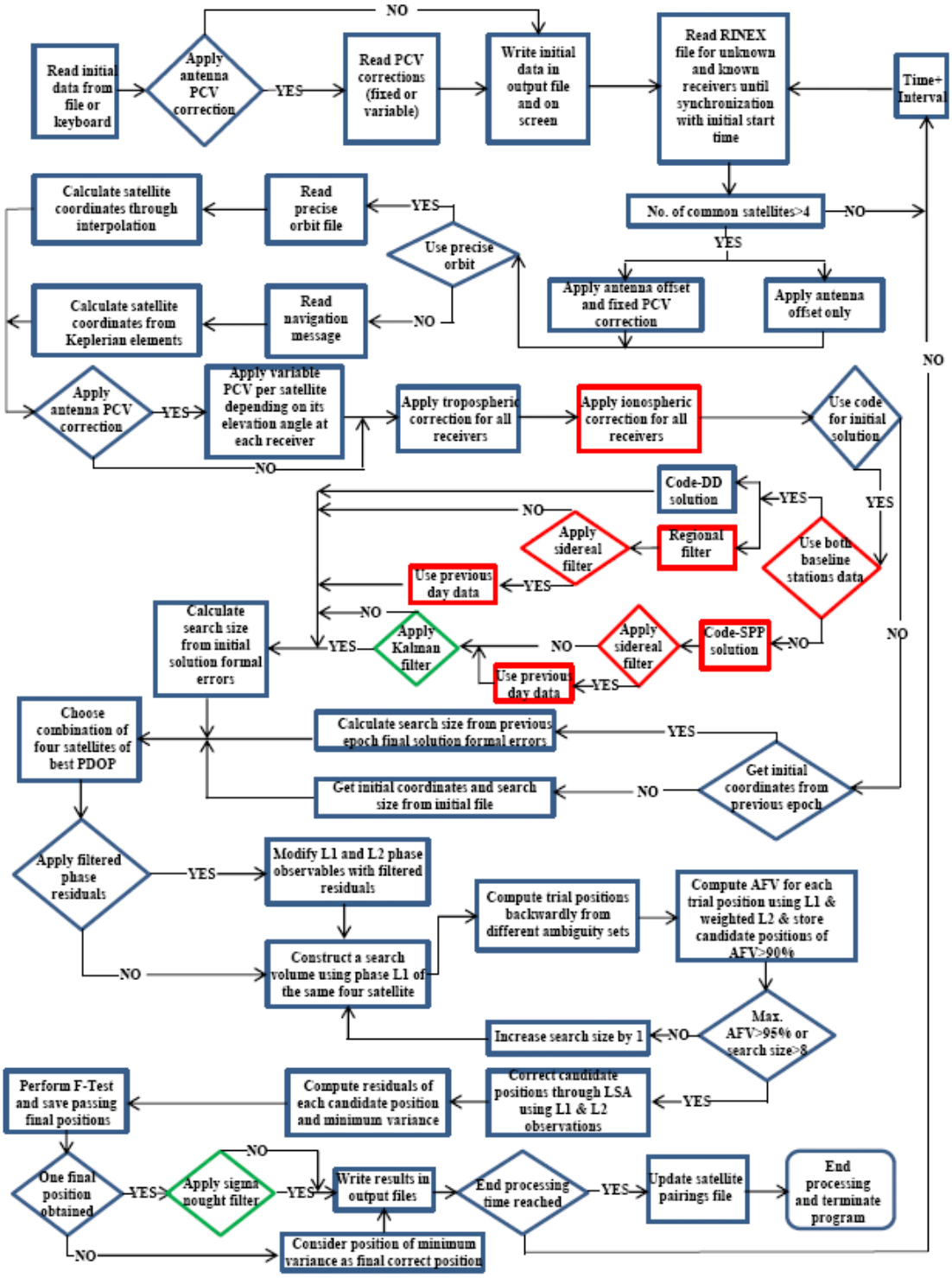

Figure 5-15 GASP software flowchart

STRUCTURAL DEFORMATION SETTLEMENT AND SHAKING SYNTHETIC TESTS

6.1 INTRODUCTION

GPS provides scientists, engineers and others interested in monitoring structural integrity, valuable information to mitigate potentially hazardous situations. Through provision of 3D coordinates together with corresponding time, GPS-derived information can be used to create predictive models for structural movements (Knecht and Manetti, 2001). The continuous comparison of these models can be used as an indicator of the health of the structure (Raziq and Collier, 2006). GPS is available for use over the entire world, day and night, and under all meteorological conditions. The availability of GPS data allows structural monitoring to be undertaken in real-time or near real-time (Ince and Sahin, 2000).

Performing such deformation surveillance using the double differencing technique requires employing multiple stations. Some of these stations must be in stable locations to form reference points, while the others (at least one) should be attached to the structure to be monitored. It is noted however that the GPS Precise Point

Positioning (PPP) technique makes the monitoring of a structure's stability possible using one station, however this technique is not applied in this research as the aim here is to solve the GPS observations epoch by epoch due to its many advantages (see Chapter 1).

Whilst a full PPP approach is not adopted the use of the Code-SPP solution is utilised to determine the GASP ambiguity function positioning inputs and to create a code-based ionospheric model as was recognised in Chapter 4. It was concluded in Chapter 5 that applying a Kalman filter to these Code-SPP results improves the accuracy of the final GASP positioning results. Also applying a σ_0 filter makes the results more reliable. Therefore the GASP software with the Code-SPP solution and the application of the Kalman and σ_0 filters will be used in this chapter.

To study the capabilities of the GASP software for structural movement detection, a synthetic moving receiver RINEX data set has been created. The RINEX files of the LEEP, TORP and HOLP IGS stations have been used to generate the synthetic data. These stations have been chosen as they are typically representative of the stations used in this research and a network of baselines has been created by adopting these stations as 'moving' stations (Table 6-1). Figure 6-1 shows the IGS station network in the Californian region, and the red lines represent the baselines which have had their data processed.

Base station	Moving station	Baseline length (km)
BRAN	LEEP	7
UCLP	LEEP	13
TROP	HOLP	20
CSN1	LEEP	23
HOLP	LEEP	27
UCLP	TORP	32
AZU1	LEEP	39
BRAN	TORP	43
CSN1	HOLP	50
CSN1	TORP	54

Table 6-1 Stations and baselines used in the structural synthetic motion trials

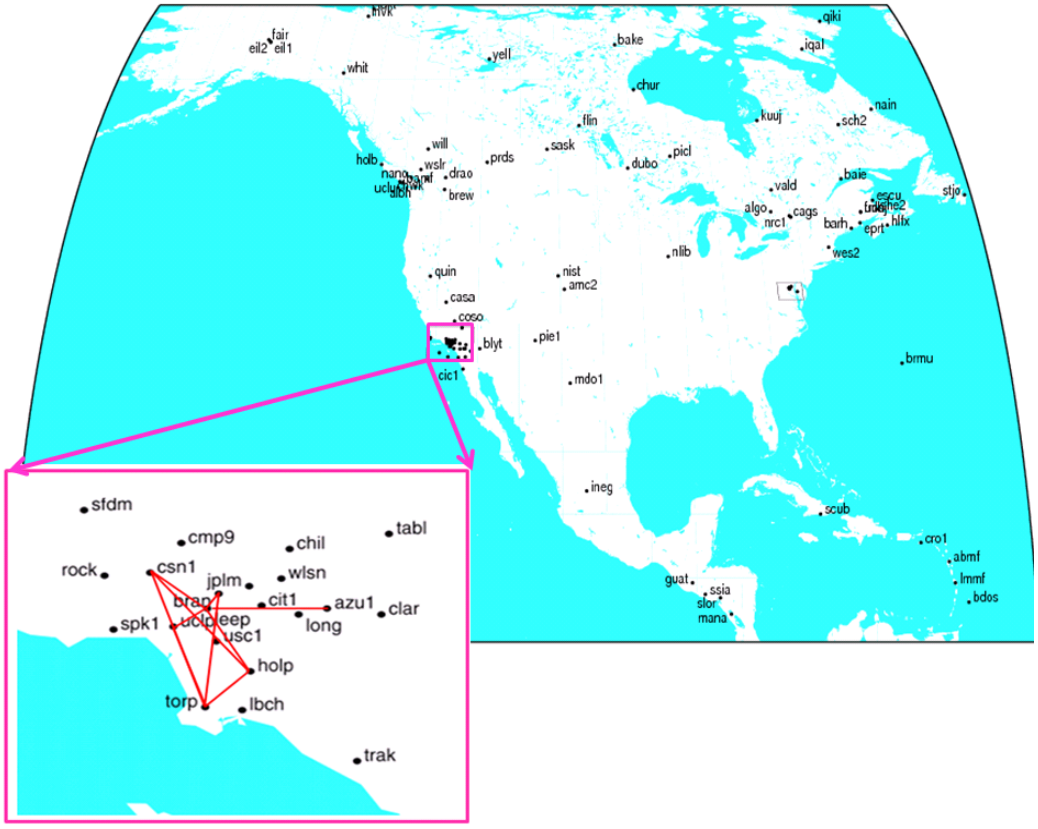

Figure 6-1 The IGS stations which have been used in this chapter. (http://igscb.jpl.nasa.gov/network/maps/all_socal.html). The red lines show the baselines which have had their data processed see Table 6-1.

A synthetic motion has been applied to the height of the 'moving' station of each baseline in Table 6-1. This has been done by employing a MATLAB based software called Tidefree (King *et al.*, 2000). The software uses the station RINEX observation file, the RINEX navigation file and a tide model (or more generally a movement model) to create a modified RINEX file. The Tidefree software modifies the RINEX file by adding or subtracting a correction to the carrier phase and the pseudorange of each observed satellite at each epoch depending on the receiver satellite geometry and the applied motion. The modified RINEX file was subsequently processed using the modified version of the GASP software as outlined in the foregoing chapters. The difference between the GASP results and the modelled height of the station (i.e. its known height plus the added model variations) has been analysed. Two types of structural movements have been simulated: settlement and shaking.

To check whether the epoch movement is a step change, a shaking wave or an outlier the following progressive movement criteria have been used:

$$\left((h_2 - h_1) > 3\sigma\right) \text{ and } \left((h_3 - h_2) > 3\sigma\right) \text{ and } \left((h_3 - h_1) > 3\sigma\right) \tag{6.1}$$

Where h_3 is the computed height of the tested epoch, h_2 is the computed height of the previous epoch to the tested epoch, h_1 is the computed height of the epoch before the h_2 epoch, and σ is formal error of the height difference obtained at the previous to the tested epoch. Figure 6-2 shows that:

- if $\left((h_2 - h_1) > 3\sigma\right)$ and $\left((h_3 - h_2) > 3\sigma\right)$ are true only, then the movement is an outlier.
- if $\left((h_2 - h_1) > 3\sigma\right)$ and $\left((h_3 - h_1) > 3\sigma\right)$ are true only, the movement is settlement.
- if $\left((h_2 - h_1) > 3\sigma\right)$ and $\left((h_3 - h_2) > 3\sigma\right)$and $\left((h_3 - h_1) > 3\sigma\right)$ are true then the movement is a shaking wave.

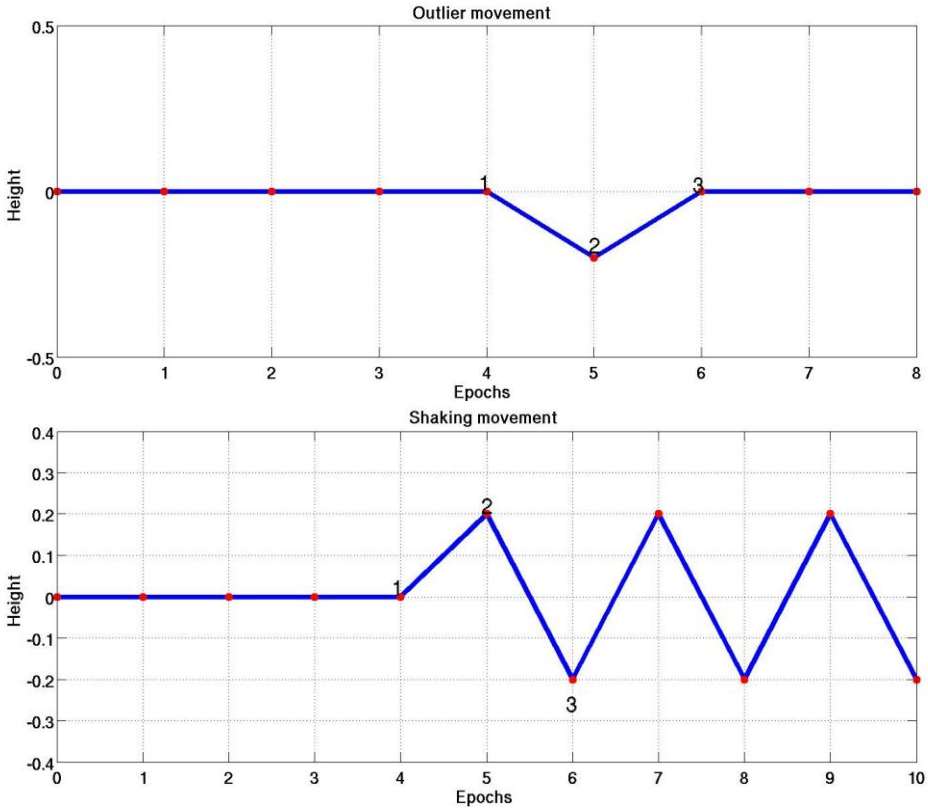

Figure 6-2 Progressive movement criteria

6.2 SETTLEMENT TEST

For the settlement simulation, the moving station height has been decreased by 20 cm every 2 hours starting from 2 am as shown in Figure 6-3.

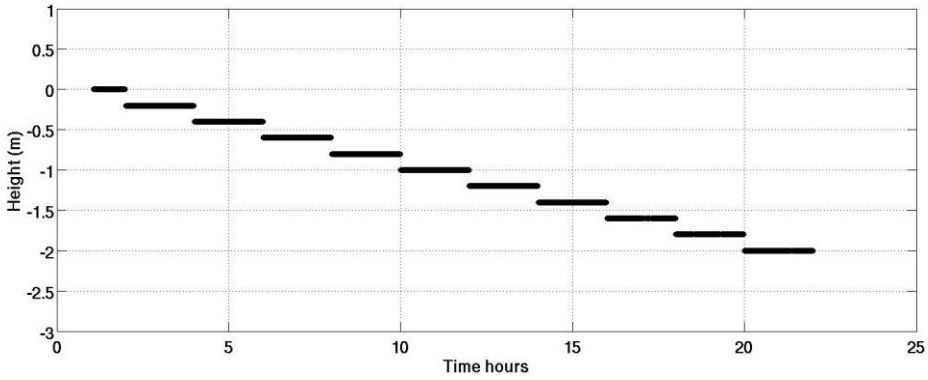

Figure 6-3 Synthetic time series displacement of station height

The modified GASP software has been used to process the height modified RINEX files, and subsequently the epochs which were removed by the application of the σ_0 filter have also been removed from the modelled height time series to allow a point by point comparison. Figure 6-4 shows the results comparison between the GASP results and the modelled height time series.

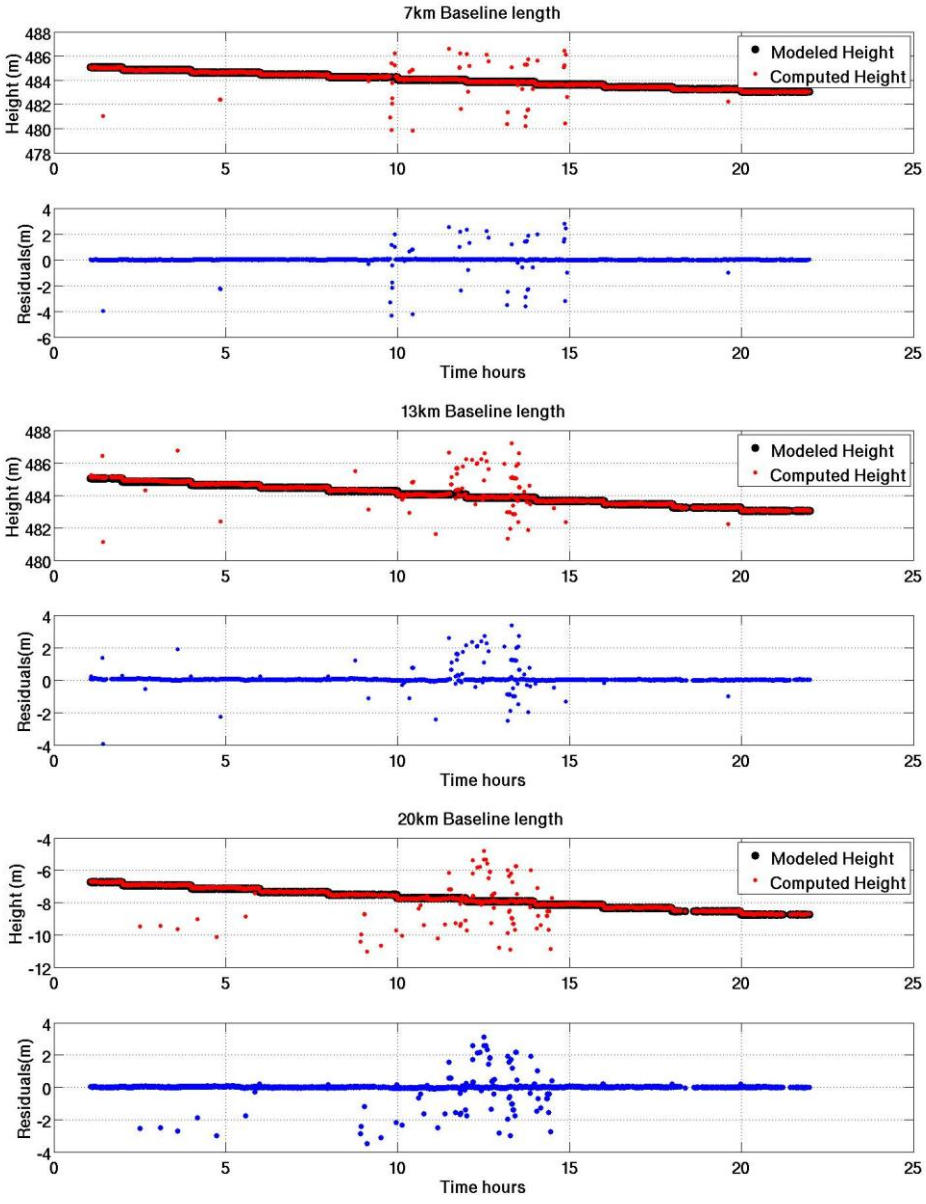

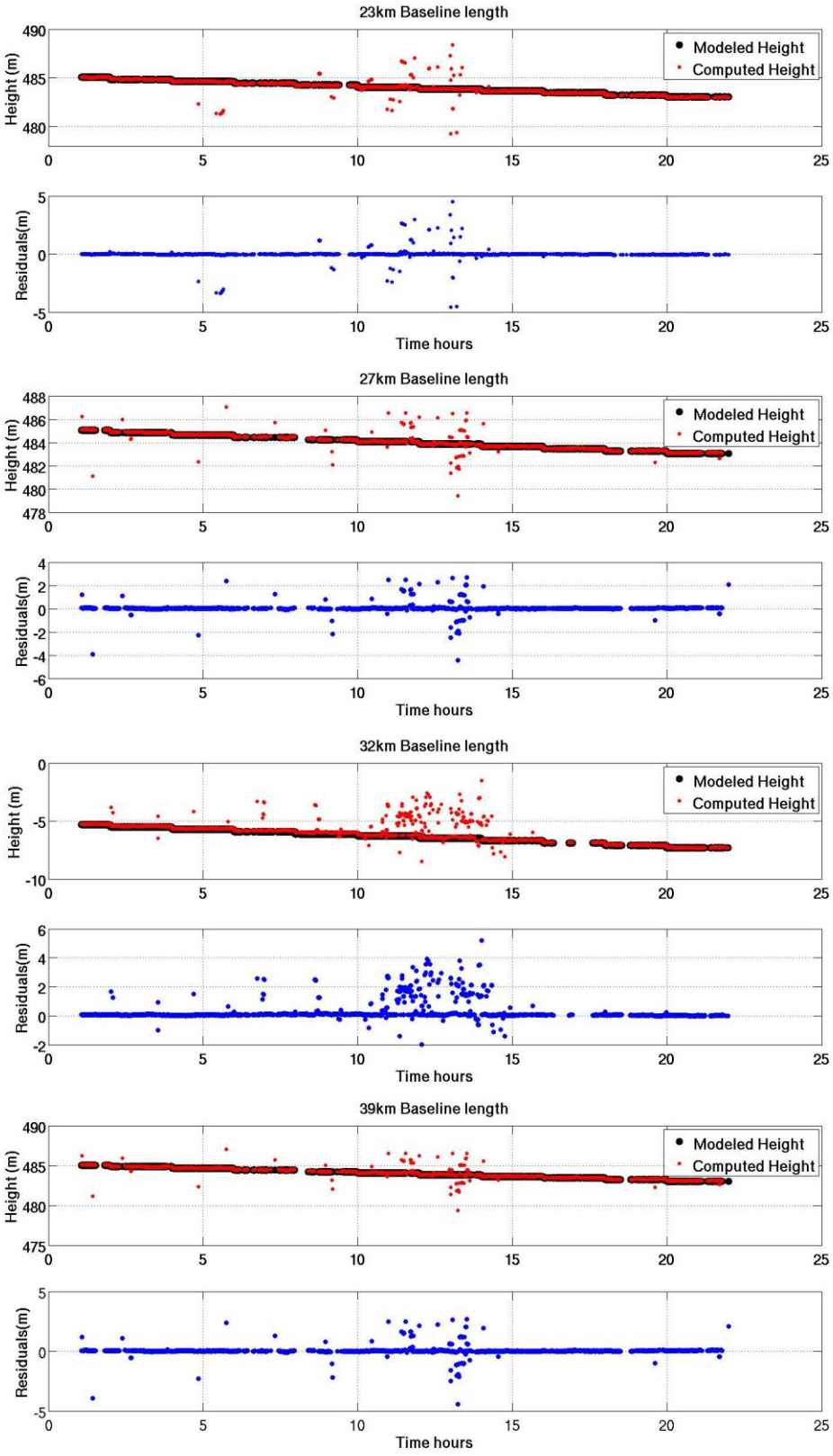
23km Baseline length
Modeled Height
Computed Height
Height (m)
Residuals(m)
Time hours
27km Baseline length
Modeled Height
Computed Height
Height (m)
Residuals(m)
Time hours
32km Baseline length
Modeled Height
Computed Height
Height (m)
Residuals(m)
Time hours
39km Baseline length
Modeled Height
Computed Height
Height (m)
Residuals(m)
Time hours

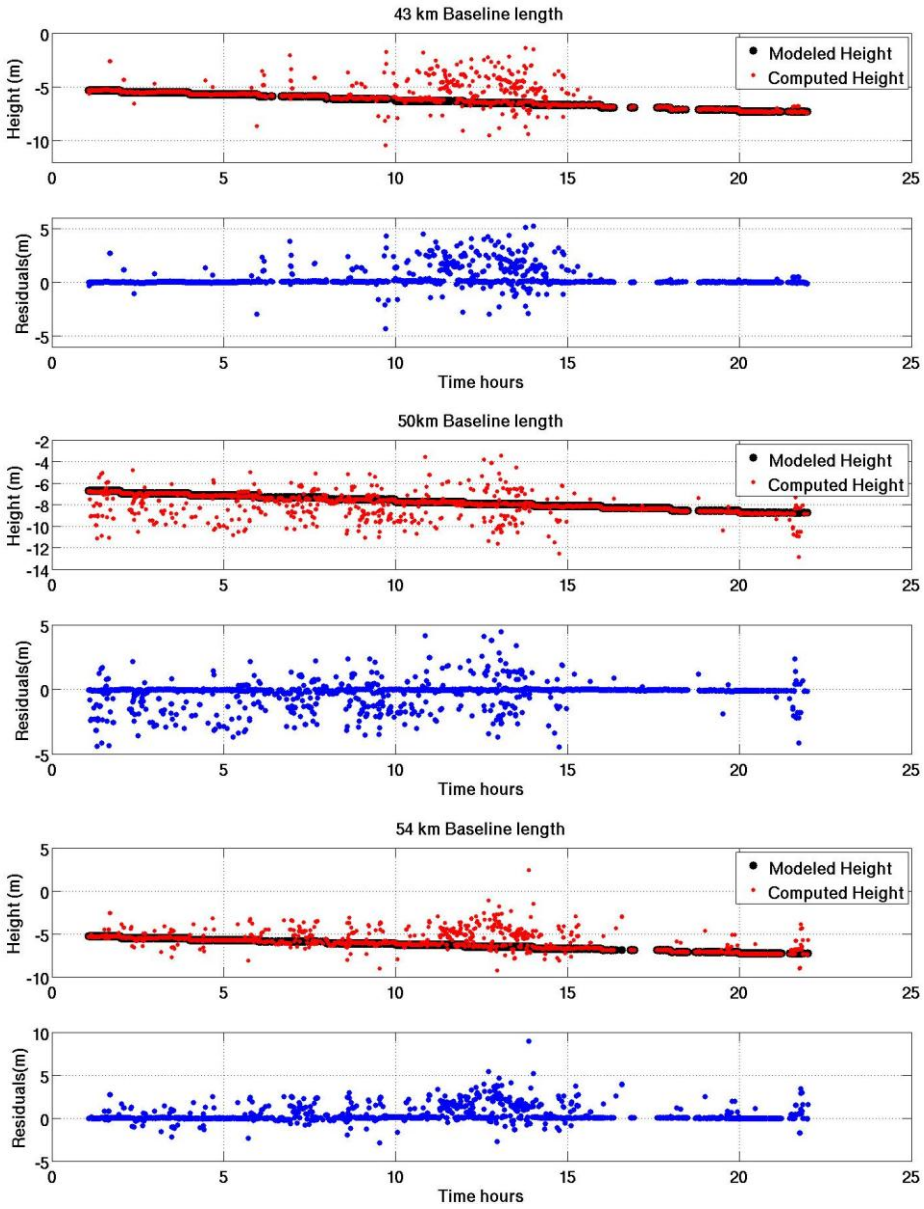

Figure 6-4 The moving stations' modelled and computed heights and the differences between them for the baselines which have been used in the settlement test

A visual inspection of Figure 6-4 shows that the modified GASP software has, in most cases successfully processed the modified RINEX files and determined the correct height values. However, it is clear that the results become noisier as the baseline length increases

To verify the ability of GASP in detecting step changes, the percentages of Type I and Type II errors of the results have been computed for each baseline in Table 6-2. Type

I and Type II errors in the context of deformation studies are defined as follows (Ott and Longnecker, 2008).

- A Type I error is when movement is present but not detected by GASP. The results in Table 6-2 are out of the 10 step changes which have been applied to the stations.

- A Type II error is when there is no actual (synthetic) movement in the station, but the GASP results indicate that there is a movement.

To check whether the epoch movement is a step change or an outlier the progressive movement criteria have been applied to all of the non-moving epochs.

Baseline Length (km)	Type I	Type II	Outlier	Number of non-moving epochs
7	0%	1.3%	3.3%	2309
13	0%	2.1%	5.1%	2266
20	0%	3.5%	7.5%	2114
23	0%	2.1%	5.1%	2231
27	0%	2.3%	5.3%	2160
32	0%	2.4%	5.4%	2002
39	0%	5.3%	11.3%	2084
43	0%	4.6%	10.6%	1984
50	0%	6.5%	12.5%	2102
54	0%	6.8%	13.8%	1988

Table 6-2 Type I and Type II errors for the step change detecting test. Type I results are based on10 events, and Type II and the outlier results are out of the remaining epochs given in the right-hand column

From Table 6-2, it can be seen that GASP is able to detect all step changes. However, at some epochs it gives incorrect detection measurements. Table 6-3 shows the

percentage of incorrect measurements at the epochs where step changes in the station height occur.

Baseline length (km)	Percentage
7	0%
13	10%
20	0%
23	10%
27	10%
32	0%
39	20%
43	20%
50	10%
54	20%

Table 6-3 The percentage of step changes that have been successfully detected but with incorrect magnitude (at the 3-sigma level)

The settlement test results indicate that the modified GASP software is able to detect the applied synthetic movement. Figure 6-4 indicates that the positioning accuracy decreases around midday in the stations' local time. This may be explained by the fact that the ionosphere reaches its maximum value shortly after midday (Ho *et al.*, 1996), and could also be due to the satellite geometry. To study the effect of the satellite geometry changes on the GASP software results, the hourly percentage of the Type II error against the hourly average of the satellite geometry PDOP values has been plotted in Figure 6-5 . (PDOP has been computed for the baseline-common satellites' geometry at the moving station location). The data best fit line with associated R-squared value has been plotted for each baseline to check whether there is a correlation between the percentage of Type II error values and the average value of PDOP.

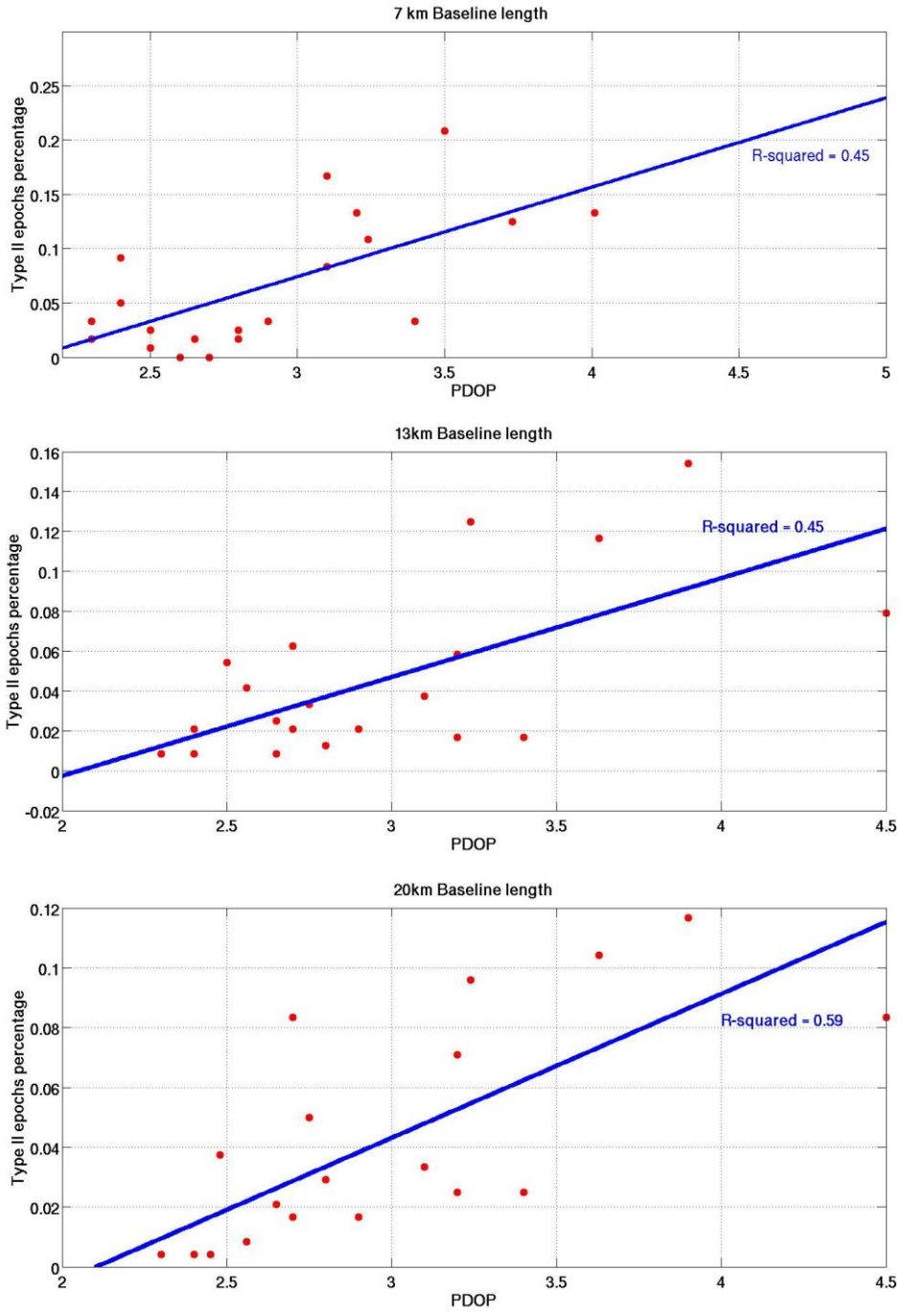
7 km Baseline length
Type II epochs percentage
PDOP
R-squared = 0.45
13km Baseline length
Type II epochs percentage
PDOP
R-squared = 0.45
20km Baseline length
Type II epochs percentage
PDOP
R-squared = 0.59

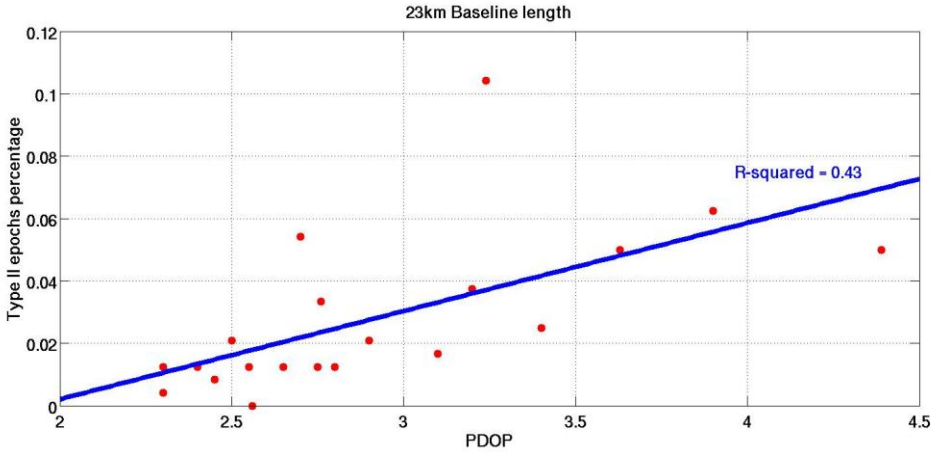
23km Baseline length
Type II epochs percentage
PDOP
R-squared = 0.43
0.12
0.1
0.08
0.06
0.04
0.02
0
2
2.5
3
3.5
4
4.5

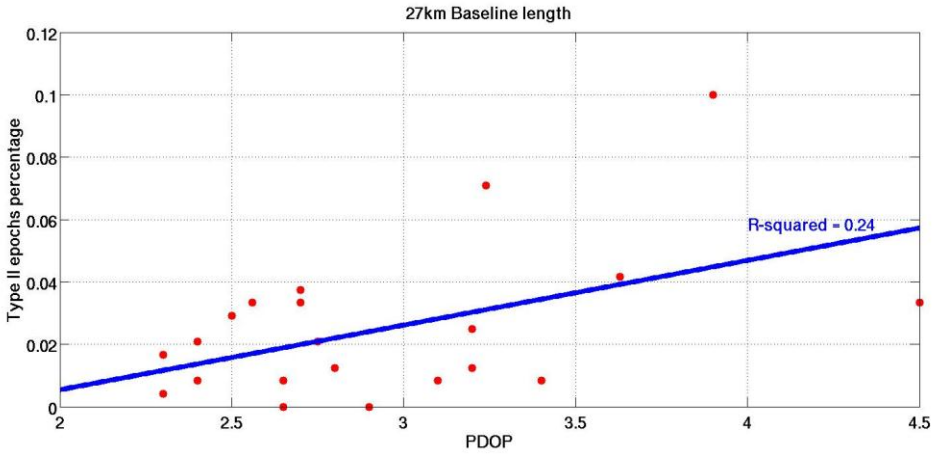
27km Baseline length
Type II epochs percentage
PDOP
R-squared = 0.24
0.12
0.1
0.08
0.06
0.04
0.02
0
2
2.5
3
3.5
4
4.5

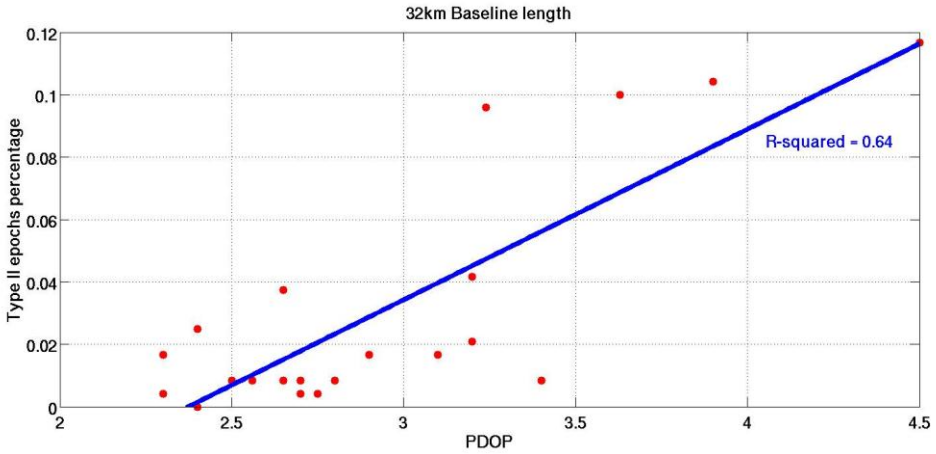
32km Baseline length
Type II epochs percentage
PDOP
R-squared = 0.64
0.12
0.1
0.08
0.06
0.04
0.02
0
2
2.5
3
3.5
4
4.5

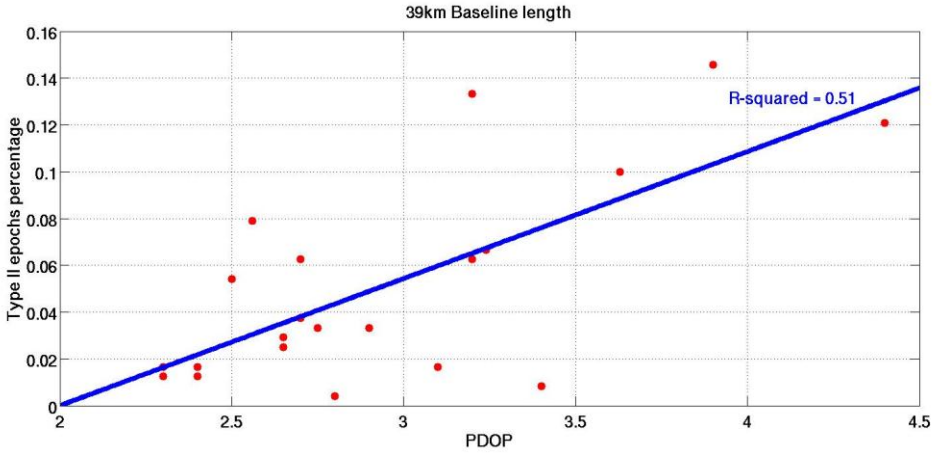
39km Baseline length
R-squared = 0.51
Type II epochs percentage
PDOP
0.16
0.14
0.12
0.1
0.08
0.06
0.04
0.02
0
2
2.5
3
3.5
4
4.5

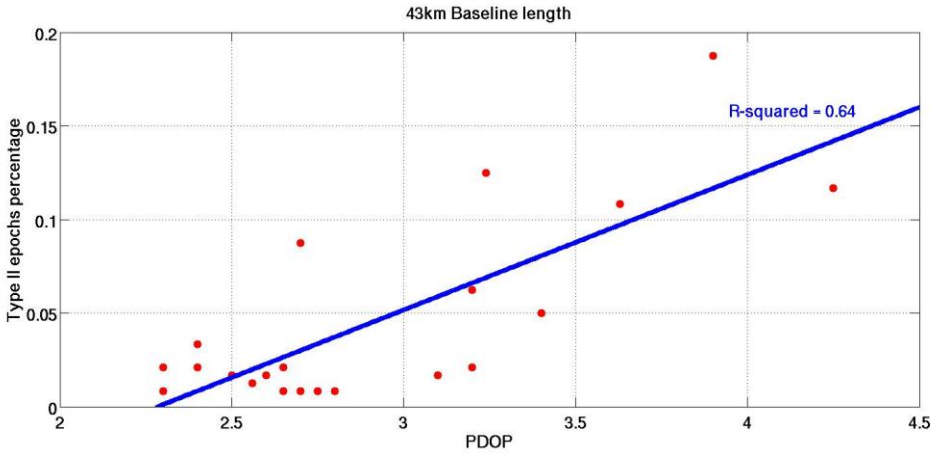
43km Baseline length
R-squared = 0.64
Type II epochs percentage
PDOP
0.2
0.15
0.1
0.05
0
2
2.5
3
3.5
4
4.5

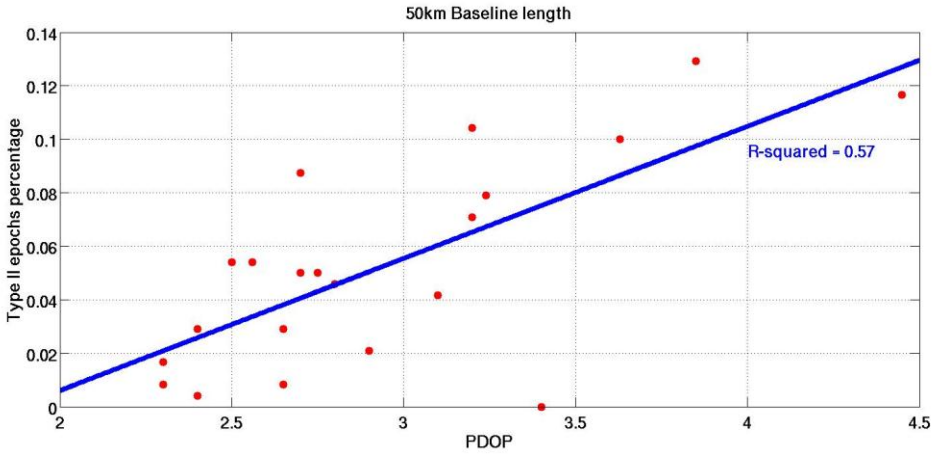
50km Baseline length
R-squared = 0.57
Type II epochs percentage
PDOP
0.14
0.12
0.1
0.08
0.06
0.04
0.02
0
2
2.5
3
3.5
4
4.5

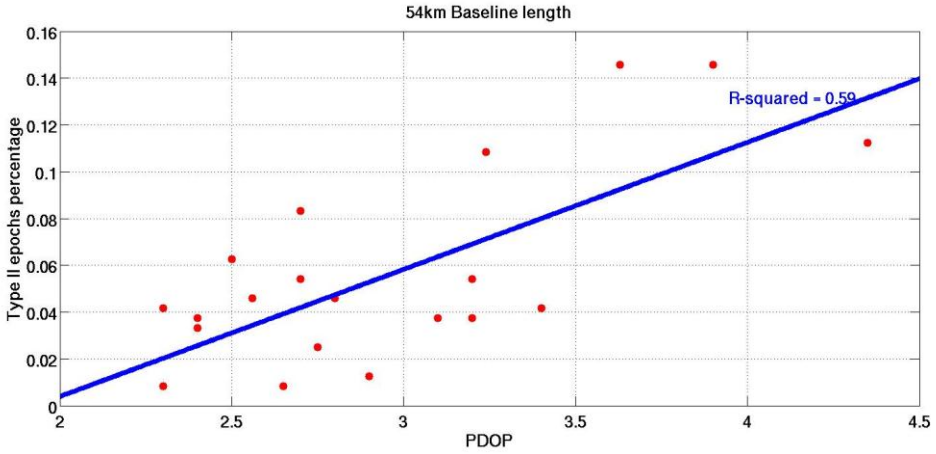

Figure 6-5 Type II errors average of each hour against the PDOP average over the same hour (21 hours data span). The blue line is the data best fit line with associated R squared value as a measure of goodness of fit.

Figure 6-5 indicates that all the R-squared value differences from zero, which indicates that there is a correlation between the PDOP and the percentage of Type II error.

Figure 6-5 shows that the probability of obtaining a false step is larger when the PDOP of the baseline-common satellites geometry is high.

The settlement test results show that the GASP software is reliable for use in detecting structural step changes. However, under certain circumstances it may give incorrect results although the probability of these false positives is small as shown in Table 6-3. For a baseline length that is less than or equal to 32 km, around 5% of results give a false indicator of a structural movement (Table 6-2). This percentage increases to 13.8% when the baseline length is 54 km. In the next section the GASP software detection reliability in identifying different shaking frequencies and amplitude will be studied.

6.3 SHAKING TESTS

In order to simulate shaking movement, five shaking time series have been developed and applied to the stations over different times during the tested day. Table 6-4 shows the starting time of each type of shaking series, and the equation used to create it. The

equations in Table 6-4 provide different shaking frequencies and amplitudes. The applied model times cover different times of the day to allow for the effect of change in satellite geometry. The period of each shaking series is 20 minutes (a 20 minute period has been chosen as it spans at least one cycle for the chosen frequencies).

Start time	Applied shaking model
03:40	$\mathrm{h_m} = \mathrm{h_0} + 0.6 * \sin(0.1\Delta\mathrm{t})$
07:40	$h_m = h_0 + 0.4 * \sin(0.05\Delta t)$
12:40	$h_m = h_0 + 0.3 * \sin(0.02\Delta t)$
17:40	$\mathrm{h_m} = \mathrm{h_0} + 0.2 * \sin(0.01\Delta\mathrm{t})$
20:40	$h\_m = h\_0 + 0.15 * sin(\Delta t)$

Table 6-4 The applied shaking movement series

Where,

h_m is the new station height.

h_0 is the known station height.

Δt is the time of the epoch relative to the beginning of the series.

Figure 6-6 shows the shaking model applied to the station heights.

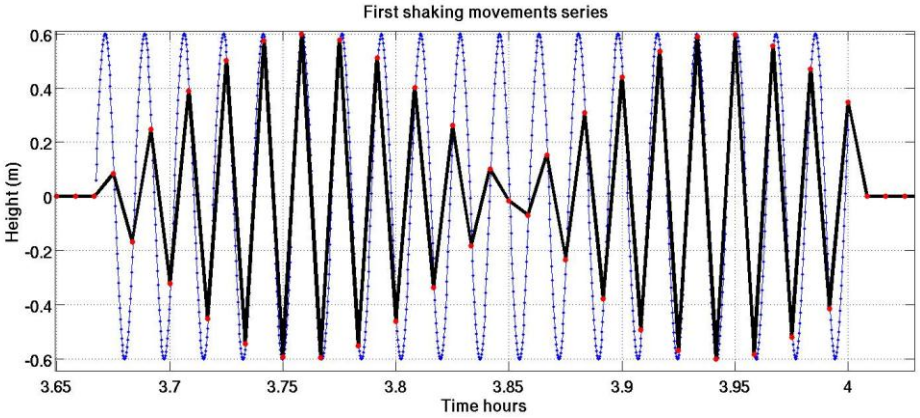

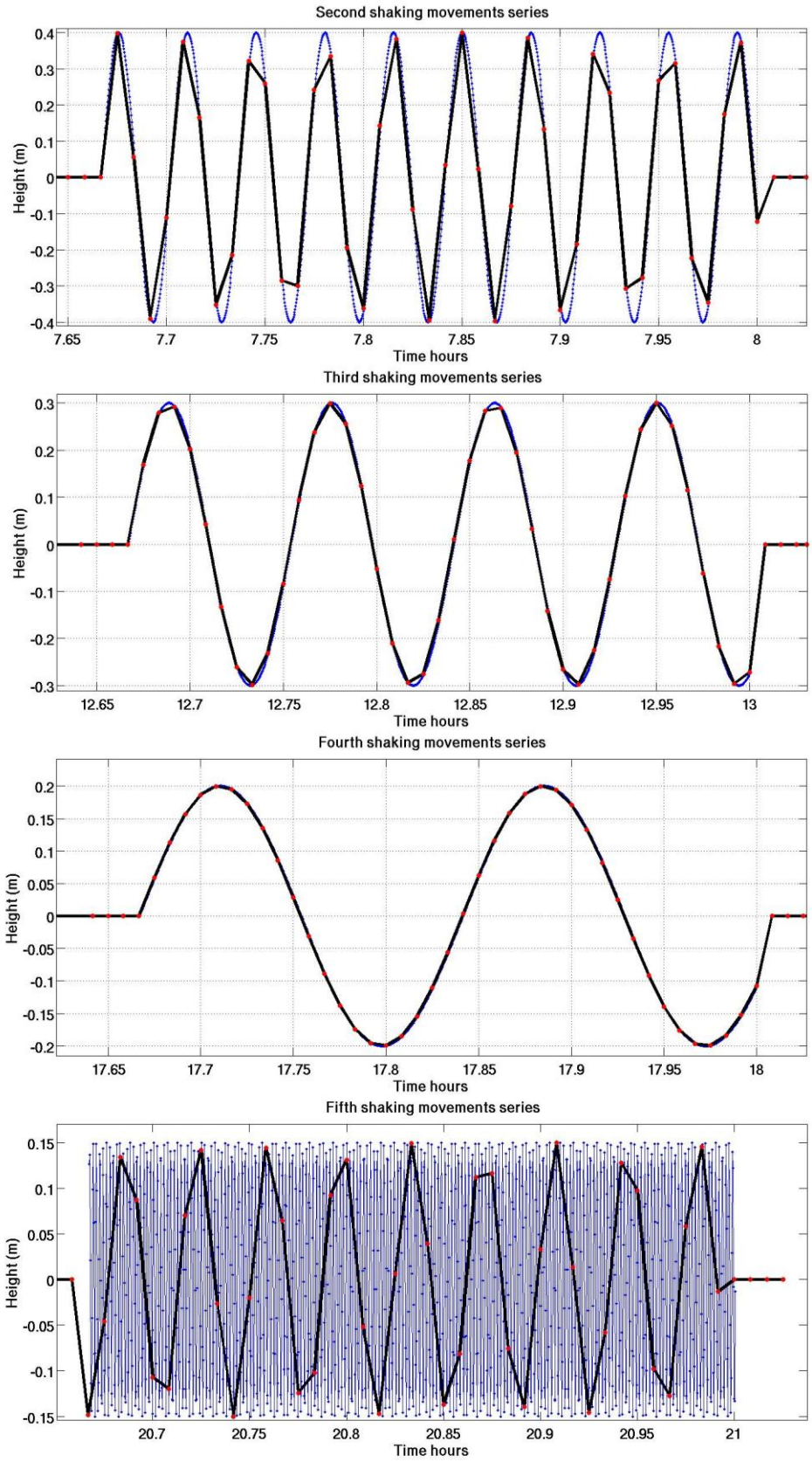

Figure 6-6 Applied time series shaking movements on station height. The black line with red dots is the applied shaking mode at 30 seconds epoch interval. The blue line is the smooth curve of the equations in Table 6-4 with a 1 second ΔT interval

To sample different satellite geometry, these tests have been done over 5 time windows on the day 66/2007 Table 6-4. Figure 6-7 and Figure 6-8 show the shaking test results of the 7 km and 54 km baselines (see Appendix C for the remaining shaking tests results).

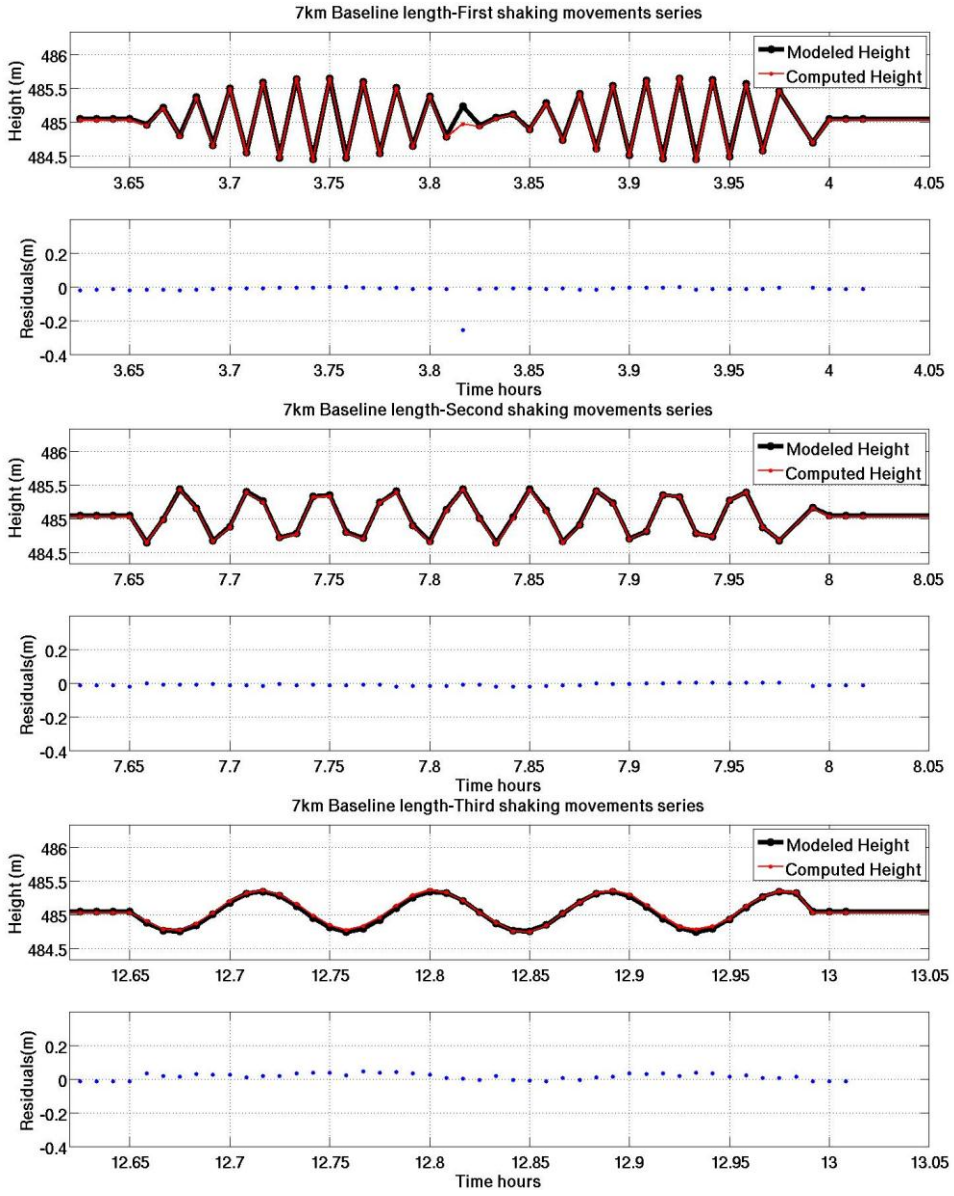

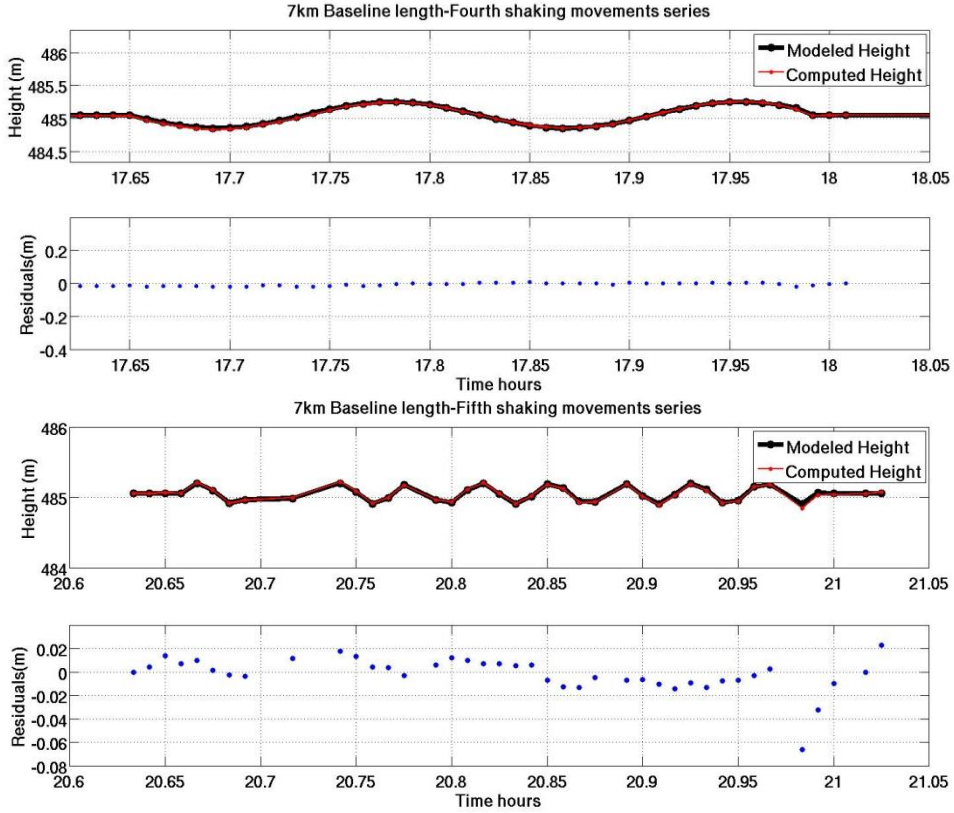

Figure 6-7 The shaking test results for the five time windows -7km baseline length.

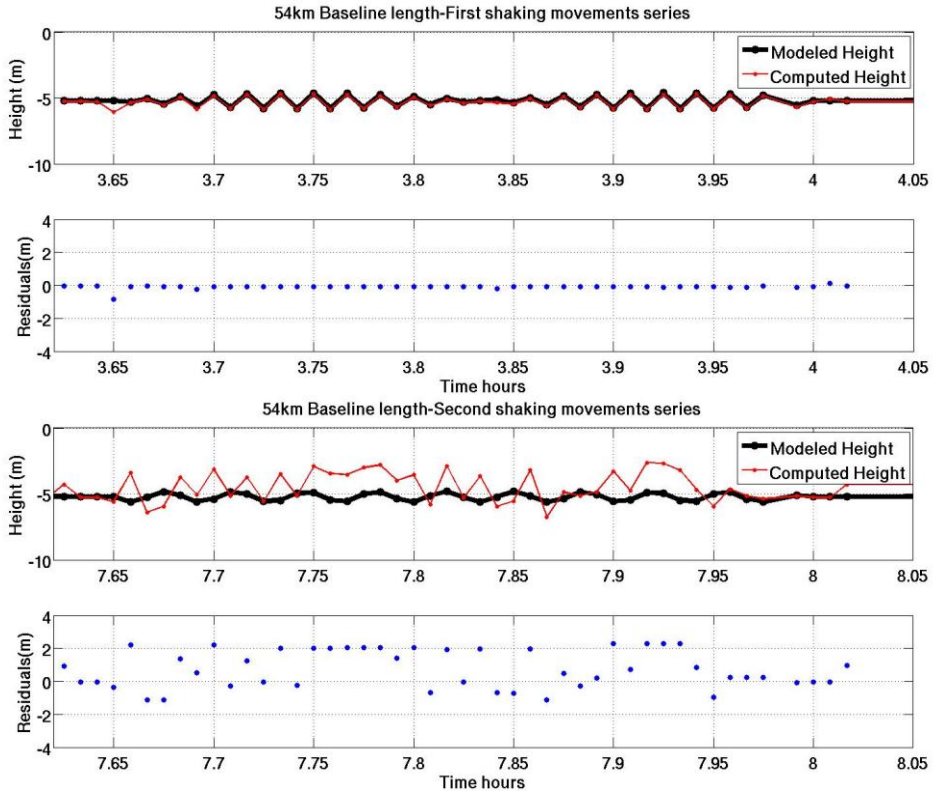

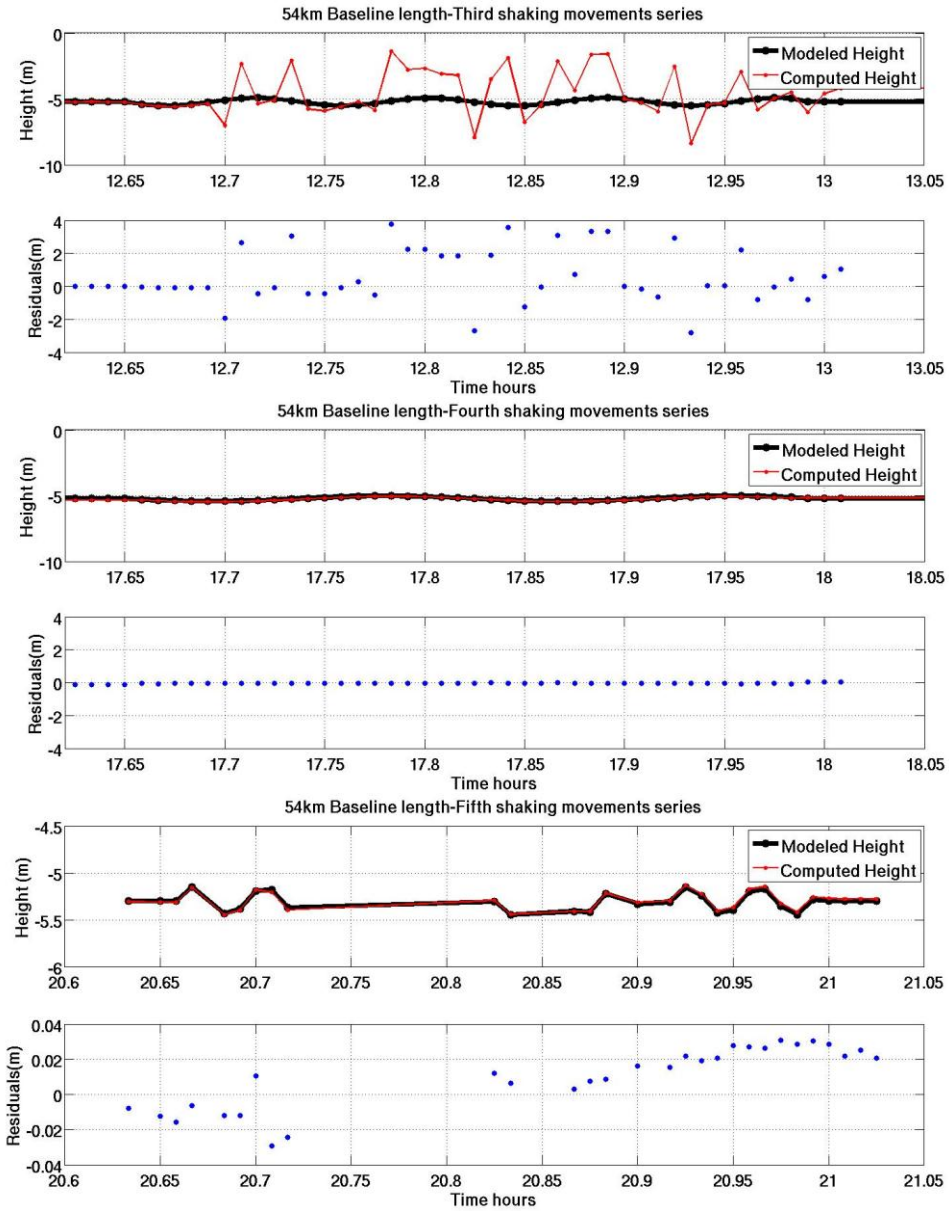

Figure 6-8 The shaking test results for the five time windows -54 km baseline length.

A visual inspection of Figure 6-7, Figure 6-8 and Appendix A suggests that the modified GASP software is able to detect the applied shaking movements. However, the tests clearly show that successful detection depends on the baseline length.

To check the ability of the GASP software in vibration identification, Type I and Type II errors have been computed and are shown in Table 6-5. Here a Type I error is identified when a vibration is present but not recognised by GASP, whilst a Type II

error is identified under the conditions when the GASP results show a shaking wave at an epoch where the station is static.

Baseline length (km)	Type I	Type II	Number of non-moving epochs
7	6.1%	1.1%	2209
13	4.0%	0.7%	2066
20	5.4%	3.2%	1914
23	4.1%	1.2%	2031
27	6.1%	1.1%	1960
32	8.2%	2.1%	1802
39	6.8%	5.5%	1884
43	11.3%	6.3%	1784
50	6.9%	7.1%	1902
54	6.8%	5.6%	1788

Table 6-5 Type I and Type II errors for the shaking detecting test. Type I results are out of 200 epochs while Type II results are out of the remaining epochs given in the right-hand column

The presence of shaking has been defined by applying the progressive movement criteria (see section 3.1) Table 6-5 indicates that GASP is able to detect a high percentage of the applied shaking movements.

Time is a crucial factor in deformation monitoring, and the earlier a deformation is recognised, the greater the possibility of taking corrective measures to mitigate its damage. Table 6-6 shows the ability of GASP to detect the beginning of each shaking series for each baseline in Table 6-1.

Baseline length km / Shaking test	7	13	20	23	27	32	39	43	50	54
Test 1	✓	✓	✓	✓	✓	✓	✓	✓	✓	✓
Test 2	✓	✓	✓	✓	✓	✓		✓	✓	✓
Test 3	✓	✓	✓	✓		✓	✓	✓	✓	✓
Test 4	✓	✓	✓	✓	✓	✓	✓		✓	✓
Test 5	✓	✓	✓	✓	✓	✓	✓	✓	✓	✓
Successful percentage %	100	100	100	100	80	100	80	80	100	100

Table 6-6 The successful of detecting the starts of the vibrations

Table 6-6 shows that GASP is able to detect a movement instantaneously in at least 80% of the cases, which makes it reliable software for structural health monitoring over a variety of baseline lengths.

6.4 SUMMARY AND CONCLUSION

In this chapter the modified GASP software has been shown to give reliable monitoring results. However, the degree of this reliability is baseline length dependent and also relies on the observed satellite geometry (PDOP). As a general observation using more satellites in GASP tends to improve the accuracy. In the urban canyon this may be achieved by involving satellites from other satellite- based systems (e.g. GLONASS). However, GASP is currently coded to employ GPS satellites only. The GASP software is an epoch by epoch processing software; therefore the errors which may affect the results of the current epoch are not the same for other epochs. Taking advantage of this, it is recommended to check the current epoch result against the surrounding epochs' results to distinguish between the true and false computed movement. Moreover, this check can be used to improve the accuracy of detected structural movement when a step change occurs at an epoch. Applying this test makes the structural motion monitoring with the GASP software more robust.

In the foregoing work the Standard Error of Unit Weight of the carrier phase residuals (σ_0) thresholds have been chosen to ensure that at least 80% of the obtained results

are within 10 cm around the true position (see Chapter 5). Therefore, the results of both settlement and shaking tests show that the software is able to detect any movement with magnitude greater than 10 cm with a high success rate. However, some movements' magnitudes were less than 10 cm during the applied shaking movement series, which makes the percentage of Type I errors in the associated test results higher than that of the settlement test (where the step-change was fixed at 20 cm). The study of Type I and Type II errors percentage for both the applied movement tests indicates that at least 84.4 % of the software results are correct.

CONCLUSIONS AND RECOMMENDATIONS

7.1 A SUMMARY OF WORK

This chapter summarises the topics which have been discussed in this research, and recommendations for future work will be given at the end which arise from the outcomes of the research.

The main aim of the research was to extend the use of single epoch GPS software (GASP) over long baselines with increased accuracy, which provides fast data processing, reduces the cost of the GPS application by reducing the number of required base stations and allows the base station to be away from the motion that affects the monitored receiver. This was achieved by improving the quality of the software's ambiguity function inputs (i.e. the moving station initial position and the GPS phase measurements) (Chapters 4 and 5). Employing a single epoch GPS software provides fast data processing, which allows the obtaining of an object's movements to be computed swiftly. Fast GPS data processing is valuable especially

when monitoring a structural deformation, where having real time or near real time positioning data could be crucial for safety and stability purposes.

In order to understand how the GPS system works, its hardware and transmitted signals were reviewed. This review included studying the equations which can be created from the GPS signals. The errors on the GPS observations and their effect on the software positioning accuracy over long baselines were also reviewed in detail. Some of the available corrections for these errors were listed (Chapter 2).

Various methods of using the GPS observations were discussed. These included the formation of differencing techniques, observation linear combinations, static and kinematic cases, and the use of various phase ambiguity resolution methodologies. The effects of applying some available correction models were also stated. These models are available to treat the satellite hardware and clock biases, the receiver hardware and clock biases and the atmospheric effects on the propagation of the GPS signals. Various ambiguity resolution functions (mainly the Ambiguity Function Method) were listed and discussed in order to understand their working mechanism (Chapter 2).

GASP uses a double differencing technique, which reduces the effects of the satellite hardware and clock biases, the Earth rotation and solid Earth tidal deformation. It also employs the Saastamoinen tropospheric model and Niell Mapping Function to mitigate the effect of the troposphere on the results. Thus it was concluded that the main error which prevents the extension of the software applications over long baselines is the ionosphere (Chapter 2).

An introduction to the physics of the ionosphere and its effect on GPS observations was covered. Modelling the ionospheric delays using GPS dual frequency observations was outlined. Also, some of the available ionospheric correction methodologies were described. The availability of using these methodologies in this research was studied. As a result, it was found that some of these methodologies cannot be applied to the software for a number of reasons (such as the importance of

the integer nature of the phase ambiguity in the ambiguity resolution functions, and also the use of one base receiver only) (Chapter 3).

The GASP software was designed to use double differencing code observations to find the initial 'trial' position of the unknown station into the software ambiguity function. The success of the software in identifying the correct ambiguity set is directly related to the quality of this initial 'trial' position. The double differencing technique reduces the effect of the ionosphere. To further mitigate the ionospheric effect, the IGS single layer global ionospheric model was applied to the software. Moreover, a code-based local zenith ionospheric model was created to enhance the removal of the ionospheric effect on the GPS phase observations (Chapter 4).

To find the best positioning inputs (approximate coordinates and corrected carrier phases) to the software ambiguity function, various GPS pseudorange observation solutions were tested. These solutions included using double differencing and un-differencing techniques. Sidereal and regional filters were also applied to the pseudorange observation solutions (Chapter 4).

A Kalman filter was applied to the pseudorange solution results to decrease the noise level of the code-based ionospheric model. The phase measurements σ_0 value was used to filter the final GASP positioning results (Chapter 5).

Finally, the modified software was tested for its ability to detect different types of structural movements (Chapter 6).

7.2 CONCLUSIONS

A number of conclusions can be extracted from this thesis. The following are the main conclusions:

1) It is possible to reduce the effect of the ionosphere by applying a double differencing technique. However, the efficiency of using this technique in resolving the effect of the ionosphere is baseline length dependent. Therefore

applying other corrections in addition to it is essential in order to increase the processing of long baseline data with high accuracy (Section 4.2).

2) The implementation of the IGS 2D ionospheric model has improved the results of GASP. Yet this improvement is limited due to the fact that the spatial resolution of the model is too coarse to affect baselines shorter than several tens of kilometres (Section 4.2).

3) Applying an ionospheric model which is based on measuring the ionospheric delays at a number of base stations (e.g. the regional ionospheric model and the IGS model) is affected by the inter-frequency bias in the satellite and the receiver which varies from station to station (Section 4.2).

4) Using the Code-SPP solution results in the GASP software ambiguity function giving better results than using the Code-DD solution. However, using Code-SPP requires applying correction models for the GPS observation errors that are later cancelled when applying the differencing technique (Section 4.3).

5) There is a regional correlation between the Code-SPP solution positioning results. Therefore applying a regional filter to the Code-SPP solution positioning results improves the quality of the ambiguity function positioning inputs, although it increases their noise level (Section 4.4).

6) For a stationary or near-stationary receiver, multipath causes the pseudorange observation solution results to approximately repeat their values every sidereal day. Therefore, applying a sidereal filter to the Code-SPP or regional filter yields improved positioning input for the ambiguity resolution function. However, its main drawback is that it is only available in the case of a stationary or near-stationary receiver. Furthermore, it also requires the availability of the station data for a mean sidereal day before processing the epochs, and this solution methodology reduces the software processing speed (Section 4.5).

7) Applying a Kalman filter to the Code-SPP results reduces the noise level on the code-based ionospheric model, which improves the quality of the corrected GPS phase measurements (Section 5.3).

8) Applying a σ_0 threshold helps to filter the final coordinate results and improve their reliability. On the other hand, it has a negative aspect as it rejects some of the positioning outputs, which affects the availability of the results, particularly for long baselines. However, the single epoch nature of the GASP software means that potential useful coordinate solutions are maximised (Section 5.4).

9) Using the modified GASP with Code-SPP and IGS ionospheric model, the Kalman filter and σ_0 filter improves the reliability of the GPS single epoch positioning accuracy, compared with the previous version of GASP (Chapters 5 and 6).

10) The modified GASP software gives reliable monitoring results. However this reliability is satellite geometry (PDOP) dependent. GASP is able to detect the beginning of a 20 cm structure movement over baseline lengths up to 54 km in at least 80% of the cases, which makes it reliable software for structural health monitoring (Chapter 6).

11) The modified software can be used to detect a step change with a high reliability, which makes monitoring structural settlements (e.g. embankment, foundation of a dam or a building etc.) achievable. Also, it is able to detect a shaking movement, which allows for the monitoring of rapid structural movements (e.g. vibrations in structures such as long bridges and tall buildings, movements that occur during earthquakes etc.) (Chapter 6).

7.3 RECOMMENDATIONS AND FUTURE WORK

In addition to the L1 and L2 signals, the new generation of the GPS satellites (Block IIF) transmit a new civilian-use GPS signal (L5) with a 1176.45 MHz frequency.

This new signal can be used in GASP to improve the estimation of the ionospheric delay (which is frequency dependent). However, this signal allows the formation of additional linear combinations which can be used to give better ambiguity resolution (Hatch *et al.*, 2000). It can be used to form wide-lane combinations to increase the speed of the ambiguity resolution procedure by reducing the number of possible candidates (Urquhart, 2009). Also, a narrow lane combination can be formed using it to enhance the accuracy of the ambiguity resolution accuracy (Feng *et al.*, 2007).

Additional satellite signal observations can be obtained by employing the GLONASS system in the solution. GLONASS satellites transmit signals at different frequencies. Therefore the phase observation double differencing strategy does not remove the receiver clock bias which affects the ambiguity resolutions (Wang, 2000). Several mathematical and stochastic modelling methodologies have been introduced to overcome this issue. Most of these methods depend on the use of the GLONASS pseudorange observations (Wang, 2000). The GLONASS pseudorange observations can be used together with the GPS pseudorange observations to find accurate positioning inputs into the GASP ambiguity function.

A network of stable base stations can be used to generate a local tomographic ionospheric model (Odijk *et al.*, 2000). Using a network of base stations to create an ionospheric model enhances the ability to perform carrier-phase ambiguity resolution (Fortes *et al.*, 2000). This methodology can provide an ionospheric estimation epoch by epoch. This method can be applied where a network of stable base receivers are available only. For example an available network in the structure region can be used to monitor structural movements. However it cannot be used to monitor widespread movements (e.g. earthquakes).

Further recommendations for improving the GASP result reliability:

- Studying the effect of the available number of shared satellites on the ambiguity function mechanism. This can be done by preventing the software from using a certain number of satellites and re-running the software to compare the results.

- Applying a sidereal filter to the final GASP ambiguity function positioning results to study the effect of removing the multipath from the GPS phase measurement.

- It will be useful to test structural deformation monitoring using RINEX files with one-second intervals between the epochs. This will allow for the analysis of higher frequency movement.

- Monitoring vehicle motion to check the reliability of the software in monitoring high speed movement over different baseline lengths. This can be done by moving the vehicle around the area where a nearby base receiver will always be available to compute an accurate position for the vehicle.

- Filtering the results after they have been processed by the GASP software to distinguish between the true and false structural movements. This can be done by studying windows of the GASP positioning results.

REFERENCES

Abdel-salam, M. (2005) Precise Point Positioning Using Un-Differenced Code and Carrier Phase Observations. PhD Thesis thesis. University of Calgary.

Al-Haifi, Y. M. H. (1996) Short Range GPS Single Epoch Ambiguity Resolution. PhD Thesis thesis. University of Newcastle upon Tyne.

Bevis, M., Businger, S., Herring, T., Rocken, C., Anthes, R. and Ware, R. (1992) 'GPS meteorology- Remote sensing of atmospheric water vapor using the Global Positioning System', Journal of Geophysical Research, 97, (D14), pp. 15787-15801.

Biagi, L., Pietrantonio, G. and Riguzzi, F. (2006) 'Tidal errors and deformations in regional GPS networks', Geodetic Deformation Monitoring: From Geophysical to Engineering Roles, pp. 73-82.

Bock, Y., de Jonge, P. J., Honcik, D., Bevis, M., Bock, L. and Wilson, S. (2001):Proceedings of 10th FIG International Symposium on Deformation Measurements, Orange, California, USA.

Böhm, J., Niell, A., Tregoning, P. and Schuh, H. (2006) 'Global Mapping Function (GMF): A new empirical mapping function based on numerical weather model data', Geophys. Res. Lett, 33, (7), pp. L07304.

Braasch, M. S. and Van Dierendonck, A. J. (1999) 'GPS receiver architectures and measurements', Proceedings of the IEEE, 87, (1), pp. 48-64.

Chen, D. (1993) The Sixth International Technical Meeting of the Satellite Division of the Institute of Navigation, ION GPS-93. Salt Palace Convention Centre, Salt Lake City, Utah, USA,

Cheng, P., John, W. and Zheng, W. (2002) 'Large structure health dynamic monitoring using GPS technology', FIG XXII International Congress, Washington, DC USA, pp.

Choi, K., Bilich, A., Larson, K. and Axelrad, P. (2004) 'Modified Sidereal Filtering: Implications for High-Rate GPS Positioning', Geophysical Research Letters, 31, (L22608).

Colombo, O., HernandezPajares, M., Juan, M. and Sanz, J. (2000) The IEEE "PLANS 2000" Meeting. California, USA, March 13-16.

Colombo, O. L., Hernández-Pajares, M., Juan, J. M., Sanz, J. and Talaya, J. (1999) 'Resolving Carrier-Phase Ambiguities On The Fly, At More Than 100 km From Nearest Reference Site, With The Help Of Ionospheric Tomography', pp. 14-17.

Corbett, S. J. (1994) GPS Single Epoch Ambiguity Resolution for Airborne Positioning and Orientation. PhD Thesis thesis. University of Newcastle upon Tyne.

Corbett, S. J. and Cross, P. A. (1995) 'GPS single epoch ambiguity resolution', Survey Review, 33, (257), pp. 149-160.

Counselman, C. and Gourevitch, S. (1981) 'Miniature Interferometer Terminals for Earth Surveying: Ambiguity and Multipath with Global Positioning System', IEEE Transactions on Geosciences and Remote Sensing, Volume G-19, No.4, p.pp.244-252.

Cross, P. A. (1994) Advanced Least Squares Applied to Position Fixing. London: University of East London (Working Paper No.6).

Dach, R., Hugentobler, U., Fridez, P. and Meindl, M. (2007) 'Bernese GPS Software Version 5.0', Astronomical Institute, University of Bern.

Davis, J. L., Herring, T. A., Shapiro, II, Rogers, A. E. E. and Elgered, G. (1985) 'Geodesy by radio interferometry: Effects of atmospheric modeling errors on estimates of baseline length', Radio Science, 20, (6), pp. 1593-1607.

de Jonge, P. J., Bock, Y. and Bevis, M. (2000):Proceedings of ION GPS-2000, The Institute of Navigation, Alexandria, VA, pp. 337-342.

El-Rabbany, A. (2002) Introduction of GPS.1st ed London, UK: Artech House, Inc.

Enge, P. and Misra, P. (1999) 'Special issue on global positioning system', Proceedings of the IEEE, 87, (1), pp. 3-15.

Erol, B. (2010) 'Evaluation of high-precision sensors in structural monitoring', Sensors, 10, (12), pp. 10803-10827.

Erol, S., Erol, B. and Ayan, T. (2004) 'A General Review of the Deformation Monitoring Techniques and a case study: Analysing Deformations using GPS/Levelling', 20th ISPRS Congress "Geo-Imagery Bridging Continents". Istanbul, Turkey, pp.

Feltens, J. (2003) 'The International GPS service (IGS) ionosphere working group', Advances in Space Research, 31, (3), pp. 635-644.

Feng, Y., Rizos, C. and Higgins, M. (2007) 'Multiple carrier ambiguity resolution and performance benefits for RTK and PPP positioning services in regional areas', Proceedings of ION GNSS 20th international technical meeting of the satellite division, pp. 25-28.

Fortes, L. P., Cannon, M. E. and Lachapelle, G. (2000) 'Testing a Multi-Reference GPS Station Network for OTF Positioning in Brazil'.

Forward, T., Stewart, M., Penna, N. and Tsakiri, M. (2001) The 10th FIG International Symposium on Deformation Measurements. Orange, California, USA,

Foutch, D. A., Housner, G. W. and Jennings, P. C. (1975) 'Dynamic responses of six multistory buildings during the San Fernando earthquake', California Institute of Technology.

Frei, E. and Beutler, G. (1990) 'Rapid Static Positioning based on the Fast Ambiguity Resolution Approach "FARA", Theory and First Results', Manuscripta Geodaetica, Volume 15, p.PP [325-326].

Gao, Y., Heroux, P. and Kouba, J. (1994) International Symposium on Kinematic Systems in Geodesy. Banff, Canada, August 30-September 2.

Gao, Y. and Liu, Z. Z. (2002) 'Precise ionosphere modeling using regional GPS network data', Journal of Global Positioning Systems, 1, (1), pp. 18-24.

Grewal, M. S., Weill, L. R. and Andrews, A. P. (2001) Global positioning systems, inertial navigation, and integration. Wiley Online Library.

Groves, P. D. (2008) Principles of GNSS, inertial, and multisensor integrated navigation systems.

Gunasingam, R. (2003) Single Epoch Ambiguity Resolution using Low-Cost GPS Receivers. MPhil Thesis thesis. University of Newcastle upon Tyne.

Guochang, X. (2003) 'GPS theory, algorithms and applications', in Berlin: Springer-Verlag.

Hatch, R. (1990) 'Instantaneous Ambiguity Resolution. In Kinematic Systems in Geodesy Surveying and Remote Sensing', Banff, Canada.

Hatch, R., Jung, J., Enge, P. and Pervan, B. (2000) 'Civilian GPS: The benefits of three frequencies', GPS Solutions, 3, (4), pp. 1-9.

Ho, C. M., Mannucci, A. T., Lindqwister, U. J. and Pi, X. Q. (1996) 'Global ionospheric perturbations monitored by the worldwide GPS network', Geophys. Res. Lett., 23(22), 3219–3222, doi:10.1029/96GL02763

Hofmann-Wellenhof, B., Lichtenegger, H. and Collins, J. (2001) Global Positioning System Theory and Practice.5th ed New York: Springer-Verlag/Wien.

Hopfield, H. S. (1963) 'The effect of tropospheric refraction on the Doppler shift of a satellite signal', Journal of Geophysical Research, 68, pp. 5157.

Hoque, M. M. and Jakowski, N. (2007) 'Higher order ionospheric effects in precise GNSS positioning', Journal of Geodesy, 81, (4), pp. 259-268.

Hsieh, K. H., Halling, M. W. and Barr, P. J. (2006) 'Overview of vibrational structural health monitoring with representative case studies', Journal of Bridge Engineering, 11, pp. 707.

Ince, C. D. and Sahin, M. (2000) 'Real-time deformation monitoring with GPS and Kalman Filter', Earth Planets and Space, 52, (10), pp. 837-840.

International GNSS Service (2012) IGS Product Availability. Available at: http://igscb.jpl.nasa.gov/network/list.html (Accessed: January 10, 2012).

Kalman, R. E. (1960) 'A New Approach to Linear Filtering and Prediction Problems', Transaction of the ASME,Journal of Basic Engineering, 82, pp. 34-45.

Kalman, R. E. and Bucy, R. (1961) 'New results in Linear Filtering and Prediction Theory', Journal of Basic Engineering, 83D, pp. 95-108.

Kaplan, E. and Hegarty, C. (2006) Understanding GPS: Principles and Applications.Second Edition ed: Artech House, inc.

Kim, D. and Langley, R. B. (2000) 'GPS ambiguity resolution and validation: methodologies, trends and issues', 30.

King, M., Coleman, R. and Morgan, P. (2000) 'Treatment of horizontal and vertical tidal signals in GPS data: A case study on a floating ice shelf', Earth, Planets and Space, 52, (11), pp. 1043-1047.

Klobuchar, J. A. (1987) 'Ionospheric Time-Delay Algorithm for Single-Frequency GPS Users', IEEE Transactions on Aerospace and Electronic Systems, 23, (3), pp. 325-331.

Klobuchar, J. A. (1996) 'Ionospheric Effects on GPS in Global Positioning System: Theory and Applications', Progress in Astronautics and Aeronautics, American Institute of Aeronautics and Astronautics, I, pp. 163.

Knecht, A. and Manetti, L. (2001) 'Using GPS in structural health monitoring', 8th annual international symposium on smart structures and materials, Newport Beach USA, pp. 4-8.

Kouba, J. (2009) 'A guide to using International GNSS Service (IGS) products', Avaialble at: http://igscb. jpl. nasa. gov/components/usage. html.

Kouba, J. and Héroux, P. (2001) 'GPS Precise Point Positioning using IGS orbit products', GPS Solutions, 5, (2), pp. 12-28.

Lambeck, K. (2005) The Earth's variable rotation: geophysical causes and consequences. Cambridge Univ Pr.

Lanyi, G. (1984) 'Tropospheric delay effects in radio interferometry', The Telecommunications and Data Acquisition Progress Report 42-78, April–June 1984, pp. 152-159.

Lanyi, G. E. and Roth, T. (1988) 'A comparison of mapped and measured total ionospheric electron content using global positioning system and beacon satellite observations', Radio Science, 23, (4), pp. 483-492.

Leick, A. (2004) GPS Satellite Surveying.Second Edition ed New York: John Wiley & Sons Inc.

Liu, G., Zhu, Y. and Zhou, R. (2005) 'A new approach of single epoch GPS positioning for landslide monitoring', ACTA Seismologica Sinica, 18, (4), pp. 427-434.

Lovse, J. W., Teskey, W. F. and Cannon, M. E. (1995) 'Dynamic deformation monitoring of tall structure using GPS technology', Journal of Surveying Engineering, 121, pp. 35.

Mader, G. L. (1999) 'GPS antenna calibration at the National Geodetic Survey', GPS Solutions, 3, (1), pp. 50-58.

Maybeck, P. (1979) Stochastic Models, Estimation, and Control. New York: Academic Press, Inc.

Meng, X. (2002) Real-time Deformation Monitoring of Bridges Using GPS/Accelerometers. PhD Thesis thesis. The University of Nottingham.

Nickitopoulou, A., Protopsalti, K. and Stiros, S. (2006) 'Monitoring dynamic and quasi-static deformations of large flexible engineering structures with GPS: Accuracy, limitations and promises', Engineering Structures, 28, (10), pp. 1471-1482.

Niell, A. E. (1996) 'Global Mapping Functions for the Atmosphere Delay at Radio Wavelengths', Journal of Geophysical Research, 101, (No.B2), pp. 3227-3246.

Odijk, D. (2000) 'Improving ambiguity resolution by applying ionosphere corrections from a permanent GPS array', Earth, Planets and Space, 52, (10), pp. 675-680.

Odijk, D., Teunissen, P. J. G. and Tiberius, C. (2002) 'Triple-Frequency Ionosphere-Free Phase Combinations for Ambiguity Resolution', Proceeding of the ENC-GNSS.

Odijk, D., van der Marel, H. and Song, I. (2000) 'Precise GPS positioning by applying ionospheric corrections from an active control network', GPS Solutions, 3, (3), pp. 49-57.

Ott, L. and Longnecker, M. (2008) An introduction to statistical methods and data analysis. Duxbury Pr.

Petrie, E. J., King, M. A., Moore, P. and Lavallée, D. A. (2010) 'Higher order ionospheric effects on the GPS reference frame and velocities', J Geophys Res, 115, (B3), pp. B03417.

Ragheb, A. (2007) Filtered and semi-continuous single epoch GPS for deformation monitoring. PhD Thesis thesis. University of Newcastle upon Tyne.

Ragheb, A. E., Edwards, S. J. and Clarke, P. J. (2010) 'Using Filtered and Semicontinuous High Rate GPS for Monitoring Deformations', Journal of Surveying Engineering, 136, pp. 72.

Raquet, J. F. (1998) 'Development of a method for kinematic GPS carrier-phase ambiguity resolution using multiple reference receivers', in Citeseer.

Raymund, T. D., Austen, J. R., Franke, S. J., Liu, C. H., Klobuchar, J. A. and Stalker, J. (1990) 'Application of computerized tomography to the investigation of ionospheric structures', Radio Science, 25, (5), pp. 771-789.

Raziq, N. and Collier, P. (2006) 'High precision GPS deformation monitoring using single receiver carrier phase data', in Sanso, F. and Gil, A. J.(eds) Geodetic Deformation Monitoring: from Geophysical to Engineering Roles. Vol. 131, pp. 95-102.

Rutledge, D., Gnipp, J. and Kramer, J. (2001) The 10th FIG International Symposium on Deformation Measurements. Orange, California, USA,

Saastamoinen, J. (1972) 'Contribution to the Theory of Atmospheric Refraction', Journal of Geodesy, 46, (3), pp. pp.279-298.

Schaer, S. (1999) Mapping and Predicting the Earth's Ionosphere Using the Global Positioning System. PhD Thesis thesis. University of Bern.

Seeber, G. (2003) Satellite Geodesy: Foundations, Methods, and Applications.2nd ed Berlin New York: Walter de Gruyter.

Spofford, P. R. and Remondi, B. W. (1994) 'The national geodetic survey standard GPS format SP3', SP3-a format) available from the IGS website: http://igscb.jpl.nasa.gov/igscb/data/format/sp3.txt.

Teunissen, P. J. G. (1995) 'The least-squares ambiguity decorrelation adjustment: a method for fast GPS integer ambiguity estimation', Journal of Geodesy, 70, (1), pp. 65-82.

Teunissen, P. J. G. and Kleusberg, A. (1998) GPS for Geodesy.2nd ed Berlin-Heidelberg-New York: Springer-Verlag.

Tiberius, C. and Kenselaar, F. (2003) 'Variance component estimation and precise GPS positioning: case study', Journal of Surveying Engineering, 129, pp. 11.

Urquhart, L. (2009) 'An analysis of multi-frequency carrier phase linear combinations for GNSS', Techn. Report, (263).

Vanicek, P. and Krakiwsky, E. J. (1986) 'Geodesy, the concepts', Amsterdam; New York: North Holland; New York, NY: Sole distributors for the USA and Canada, Elsevier Science Pub. Co., 1986. 2nd ed., 1.

Wang, J. (2000) 'An approach to GLONASS ambiguity resolution', Journal of Geodesy, 74, (5), pp. 421-430.

Welch, G. and Bishop, G. (1995) 'An introduction to the Kalman filter', University of North Carolina at Chapel Hill, Chapel Hill, NC, 7, (1).

Wells, D. E. (1974) 'Doppler satellite control', Geodesy and Geomatics Engineering Technical Reports; 29.

Wells, D. E., Beck, N., Delikaraoglou, D., Kleusberg, A., Krakiwsky, E. J., Lachapelle, G., Langley, R. B., Nakiboglu, M., Schwarz, K. P. and Tranquilla, J. M. (1986) 'Guide to GPS-Positioning: Fredericton', NB, Canada (Canadian GPS Associates).

Witchayangkoon, B. (2000) Elements of GPS precise point positioning. thesis. University of New Brunswick.

Wübbena, G., Menge, F., Schmitz, M., Seeber, G. and Völksen, C. (1996):Institute of Navigation.

Xu, G. (2007) GPS: theory, algorithms, and applications. Springer Verlag.

Zhu, S. and Groten, E. (1988) 'Relativistic effects in GPS', GPS-Techniques Applied to Geodesy and Surveying, pp. 41-46.

Zumberge, J. F., Watkins, M. M. and Webb, F. H. (1997) 'Characteristics and applications of precise GPS clock solutions every 30 seconds', NAVIGATION-LOS ANGELES AND WASHINGTON-, 44, pp. 449-456.

STATISTICAL FACTORS OF THE RESULTS OF ALL TESTED DAYS

The RINEX files of the stations in Table 4-1 have been downloaded for different dates and over various periods over different years (days 66, 190 and 320 in years 2007, 2009 and 2011). Each of the following ten figures show the final GASP software position Median Absolute Deviation (MAD), the probability of getting positions within 10 cm around the true position, and the percentage of epochs which give an Ambiguity Function Value (AFV) larger than 0.9 over different baseline lengths, when each of the solutions in Table 4-2 results only are used as the initial inputs into the ambiguity function, respectively.

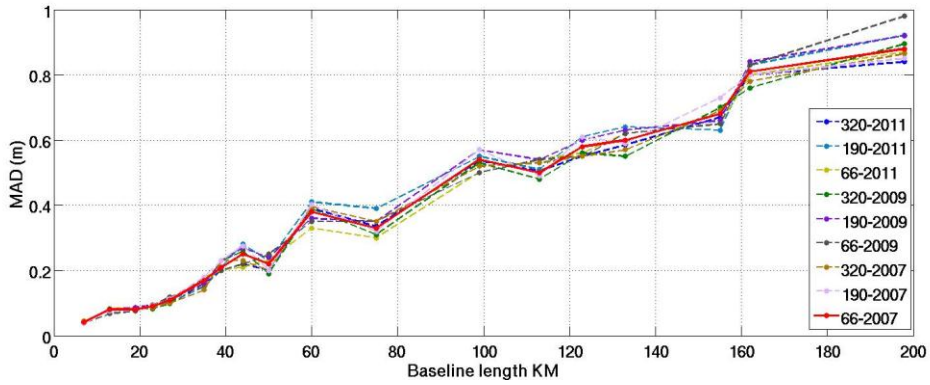

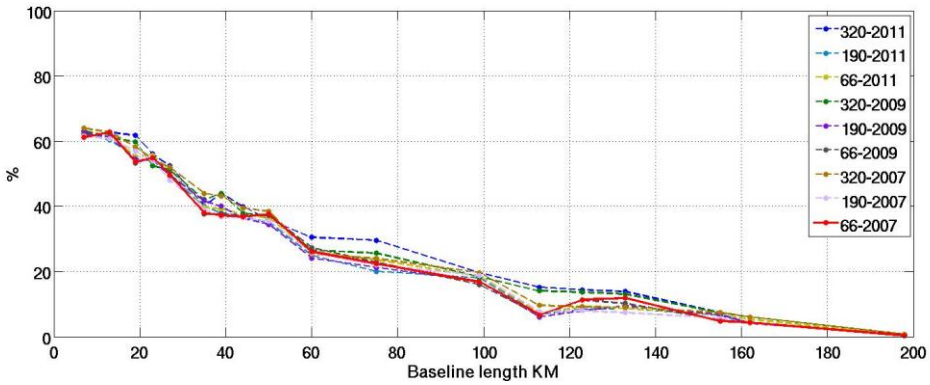

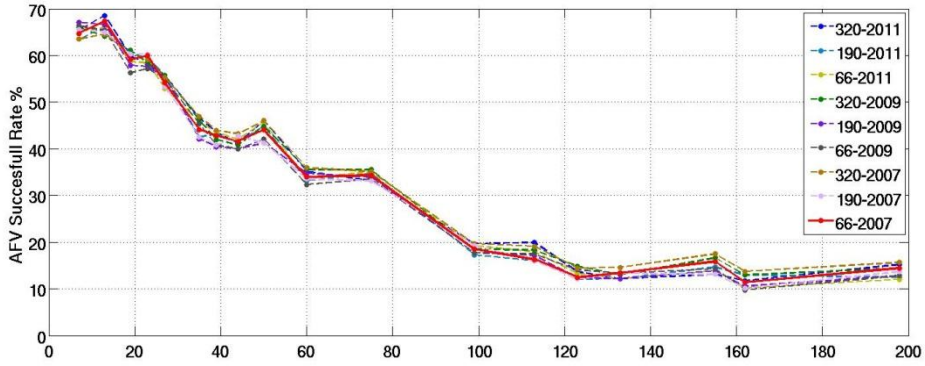

Figure A-1 Solution1: Code-DD solution without applying any ionospheric correction, GASP software final results statistical factors.

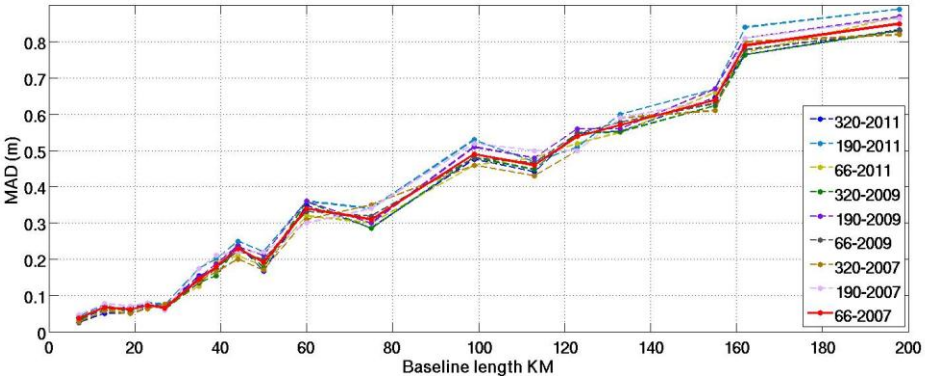

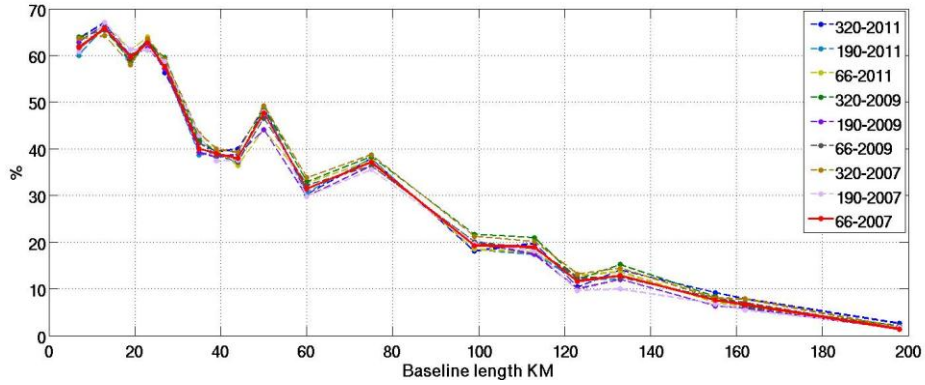

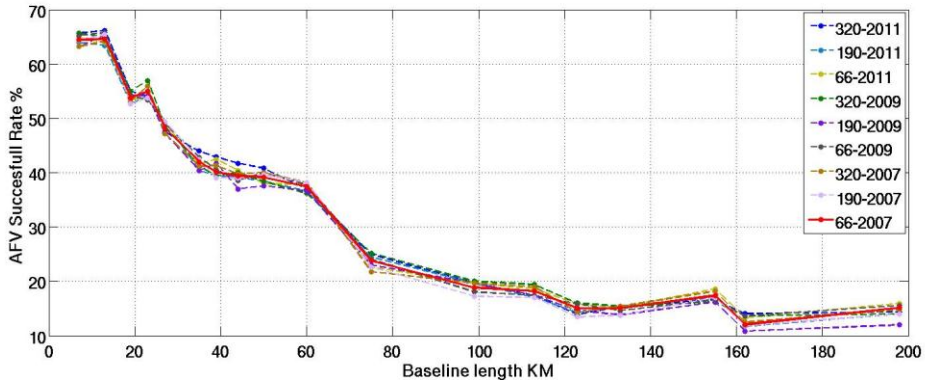

Figure A-2 Solution2: Code-DD solution with the implementation of the IGS 2D ionospheric model, GASP software final results statistical factors.

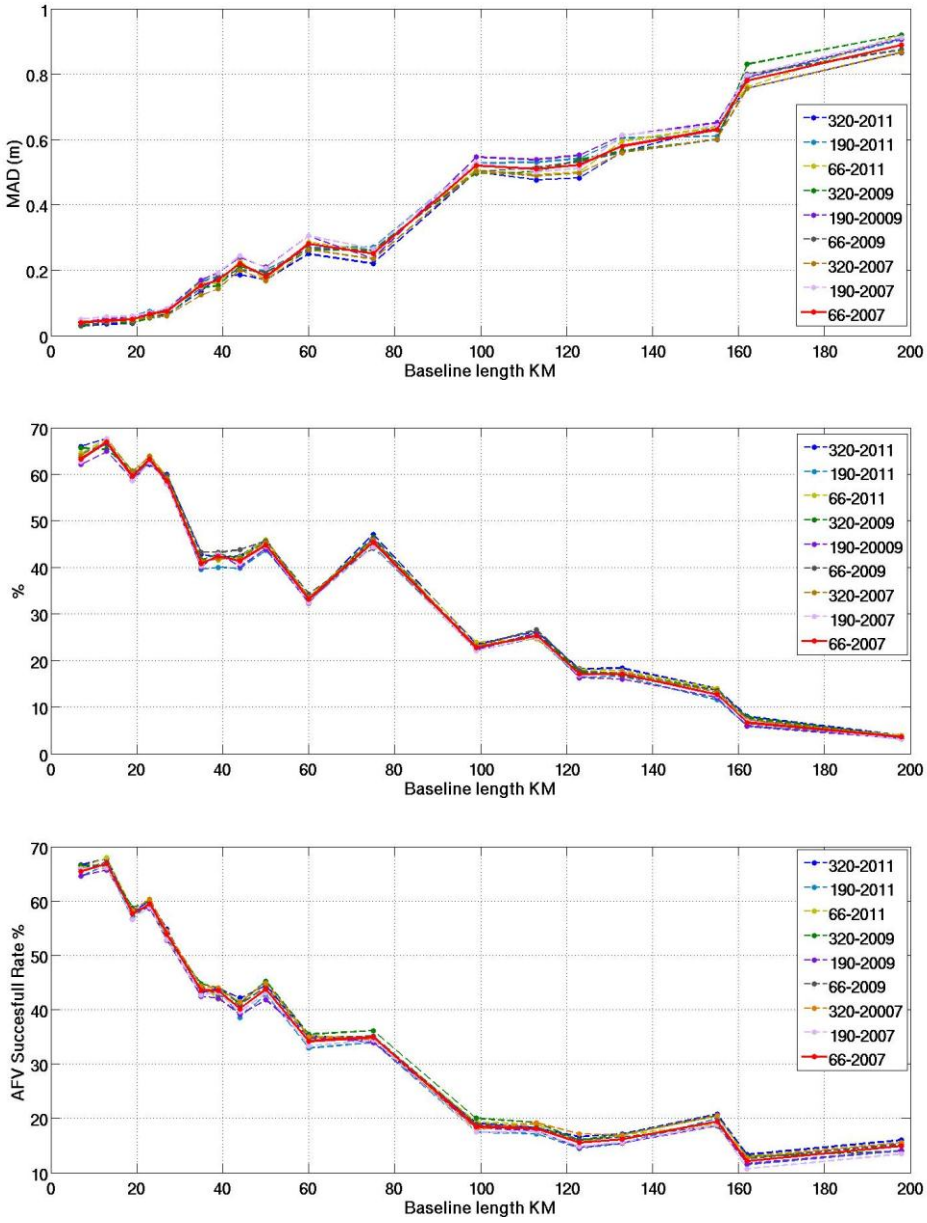

Figure A-3 Solution3: Code-DD solution with the implementation of the IGS 2D ionospheric model and Geo-free ionospheric correction, GASP software final results statistical factors.

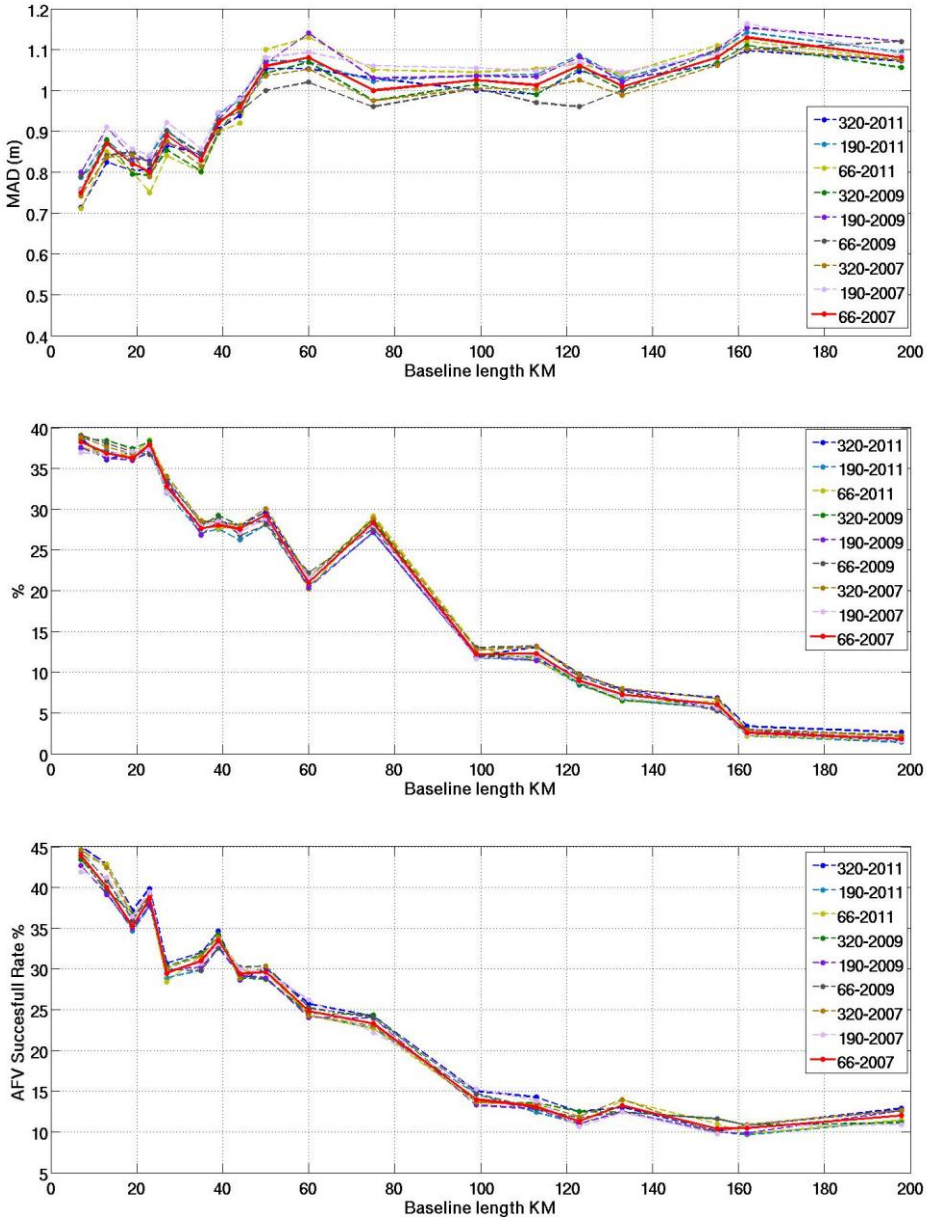

Figure A-4 Solution 4: Code-SPP solution without applying any ionospheric correction, GASP software final results statistical factors.

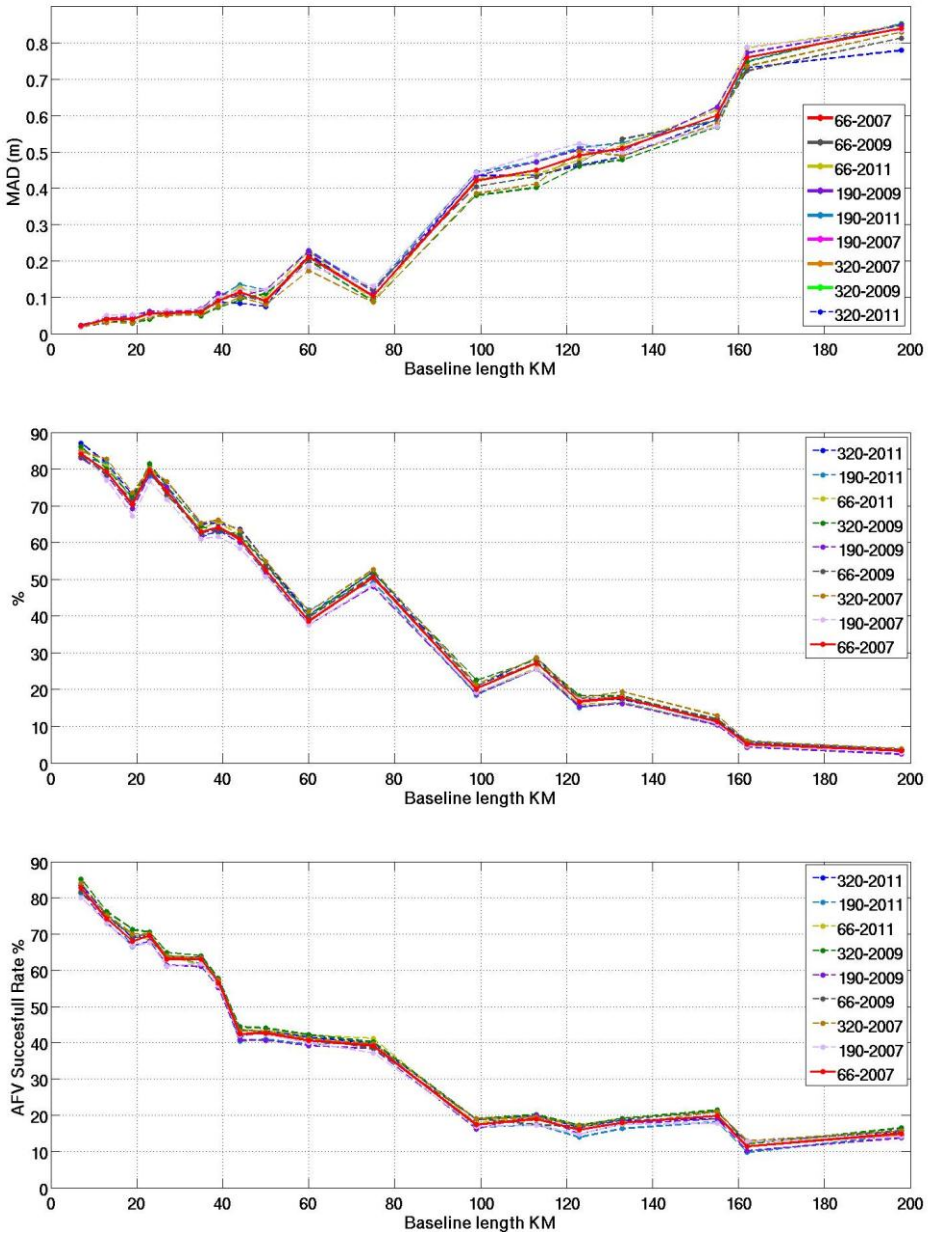

Figure A-5 Solution 5: Code-SPP solution with the implementation of the IGS 2D ionospheric model, GASP software final results statistical factors.

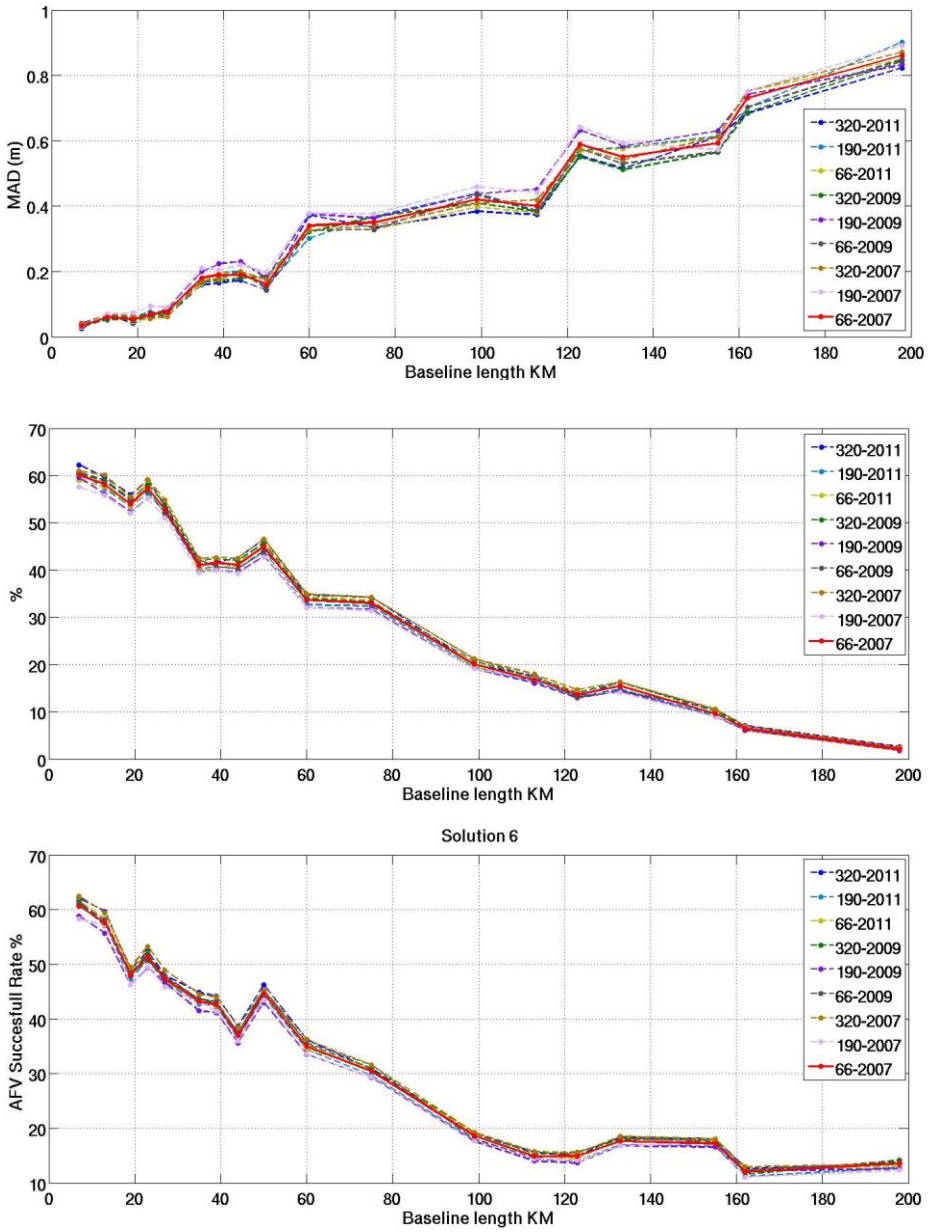

Figure A-6 Solution 6: Code-SPP solution with the implementation of the DCBs correction only, GASP software final results statistical factors.

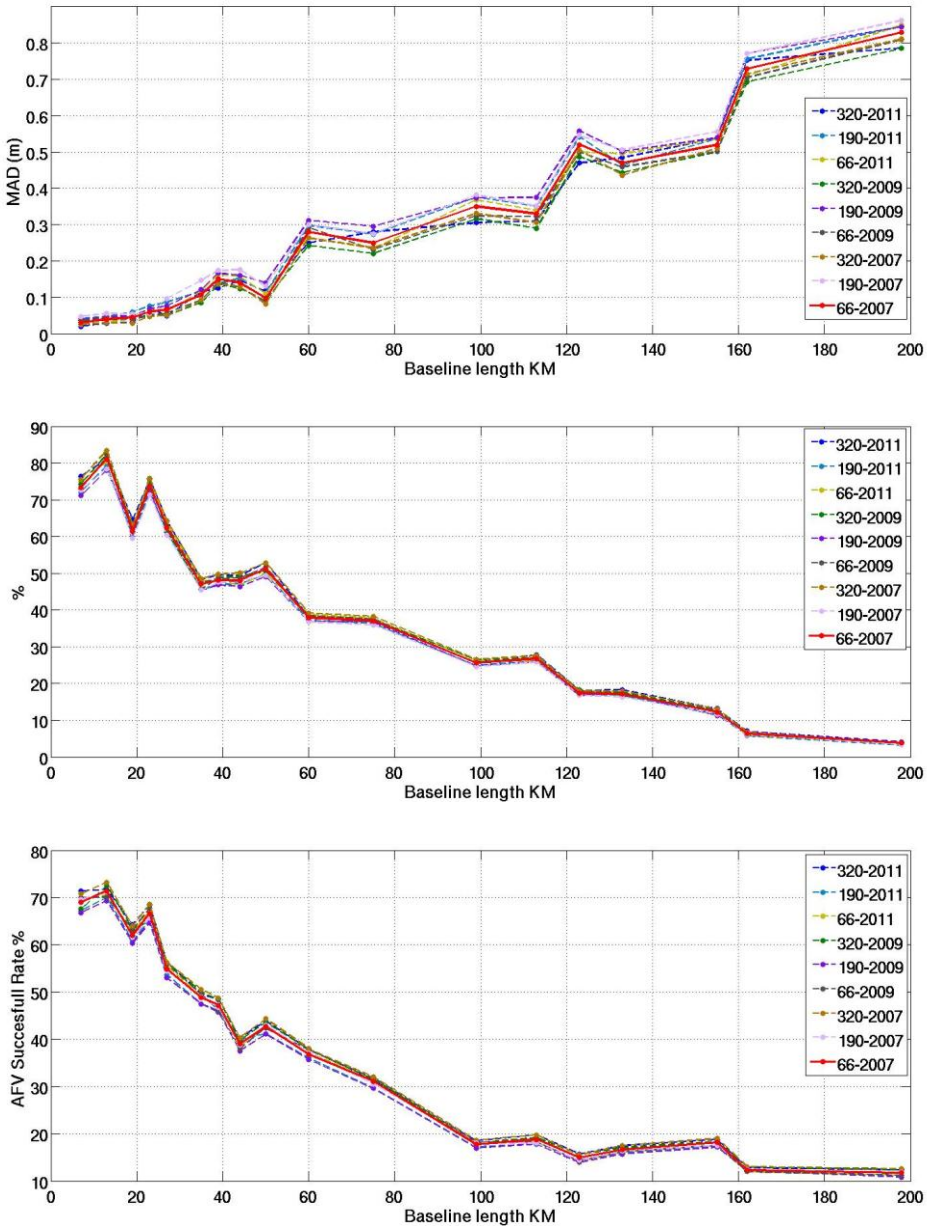

Figure A-7 Solution 7: Regional filter solution without applying any ionospheric correction, GASP software final results statistical factors.

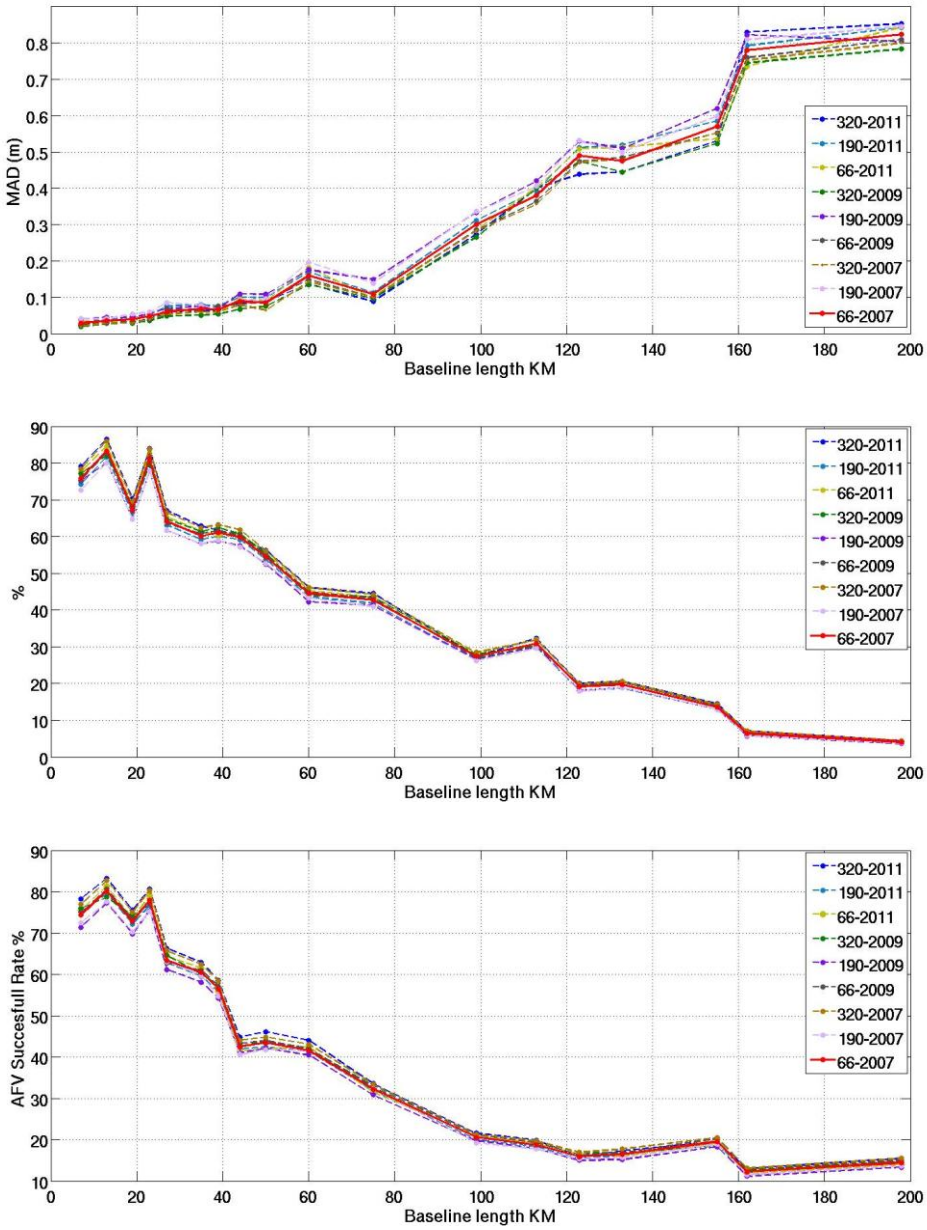

Figure A-8 Solution 8: Regional filter solution with the implementation of the IGS 2D ionospheric model, GASP software final results statistical factors.

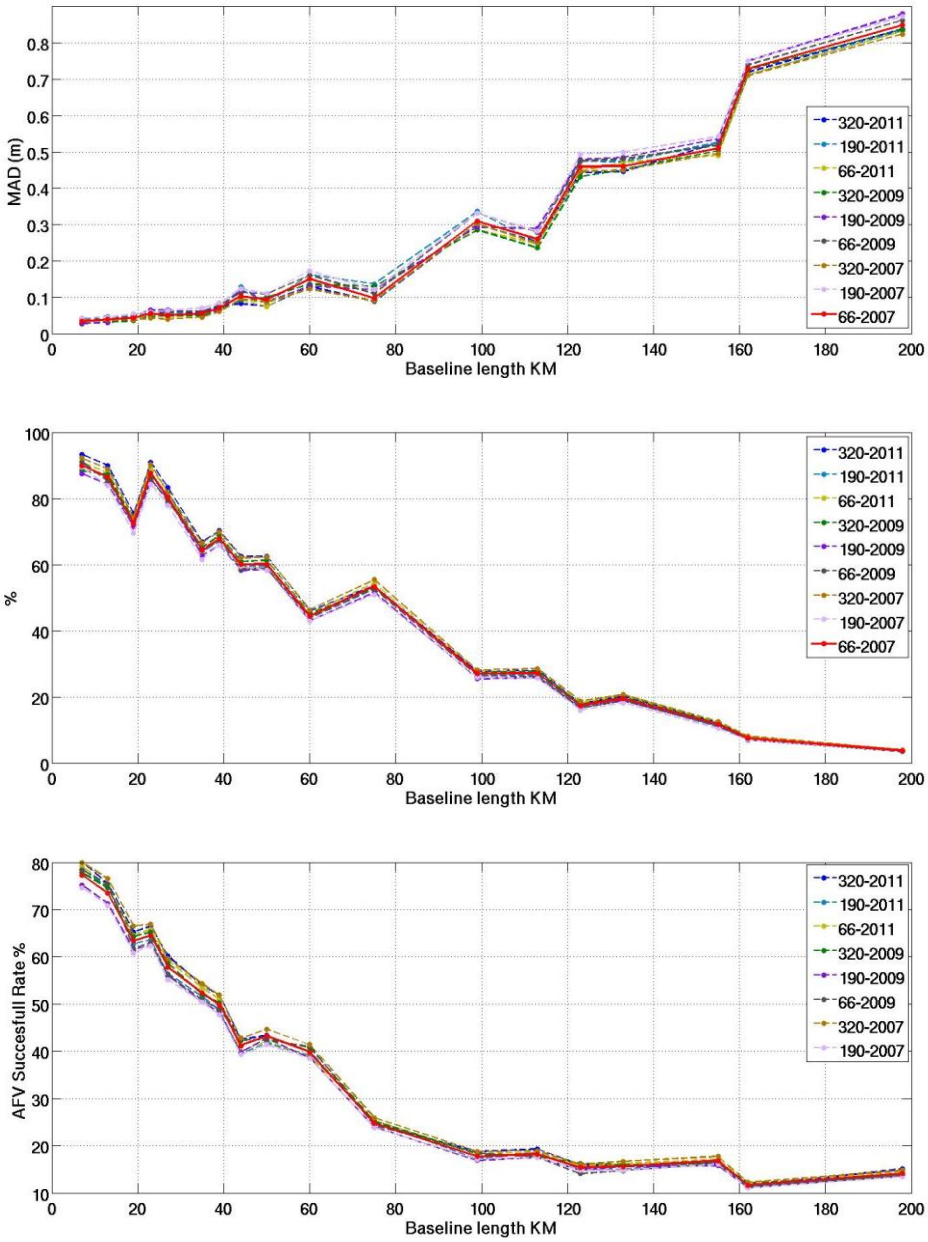

Figure A-9 Solution 9: Sidereal filter solution without applying any ionospheric correction, GASP software final results statistical factors.

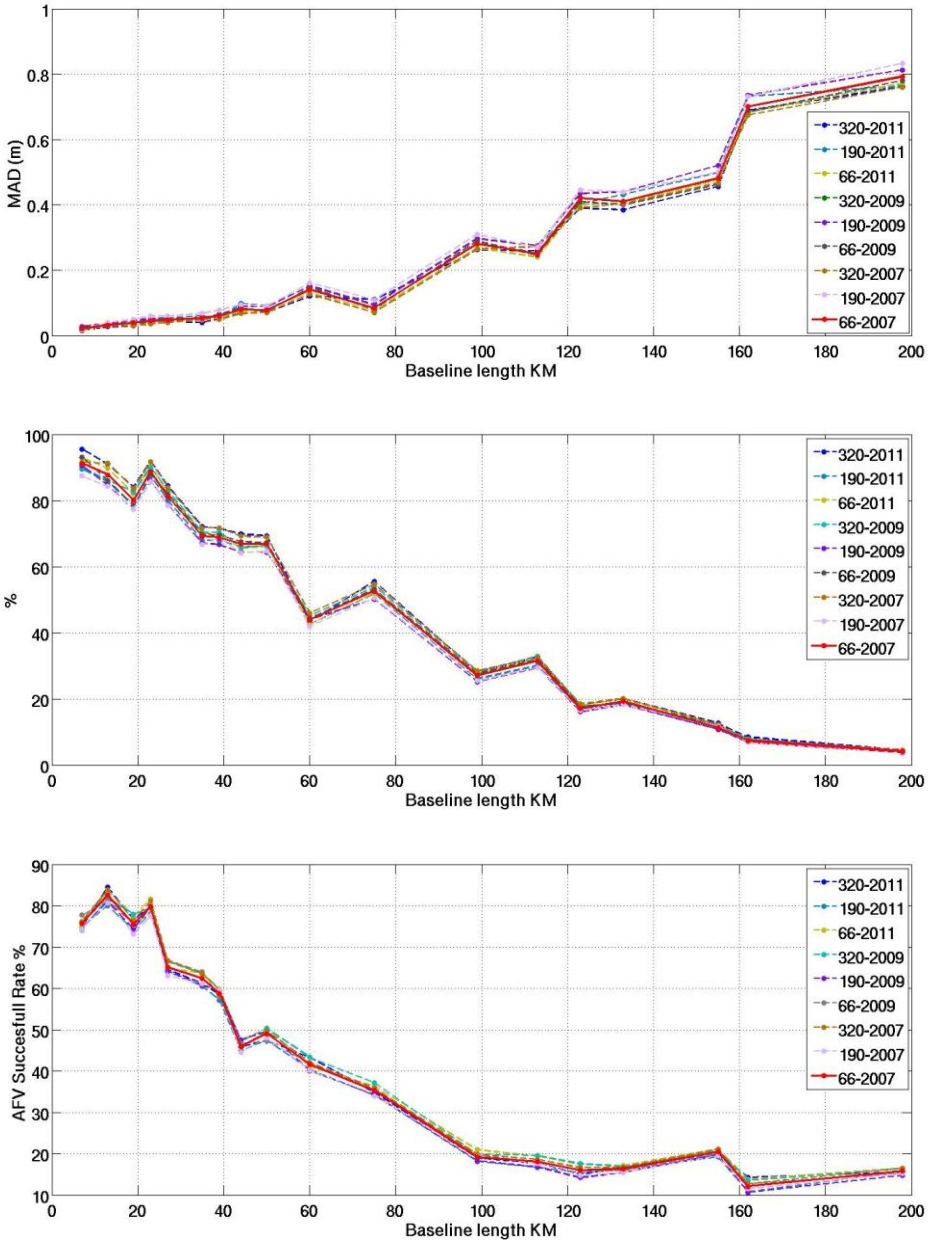

Figure A-10 Solution 10: Sidereal filter solution with the implementation of the IGS 2D ionospheric model, GASP software final results statistical factors.

REGIONAL FILTER RESULTS

Each of the following figures shows the results of applying a regional filter on the undifferenced code solution (Code-SPP) results (the receiver clock offset, the ionospheric value at the station zenith point and the differences between the computed positions and the true position coordinates) for each baseline in Table 4-1 over the 21 hours on the day 66/2007, respectively.

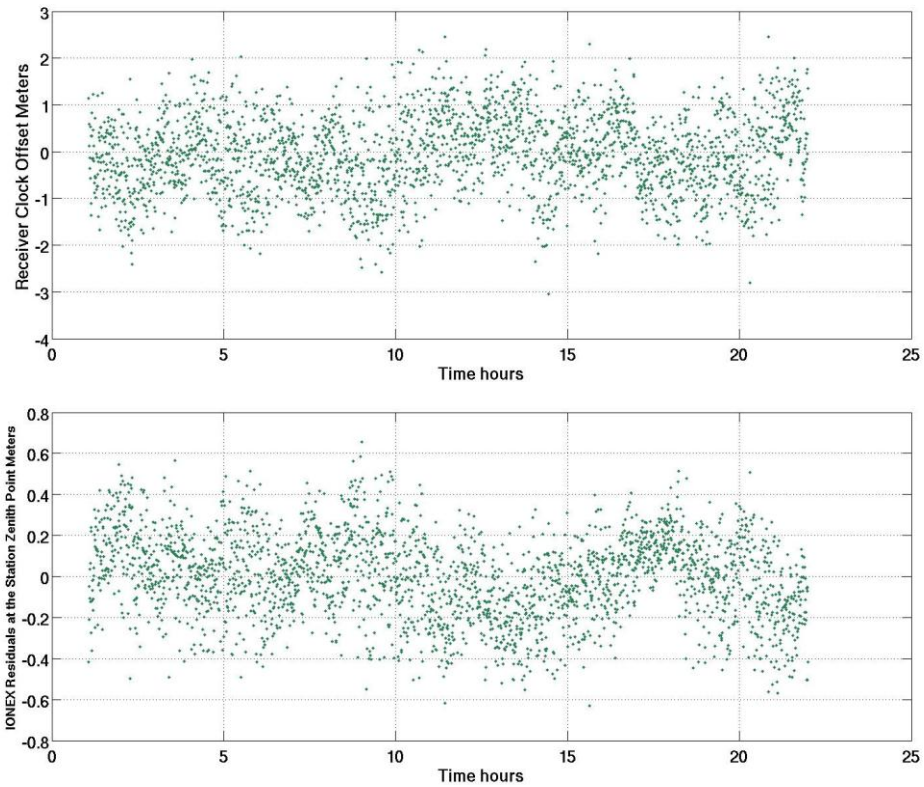

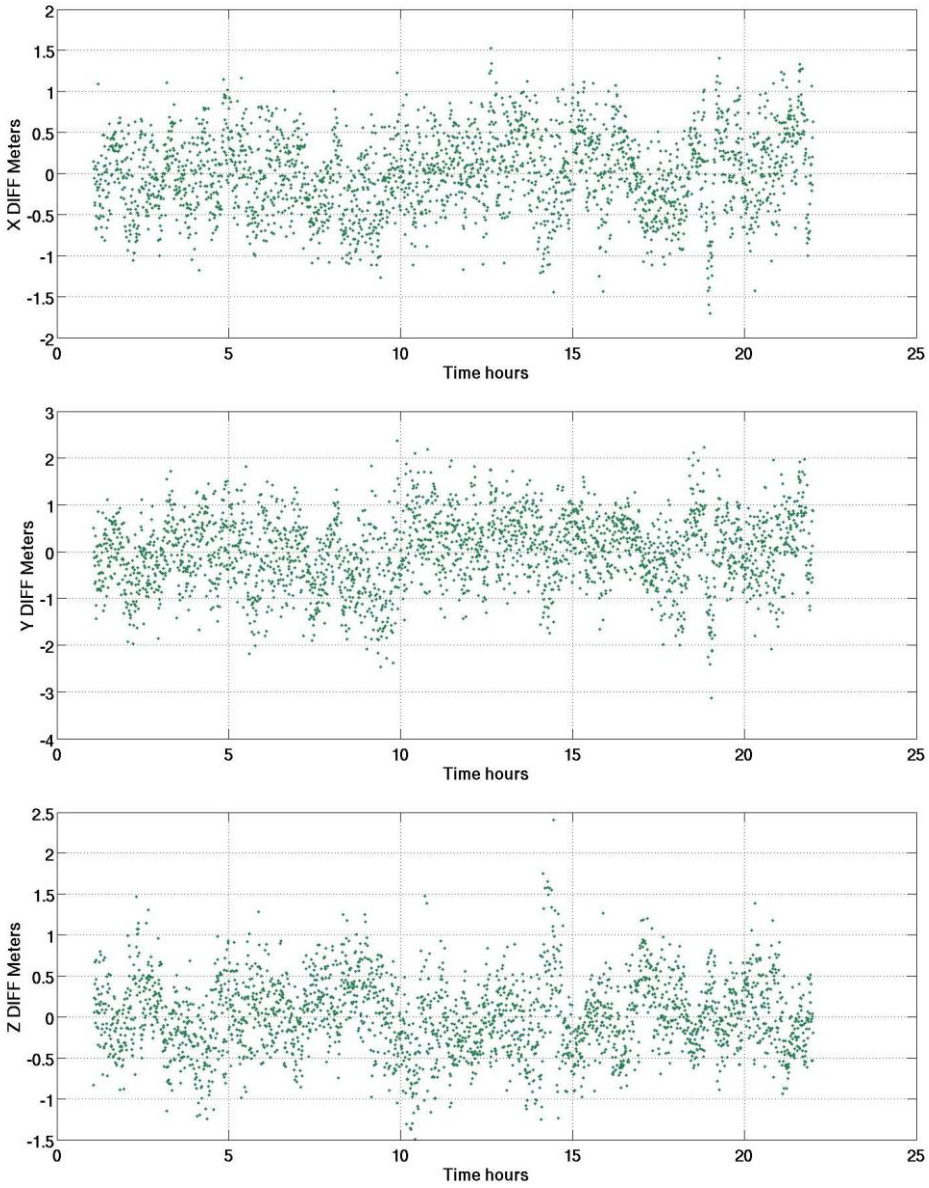

Figure B-11 Regional filter code solution: 7 KM baseline results

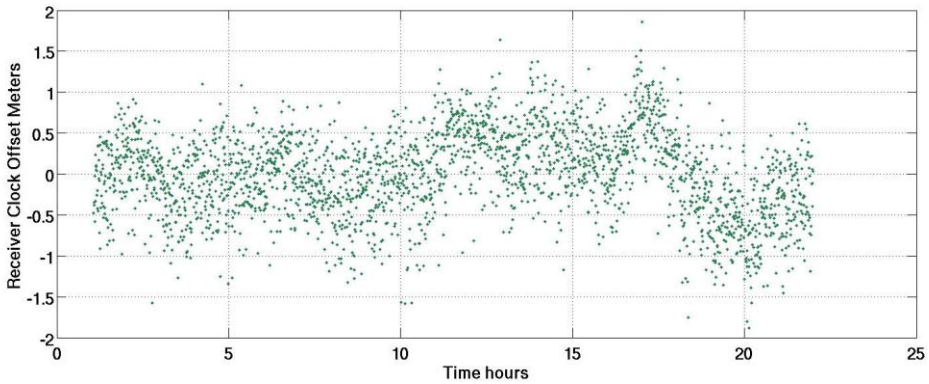

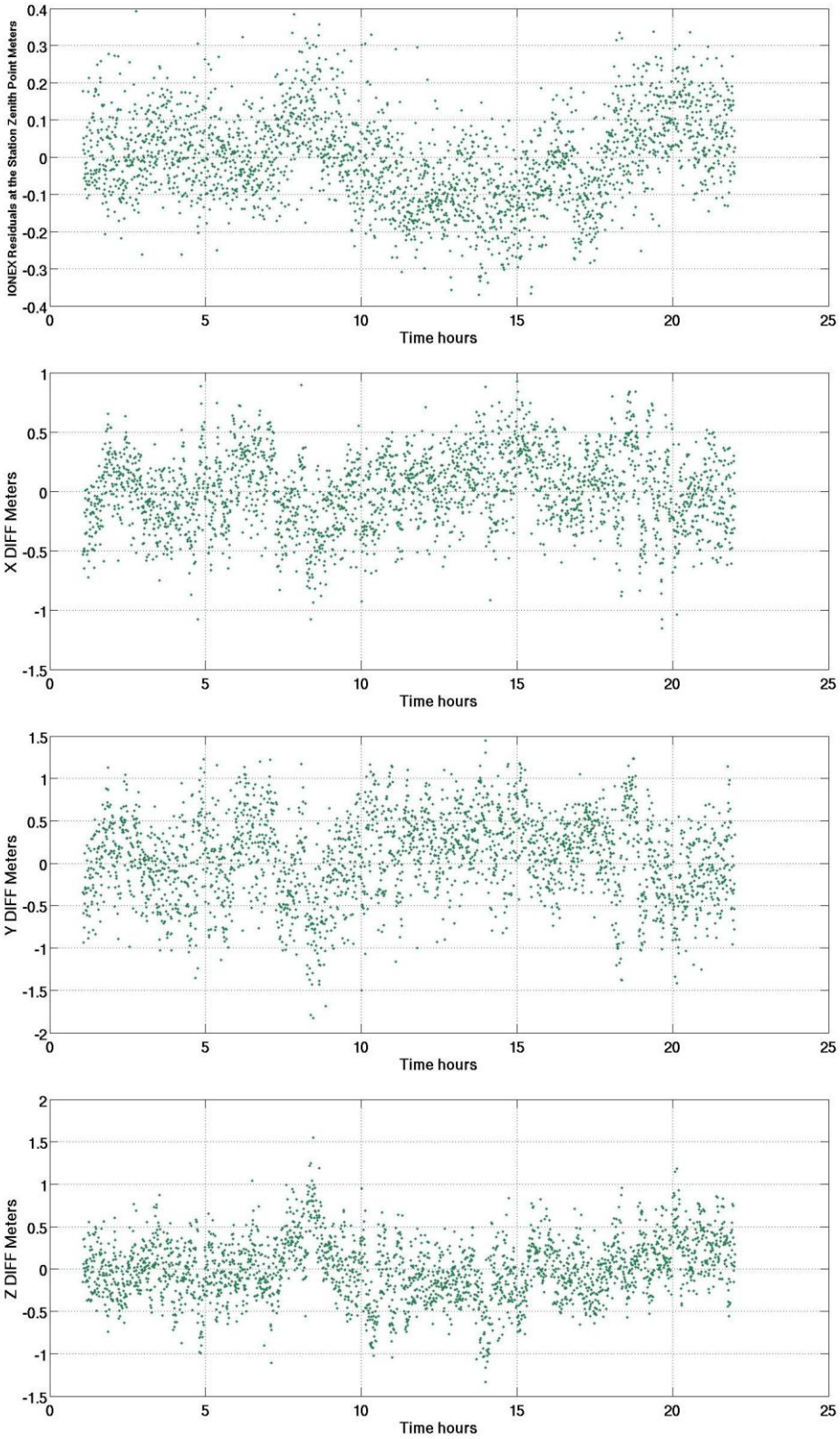

Figure B-12 Regional filter code solution: 13 KM baseline results

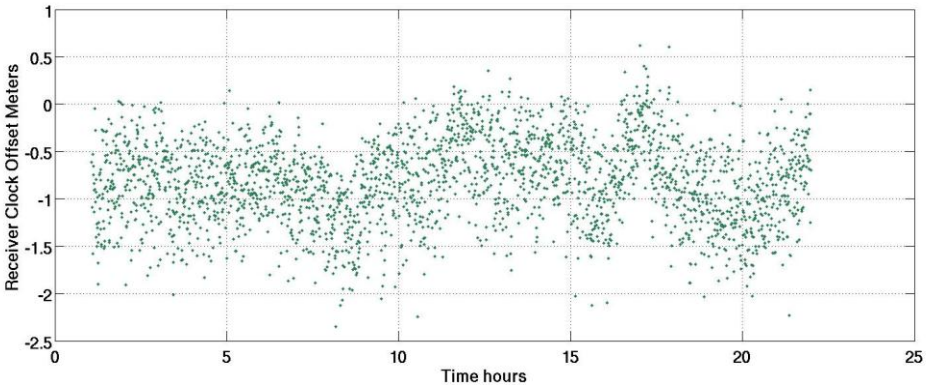
Receiver Clock Offset Meters
1
0.5
0
-0.5
-1
-1.5
-2
-2.5
0
5
10
15
20
25
Time hours

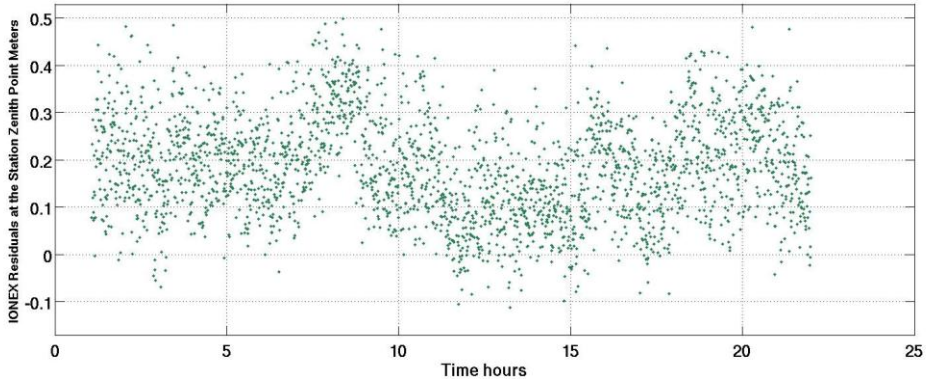
IONEX Residuals at the Station Zenith Point Meters
0.5
0.4
0.3
0.2
0.1
0
-0.1
0
5
10
15
20
25
Time hours

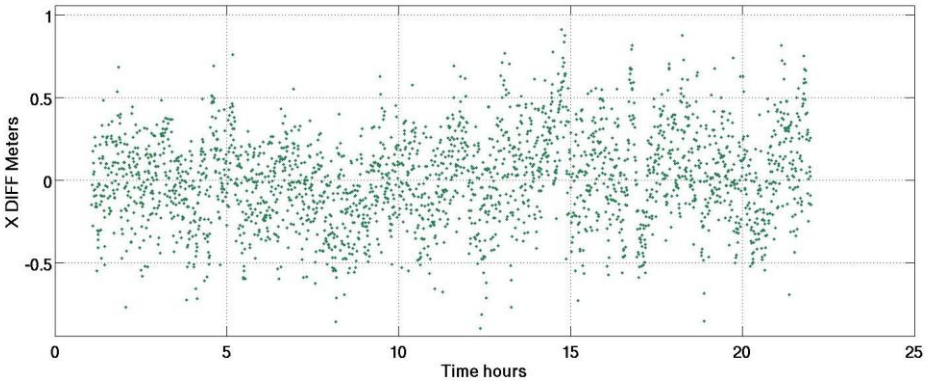
X DIFF Meters
1
0.5
0
-0.5
0
5
10
15
20
25
Time hours

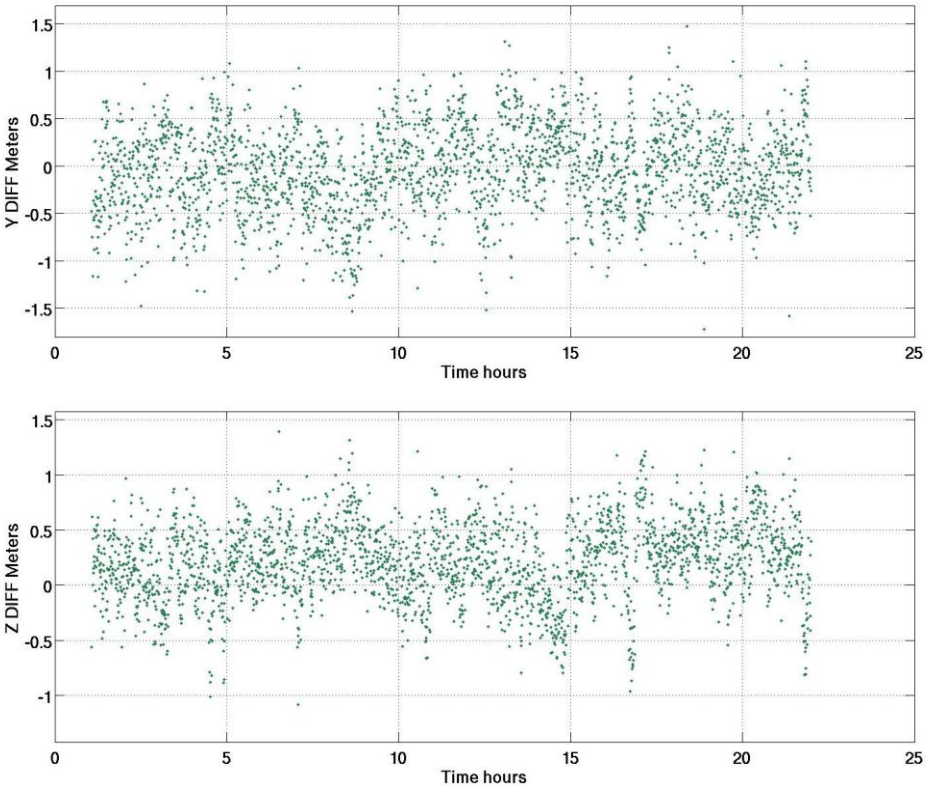

Figure B-13 Regional filter code solution: 19 KM baseline results

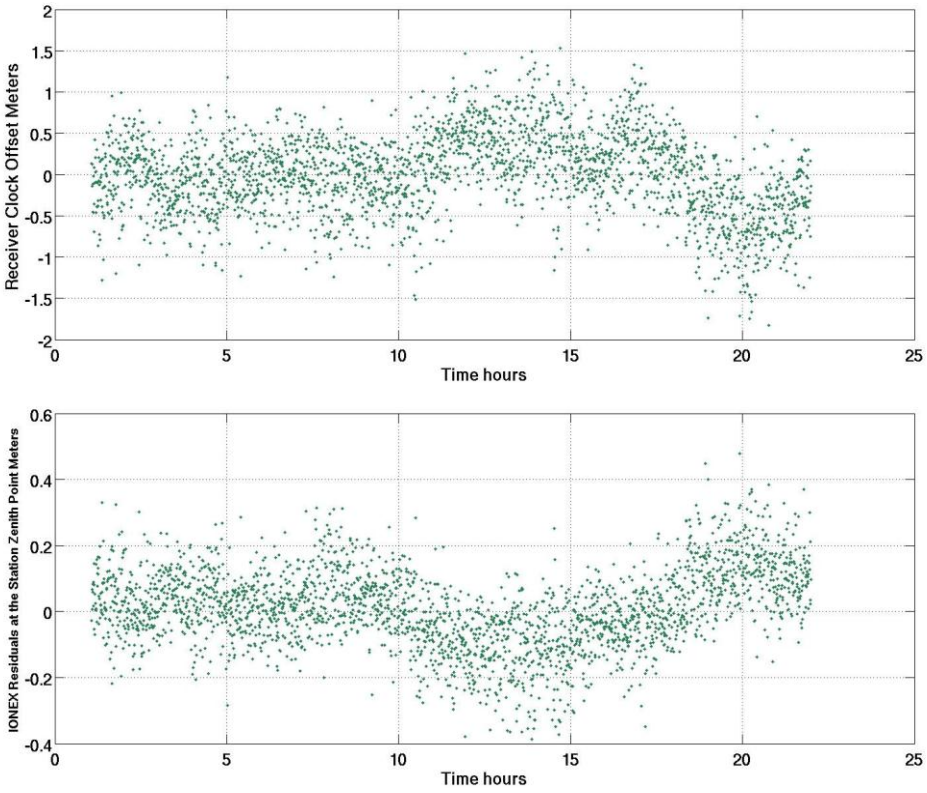

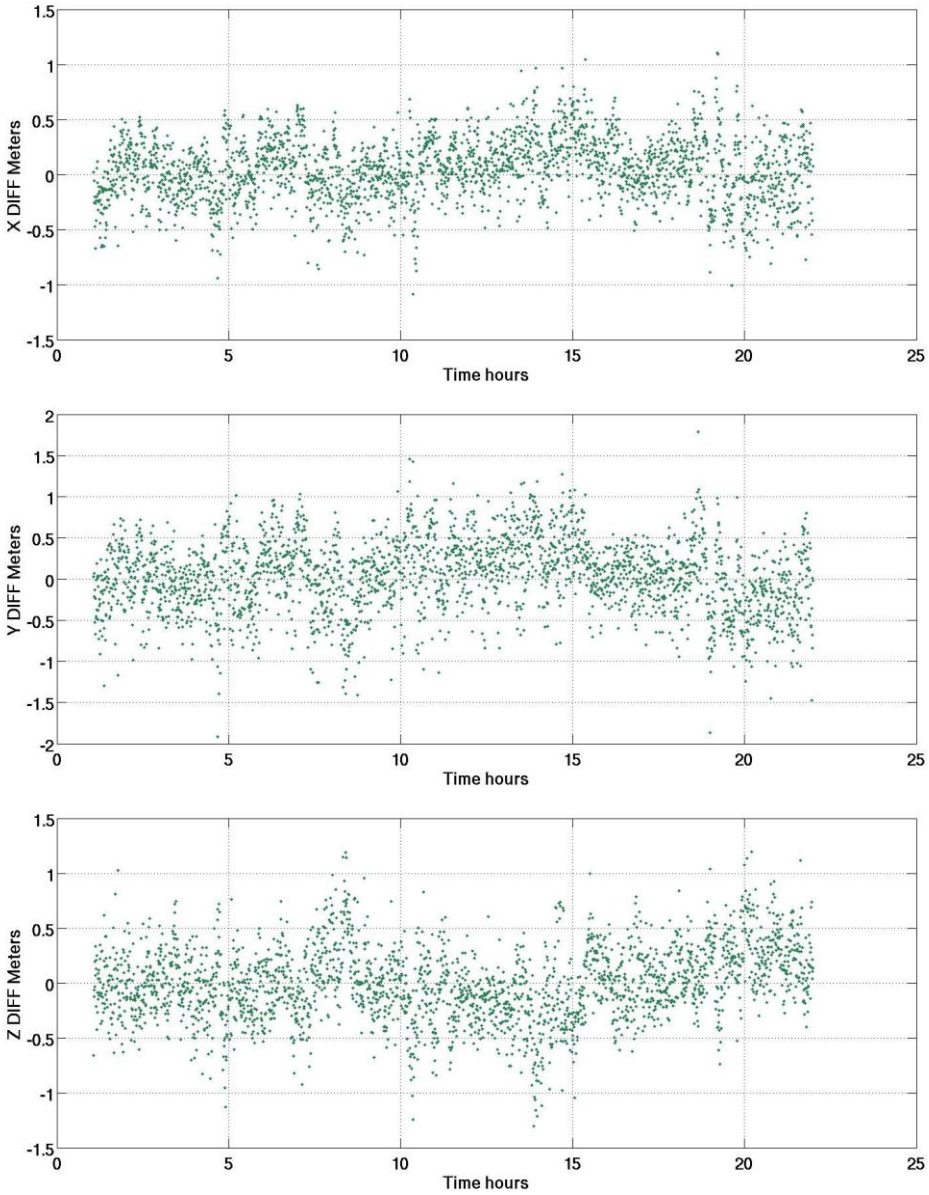

Figure B-14 Regional filter code solution: 23 KM baseline results

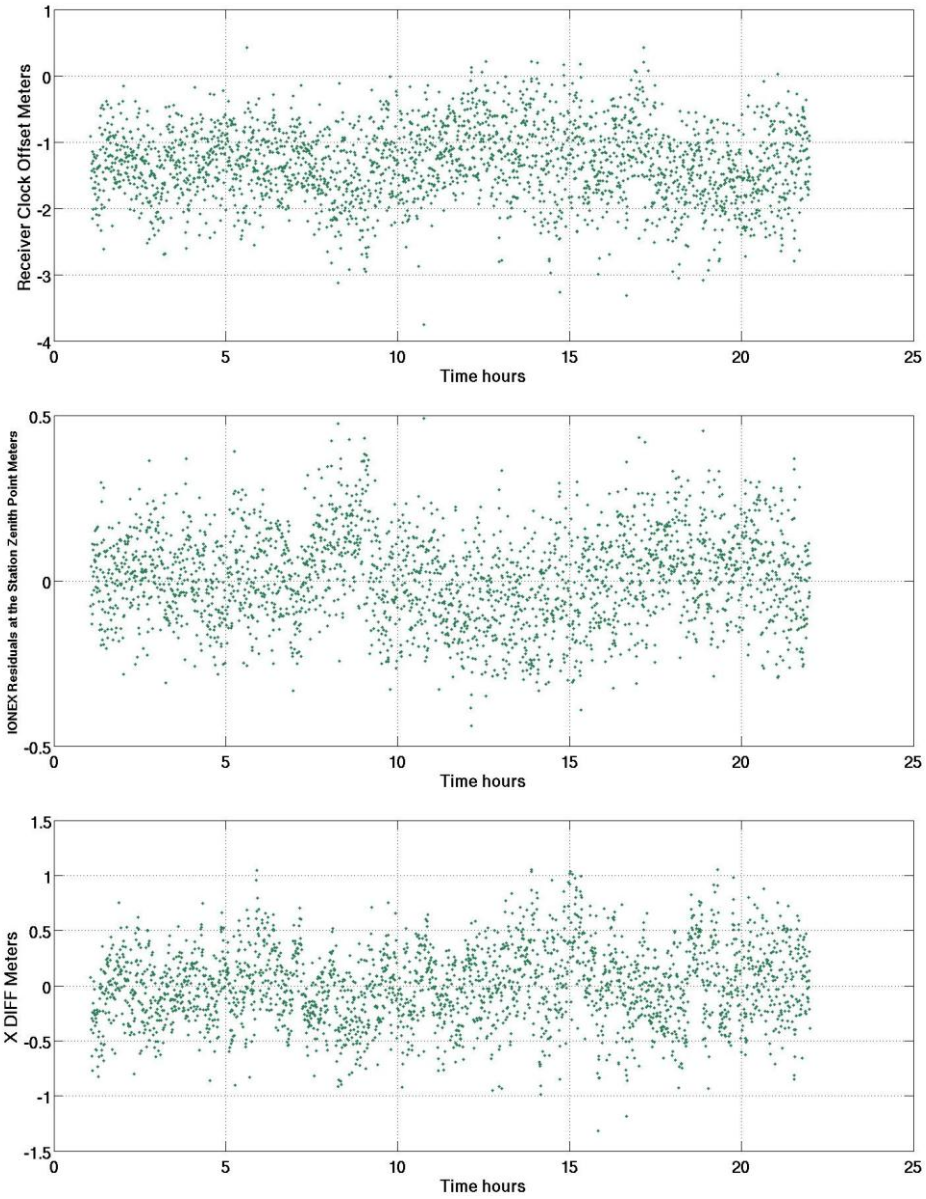
Receiver Clock Offset Meters
Time hours
IONEX Residuals at the Station Zenith Point Meters
Time hours
X DIFF Meters
Time hours

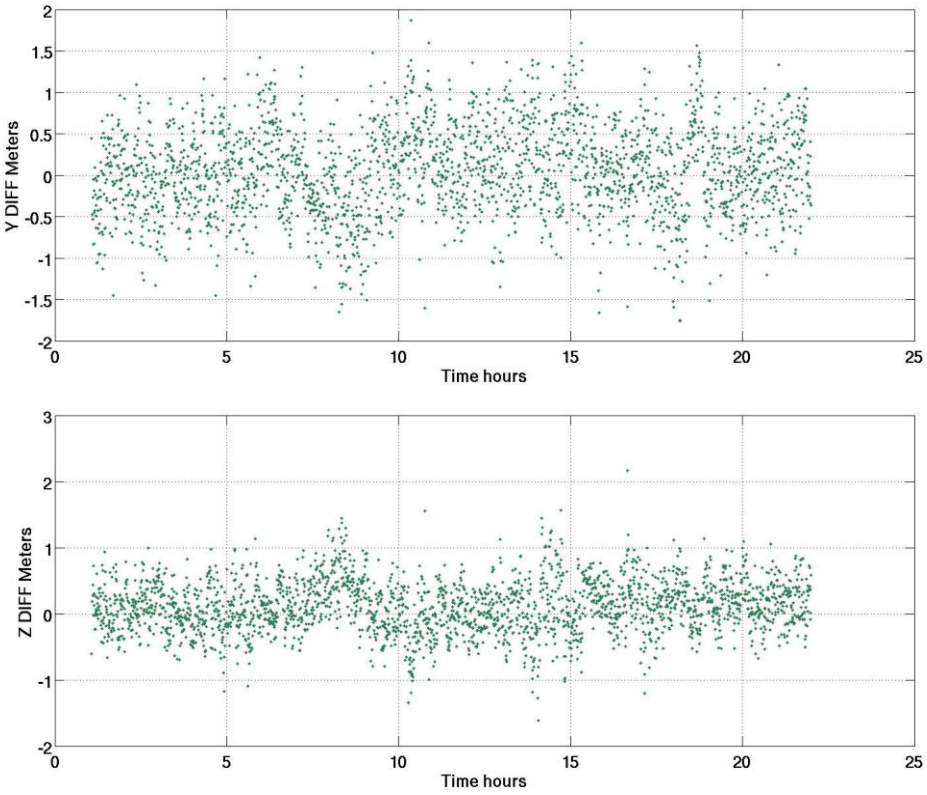

Figure B-15 Regional filter code solution: 27 KM baseline results

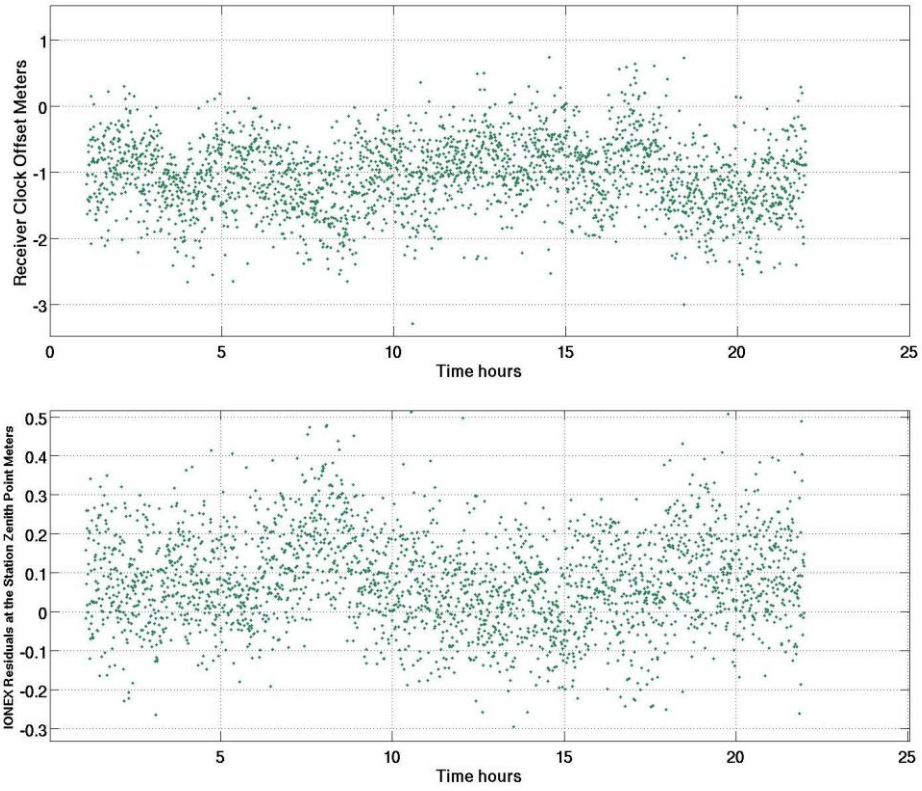

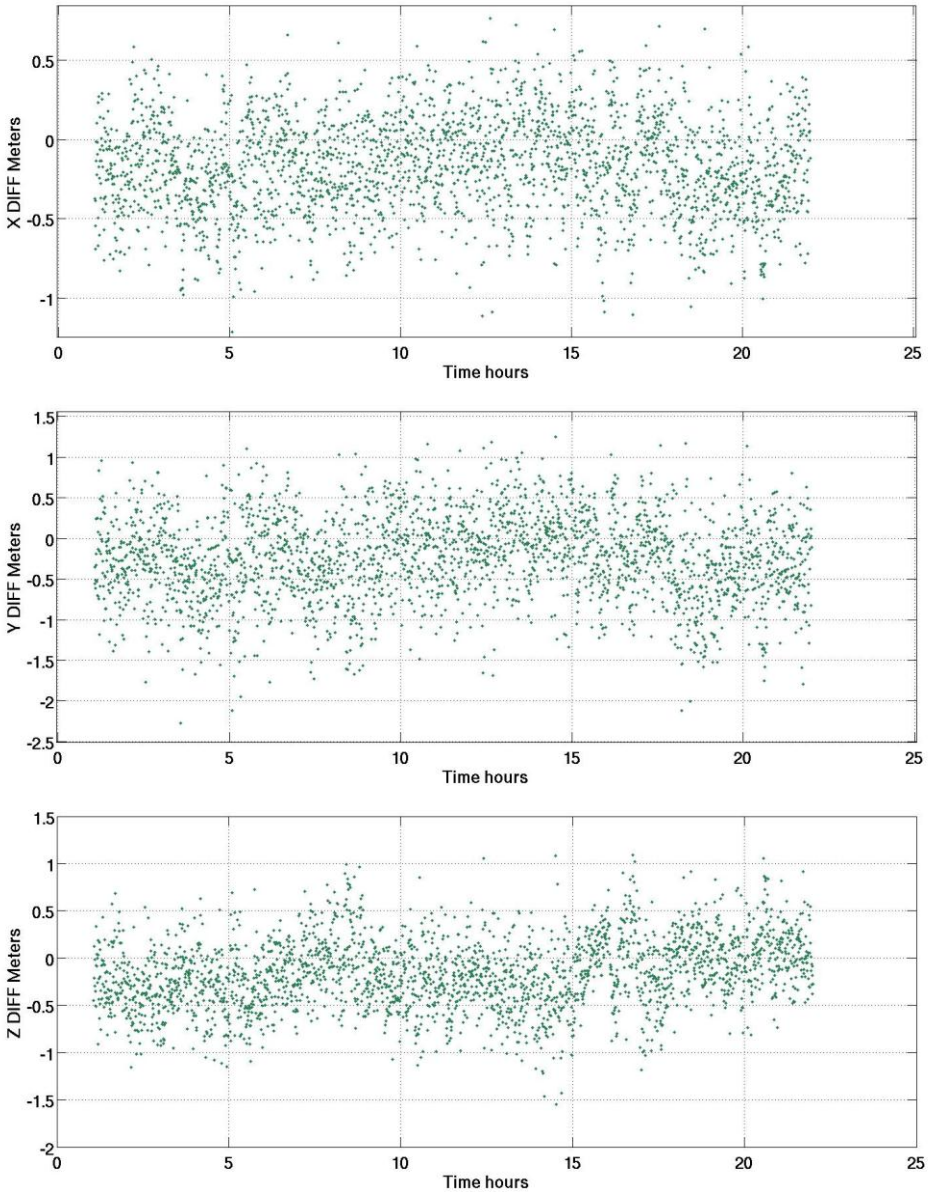

Figure B-16 Regional filter code solution: 35 KM baseline results

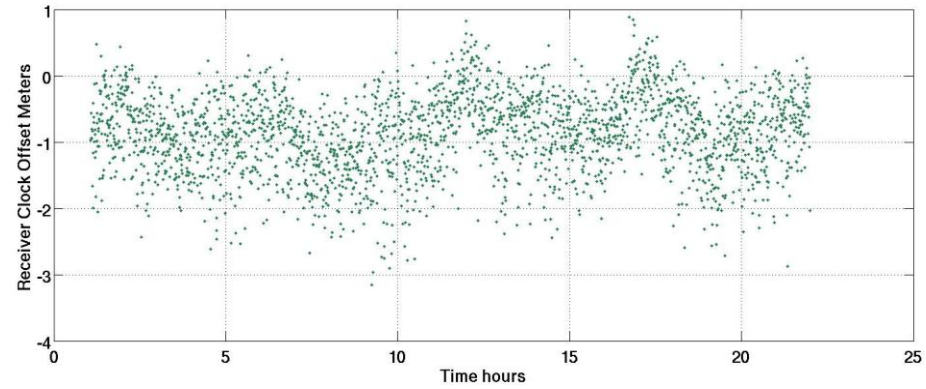
Receiver Clock Offset Meters
1
0
-1
-2
-3
-4
0
5
10
15
20
25
Time hours

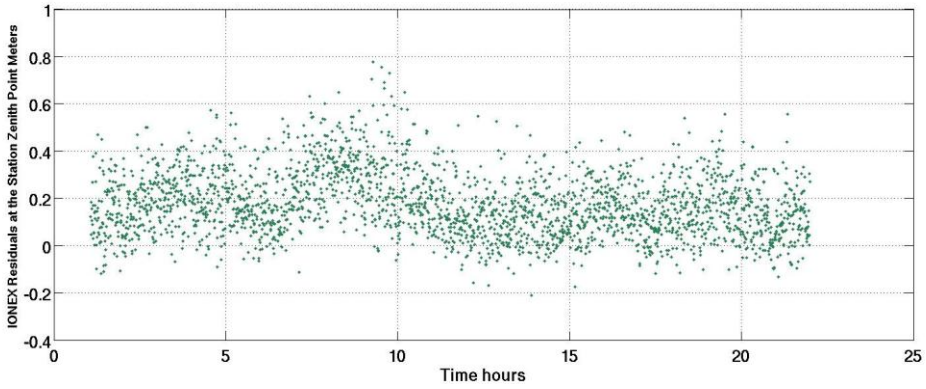
IONEX Residuals at the Station Zenith Point Meters
1
0.8
0.6
0.4
0.2
0
-0.2
-0.4
0
5
10
15
20
25
Time hours

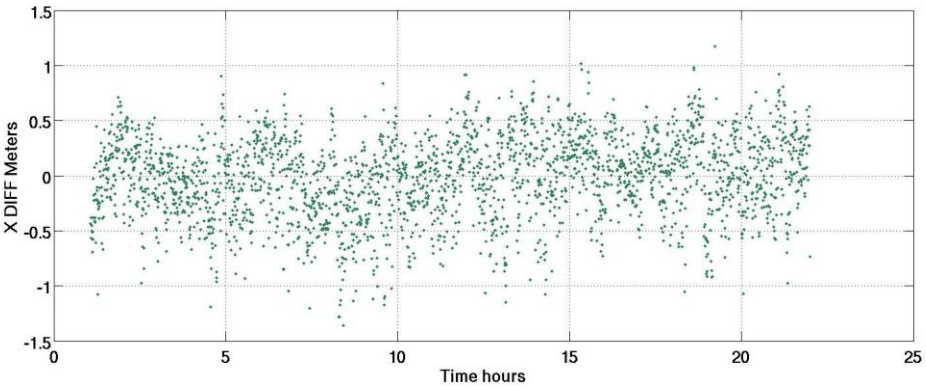
X DIFF Meters
1.5
1
0.5
0
-0.5
-1
-1.5
0
5
10
15
20
25
Time hours

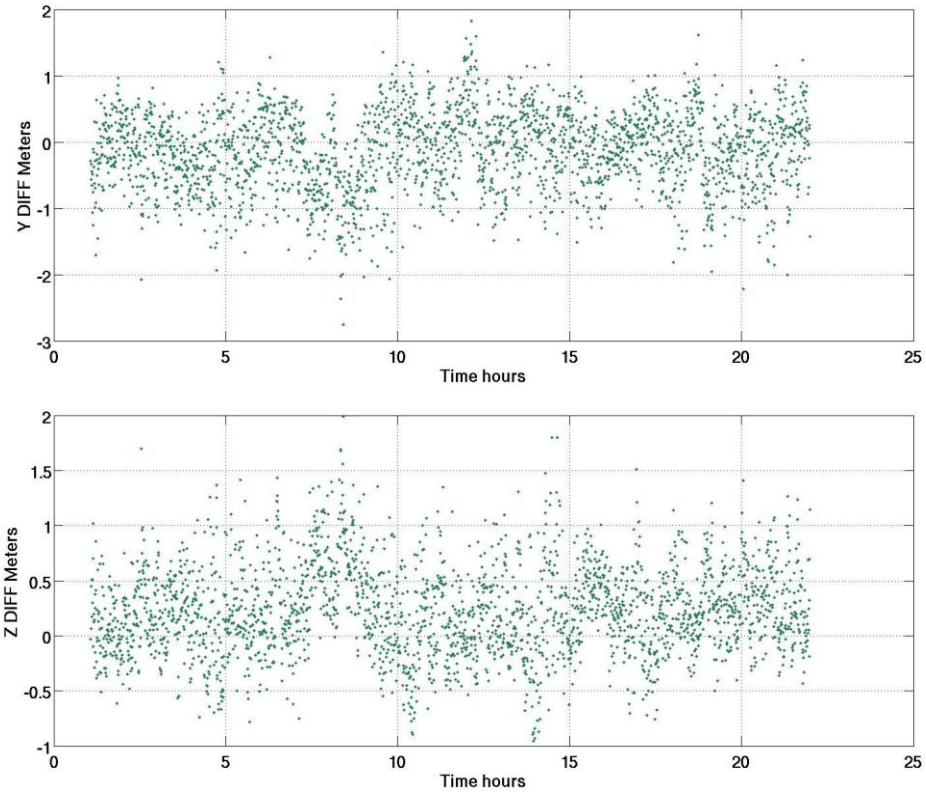

Figure B-17 Regional filter code solution: 39 KM baseline results

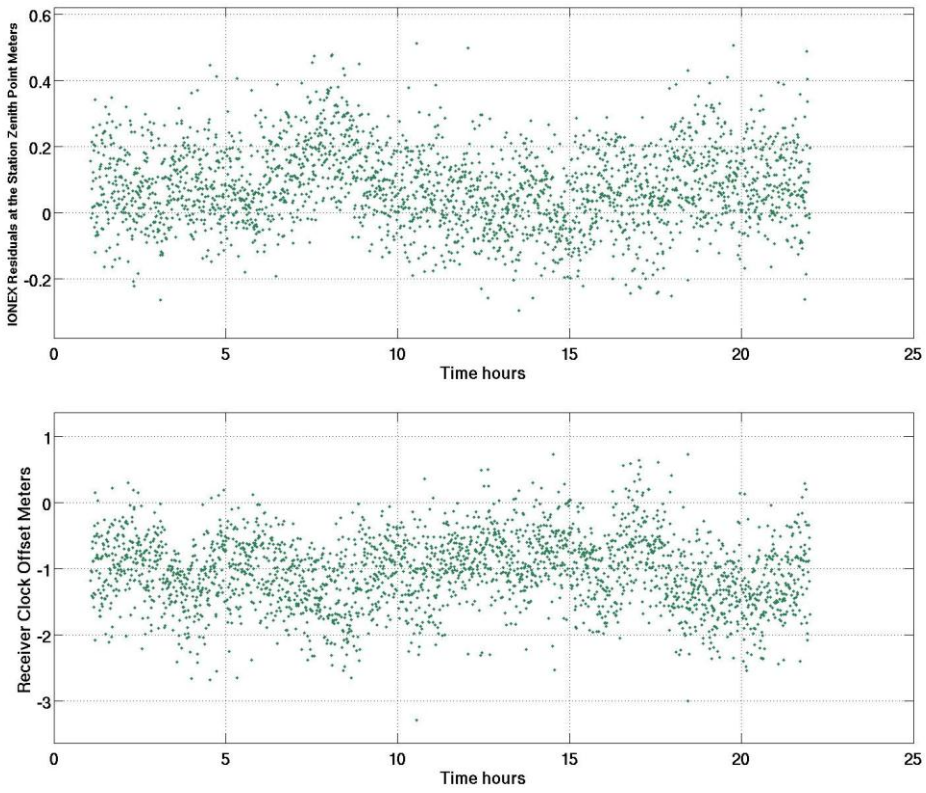

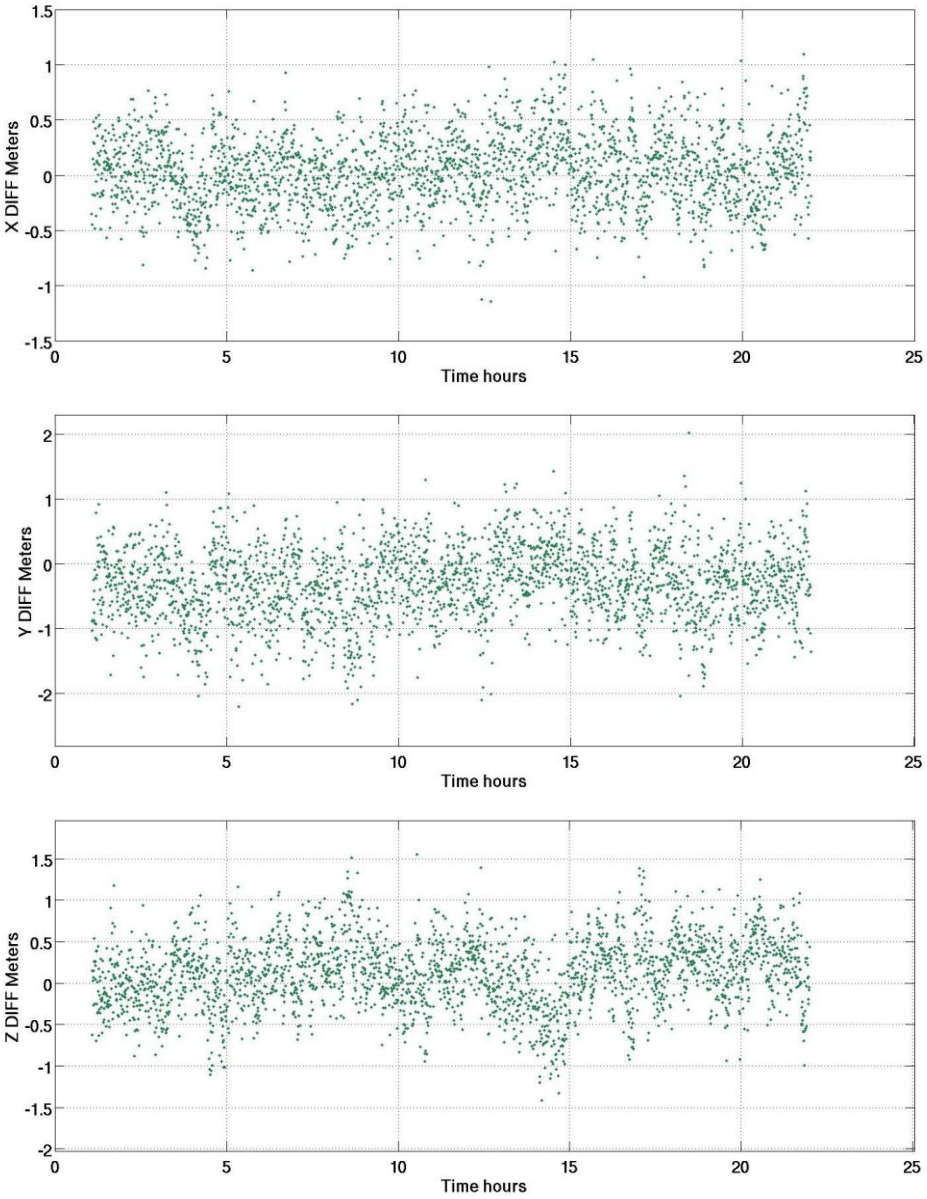

Figure B-18 Regional filter code solution: 44 KM baseline results

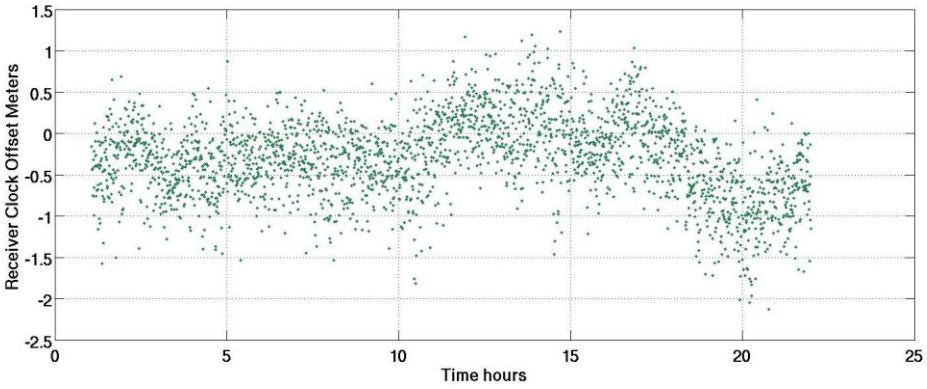

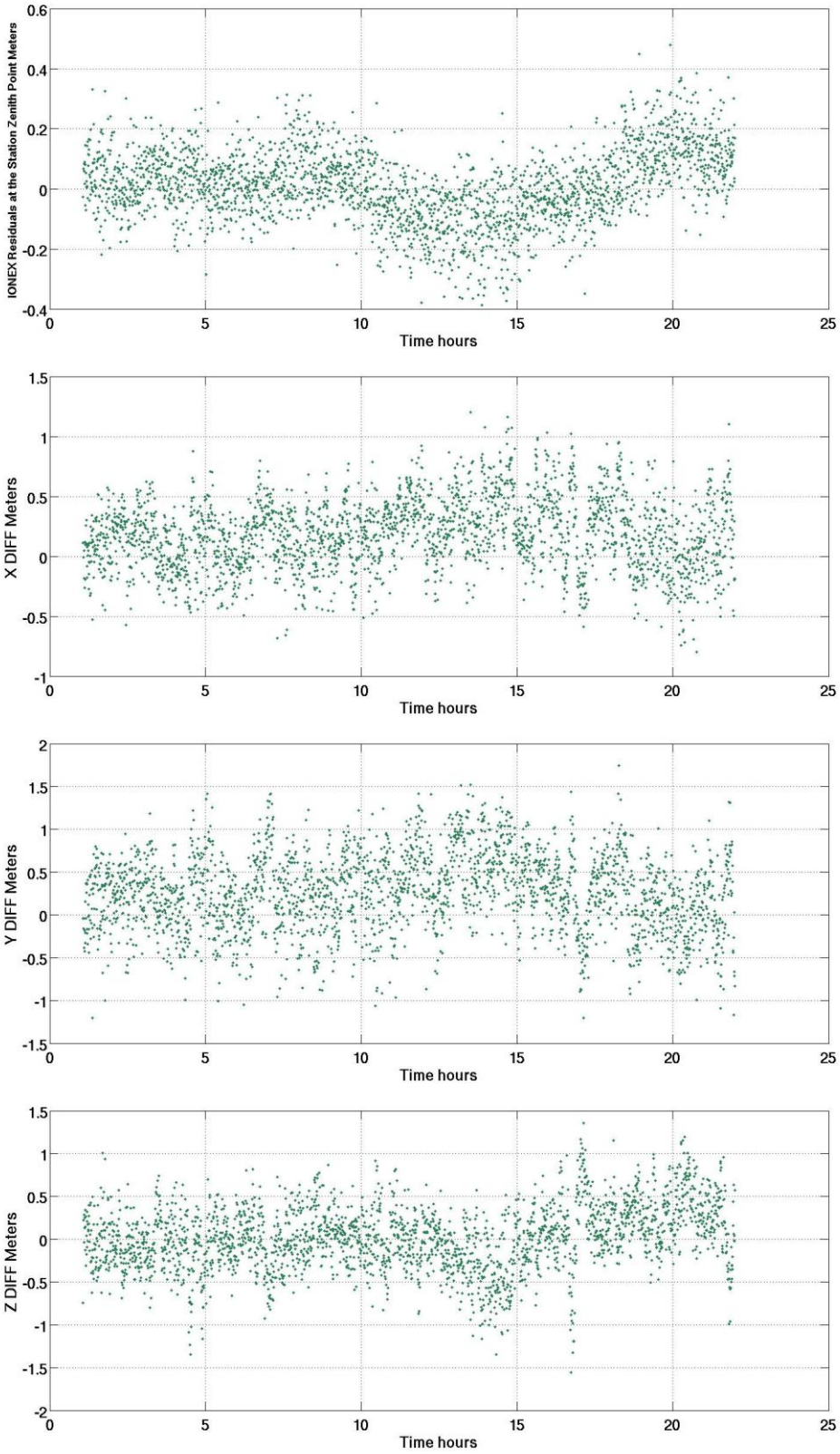

Figure B-19 Regional filter code solution: 50 KM baseline results

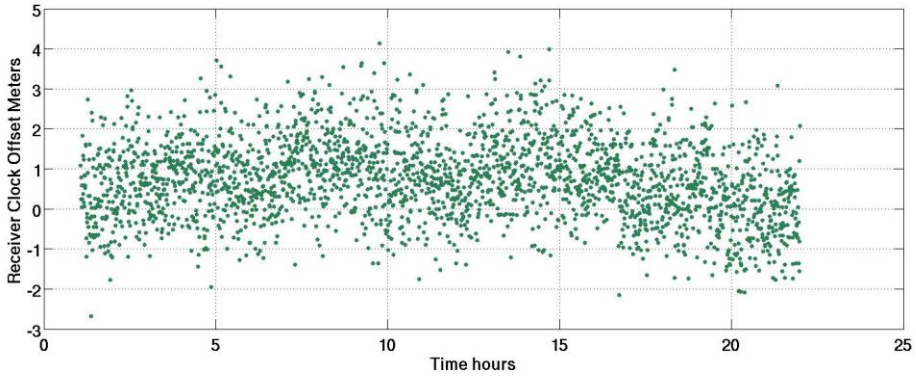
Receiver Clock Offset Meters
Time hours

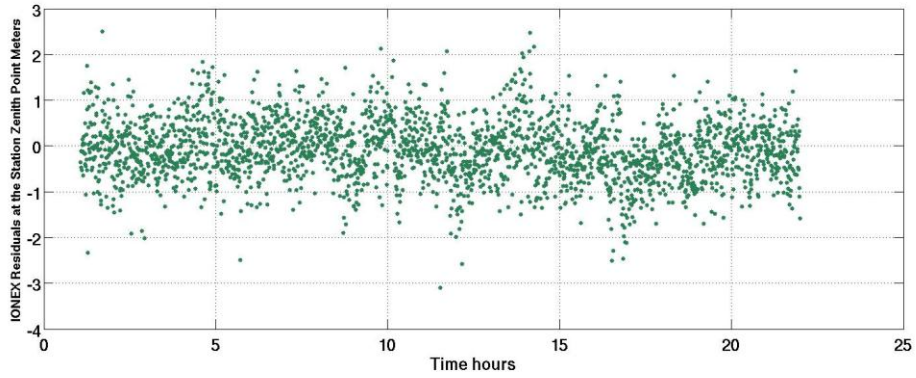
IONEX Residuals at the Station Zenith Point Meters
Time hours

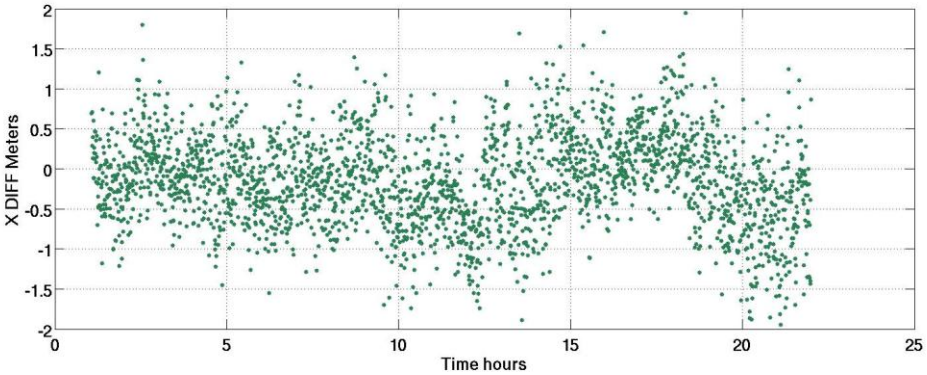
X DIFF Meters
Time hours

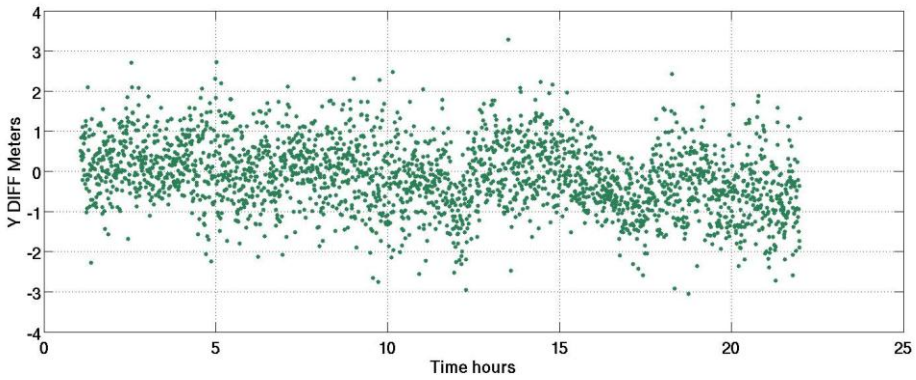
Y DIFF Meters
Time hours

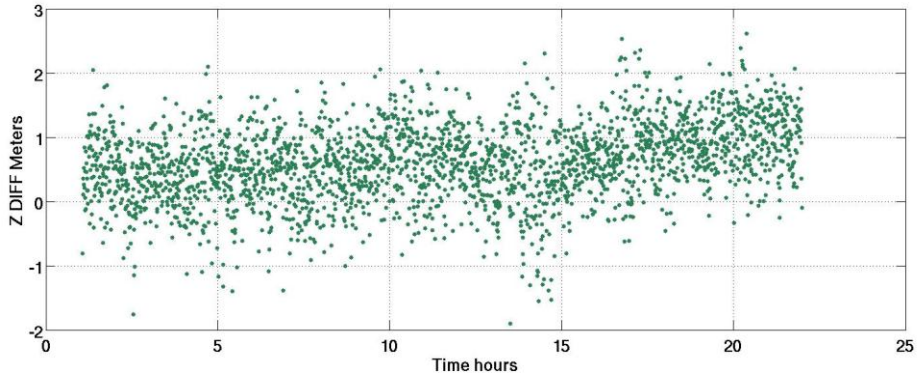

Figure B-20 Regional filter code solution: 60 KM baseline results

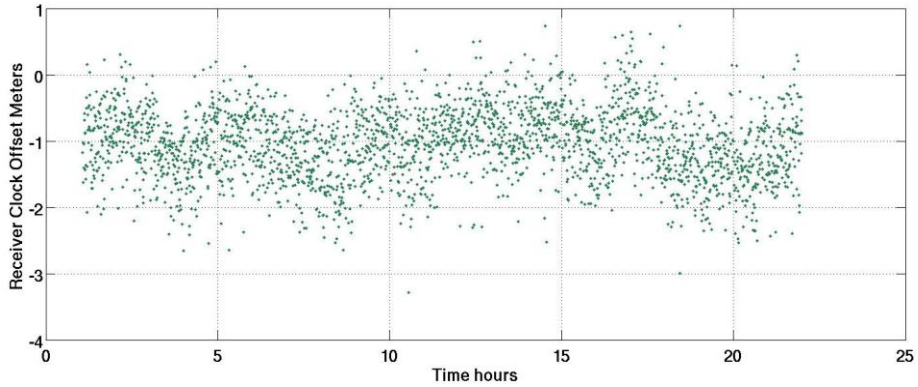

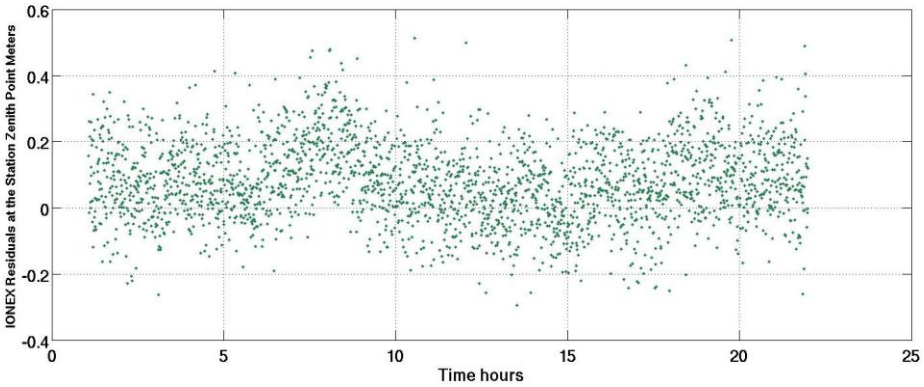

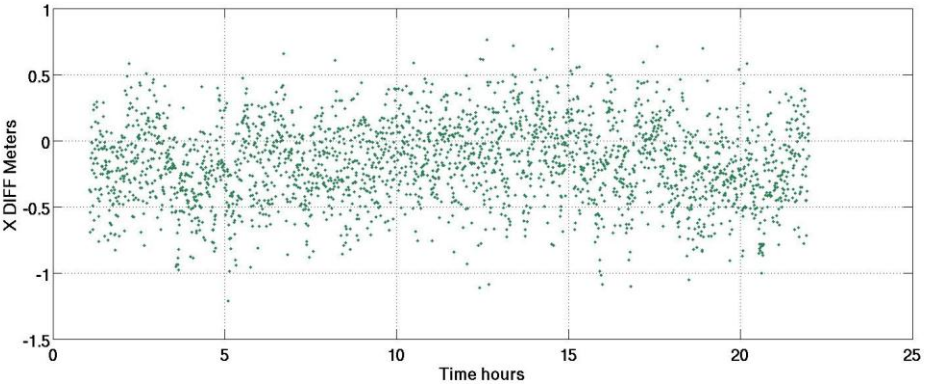

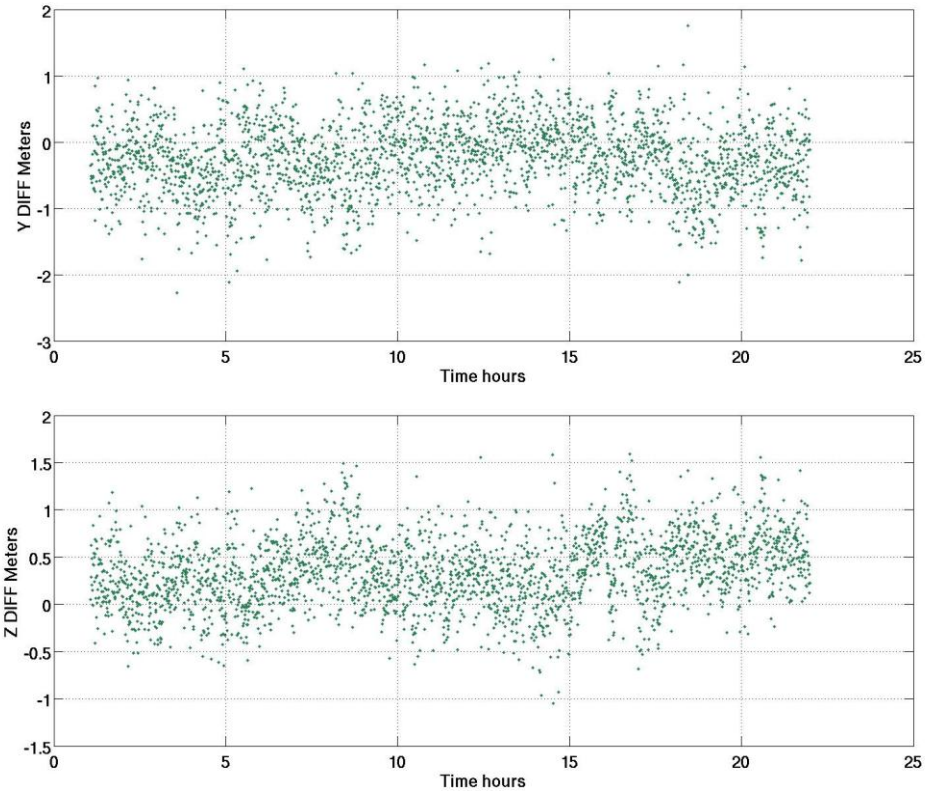

Figure B-21 Regional filter code solution: 75 KM baseline results

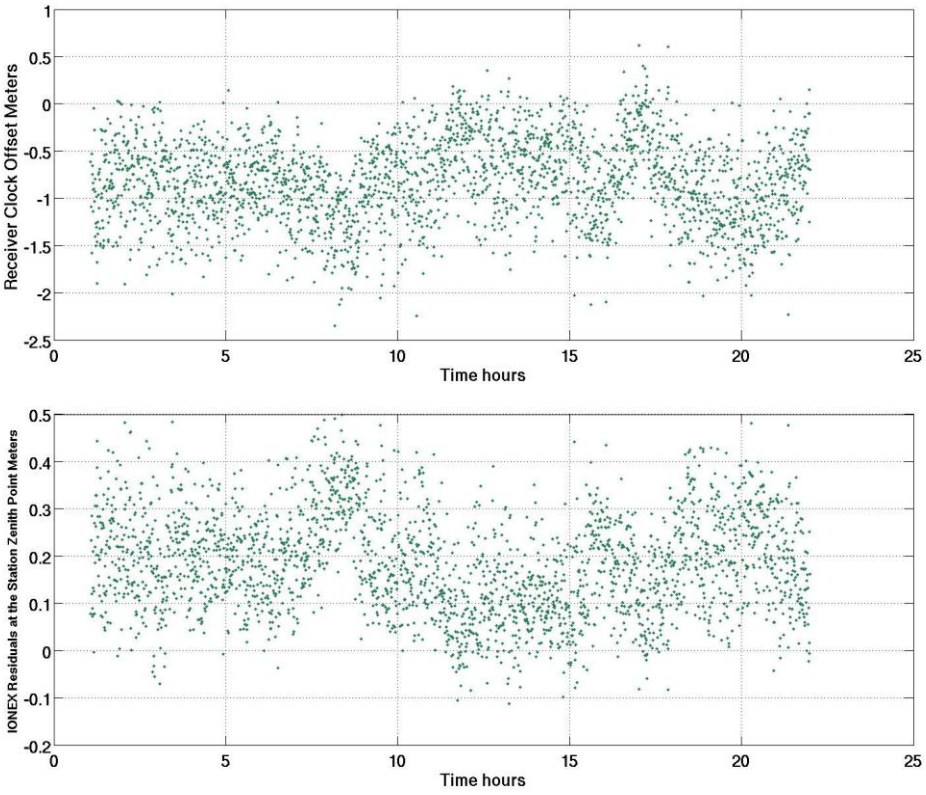

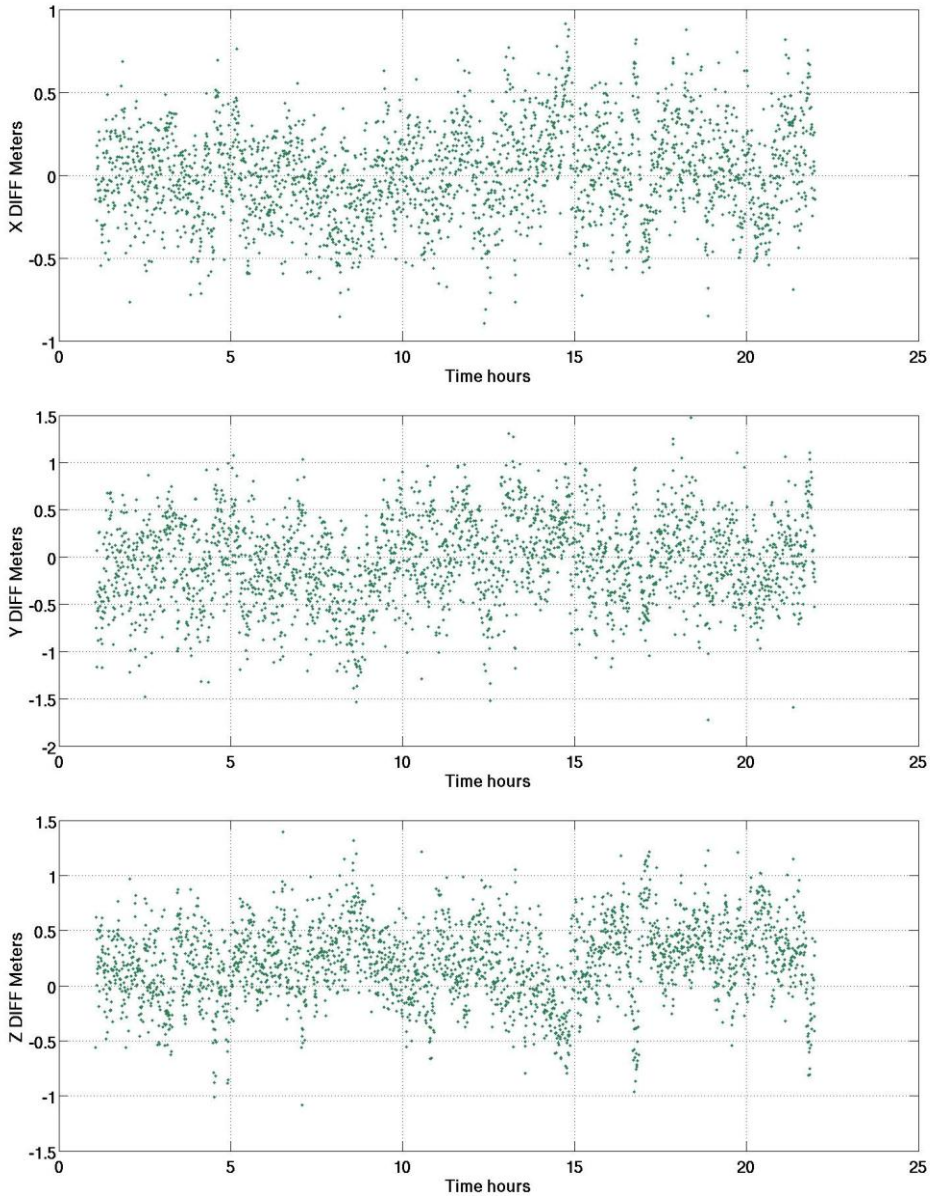

Figure B-22 Regional filter code solution: 99 KM baseline results

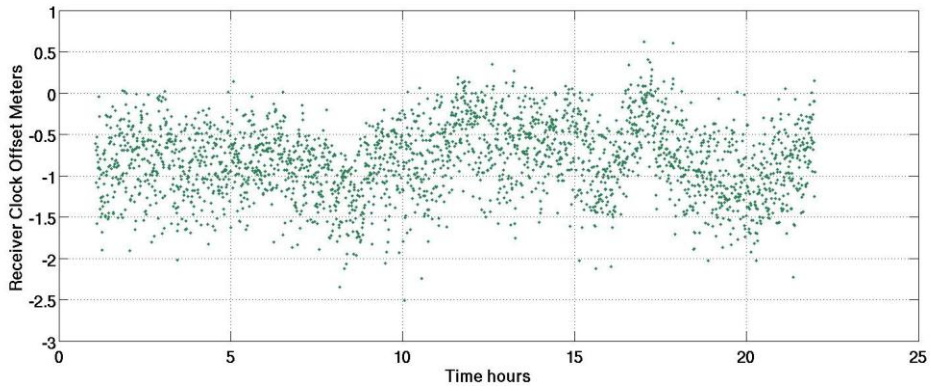

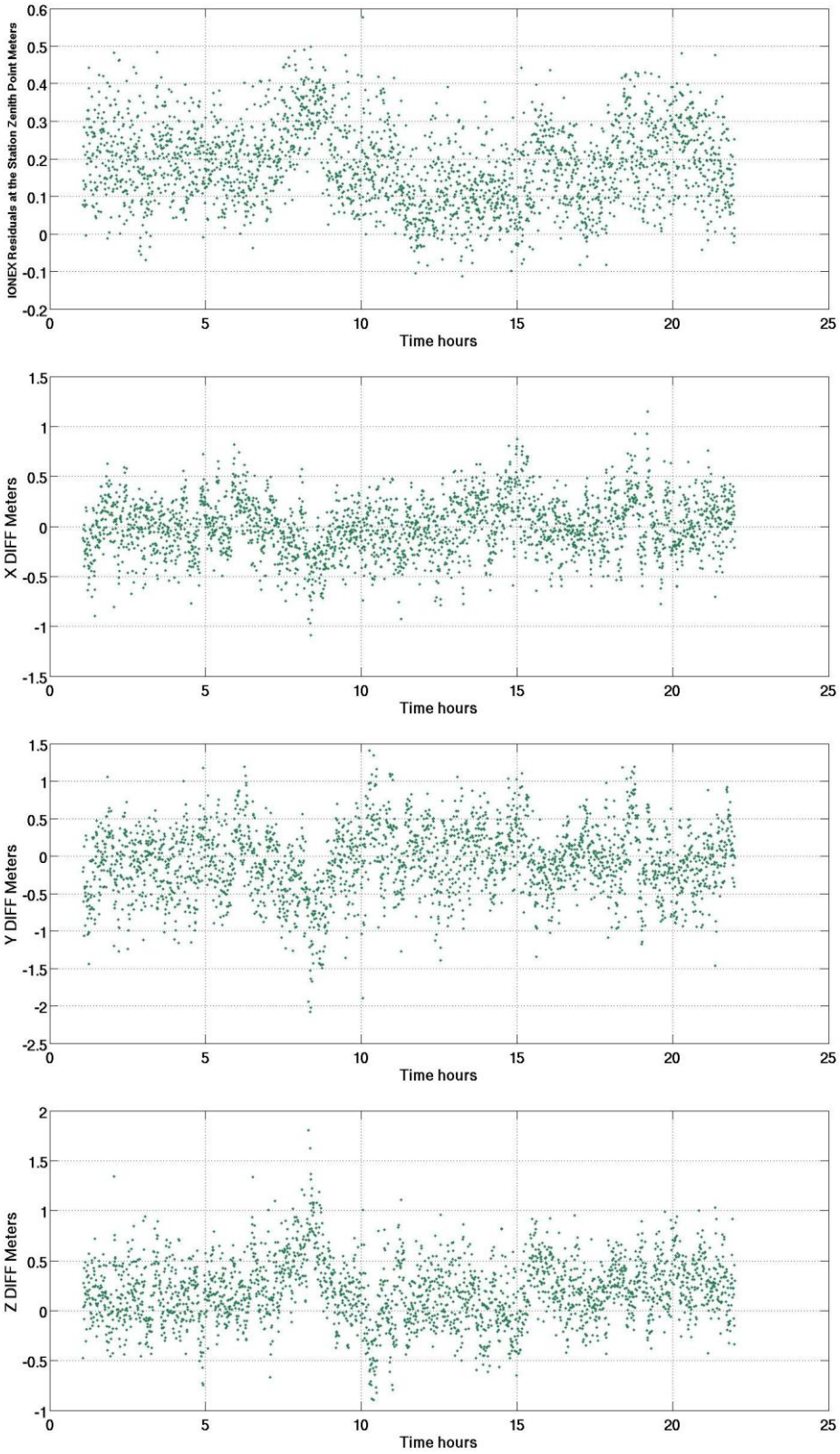

Figure B-23 Regional filter code solution: 113 KM baseline results

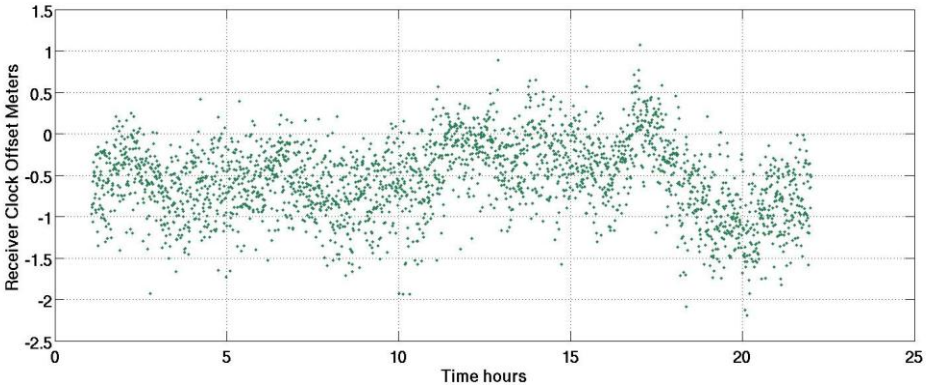
Receiver Clock Offset Meters
1.5
1
0.5
0
-0.5
-1
-1.5
-2
-2.5
0
5
10
15
20
25
Time hours

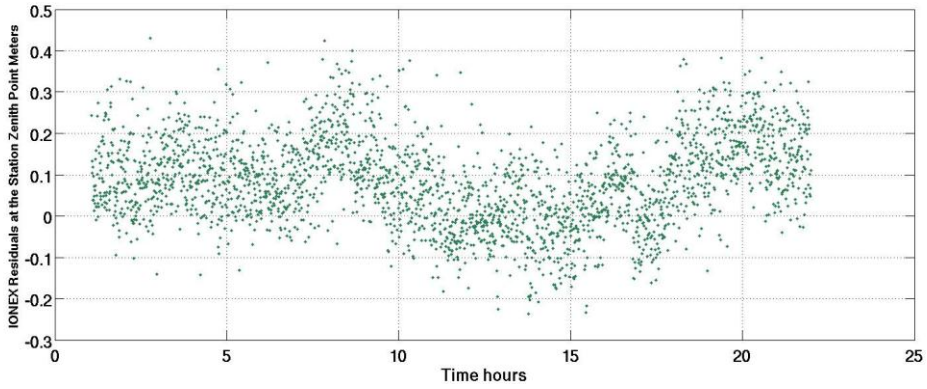
IONEX Residuals at the Station Zenith Point Meters
0.5
0.4
0.3
0.2
0.1
0
-0.1
-0.2
-0.3
0
5
10
15
20
25
Time hours

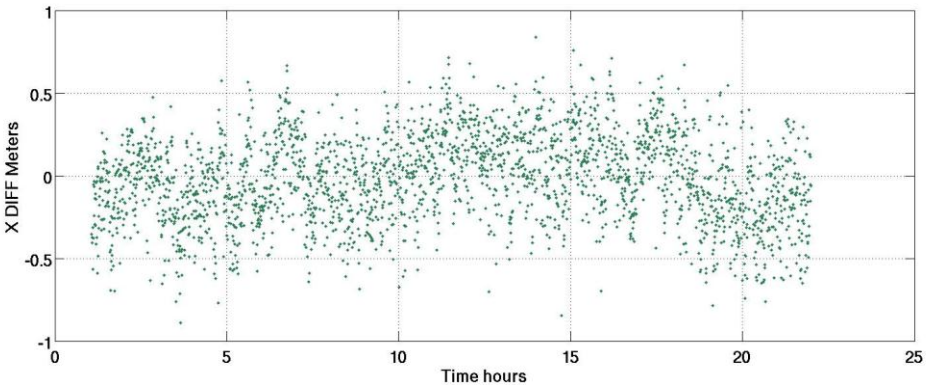
X DIFF Meters
1
0.5
0
-0.5
-1
0
5
10
15
20
25
Time hours

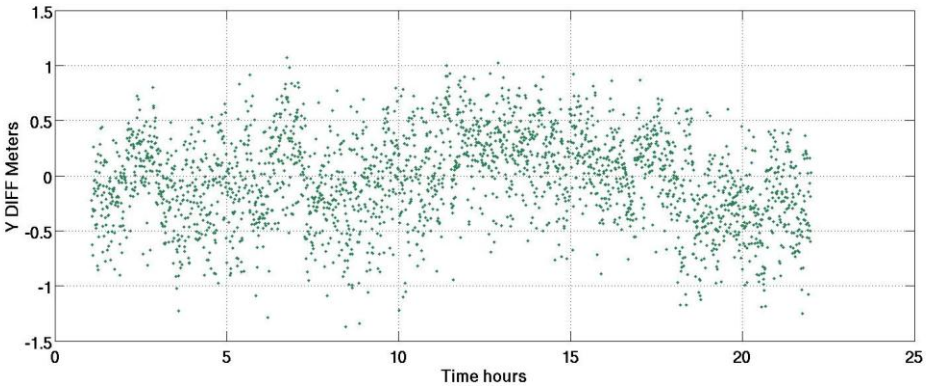
Y DIFF Meters
1.5
1
0.5
0
-0.5
-1
-1.5
0
5
10
15
20
25
Time hours

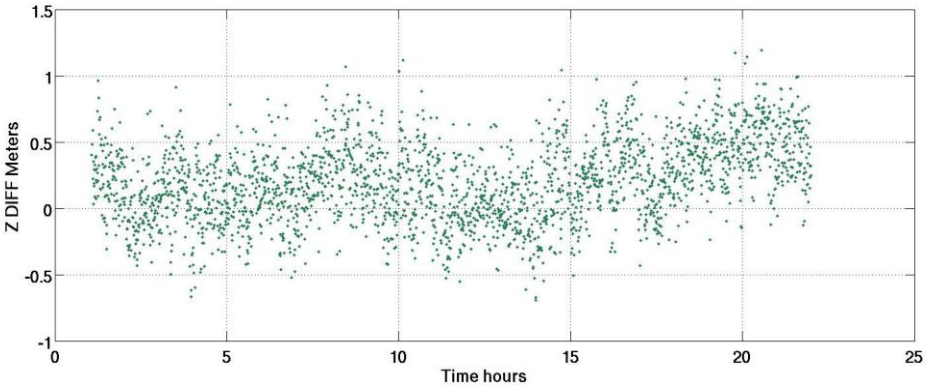

Figure B-24 Regional filter code solution: 123 KM baseline results

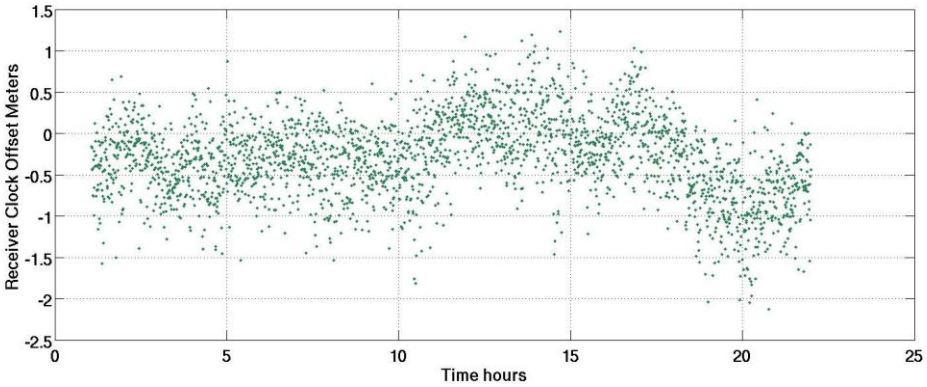

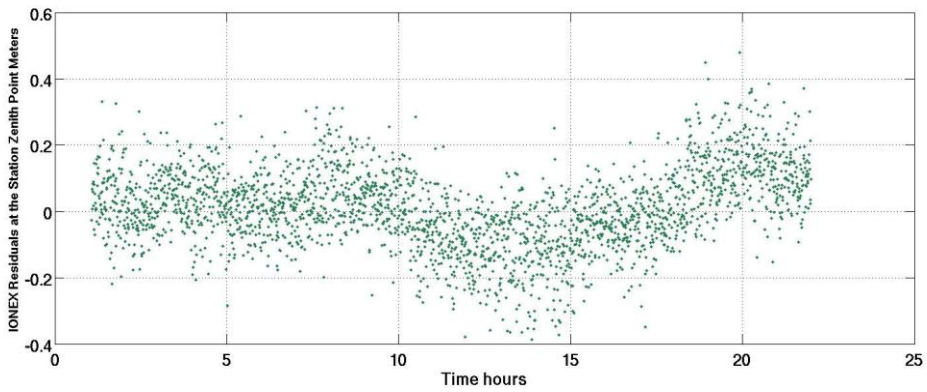

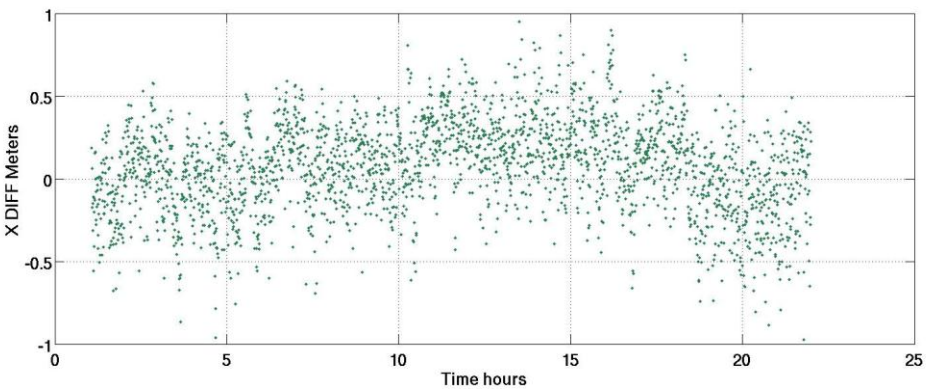

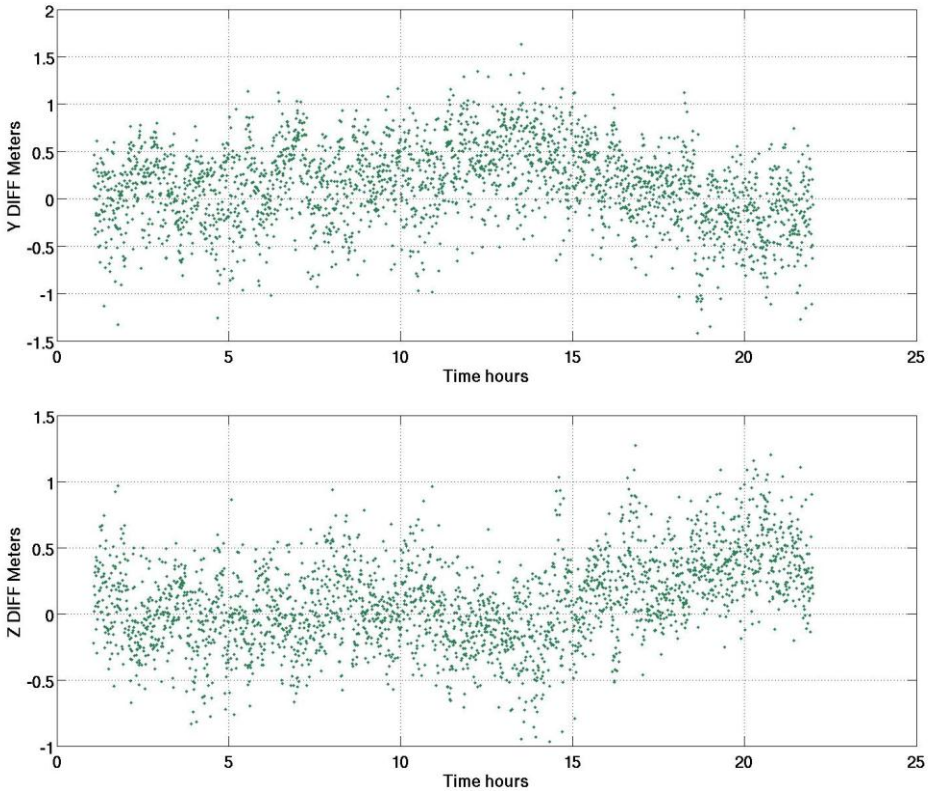

Figure B-25 Regional filter code solution: 133 KM baseline results

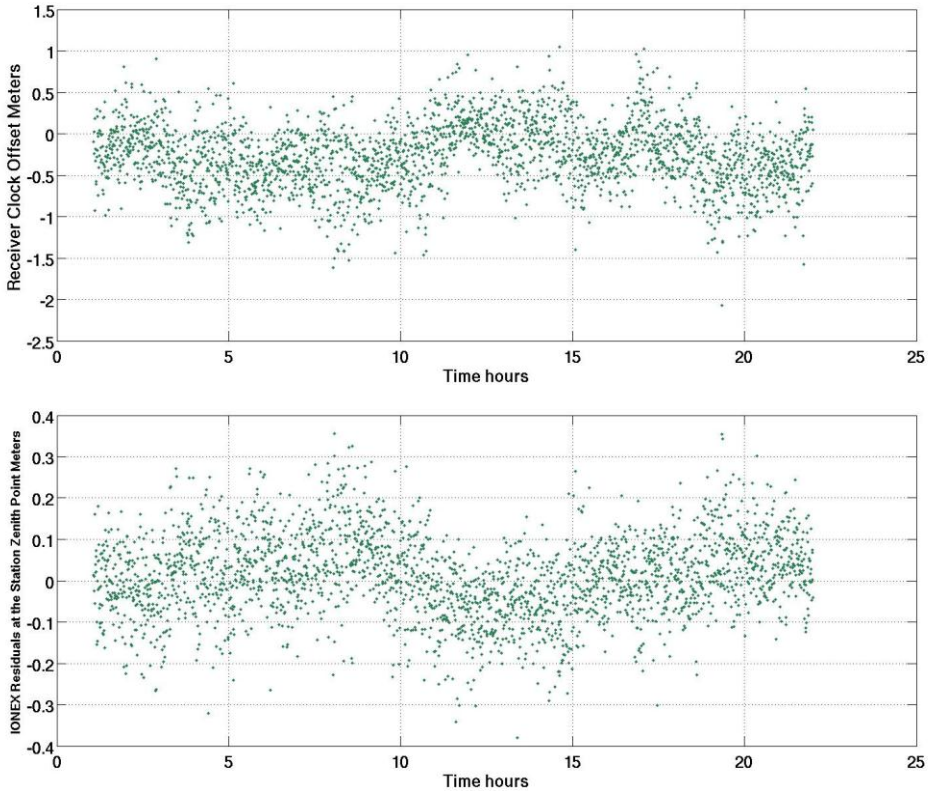

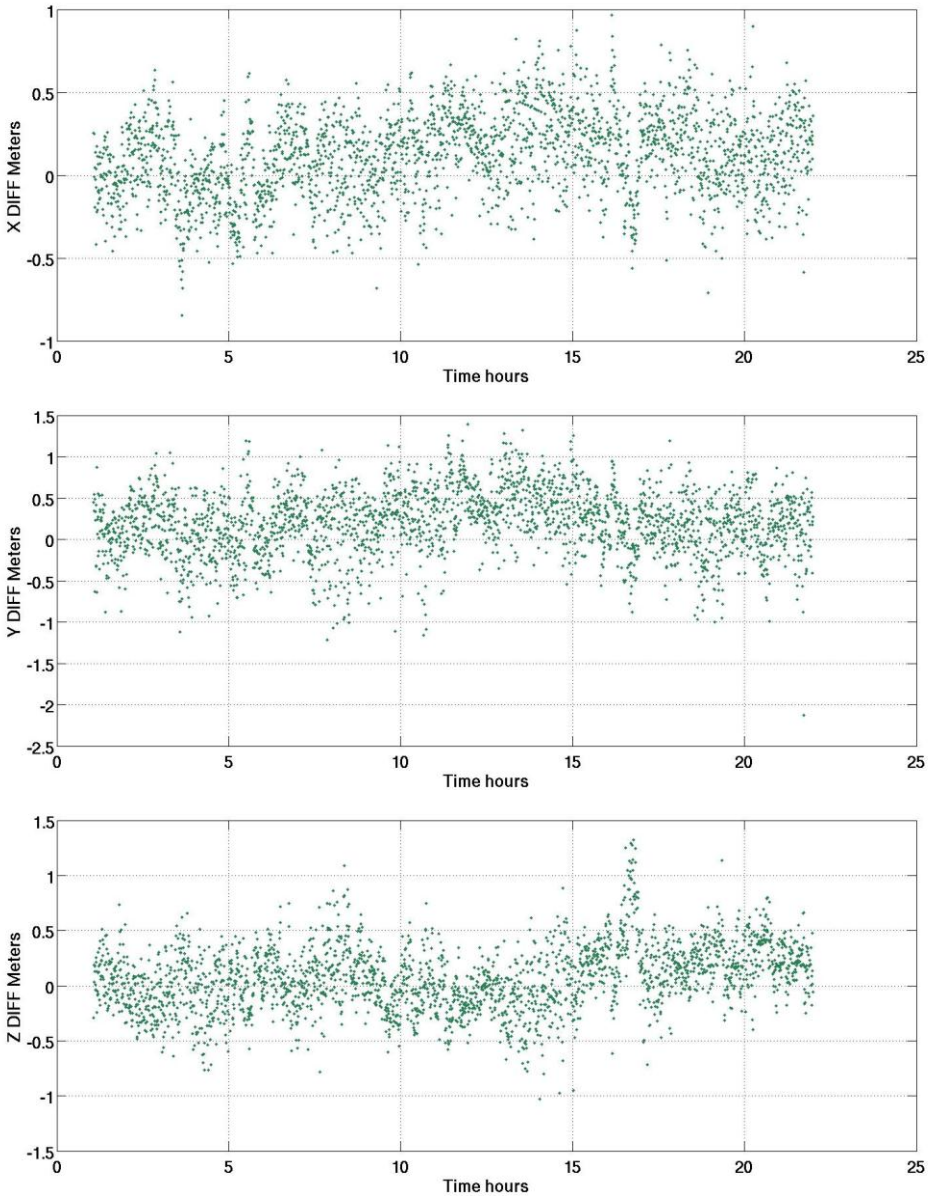

Figure B-26 Regional filter code solution: 155 KM baseline results

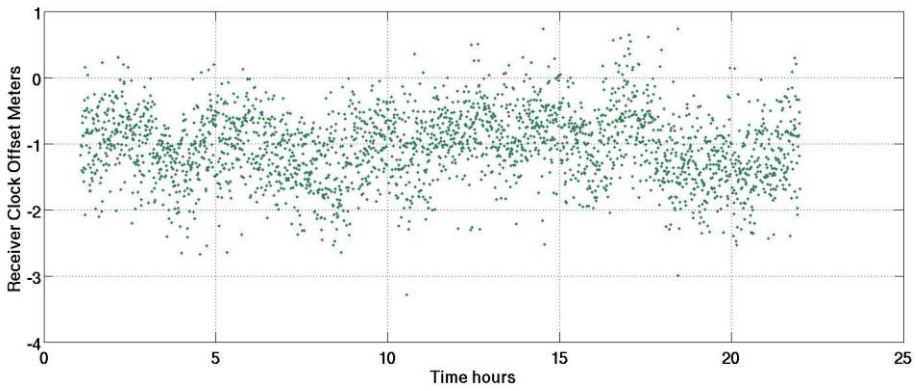

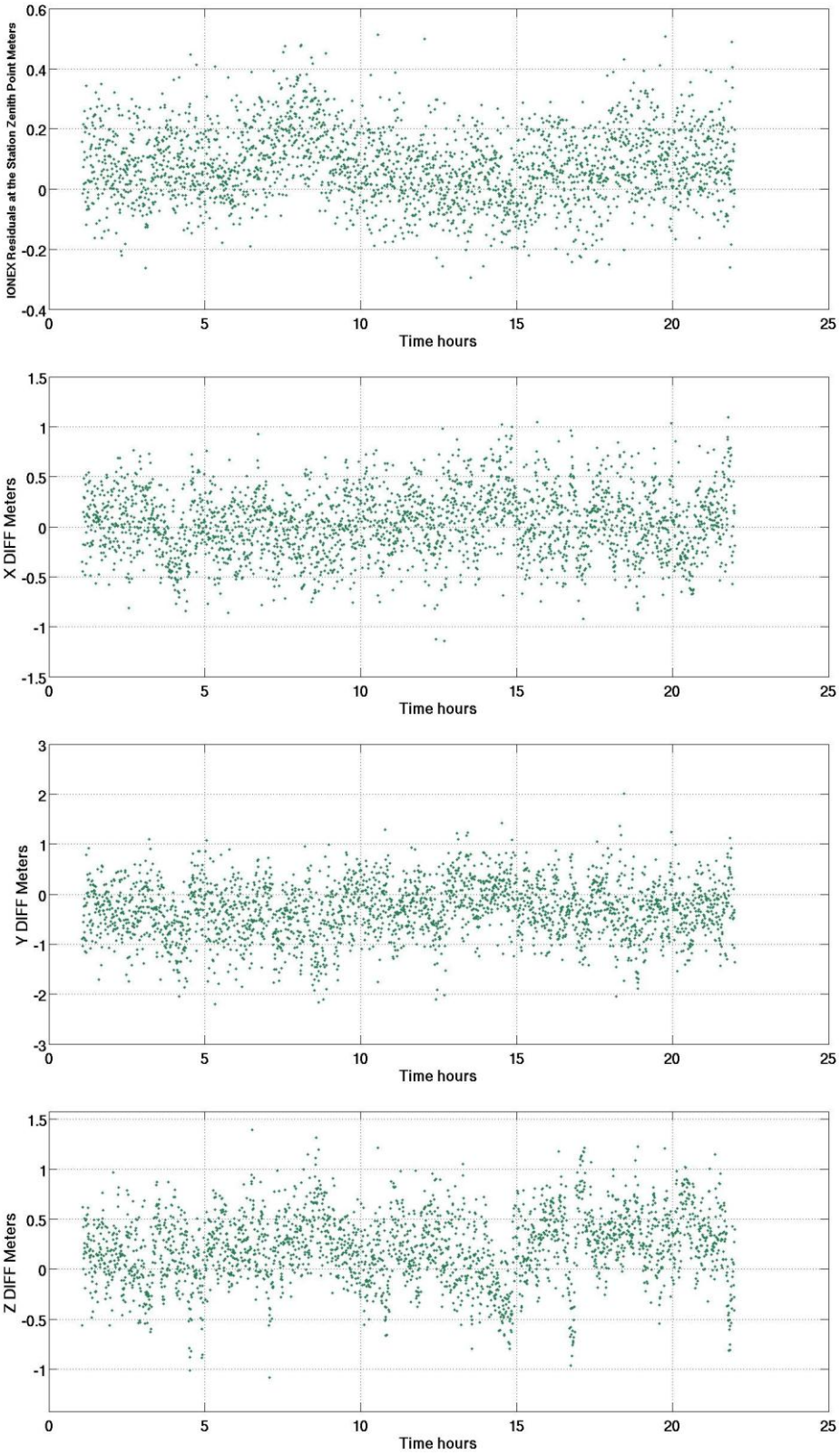

Figure B-27 Regional filter code solution: 160 KM baseline results

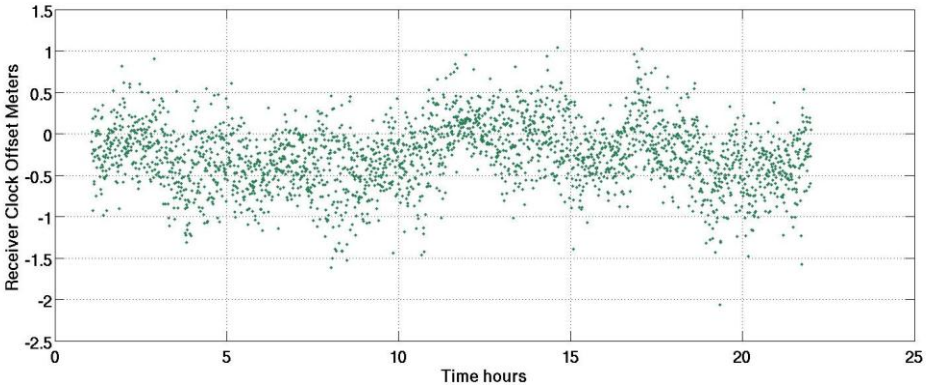
Receiver Clock Offset Meters
1.5
1
0.5
0
-0.5
-1
-1.5
-2
-2.5
0
5
10
15
20
25
Time hours

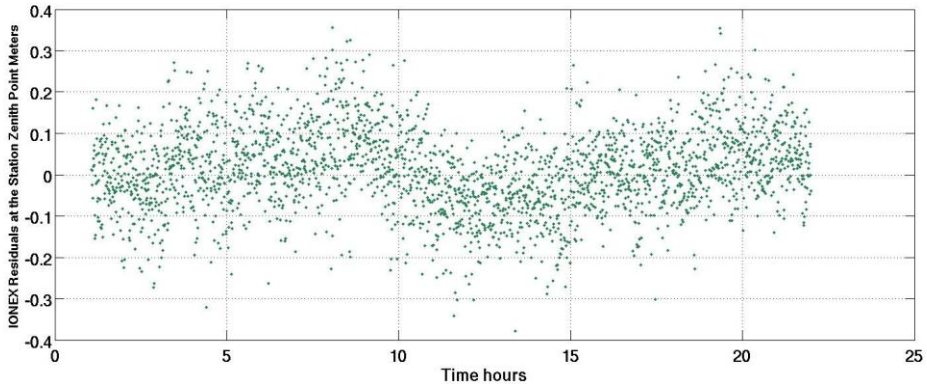
IONEX Residuals at the Station Zenith Point Meters
0.4
0.3
0.2
0.1
0
-0.1
-0.2
-0.3
-0.4
0
5
10
15
20
25
Time hours

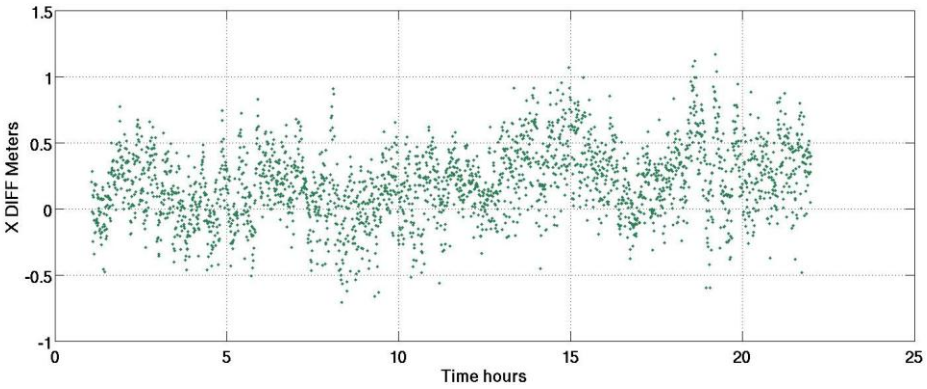
X DIFF Meters
1.5
1
0.5
0
-0.5
-1
0
5
10
15
20
25
Time hours

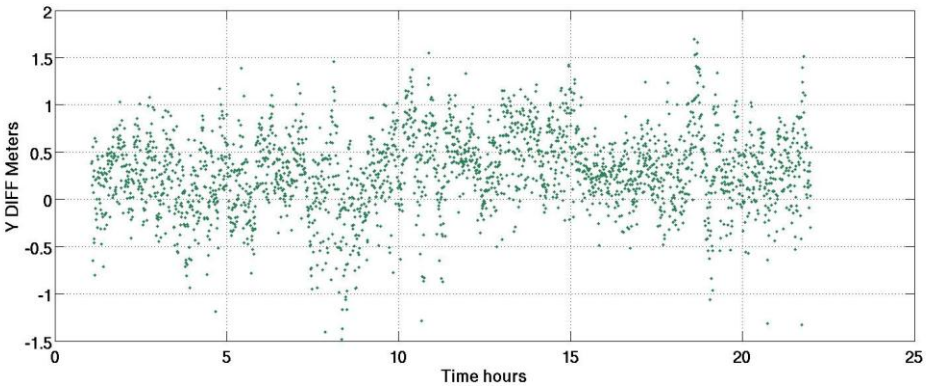
Y DIFF Meters
2
1.5
1
0.5
0
-0.5
-1
-1.5
0
5
10
15
20
25
Time hours

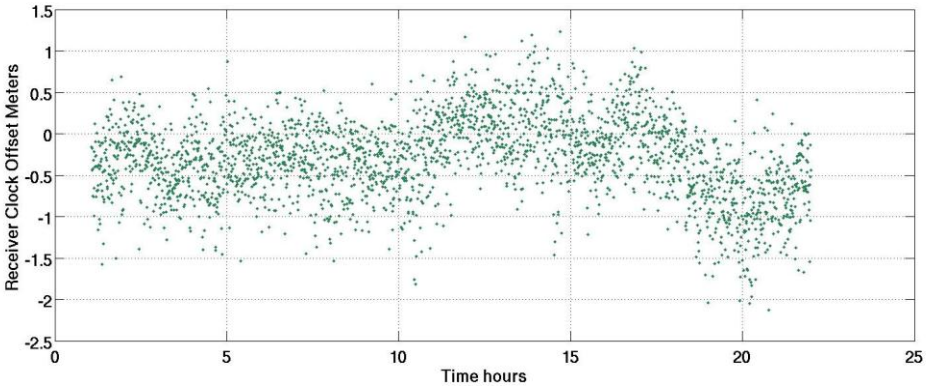

Figure B-28 Regional filter code solution: 198 KM baseline results

SHAKING TEST RESULTS

The following figures show the shaking test results of the 13 km, 20 km, 23 km, 27 km, 32 km, 39 km, 43 km and 55 km baselines respectively.

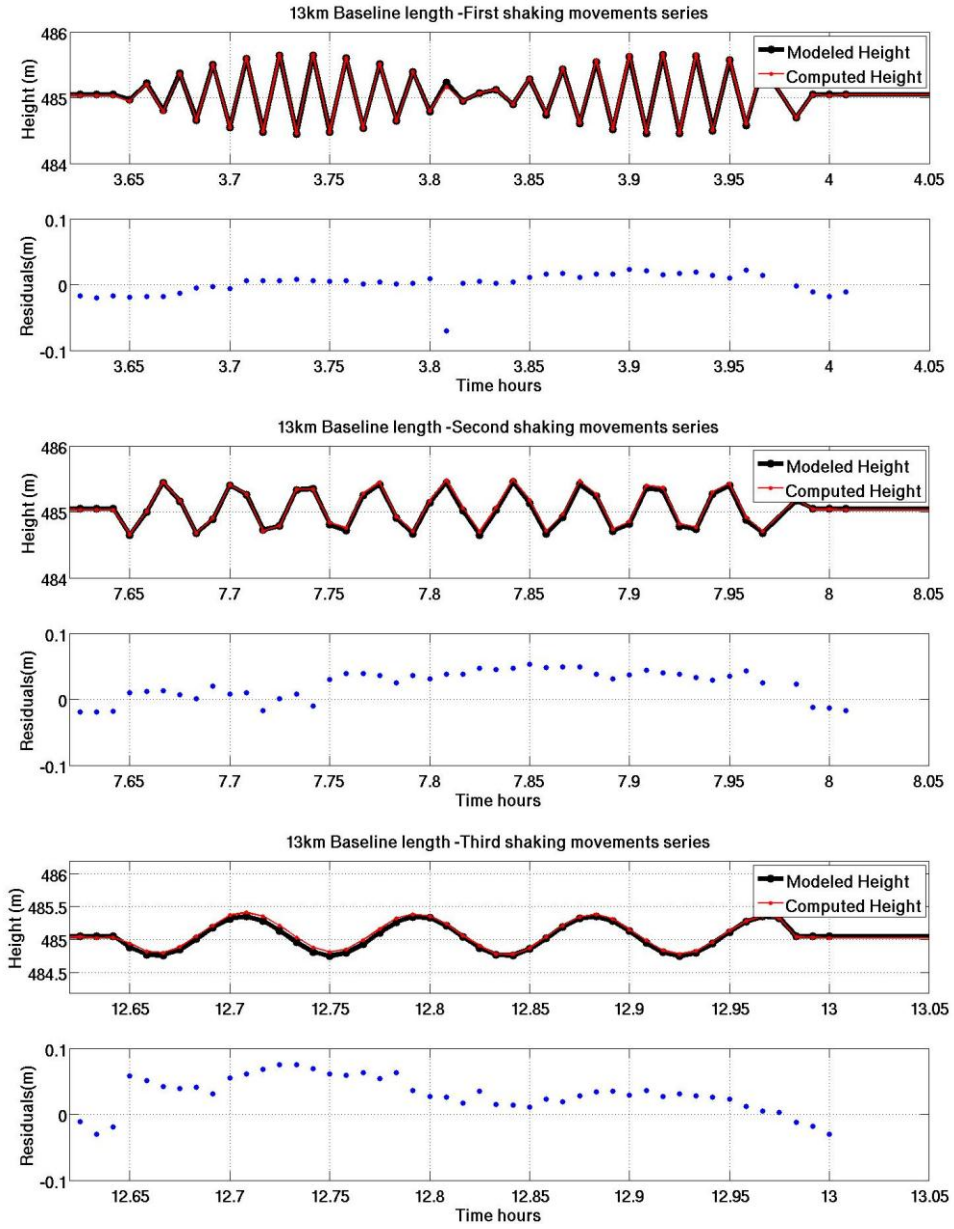

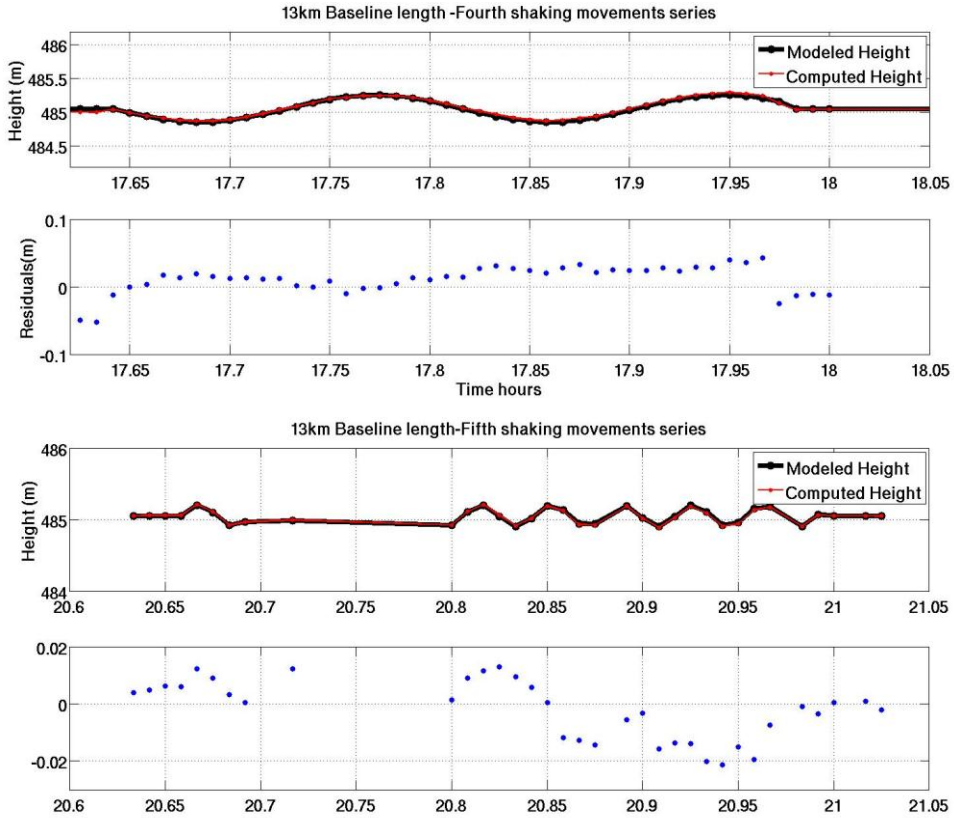

Figure C-1 The shaking test results for the five time windows -13 km baseline length.

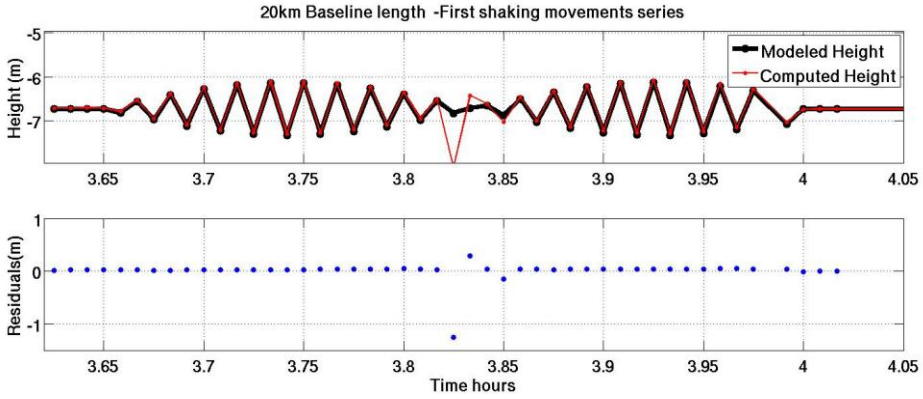

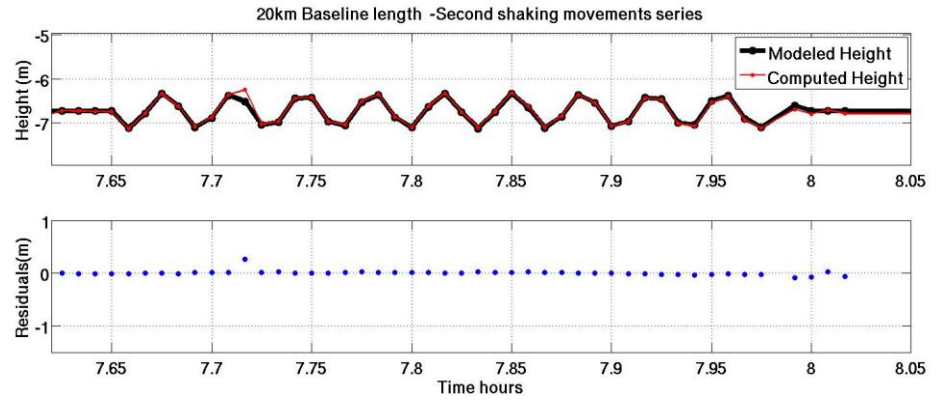
20km Baseline length -Second shaking movements series
Modeled Height
Computed Height
Height (m)
-5
-6
-7
7.65
7.7
7.75
7.8
7.85
7.9
7.95
8
8.05
Residuals(m)
1
0
-1
Time hours

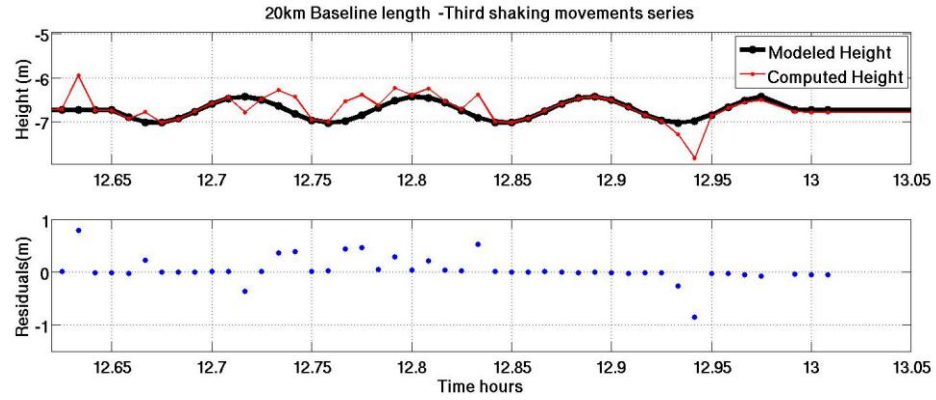
20km Baseline length -Third shaking movements series
Modeled Height
Computed Height
Height (m)
-5
-6
-7
12.65
12.7
12.75
12.8
12.85
12.9
12.95
13
13.05
Residuals(m)
1
0
-1
Time hours

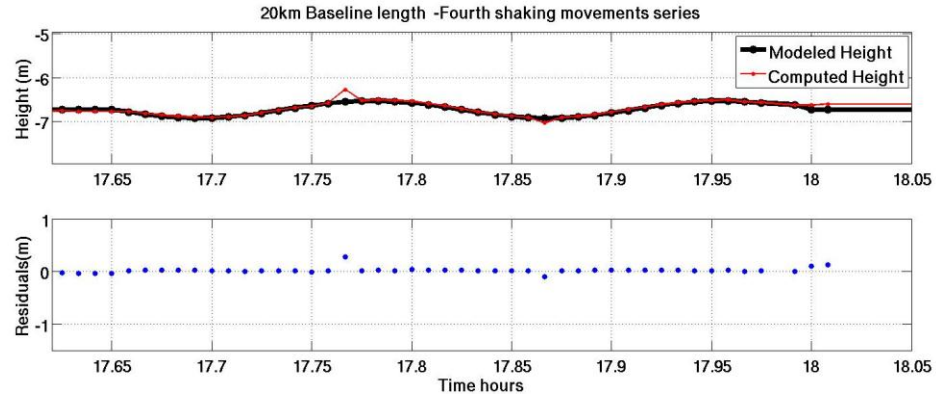
20km Baseline length -Fourth shaking movements series
Modeled Height
Computed Height
Height (m)
-5
-6
-7
17.65
17.7
17.75
17.8
17.85
17.9
17.95
18
18.05
Residuals(m)
1
0
-1
Time hours

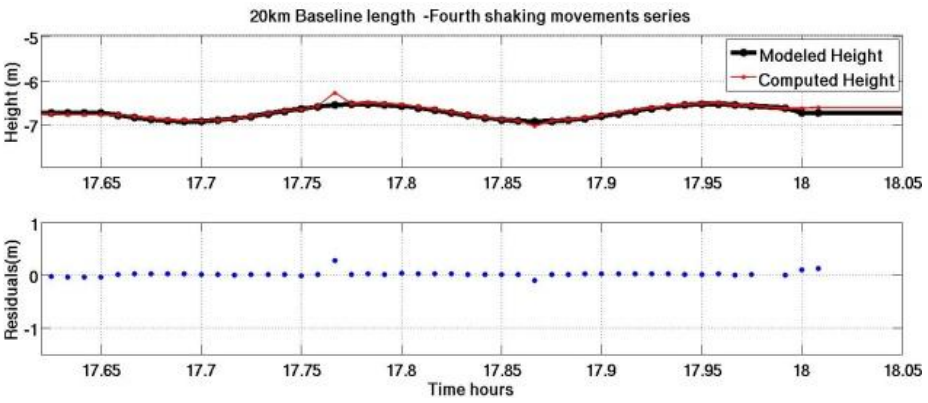
20km Baseline length -Fourth shaking movements series
Modeled Height
Computed Height
Height (m)
-5
-6
-7
17.65
17.7
17.75
17.8
17.85
17.9
17.95
18
18.05
Residuals(m)
1
0
-1
Time hours

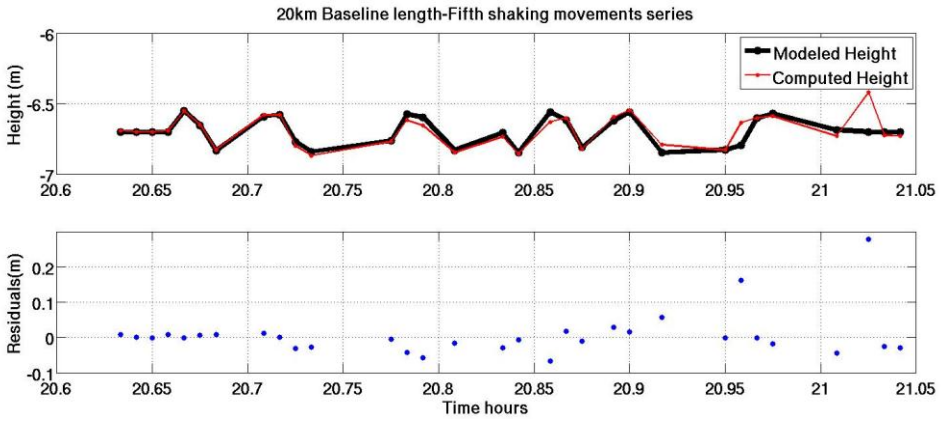

Figure C-2 The shaking test results for the five time windows -20 km baseline length.

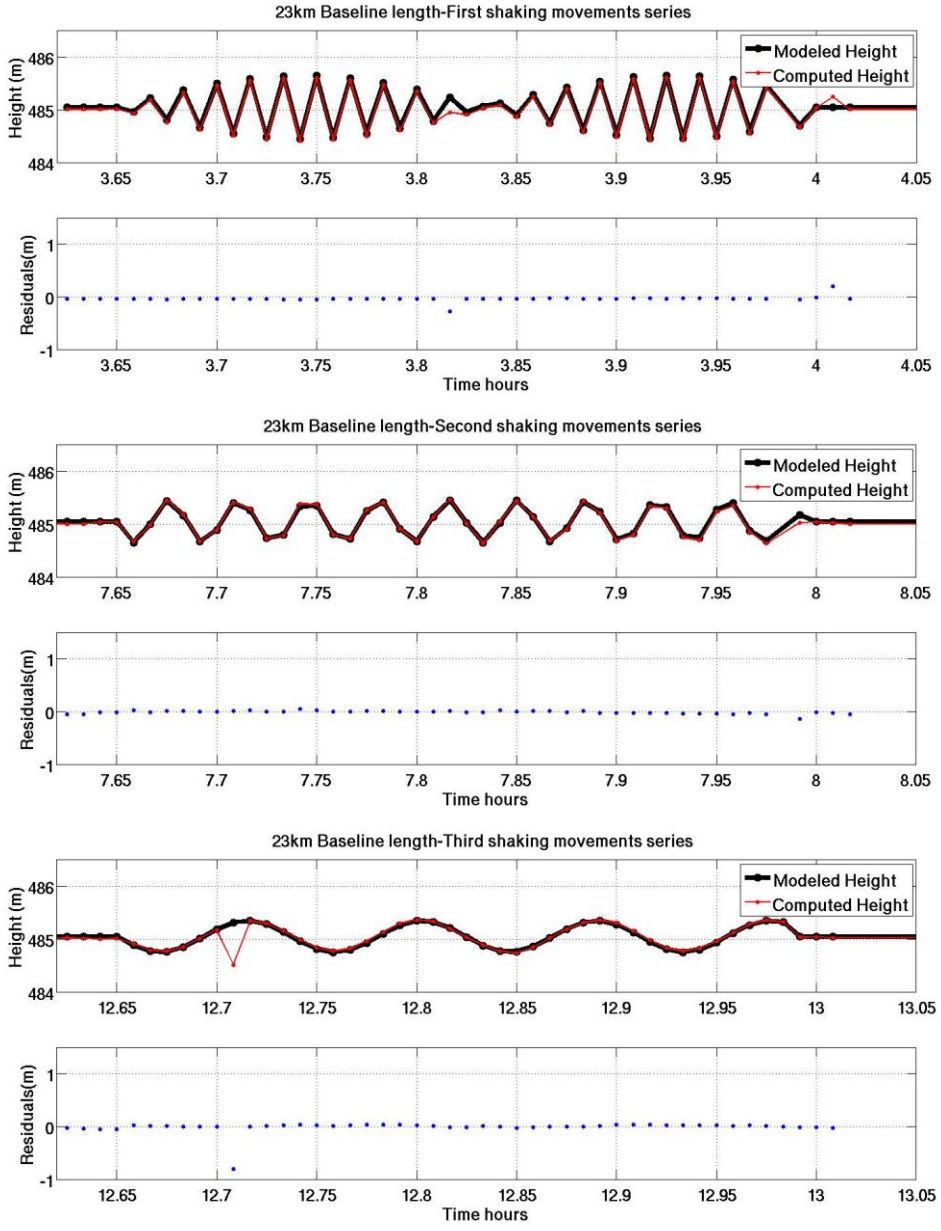

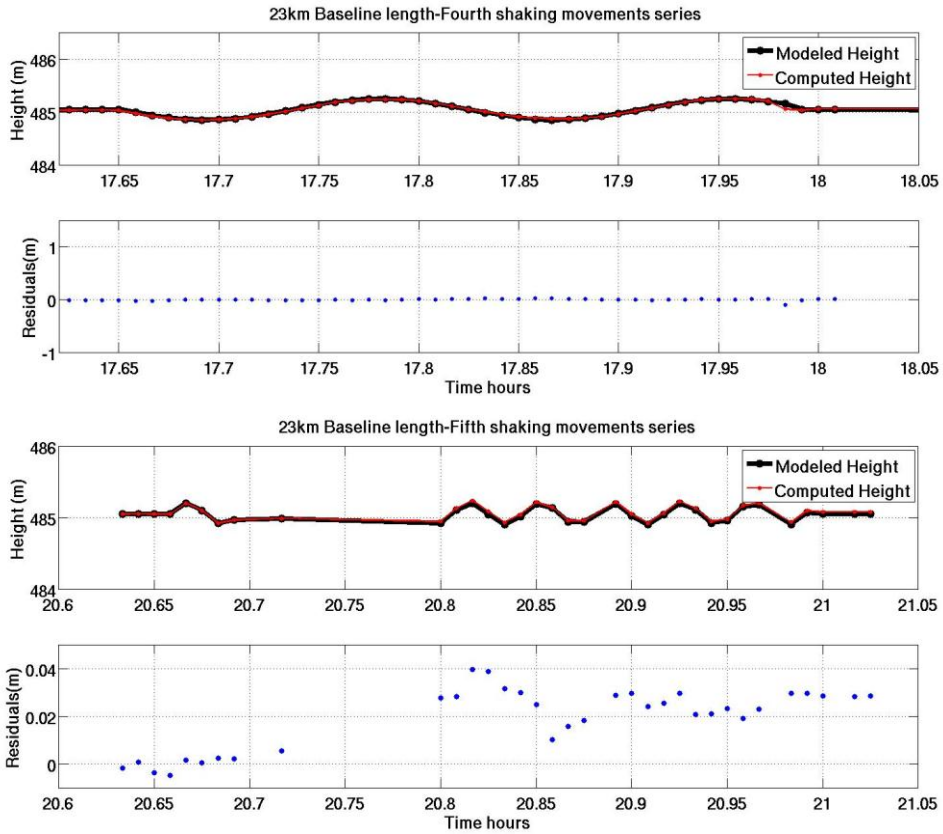

Figure C-3 The shaking test results for the five time windows -23 km baseline length.

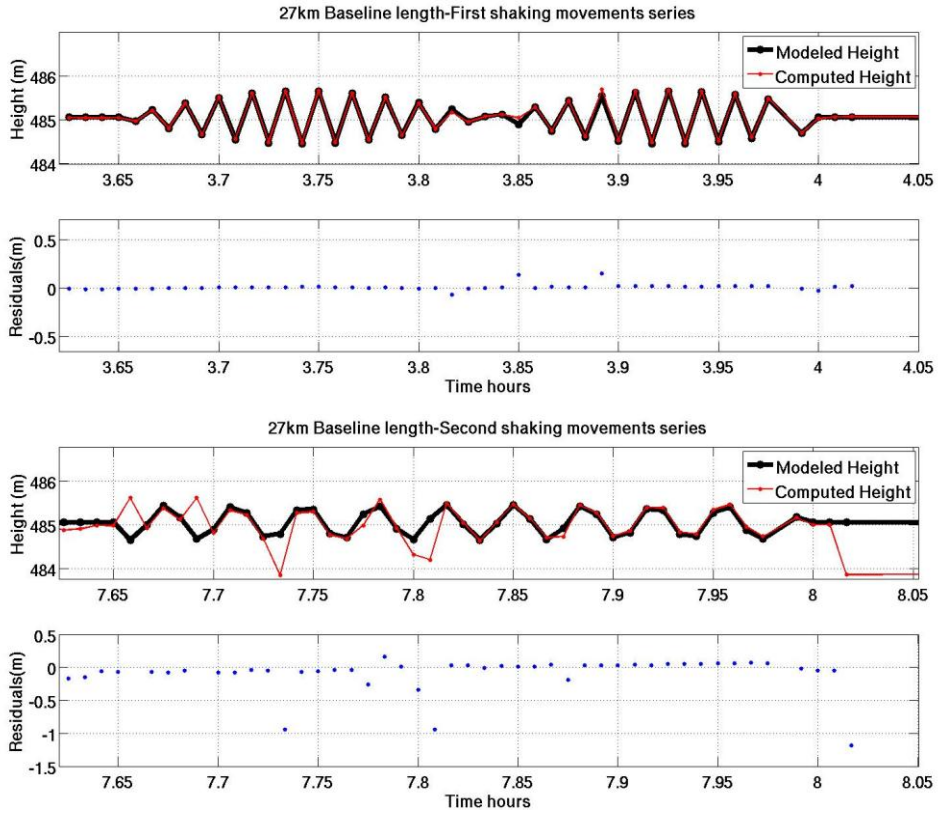

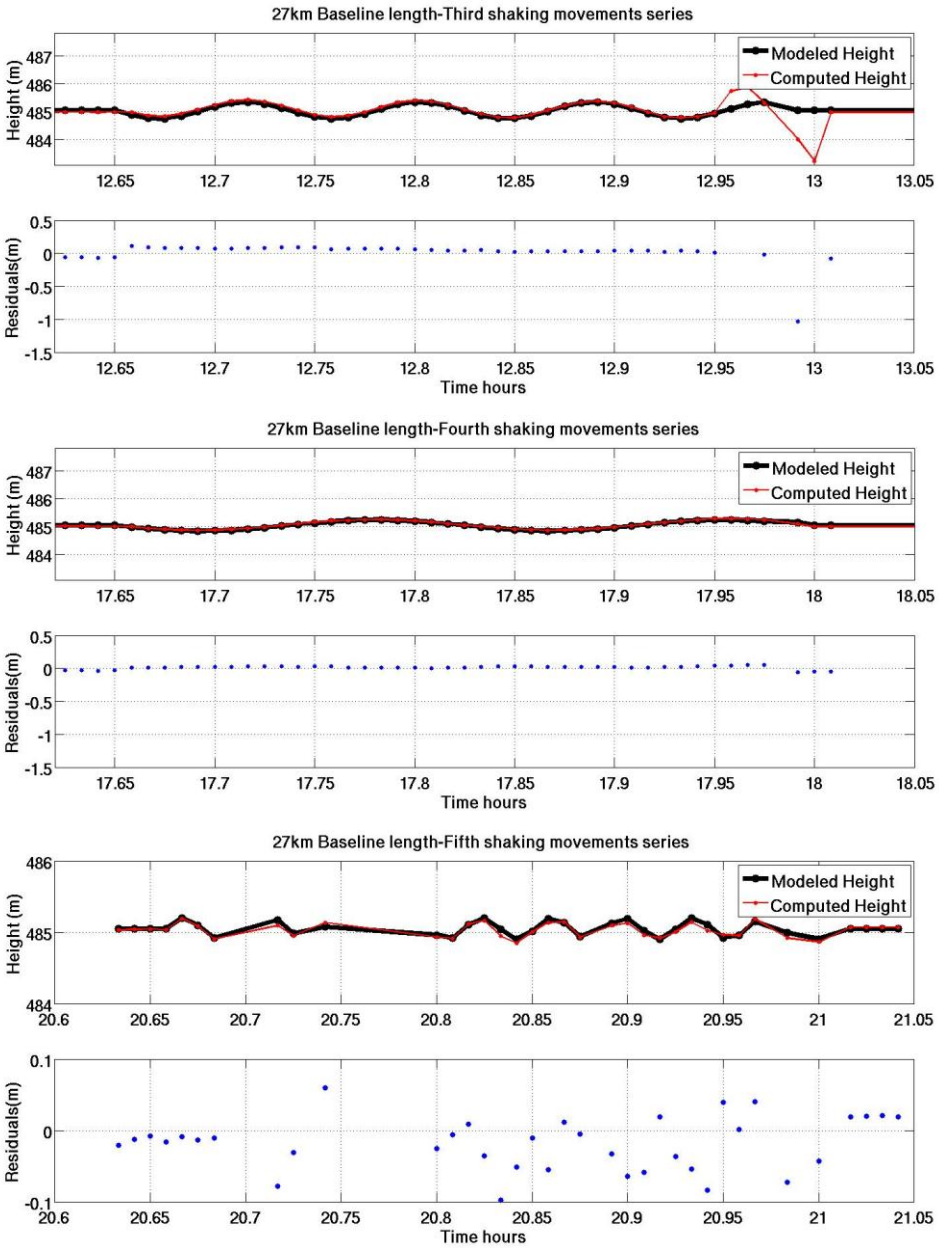

Figure C-4 The shaking test results for the five time windows -27 km baseline length.

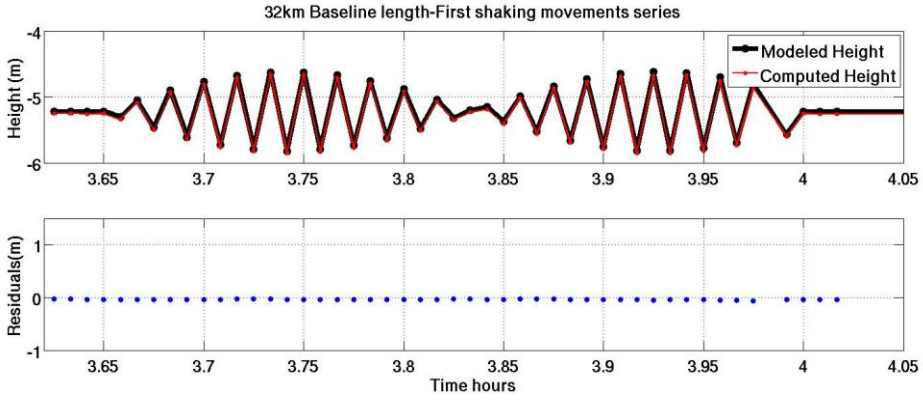

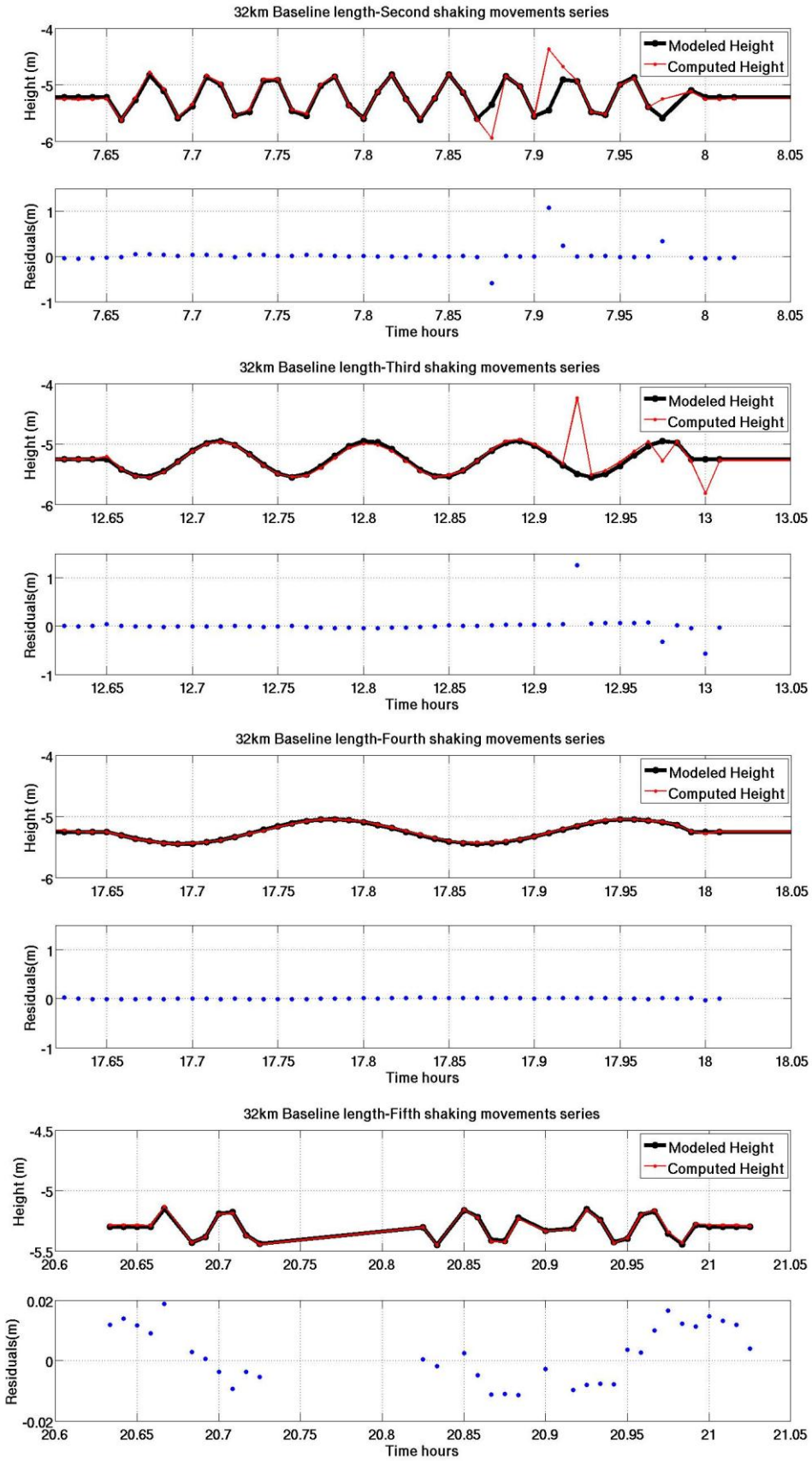

Figure C-5 The shaking test results for the five time windows -32 km baseline length.

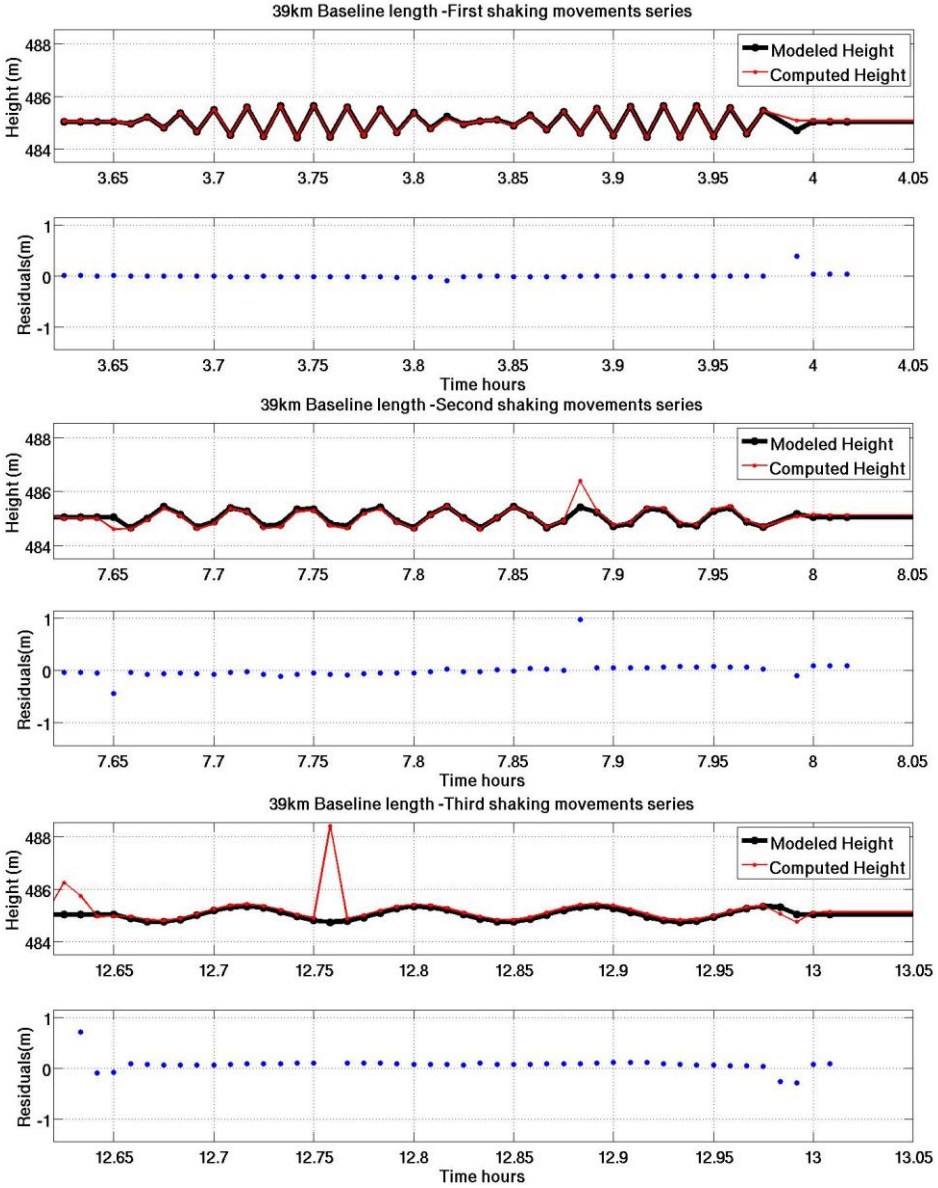
39km Baseline length -First shaking movements series
Modeled Height
Computed Height
Height (m)
Residuals(m)
Time hours
39km Baseline length -Second shaking movements series
Modeled Height
Computed Height
Height (m)
Residuals(m)
Time hours
39km Baseline length -Third shaking movements series
Modeled Height
Computed Height
Height (m)
Residuals(m)
Time hours

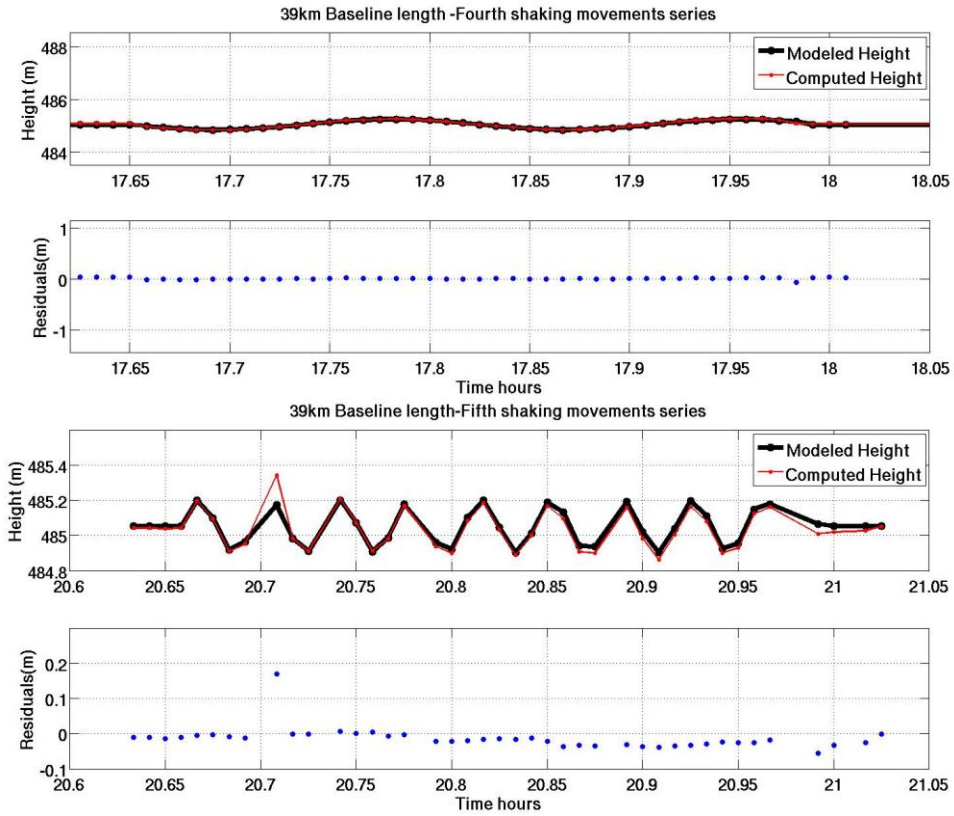

Figure C-6 The shaking test results for the five time windows -39 km baseline length.

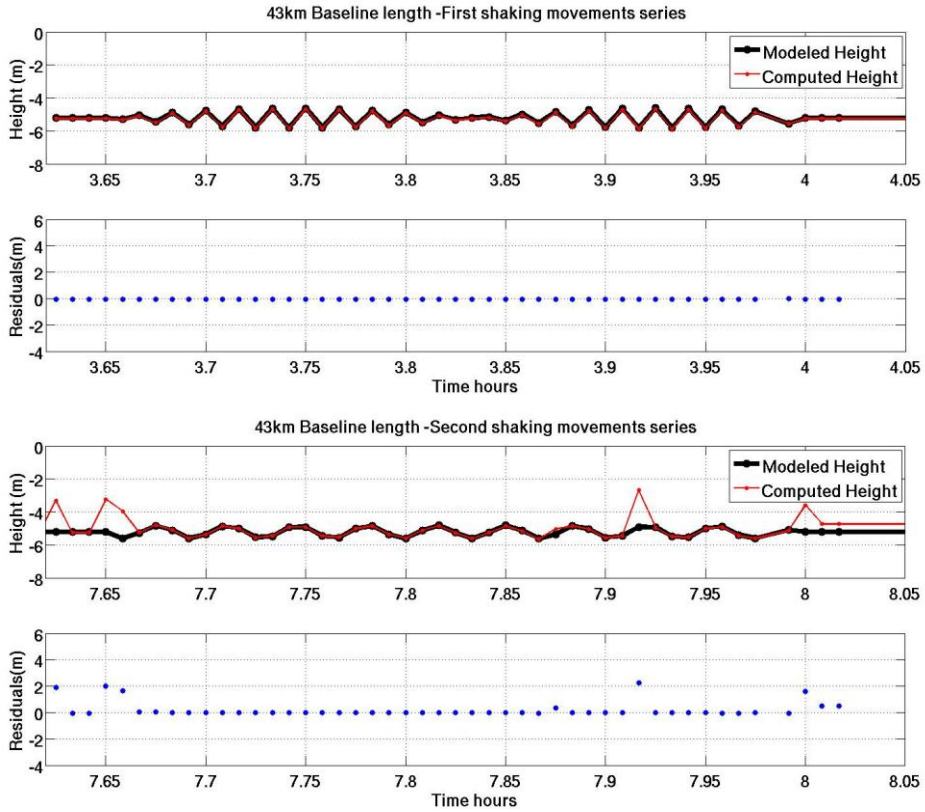

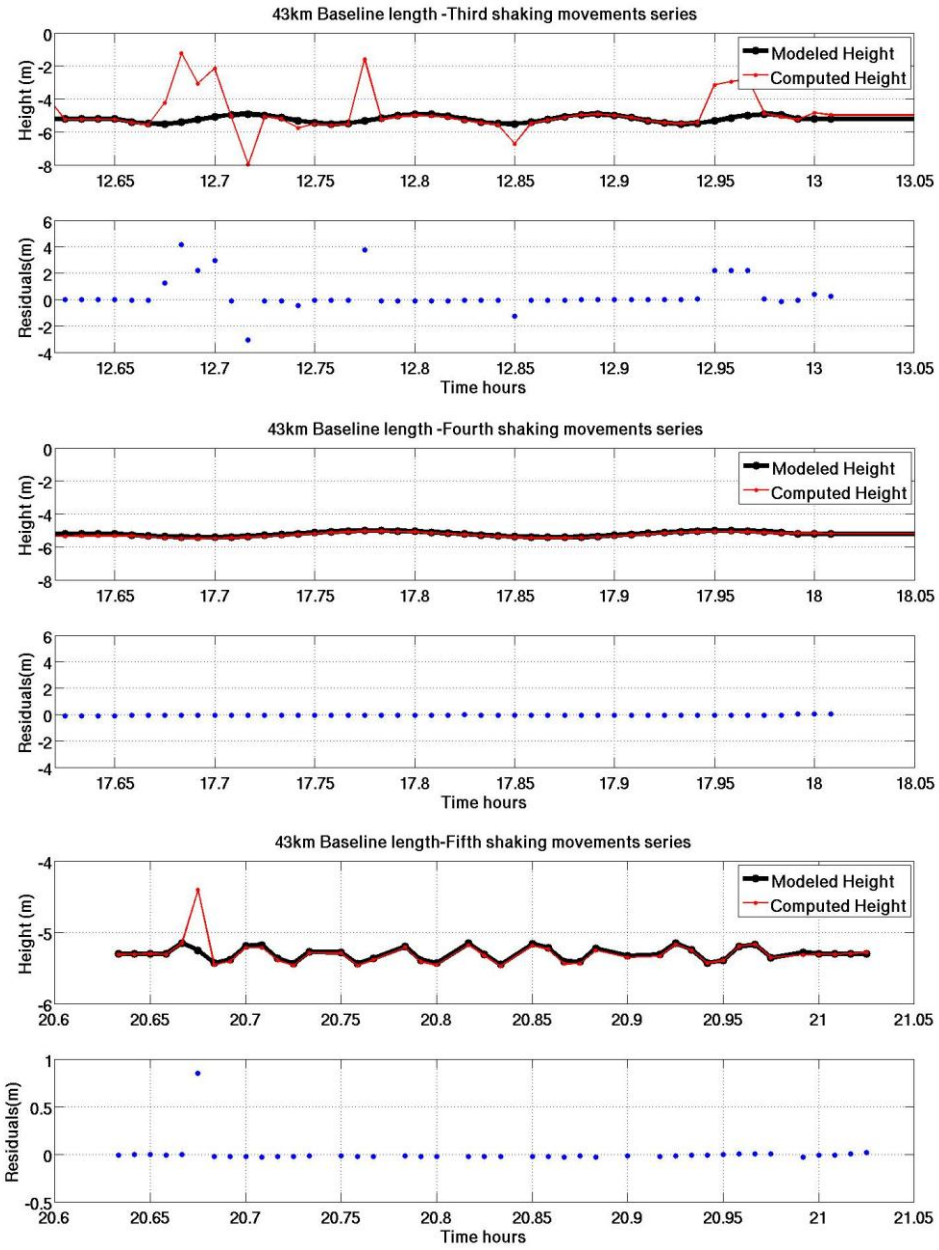

Figure C-7 The shaking test results for the five time windows -43 km baseline length.

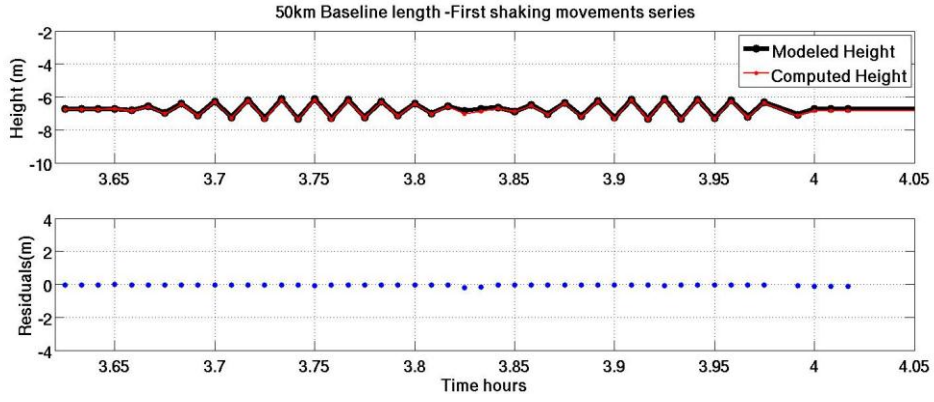

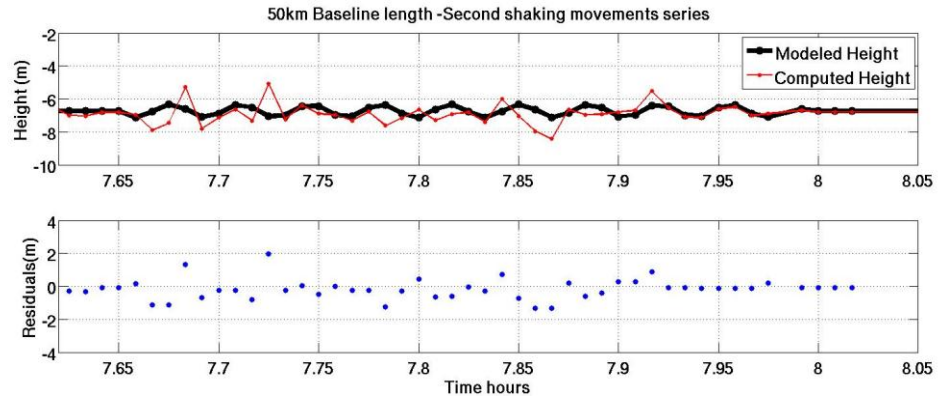
50km Baseline length -Second shaking movements series
Modeled Height
Computed Height
Height (m)
Residuals(m)
Time hours

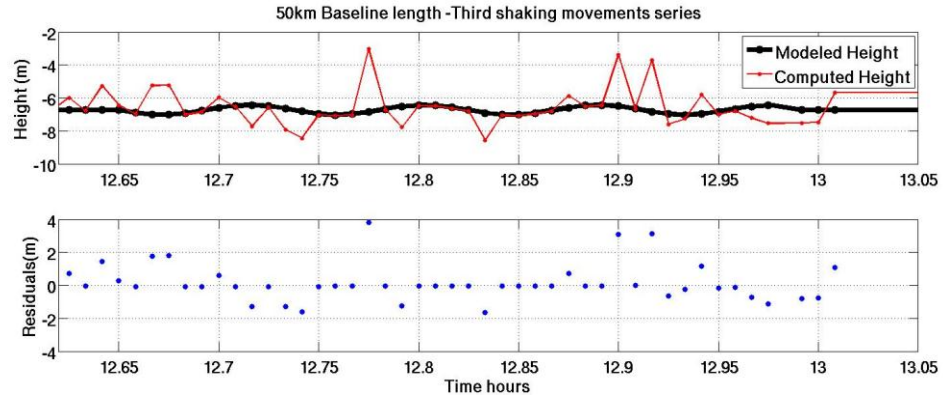
50km Baseline length -Third shaking movements series
Modeled Height
Computed Height
Height (m)
Residuals(m)
Time hours

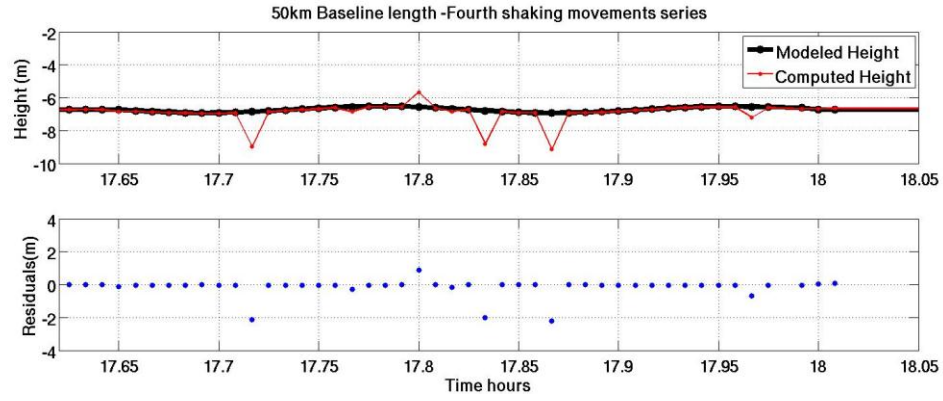
50km Baseline length -Fourth shaking movements series
Modeled Height
Computed Height
Height (m)
Residuals(m)
Time hours

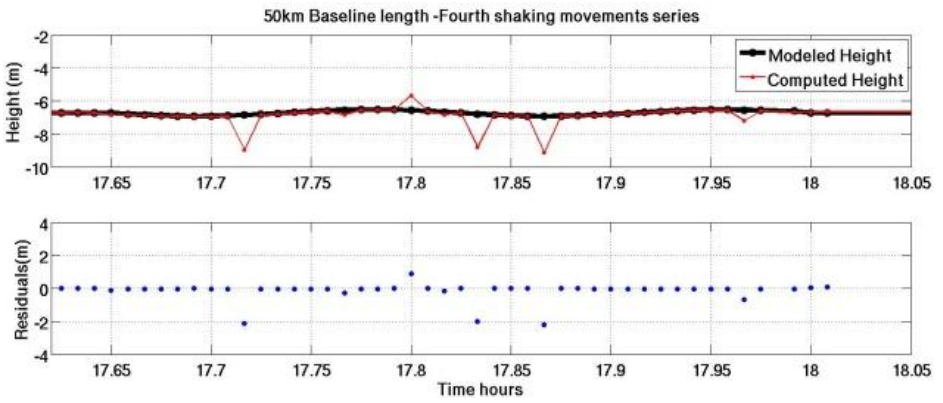
50km Baseline length -Fourth shaking movements series
Modeled Height
Computed Height
Height (m)
Residuals(m)
Time hours

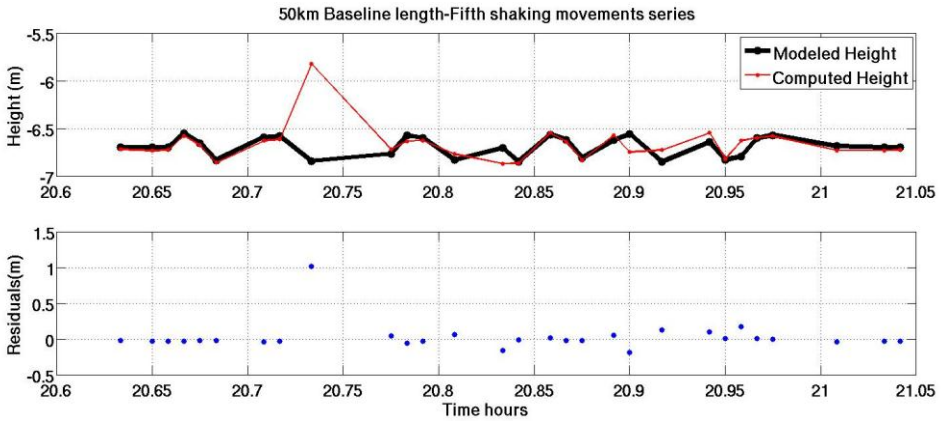

Figure C-8 The shaking test results for the five time windows -50 km baseline length.